



Durable ceramic materials for improvement of Proton Exchange Membrane electrolysis cells

Fenini, Filippo

Publication date:
2018

Document Version
Publisher's PDF, also known as Version of record

[Link back to DTU Orbit](#)

Citation (APA):
Fenini, F. (2018). *Durable ceramic materials for improvement of Proton Exchange Membrane electrolysis cells*. Technical University of Denmark.

General rights

Copyright and moral rights for the publications made accessible in the public portal are retained by the authors and/or other copyright owners and it is a condition of accessing publications that users recognise and abide by the legal requirements associated with these rights.

- Users may download and print one copy of any publication from the public portal for the purpose of private study or research.
- You may not further distribute the material or use it for any profit-making activity or commercial gain
- You may freely distribute the URL identifying the publication in the public portal

If you believe that this document breaches copyright please contact us providing details, and we will remove access to the work immediately and investigate your claim.

Durable ceramic materials for improvement of Proton Exchange Membrane electrolysis cells

Filippo Fenini

Risø Campus, 2018



DTU Energy

Department of Energy Conversion and Storage

Technical University of Denmark

Frederiksborgvej 399

Building 228

4000 Roskilde, Denmark

Phone +45 4525 3031

Preface

This thesis is submitted in candidacy for the PhD degree from the Technical University of Denmark (DTU) and it is based on the work carried at the Department of Energy Conversion and Storage in the period from October 15th 2015 to October 14th 2018. The project was mainly supervised by Professor Mogens Bjerg Mogensen and co-supervised by Senior Researcher Kent Kammer Hansen and Professor Peter Vang Hendriksen. The work was funded through the e-STORE project (contract no. 4106-00025B) by Innovationsfonden, Denmark. Three months of the work were carried out at the University of St Andrews, Scotland (UK), under the supervision of Professor John T. S. Irvine.

Risø Campus, Roskilde, October 14, 2018

Filippo Fenini

A handwritten signature in black ink, appearing to read 'Filippo Fenini'. The signature is stylized with a large initial 'F' and a long horizontal stroke.

Abstract

This work was devoted to explore different classes of oxides as potential auxiliary materials for Proton Exchange Membrane electrolysis cells (PEMEC) anodes. After the preparation of the materials, the stability in acid solutions was evaluated by chemical and electrochemical means. A conductivity target was defined as 0.1 S cm^{-1} at the temperatures of operation of a PEMEC, the typical conductivity of the electrolyte polymeric membrane.

Given the excellent corrosion stability of SnO_2 , the formation of a solid solution $\text{SnO}_2 - \text{Bi}_2\text{O}_3$ was studied to increase the *p*-type conductivity of tin oxide. Several compositions of Bi-doped SnO_2 were prepared with increasing cat.%_{Bi} (namely 0.5, 1, 1.5, 2, 3, 4, 5). The preparation procedure did not produce a solid solution. It was found that even for small cat.%_{Bi} the system was composed of a mixture of SnO_2 and $\text{Bi}_2\text{Sn}_2\text{O}_7$, a pyrochlore-structured secondary phase. Increasing the fraction of secondary phase decreased both the stability of the composites toward corrosion and the measured electrical conductivity, which did not meet the target of this study. An hypothesis was made, corroborated by evaluation of the activation energy for electrical conduction and microscopy analysis, that the nucleation of the pyrochlore phase at the grain boundaries of SnO_2 is at the origin of the decrease in conductivity and corrosion stability of the compounds.

Several compositions of MCr_2O_4 spinels (with $\text{M}=\text{Zn}, \text{Mg}, \text{Ni}, \text{NiFe}, \text{Mn}$) were prepared and tested. It was found that the materials possess excellent corrosion stability in acid conditions, but the electrical conductivity was below the target of this study. Doping with Cu and Li was conducted on NiCr_2O_4 and MnCr_2O_4 in order to increase the electrical conductivity. In the case of $\text{MnCu}_{0.25}\text{Cr}_{1.75}\text{O}_4$, $\text{MnLi}_{0.25}\text{Cr}_{1.75}\text{O}_4$ and $\text{MnLi}_{0.5}\text{Cr}_{1.5}\text{O}_4$ a pure cubic spinel phase was obtained. Compared with the conductivity of MnCr_2O_4 ($\sim 10^{-12} \text{ S cm}^{-1}$ at 70°C), the conductivity was increased to $\sim 10^{-10} \text{ S cm}^{-1}$ in the case of $\text{MnLi}_{0.25}\text{Cr}_{1.75}\text{O}_4$ and $\text{MnLi}_{0.5}\text{Cr}_{1.5}\text{O}_4$ and $\sim 10^{-4} \text{ S cm}^{-1}$ in the case of $\text{MnCu}_{0.25}\text{Cr}_{1.75}\text{O}_4$ at 70°C .

Electrochemical characterization was performed on $\text{MnCu}_{0.25}\text{Cr}_{1.75}\text{O}_4$ and NiCr_2O_4 . It was found that the material undergo only partial oxidation upon potential cycling up to 2.0 V vs SHE. It was demonstrated that HCrO_4^- and MnO_4^- are dissolution products of the materials as a consequence of the oxidation. A $\text{MnCu}_{0.25}\text{Cr}_{1.75}\text{O}_4$ -loaded PEM electrolysis cell was prepared and tested. The total cell resistance irreversible increased after increasing potentials steps. It was concluded that, despite the materials show excellent corrosion stability, the conductivity of spinel structured chromites is too low for the application in PEMEC.

Various compositions of spinel-structured MTi_2O_4 ($\text{M}=\text{Li}, \text{Mg}, \text{Mn}$) were prepared by

solid state synthesis. The materials showed high electrical conductivity at temperature of interest for a PEMEC ($\sim 30\text{-}100 \text{ S cm}^{-1}$), but it was found that they are unstable toward corrosion in acidic medium. A degradation mechanism of the materials in water was proposed, which encompass both dissolution and solid-state oxidation. It was concluded that despite the excellent electrical conductivity, MTi_2O_4 spinels are too unstable for the application in PEMEC anodes.

Resumé

Denne afhandling er fokuseret på udforskning af nye keramiske materialer som potentielt kunne anvendes som stabile strømsamlere og korrosions beskyttende afdækning af metalkomponenter i polymer elektrolyt membran elektrolyse celler (PEMEC). Efter fremstillingen af materialerne blev deres stabilitet i en stærk sur opløsning evalueret, både kemisk og elektrokemisk. Den typiske specifikke ledningsevne af en PEM er 0.1 S cm^{-1} , hvilket derfor blev fastsat som værende den laveste acceptable ledningsevne for de testede materialer. På grund af korrosionsstabiliteten af SnO_2 blev dotering af dette materiale undersøgt. Bi_2O_3 blev anvendt som dotant med henblik på at øge p-type ledningsevnen af SnO_2 . Forskellige kompositioner af Bi-doteret SnO_2 blev fremstillet, med stigende Bi kation % (cat.%_{Bi}, 0.5, 1, 1.5, 2, 3, 4 og 5%). Fremstillingsproceduren resulterede dog ikke i et enkeltfaset materiale, da det viste sig, at der ved selv små cat.%_{Bi} blev dannet $\text{Bi}_2\text{Sn}_2\text{O}_7$, som er en pyrochlor-struktureret sekundær fase. Ved en stigende brøkdel af denne sekundære fase blev der observeret et fald i både materialets korrosionsstabilitet og i den elektriske ledningsevne, der ikke levede op til den laveste acceptable ledningsevne. Der blev på baggrund af resultaterne opstillet følgende hypotese: faldet i både korrosionsstabiliteten og den elektriske ledningsevne skyldes en kimdannelse og vækst af pyrochlor-fasen i korngrænserne i SnO_2 . Denne hypotese er blevet bekræftet ved evaluering af aktiveringsenergien for den elektriske ledningsevne samt ved elektronmikroskopi.

En anden klasse af materialer, MCr_2O_4 spinel med $\text{M} = \text{Zn, Mg, Ni, NiFe}$ og Mn , blev fremstillet og testet. Denne klasse af materialer viste en fremragende korrosionsstabilitet i syreopløsninger, men deres elektriske ledningsevne var lavere end den laveste acceptable ledningsevne. Der blev derfor udført en dotering af NiCr_2O_4 og MnCr_2O_4 med Cu og Li for at øge den elektriske ledningsevne. Fremstillingsproceduren resulterede i en ren, kubisk spinel fase for materialerne $\text{MnCu}_{0.25}\text{Cr}_{1.75}\text{O}_4$, $\text{MnLi}_{0.25}\text{Cr}_{1.75}\text{O}_4$ og $\text{MnLi}_{0.5}\text{Cr}_{1.5}\text{O}_4$. Sammenlignet med ledningsevnen af den rene spinel $\text{MnCr}_2\text{O}_4 \sim 10^{-12} \text{ S cm}^{-1}$ ved 70°C , blev ledningsevnen forøget til $\sim 10^{-12} \text{ S cm}^{-1}$ for hhv. $\text{MnLi}_{0.25}\text{Cr}_{1.75}\text{O}_4$ og $\text{MnLi}_{0.5}\text{Cr}_{1.5}\text{O}_4$ og $\sim 10^{-12} \text{ S cm}^{-1}$ for materialet $\text{MnCu}_{0.25}\text{Cr}_{1.75}\text{O}_4$ ved 70°C . Elektrokemisk karakterisering blev udført af hhv. $\text{MnCu}_{0.25}\text{Cr}_{1.75}\text{O}_4$ og NiCr_2O_4 spinel. Ved den elektrokemiske karakterisering blev det fundet, at materialet kun undergår en delvis oxidering under periodiske ændringer i potentialet op til 2.0 V målt imod en standard hydrogen elektrode (cyklisk voltammetri). Det blev påvist, at der som følge af oxideringen dannes HCrO_4^- og MnO_4^- som opløsningsprodukter. En PEM elektrolyse celle som indeholdt $\text{MnCu}_{0.25}\text{Cr}_{1.75}\text{O}_4$ blev fremstillet og testet. Det blev her fundet, at den totale modstand i cellen målt ved samme elektrokemiske potential øges irreversibelt, når det påtrykte potential øges. Det blev derfor konkluderet, at på trods af disse spinel- materialers

fremragende korrosionsstabilitet, er de ikke anvendelige i PEMEC på grund af deres lave ledningsevne.

Titanoxid spinel med forskellige sammensætninger af MTi_2O_4 (M= Li, Mg, Mn) blev fremstillet via faststofsyntese og testet. Materialerne viste en høj elektrisk ledningsevne ($\sim 30-100 S cm^{-1}$) ved operationstemperaturen af PEMEC. Det blev dog fundet, at korrosionsstabiliteten af disse materialer i en sur opløsning ikke er tilstrækkelig. En degraderings mekanisme, som indeholder både opløsning og faststofoxidation af materialet, for disse materialer i vand er formuleret. Det konkluderes, at MTi_2O_4 ikke er anvendelig i PEMEC anoder på trods af deres høje elektriske ledningsevne på grund af deres manglende korrosionsstabilitet.

Abbreviations and relevant terminology

at.%	atomic percentage
BSD	Back Scattered Electrons Detector
cat.%	atomic percentage on the total cation content
CV	Cyclic Voltammetry
DI water	De-ionized water
E_f	Final potential in cyclic voltammetry
E_i	Initial potential in cyclic voltammetry
GC	Glassy Carbon
ICP-OES	Inductive Coupled Plasma Optical Emission Spectroscopy
mol.%	molar percentage
NGS	negative going sweep: in cyclic voltammetry, when the variation of the potential goes toward more negative potentials
OER	Oxygen Evolution Reaction
overpotential	the difference between the theoretical potential required for a process to run at a certain rate and the practical potential to achieve such rate. It can also refer to the difference between the standard electrochemical potential of a reaction and the potential at which the reaction produces a net current, assuming ideal behaviour.
PEMEC	Polymer Electrolyte Membrane Electrolysis Cell
PGS	positive going sweep: in cyclic voltammetry, when the variation of the potential goes toward more positive potentials
polarization	when an electrode is polarized, it experiences a potential difference in electrochemical potential compared with the other electrode; electrochemical work can then be carried out on the electrodes.
R(R)DE	Rotating (Ring) Disk Electrode
rpm	Revolutions per minute

Abbreviations and relevant terminology

SED	Secondary Electrons Detector
SEM	Scanning Electron Microscope
SHE	Standard Hydrogen Electrode
w.%	weight percentage
XPS	X-ray Photoelectron Spectroscopy
XRD	X-ray Diffraction

Acknowledgements

Thank you to my main supervisor *Mogens Mogensen* for being always a support and a source of new approaches and points of view on a topic that we discovered to carry so many implications and different aspects to consider. You always devoted precision and accuracy to explain scientific concepts, that has been a great teaching for me. You kept my feet on the ground when I was flying away with strange ideas or when I was digging down because of some even stranger result. Thank you to *Kent Hansen*, my co-supervisor, for being always open to discuss new ideas and experiments.

Many thanks to professor *John Irvine* for having me as a guest in his group and for the many concepts and practical aspects in solid state chemistry that I learned during my staying there; the whole JTSI group, especially *Cristian* and *Paul*, is acknowledged for being very helpful and welcoming

I greatly acknowledge *Günther Scherer* for the invaluable support and scientific advices that he gave to me through these years. Thank you, I always regarded happily your visits to Risø and I enjoyed very much all the discussions we had on so many different topics.

A big thank you goes to *Johan Hjelm*: beside always enjoying talking with you, I have to thank you for the many theoretical and practical discussion on electrochemistry, which triggered and made develop many of the results that are contained in this thesis; thank you for introducing (I could say 'enlightening') me on the use of Python and its potential in research and data analysis, it completely changed my way of working.

I wish to say thank you to Professor *Poul Norby* and *Rune Johansen*: many thanks for the help in the use of FullProf and in the concepts of structural analysis, and for always being available when I needed to collect one more pattern.

Thank you to *Katrine*, *Steffen*, *Saeed*, *Anders*, *Laila* and all the people part of the e-STORE project, for the good work done together and for making our meetings always very enjoyable.

A special thank you goes to *Alexandra Ploner*: we literally lived these years together! Many occasion appeared for having good time and dealing with problems, both scientifically and not, and you have always been there. You are a great scientist and a big friend. One of the best examples of commitment I will carry with me will be a typical conversation of ours when I was telling you about a movie I liked and you were answering about the loss of percolation of Ni particles in the proximity of the outlet.

Thank you to all my office mates in K23 during these year, from *Kristian* and *Roberto*, to the most recent, *Daniel*, *Doris* and *Marco*. Thank you for the coffee, cakes, cigarettes, we shared in these years, together with the useful discussions about science when we

needed it. The absolute informality we used in those helped in make them valuable, I believe (we can call it a science-in-flip-flops approach). I am happy we created a kind of personal Python workshop (in italian I would write 'officina'), I think it made us more productive and more willing to achieve.

Thank you to all the *friends in Risø*, PhDs, visiting, Master students, that I met in these three years, which indeed have been very long and rapid. It has been great to meet you all. Thank you also to the *friends outside Risø*, and outside Denmark in general, for always being there when I was back, despite my geographical and social disappearings.

Thank you to my parents, thank you so much for always being supportive and believing in me through these years.

Finally, a big kiss to my girlfriend *Sara*: we started this together, we know that. From when I was trying to reach you on the way to the office from the Risø Huse, it looks a long road. Indeed we made a lot, all and all (mostly flying). I thank you for everything you made for me, for all your push, and smiling, and patience that helped me to accomplish this. It's done! I am back.

Contents

Preface	i
Abstract	iii
Resumé	v
Abbreviations and relevant terminology	vii
Acknowledgements	ix
Contents	xi
1 Introduction	1
1.1 Background	1
1.2 Electrolysis of water for H ₂ production	4
1.3 PEMEC limiting factor: the anode compartment	9
1.4 Motivation and scope of the work	13
2 Preparation and Characterization techniques	15
2.1 Materials preparation	15
2.2 Structural characterization	16
2.3 Electrochemical characterization	19
2.4 Conductivity measurements	25
2.5 Chemical corrosion test	27
3 Materials: Choice, preparation and characterization	31
3.1 Bi-SnO ₂	31
3.2 Spinel	36
3.2.1 MCr ₂ O ₄	38
3.2.2 MTi ₂ O ₄	47
4 Materials: Properties	57
4.1 Bi-SnO ₂	57
4.2 Spinel	59
4.2.1 MCr ₂ O ₄	59
4.2.2 MTi ₂ O ₄	65
5 Electrochemical Characterization	73

Contents

5.1 Tafel plots and EIS on Ti felt	73
5.2 RRDE studies	77
5.3 Cell testing	94
6 General discussion, conclusion and outlook	99
Bibliography	103
A Materials and chemicals	113
B Ti felt surface area	115
C Ink formulation trials	117
D Publications and contributions	

CHAPTER 1

Introduction

1.1 Background

Renewable energy sources are nowadays a proved reality and constitute a real and economically feasible alternative to fossil fuels powered plants. In most of the developed countries, much effort is being devoted to increase the share of electricity produced by renewable sources, in order to reduce CO₂ emissions and limit the dependence on unevenly distributed oil and gas deposits. European Union has a long-standing commitment in increasing the renewable share in the energy production of the Union, with the objective of reaching a 20% global share by 2020 [1]. By 2016, 11 member States already fulfilled such targets [2]. Nonetheless, many emerging economies such as Brazil, China, India and Indonesia ranked in the top five countries for annual investment in renewable sources installation [3]. By the end of 2017, three out of five position in the ranking of the highest renewable capacity were occupied by emerging economies, with China leading in the total hydropower, solar photovoltaics (PV) and wind power capacity installed.

Indeed, installed capacity of renewable energy has grown at an increasing pace over the last years, partly due to the decreasing in installation cost of the enabling technology of such sources. For example, PV and wind turbines installation cost has decreased to 1/5 and 2/3 respectively from 2008 to 2015 [5]. However, as can be seen in figure 1.1, the growth of total installed capacity did not cause a congruent growth in renewably

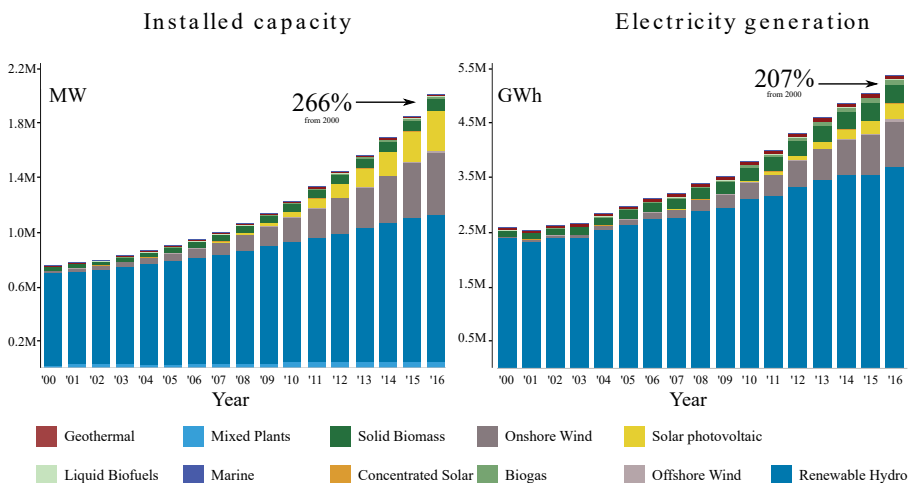


Figure 1.1: Installed capacity and electricity generation of renewable sources from 2000 to 2016. The percentage at 2016 indicate the increase where 100% is the value in 2000 (adapted from [4]).

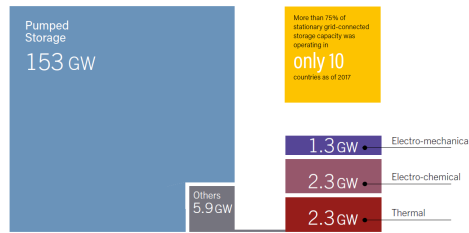


Figure 1.2: Installed storage capacity at 2017 (adapted from [3]).

generated electricity. This circumstance is easily understood if one takes in account the unpredictability and the intermittent nature of the most abundant renewable energy sources, such as wind and sunlight. Power plants are not stand alone units which can act independently but they are connected through the electrical grid. The grid must comply to the energy demand by delivering the required power while ensuring overall stable operation, and a high penetration of renewable sources in the energy system may introduce serious complications to the balancing of the grid [6]. In these terms, a failure to meet the energy demand due to insufficient production of energy (ex. several cloudy days in the case of PVs) may be as harmful as over-production compared to the required energy, which needs to match the injected energy to keep the frequency stable at the nominal grid value. In the latter case, the surplus energy is either lost or needs to be injected to another energy market. The phenomenon of *negative pricing* of the energy is becoming more common lately in countries with a high number of wind farms such as Denmark and Sweden; some states such as China, California and Germany were even forced to give up part of the renewable plants installed to ensure grid stability [7]. The primary technological concern is shifting from producing carbon-free and economically sustainable energy to ensuring the reliability of non-conventional energy sources in an energy market scenario.

Energy storage and energy conversion

The origin of the limitations in renewable energy production is the lack of sufficient electricity **storage** capacity of the energy produced by renewable source. Conventional power plants operations are finely tuned to match the consumption foreseen in advance by the final users but they also can respond fast by the activation of redundant capacity. They are *dispatchable* generators, the energy can be produced when needed. This principle cannot be applied to renewable sources, which are usually referred as *non-dispatchable* generators. The harvested resource is the limiting and controlling factor and the energy must be produced when *available*, which does not necessarily coincide to when it is needed. The International Renewable Energy Agency (IRENA) explicitly stated in a recent report [8] that energy storage will be the at the heart of the energy transition: the solid availability of conventional power sources will be ensured by coupling renewable energy generation to efficient energy storage. Figure 1.2 shows the total installed storage capacity worldwide. Pumped hydro storage greatly distances all

the other technologies combined: it is an established and reliable technology, but it is geographically limited by land morphology and carries very low energy density. Other forms of storage of electricity as such include electro-mechanical storage, namely the fly wheel technology, and electro-chemical storage, with the plethora of battery types, super capacitors, redox flow batteries to cite the most famous [7, 8]. These devices effectively store electricity, which can be released at a later stage. The efficiency of the charge-discharge cycle (a.k.a 'round-trip' efficiency) are generally high ($> 80\%$ [9]). Nonetheless, there is not a technology which can be regarded as the sole and absolute course of electricity storage, since all these technologies possess different response times and power density. Each application may need different levels of power, stability and autonomy and different electrical storage will then fit better. It is now clear that an energy management where storage is part of the core will be a multi-strategy approach where several technologies each best fitted for a specific location or application will need to communicate and cooperate efficiently and flawlessly.

A different approach to energy storage comes into place when the electricity is stored in a carrier which can be physically taken away from the location where the electricity is stored. In that case, electricity is transformed into a new form of energy, often by using part of it to drive chemical reactions, and one can properly define the process as energy **conversion**. Separating the storage carrier from the converting device effectively decouples the storage capacity from the size of the device itself. Similarly to pumped hydro power, even a low-energy-density form of storage becomes attractive when the capacity is only linked to the size of the storehouse where the carrier is held.

Electricity to chemicals in a renewable energy system

Historically, the major process where electricity is converted into chemicals has been electrolysis. The whole Cl_2 and chloro-alkali industry is based on either brine or molten salt electrolysis [10] and all the metallic Al produced worldwide is made by electrolysis of Al_2O_3 via the Hall-Héroult process [11]. The attention on electrochemical energy conversion fostered by the need of storage capacity is also giving momentum to other concepts of energy conversion, often referred as power-to-gas and power-to-chemical operations, to produce chemicals which are conventionally produced from fossil fuels [12]. Most notably, CO_2 electro-reduction [13] and NH_3 electro-synthesis [14] are lately receiving enormous interest. Indeed, fossil reserves exploitation are only partly devoted to energy production, and our society is dependent from petrochemical industry in so many applications. Therefore, emergence of a non-fossil energy system is calling for a change in paradigm on a wide scale. I already discussed how renewable energy production is inherently linked to energy storage development. To relinquish carbon-based reserves implies also finding alternative approaches to the production of commodities of essential importance, such as chemicals, synthetic materials, pharmaceutical products and fertilizers.

In this scenario, electrolysis of water is meant to acquire an immense importance in a post-fossil fuels economy. The products of water electrolysis are H_2 and O_2 . H_2 can act as both an energy carrier and an industrial commodity. As a fuel, it carries

the highest specific energy compared even with gasoline and coal, it can be burnt without any polluting emission to produce heat or be transformed back to electricity by the use of a fuel cell. Probably more significantly, hydrogen is employed in many relevant industrial processes for chemical, metallurgical and food industry. To visualize the fundamental importance of H_2 as a commodity it is enough to write down the reaction $3H_2 + N_2 \rightarrow 2NH_3$ and then have a look to any prediction of Earth's population growth. It is currently produced mainly by steam reforming of methane, an energy intensive process which accounts for almost 2% of the total world energy production [7].

Many studies evaluated that oil and coal reserves will not be exhausted before many decades [7]. Even so, the necessity of going beyond fossil fuels is pressing: CO_2 level increase and pollution naturally related to carbon-materials combustion are developing more and more concern in a public opinion with an unprecedented level of awareness of the environmental issue. In my opinion, it is electrochemistry that will provide the tools for both a sustainable energy system and a circular economy.

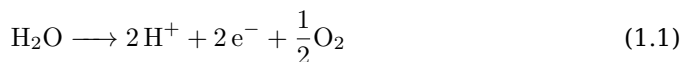
1.2 Electrolysis of water for H_2 production

Electrolysis indicates a process where energy in the form of electricity is used to drive a non-spontaneous reaction. The process is conducted in an electrochemical cell, composed of an *anode* and a *cathode*, the electrodes where oxidation and reduction take place respectively. The electrodes are separated by the *electrolyte*, an ion conducting medium. The presence of the electrolyte prevents direct electronic conduction between cathode and anode and allows the electrodes to polarize when a potential is applied.

In the case of water electrolysis, water is split into gaseous H_2 and O_2 . The reaction can be split into its constituent half-reactions, and in the case of acidic environments it can be written as:

Anode

Oxygen Evolution Reaction (OER)



$$E^\circ = 1.23 \text{ V vs SHE}$$

Cathode

Hydrogen Evolution Reaction (HER)



$$E^\circ = 0.00 \text{ V vs SHE}$$

$$(1.3)$$

Total

Water Splitting Reaction (WSR)



The reaction can be driven both in acidic and alkaline environment. The standard potentials of the single half-reaction depend on the pH of the environment, but the standard reversible potential E° is fixed to 1.23 V vs SHE by the ΔG° of the reaction. Since H₂ and O₂ are elemental molecules, $\Delta G^\circ = -\Delta_f G_{\text{H}_2\text{O}(l)}^\circ$, where $\Delta_f G_{\text{H}_2\text{O}(l)}^\circ$ is the free energy of formation of water and it is equal to -237.35 kJ mol⁻¹ [15]. The ΔG° of the reaction is positive and therefore energy must be provided for the reaction to occur. It is noteworthy to mention that $\Delta_f H_{\text{H}_2\text{O}(l)}^\circ = -285.8 \text{ kJ mol}^{-1}$; the final value ΔG° is lower due to the positive value of ΔS° related to the reaction (every two molecules of water three molecules of gas are formed). It is possible to define a *thermoneutral* potential as $E_{TN} = -nF\Delta H^\circ = 1.48 \text{ V}$ at which the difference in potential is big enough to deliver all the energy required by the electrolysis processes and the reaction can proceed adiabatically [16]. This implies that the reaction can occur with a potential difference equal to E° , but the reaction will absorb heat from the environment to come to completion. External heating must be continuously provided for the reaction to occur isothermally at potentials below E_{TN} . Since both ΔH° and ΔS° are positive, electrolysis of water will benefit in general from increasing the temperature at which the reaction is conducted [17]. ΔG will eventually become negative at high temperatures. In fact, ΔG is still negative at 1000°C [18].

In practice, the potential of an operating electrolysis cell can be much different from E° . Other electrochemical and electrical contribution will increase the overall cell potential difference E_{cell} , which can be expressed as :

$$E_{cell} = E_{rev} + \eta_{anode} + \eta_{cathode} + IR_\Omega + \eta_{mass} \quad (1.5)$$

In equation 1.5, E_{rev} is the theoretical thermodynamic equilibrium potential of the reaction 1.4 at the temperature and pressure at which the cell is operated.. The overpotential contributions, η , refer to the extra potential that needs to be applied to the cell in order to achieve the desired rate.

- η_{anode} and $\eta_{cathode}$ can be described as the kinetic overpotentials, since they are related to actual rate of the reaction which produces the current running through the cell. As modeled by the known equation of Butler-Volmer [19], a certain overpotential is always required to run a reaction in the anodic or cathodic direction. Such overpotentials depend on the energy barrier that is necessary to overcome in order to obtain the products, consequently they are not specific of the reaction but rather of the the reaction taking place on the electrode material (catalyst).
- IR_Ω refers to the voltage that is required to run the cell current I through R_Ω according to Ohm's law, where R_Ω is the sum of the purely ohmic resistances arising

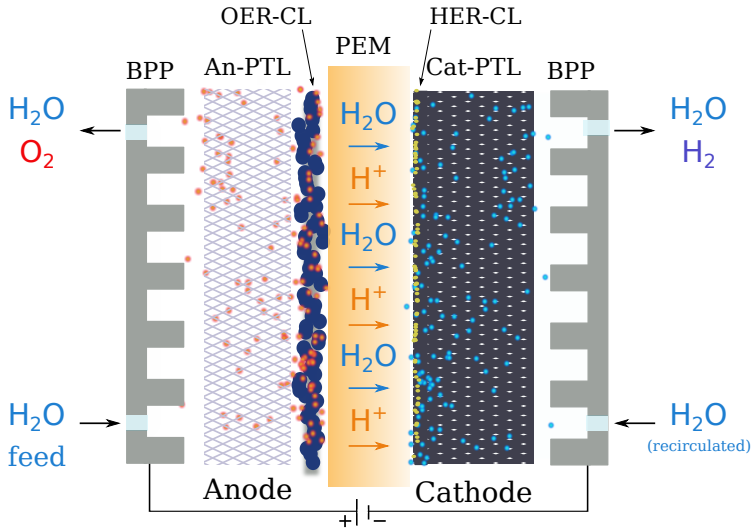


Figure 1.3: Schematic representation of a PEM electrolysis cell.

from the components that constitute the cell itself.

- η_{mass} refers to the mass transport overpotential, which arises when current densities are so high that the mass flow rate of reactant reaching the electrode becomes the limiting factor of the reaction itself.

Proton Exchange Membrane Electrolysis Cell

The technology of water electrolysis is commonly classified in terms of type of electrolyte, since it determines all the other components or conditions a cell need in order to operate (e.g. catalyst material, metallic components, temperature of operation etc.). Three types of electrolyte are conventionally reported: (i) Alkaline Electrolysis Cells (AEC), (ii) Solid Oxide Electrolysis Cells and (iii) Proton Exchange Membranes Electrolysis Cells (PEMEC).

Figure 1.3 depicts a scheme of a typical configuration of a PEM electrolysis cell [20]. Anode and cathode are separated by the electrolyte (PEM) which is a solid proton-conducting membrane. It is constituted by a perfluorosulfonated polymer, also referred as perfluorosulfonic acid (PFSA) given its ability to easily exchange protons at the sulfonated groups [21]. Therefore, the membrane is regarded as being acidic in nature. The fluorinated backbone gives structural and chemical stability. Conventional PFSA membranes need to be hydrated to conduct protons, thus the temperatures of unpresurized operations must be kept $< 100^{\circ}\text{C}$. Many types of membranes are currently available (e.g. Nafion[®] (DuPont), Aquivion[®] (Solvay), Flemion[®] (AGC Chemicals Americas)) with different chain lengths, number of branches and degree of sulfonation. During cell operation, H_2O , which is fed from the anode, is transported to the cathode due to electro-osmotic drag.

	AEC	PEMEC	SOEC
Operation parameters			
Cell temperature (°C)	60-90	50-80	700-900
Typical pressure (bar)	10-30	20-50	1-15
Current density (A cm ⁻²)	0.25-0.45	1.0-2.0	0.3-1.0
Flexibility			
Load flexibility (% of nominal load)	20-100	0-100	-100/+100
Cold start-up time	1-2 h	5-10 min	hours
Warm start-up time	1-5 min	< 10 s	15 min
Efficiency			
Nominal stack efficiency (LHV)	63-71%	60-68%	100%*
... specific energy consumption (kWh Nm ⁻³)	4.2-4.8	4.4-5.0	3
Nominal system † efficiency (LHV)	51-60%	46-60%	76-81%
... specific energy consumption (kWh Nm ⁻³)	5.0-5.9	5.0-6.5	3.7-3.9
Available capacity			
Max. Nominal power per stack (MW)	6	2	< 0.01
H ₂ production per stack (Nm ³ h ⁻¹)	1400	400	< 10
Cell area (m ²)	< 3.6	< 0.13	< 0.06
Durability			
Life time (kh)	55-120	60-100	(8-20)‡
Efficiency degradation (%/a)	0.25-1-5	0.5-2.5	3-50
Economic parameters			
Investment cost (€ kW ⁻¹)	800-1500	1400-2100	(> 2000)‡
Maintenance costs (% of investment costs per year)	2-3	3-5	n.a.

* Operating at thermoneutral voltage

† Including auxiliaries heat supply (SOEC)

‡ High uncertainty due to pre-commercial status of SOEC

Table 1.1: Summary of parameters of state-of-the-art of water electrolysis technologies, reproduced with permission from [17] Copyright © 2018 Elsevier

The electrodes are constituted by the catalyst layers (CL) in contact with the electrolyte where OER and HER take place. The water goes through the anode porous transport layer¹ (An-PTL) and reaches the catalyst layer (OER-CL) where it is split in O₂ and H⁺ according to reaction 1.1. Protons travel through the membrane and reach the cathode catalyst layer (HER-CL) where they are reduced and recombined in H₂ according to reaction 1.2. Hydrogen then leaves the compartment through the cathode porous transport layer (Cat-PTL) together with the water which was dragged through the membrane. The cell is encased in bipolar plates (BPPs) which distribute the current to the whole cell. They are usually carved with flow channels to guarantee in-flow of reactant and out-flow of products.

Differently from PEM fuel cells, anode and cathode compartments are very different in PEMEC. The cathode compartment is similar to the electrodes found in fuel cells: it is constituted by a carbon-based PTL (e.g. carbon paper) and the catalyst contained in

¹Porous transport layers are also referred as Current Collectors in the literature.

the HER-CL is Pt, which offers the minimum η for hydrogen evolution in acidic medium.

The catalyst in OER-CL is most commonly IrO₂ or a solid-solution IrO₂ - RuO₂, which are the best known catalyst for OER reaction in acidic medium². The anode compartment is exposed to very oxidising conditions given the high overpotentials that are required for running OER. As a consequence, carbon-based materials cannot be used as PTLs because carbon is oxidised very rapidly in such conditions [24] leading to degradation of the whole PTL-CL assembly in the anode. The acidic environment created by the PFSA further limits the range of materials that can be used in the anode compartment. Ti is usually used as material for An-PLTs, given its excellent corrosion resistance after the surface is passivated with an oxide layer. Typical An-PLTs come in the shape of fibrous/porous bodies of metallic Ti to ensure the necessary flow.

PEMEC technology encompasses the key features required for a renewables-driven energy conversion device. Table 1.1 compares the three different electrolysis technologies with some data of technological relevance. The high ionic conductivity of PFSA membranes greatly reduces the ohmic resistance of the cell. It is able to deliver high current density in a broad dynamic range. The low permeability to gases of PFSA membranes implies that the H₂ produced is of very high purity: while AEC deliver hydrogen at a purity level close to 99.8 which later requires further purification processes, PEMEC can produce H₂ with a purity level of 99.999 (a grade acceptable for use in fuel cells) [25]. This characteristic as well determines the broad dynamic range of PEMEC, since even at low current densities the interdiffusion of H₂ and O₂ between the electrodes through the membrane is still very small and the formation of hazardous gas mixtures is prevented. The good mechanical stability of PFSA membranes also allows to operate at differential pressure between cathode and anode; H₂ needs to be compressed in order to be stored and the production of an already partially pressurized gas decreases the costs related to storage. Nonetheless, it should be mentioned that pressurized operations increase the diffusion of H₂ to the anode compartment, as a result the dynamic is reduced. Fast system response and start time are unmatched when compared with the other technologies (SOEC need to remain in idle operation during inactivity time due to extremely long heat-up cycles) and well cope with the variability and unpredictability of renewable electricity generation [26]. PEMEC are extremely compact compared with AEC, so they can easily be delivered in modular units that allow both centralized and distributed hydrogen generation. Typically, companies deliver PEMEC stacks in containers which combine within the water management and purification system and all the balance of plant required for the stack to operate [27, 28].

In conclusion, PEMEC technology is extremely attractive for hydrogen generation.

²RuO₂ requires the smallest overpotential for OER [22] but it also undergoes dissolution while O₂ is evolved. IrO₂ is slightly less active but much more stable, consequently it is the only catalyst with technological relevance. Solid solutions IrO₂ - RuO₂ are attempts to increase catalyst activity while maintaining an acceptable stability. Danilovic *et al.* [23] recently studied the activity-stability relation of several electrochemically grown metal oxides, including Pt, Au, Ir, Ru and Os. Interestingly, they showed that the activity increased as the tendency of metals to bind oxygen increased, and then followed the series Au \ll Pt \ll Ir \ll Ru \ll Os. Osmium oxide showed the smallest η toward oxygen evolution by far. Yet, the dissolution proneness was close to four times the one of ruthenium oxide and therefore the material as such does not carry any technological interest.

Differently from SOEC, they are currently in the commercialization stage, even if limited to small and medium sized units. The reason is predominantly the higher capital cost compared with the more mature technology of alkaline electrolysis, which requires close to half the capital investment compared to PEMECs technology. The following section is dedicated to describe the origin of such higher cost and the efforts to date conducted to improve the competitiveness of PEMEC technology.

1.3 PEMEC limiting factor: the anode compartment

The concept of PEM electrolysis was developed by General Electric Co. (USA) in the late '60s in the framework of the space race, with potential of other specialized application, such as delivery of breathable air in submarines. The first scientific publication on PEM (or SPE, solid polymer electrolyte, as it was also referred in the past) was made by Russel, Nuttal and Fickett in 1973 [29]. Even if PEM fuel cells and PEM electrolyzers are not very different in terms of 'age' of the technology, PEMECs have only partially benefited from the enormous effort invested in the development of PEM fuel cells over the last decades [30]. Better and thinner membrane contributed to decreasing the overall cell resistance. The loading of Pt on the cathode side have been reduced sensibly since the first demonstrations down to the fraction of $\text{mg}_{\text{Pt}} \text{cm}^{-2}$ that are now state-of-the-art [20] but the loading of IrO_2 are still on the order of $\text{mg}_{\text{Ir}} \text{cm}^{-2}$, 5-10 times the loading of Pt on the cathode side. Moreover, the type and morphology of An-PTLs did not change much from the first demonstrations of the technology in the 1980's [31, 32].

The conditions experienced by the material of the anode compartment are commonly referred as harsh, due to the concurrence of low pH (as a consequence of the presence of the proton exchange membrane) and very oxidising environment (the materials must withstand the high potential deployed to run OER while immersed in O_2 -saturated water).

As a matter of fact, the actual pH encountered in contact with the PEM membrane has not been rigorously defined. The most common values reported tell a pH of 0-3, but they are only an estimation [20, 33, 34]. Moreover, measurement of the pH conducted on the outlet water in PEM fuel cells reported considerably higher values, with $\text{pH}=3.5$ - 5.5 [35, 36]. Langemann *et al.* [37] measured the pH of the recirculated water fed to the cathode and to the anode of a PEMEC and observed a decreased in the pH value after 50 h of operation to a value of 3.5 and 4.5 for anode and cathode respectively³. It is possible to imagine even higher values of pH in the case of a PEMEC, given the fact that the electrodes are flooded with water during operation.

If the value of the pH experienced in contact with the proton conducting membrane is still a debate, high potential is an inherent reality in the anode compartment. Assuming

³Here the schematic structure of the cells used in reference [36] (fuel cell) and [37] (electrolysis cell) are reported. Reference [35] only reported the data without specifying the structure of the cell used for the measurements. From left to right, from anode to cathode:

[36]: carbon paper | 0.2 or 0.4 $\text{mg}_{\text{Pt}} \text{cm}^{-2}$ | PFSA membrane (proprietary) | 0.4 $\text{mg}_{\text{Pt}} \text{cm}^{-2}$ | carbon paper
 [37]: Pt-coat. Ti | sint. Ti pow. | 2.2 $\text{mg}_{\text{IrO}_2} \text{cm}^{-2}$ | Nafion® 117 | 0.8 $\text{mg}_{\text{Pt}} \text{cm}^{-2}$ | carbon paper | Pt-Au-coat. Ti

perfectly reversible reactions, driving the reaction in acidic environment means that the anode will experience *at least* a potential applied of 1.23 V vs SHE. In the cathode, the overpotential required for high current densities is small given the excellent reversibility of HER on metallic Pt. This is not the case for OER. The recognized best catalyst for OER, RuO₂, shows an overpotential of roughly 0.2 V both in alkaline and acidic environment [22], which means that materials in the anode compartment will experience a potential of at least ~1.5 V at the locus where OER takes place. Real experienced potentials will be much higher at high current densities, also considering the overpotentials coming from HER kinetics and ohmic contributions. Such potentials are high enough to oxidise almost any element at a certain extent and many oxides [38]. The harshness encountered in the anode compartment is in fact the origin of the economical limitations that PEMEC technology suffers: necessity of high loading of IrO₂ due to the lack of a catalyst support and necessity of (precious-metal-coated-) Ti bipolar plates and porous transport layer.

A catalyst support for OER catalysts

IrO₂ (or RuO₂ - IrO₂ mixture) is still the best catalyst for OER in acidic environment. Ir is an extremely scarce and expensive element [39] and it is produced as a by-product of Pt, Ni and Cu extraction: not only its price is going to rise even more once the request approaches the supply capacity, but also the low abundance of Ir on the planet will not allow PEMEC technology to become relevant (on the GW/TW scale) without a significant increase in power density of the cells, i.e. GW/kg_{Ir} [40]. The high loading of anode catalyst currently used in commercial PEMECs are a consequence of the lack of a support material able at the same time to resist corrosion and conduct electricity, ensuring the flow of electrons from the catalyst to the current collector. High catalyst loading provides good electrical contact at the cost of reducing greatly catalyst utilization, while the catalyst is such a rare material. It is of primary interest to maximise the use of Ir in PEMEC, considering that no valid alternative catalyst has been found so far.

One approach is to prepare composite materials where IrO₂ is mixed with a cheap and corrosion resistant material. De Pauli and Trasatti [41] studied the composite IrO₂ - SnO₂, finding that the composite retained the original activity for compositions >10mol.% IrO₂. Oakton *et al.* [42] studied the system IrO₂ - TiO₂ and suggested that TiO₂ enhanced the stability of the catalyst, even if their accelerated test did not apply potentials >1.6 V vs SHE. Recently, SrIrO₃ [43] and the pyrochlore Y₂Ir₂O₇ [44] has been proposed as highly active catalyst for OER where Ir is 'diluted' in a poly-metal oxide compound. Both the materials leach out the secondary metal ion present together with Ir during OER conditions. The increased activity comes from the important surface reconstruction that the material undergo as a consequence of dissolution, which leaves behind a high-surface poorly-crystalline material which presents higher activity. It is reported that amorphous IrO₂ is usually more active than the material in a crystalline form [23, 45, 46], even if at the price of a greater instability and proneness to dissolution.

Yet, the development of a robust catalyst support has never ceased to be attractive given the possibility of better control the size and utilization of the catalyst once it is

deposited on a substrate. Much effort has been devoted to this topic. As a consequence of the potentials involved in the application, the research has always focused on ceramic materials. The use of ceramic materials as catalyst supports has been proposed also for PEM fuel cells [47]. In an electrochemical cell, the catalyst support needs to be conductive not to introduce detrimental overpotential in cell operation due to ohmic losses; as Trasatti says [22], “if a material shows a lower overpotential because it is mainly a better conductor, this is as a whole regarded as a better electrocatalyst”. Finding a ceramic material which is both electronically conductive below 100 °C and stable in acidic oxidising environment turns out to be far from trivial, and the research on the topic has focused on increasing the conductivity of widely recognized corrosion resistant materials. Carbides [48–50] and nitrides [51, 52] have attracted attention given their high electrical conductivity, but they also proved to be unstable under anodic polarization [53, 54]. TiO_2 is known to be very insoluble in acidic conditions but it is an insulator. Many studies evaluated the activity of IrO_2 loaded on doped titania as a catalyst support, for example W- TiO_2 [55] and Nb- TiO_2 [56, 57]. Slavcheva *et al.* studied the activity of IrO_2 supported on reduced titania (known also as Magnéli phases or by their commercial name, Ebonex[®]) indicating that the catalyst exhibited enhanced activity and durability [58], even if their accelerated testing procedure did not exceed an applied potential of 1.5 V vs SHE. The most studied oxide material as catalyst support is with no doubt doped SnO_2 [59–68]. The research focused especially on Sb doped SnO_2 (ATO) in light of its good conductivity and a lot of effort has been dedicated to prepare nanosized ATO and obtain a greater surface area where IrO_2 can be anchored. Nonetheless, Geiger *et al.* [69] studied the stability limits of doped SnO_2 , including ATO and showed that Sb dissolved preferentially upon potential cycling, which means that the residual material is enriched in SnO_2 . Similar results were showed by Cognard *et al.* [70], who found that the dissolution of Sb from ATO nanoparticles left behind a core shell structure with a surface enrichment in SnO_2 . That caused a reduction of performances due to a decrease in conductivity of the material (SnO_2 , as TiO_2 , is in fact an insulator at the temperatures and p_{O_2} of interest [71]).

Only very recently possible ancillary effects of the catalyst support on performance of OER catalyst have started to be investigated. In heterogeneous catalysis, the existence of metal-oxide support interaction is a well known phenomenon (for example [72]), which influences the functioning of the catalyst. It can be envisaged that supporting IrO_2 on a proper material could reveal similar effects, and significantly enhance the stability and the activity of the catalyst. As a matter of fact, state-of-the-art OER catalysts have stability issues: the dissolution of Ir during OER has been extensively reported [46, 73–75] and must be kept in consideration for further development of the technology. The dissolution of Ir appears to be connected to the material reaching an oxidation state bigger than +4 [23] when high current density cause the potential to increase above 1.5 V vs SHE. Oh *et al.* [76] measured the oxidation state of Ir in IrO_2 loaded on carbon and on nanosized ATO and they observed that the average oxidation state was +4 and +3.2 for IrO_2 loaded on carbon and ATO respectively. They report an increase in the stability of the catalyst upon dissolution due to Ir not accessing high oxidation states as

a consequence of the interaction with the ATO support, even if a comparison with pure IrO_2 is not reported in the study. Sun, Zhou *et al.* [77, 78] studied the effect of strain in enhancing the activity of IrO_2 . They report lower overpotential and higher mass activity compared with pure IrO_2 . The strain was obtained by anchoring IrO_2 on MnO_2 , which it was hypothesized to induce a deformation of the $[\text{IrO}_6]$ octahedron in the rutile structure of IrO_2 .

Corrosion resistant and conductive PTLs and BPPs

Despite the presence of extremely expensive precious metal catalyst, together PTLs and BPPs account for more than the 60% of a PEMEC stack cost [79]. Using Ti is a forced choice for both PTLs and BPPs given the requirements of corrosion resistance, even if it is anything but ideal. Ti is a relatively expensive metal (Ti grade 2, commonly used in PEMECs components [20], is more than twice as expensive as 316L stainless steel per unit mass [80]) and on top of that it is also difficult (read costly) to form [81] and machine [82]. Both BPPs and PTLs need to (i) offer a minimal-resistance path for the current running through the cell and at the same time (ii) guarantee unimpeded flow of water/ O_2 to/from the catalyst layer.

Ti is very resistant to corrosion even in strong acid in force of the layer of oxide that forms almost instantly when it is exposed to air or oxidising conditions [83, 84]. The composition of the passivation layer is predominantly TiO_2 , which is a well-known electrical insulator. Ti components need therefore to be protected from excessive thickening of the oxide layer to avoid increase in the through-plane resistance of the cell. Coating are also required if Ti is used in the cathode side of a PEMEC, since H_2 embrittlement of Ti is a well reported phenomenon [85].

Au- and Pt-coated Ti BPPs were already studied for PEM fuel cells applications [86, 87]: noble metals coatings greatly enhance the performances in terms of contact resistance within the cell but also increase the overall cost of the cell itself. Alternative Ti coatings based on nitrides have been proposed [88, 89] but they showed to undergo oxidation under anodic polarization. Lædre *et al.* [90] measured the interfacial contact resistance (ICR) of several steels and metals (including Ti, W, Mo, Ta, Nb) before and after polarization up to 2 V vs SHE. The lowest current densities were produced by Ti, Ta and Nb, which also showed a negligible weight loss, as a consequence of the formation of passivating oxide layers on the metal surface. Those materials showed concomitantly the biggest increase in the ICR due to the poor conducting properties of the surface oxide layer.

Stainless steel bipolar plates are particularly attractive given the lower cost and easier manufacturing [91]. Differently from fuel cells applications, the increase in weight due to the substitution of Ti with steel would not be an issue, since electrolyzers are predominantly envisaged for statical applications. Stainless steel is more prone to corrosion compared to Ti, and a coating must be applied to avoid degradation. Moreover, large leaching of Fe ions in a PEMEC cannot be tolerated, since when Fe comes in contact with the PFSA membrane triggers Fenton reactions in the presence of O_2 and causes severe degradation of the polymer [92]. Gago *et al.* [93] tested Crofer[®] 22H stainless

steel BPPs coated with $\sim 50 \mu\text{m}$ of Ti and $\sim 1 \mu\text{m}$ Pt and showed that such coating guaranteed protection to stainless steel during cell operation. Provided such coating, they also suggest that less noble but cheaper and more conductive materials such as 314 steel, Cu and Al would be worth to test as materials for BPPs.

Current commercial electrolyzers apply Pt or Au coatings on the Ti of both BPPs and PTLs in order to ensure performance and durability. Nevertheless, recently Rakousky *et al.* [94] showed that Pt coating can detach from the PTL when a PEMEC is operated at high current densities (up to 3 A cm^{-2}). PTLs can exist in different forms: the best reported performances are obtained with porous bodies of sintered Ti particle [20], where different pore size can be adjusted by selecting different dimension of starting Ti particles; on the other hand, other morphologies such as felts, foams and expanded meshes come at a lower cost [91]. The structure of the PTLs is important on account of the complex gas/liquid flow regime that establishes during cell operation and it has been shown that the porosity of the PTL can influence the performance of a PEMEC [95]. Much effort is being devoted lately in developing optimal morphology of PTLs [96–98].

1.4 Motivation and scope of the work

The issues connected with PEMEC technology are essentially a material science problem. No enhancement of catalyst utilization will be possible until a catalyst support becomes available for IrO_2 . Substituting the 'non-catalytic' precious metals used for increasing the contact resistance of BPPs and PTLs with cheaper materials can have a strong impact on the stack cost; so does avoiding the use of Ti. It is clear from the literature that oxides are the only materials which are stable in the conditions of the anode compartment, either as materials *per se* (catalyst) or as passivating layers (the cause of protection of Ti-based BPPs and PTLs), in light of their inherent thermodynamic stability in oxidising conditions. To date, the only catalyst supports for IrO_2 with encouraging stability are oxides. Moreover, effective protection of stainless steel interconnects was obtained by dense coating of oxide materials, in the case of solid oxide fuel cells [99]. Oxides can present the most diverse properties depending on structure and composition, but not many classes of materials have been investigated in the field of PEM electrolysis and only a few studies tried to describe their modes of degradation on a chemical and electrochemical level. Even if many ceramic materials can be considered insulators at the relevant temperatures of PEMECs, many exhibit greater electrical conductivity than typical PFSA membranes ($\sim 0.1 \text{ S cm}^{-1}$ at the operation temperatures of a PEMEC) and their electrical properties could be sufficient for the application.

The scope of this work was to explore different oxide-based materials as possible constituents of PEMEC anode components. The work was devoted to study the structural and electrical properties of different oxides prepared in this study, together with an evaluation of their stability toward corrosion in acidic environment and temperatures comparable with those employed during PEMECs operation. The primary parameter used in the project for selecting the candidates for the tests was reported corrosion resistance of the ceramic. Since the chemistry and electrochemistry of a material exposed

to the operational conditions of a PEMEC determines its stability, a particular attention has been given to characterize the materials *on their own* in the conditions than can be encountered in an anode compartment of a PEMEC. The purpose was to understand, when possible, the origin and modes of degradation. Specifically, develop a methodology to study the behaviour of ceramic materials when exposed to high potentials (e.g. 2V vs SHE) was considered of great importance and pursued. The task carried some intrinsic complications as it will be discussed later in the thesis.

Structure of the thesis

The description of the experimental procedures and results in this thesis is divided in five chapters. Some experimental details and calculations that were considered relevant but unnecessary in the main body of the text can be found in appendices **A**, **B** and **C**. Appendix **D** reports the paper and contributions that were delivered during the course of this PhD.

Chapter 2 describes the experimental techniques and instrumentation used during this work for preparation and characterization of the materials under study. Some theoretical background is also reported for the techniques or procedure which were used more extensively.

Chapter 3 reports the results of the preparation and structural characterization of the materials under study. A literature review can be found at the beginning of the section of each material to motivate the choice of the material and present previous studies.

Chapter 4 shows the conductivity measurements conducted on the prepared materials, together with the result of the corrosion tests operated on them. Further structural characterization on the tested samples is reported and, in some cases, degradation mechanism are proposed.

Chapter 5 describes the electrochemical characterization that was conducted on Ti felt and on the ceramic material. Prior to the section on characterization of ceramics, a review on the methodology of electrode preparation is included. A preliminary ceramic-loaded PEMEC test is presented.

Chapter 6 summarizes the results described in the previous chapters and reports some possible outlooks.

CHAPTER 2

Preparation and Characterization techniques

2.1 Materials preparation

Solid state synthesis

Solid state synthesis constitutes the classical method for the preparation of ceramic materials. The powdered reactants are mixed together; then the temperature is raised to a level where the rate of solid state reactions (notoriously slow at low temperatures) is fast enough to bring the reaction to completion in a time scale of practical utility.

Solid state synthesis has the advantage of being easy to perform and to scale to big quantities of product. The atmosphere where the synthesis is conducted can be easily adjusted to what the preparation requires. Usually, synthesis conducted in air are performed in electric furnaces in static atmosphere. When a reducing environment is needed, different atmospheres can be used depending on the reactivity of the materials implied in the preparation and to the reducing power needed for the synthesis (typical gas compositions include 5% H₂/Ar, pure Ar, pure N₂, CO-CO₂ mixtures). When H₂ is used, it is a common practice to run the reactions in a tube furnace where the gas is continuously flown the furnace. This is to avoid the formation of hazardous pressurized gas mixtures containing H₂. Another option to conduct solid state synthesis in reducing conditions is to run the reaction in vacuum, either in a vacuum oven or enclosing the reactants in an evacuated tube, the material of the tube depending on the temperature the synthesis require.

The preparation often require multiple steps, where the material is again crushed and a new heat treatment is conducted. A crucial step in this kind of preparation is often how the mixing of the raw materials is conducted before the heat treatment. Commonly, the starting mixture is crushed in a mortar or ball milled to ensure a proper mixing. A coarse granulometry of the starting materials may result in incomplete reaction and require multiple stages of re-crushing and re-heat treat. The samples can also be pressed into pellets before the synthesis to increase the contact of the powders and favour solid state reactions.

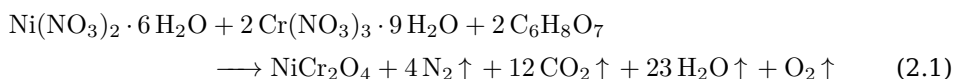
Nitrate combustion

Nitrate combustion synthesis is an excellent method to guarantee homogeneity in the reacting mixture of the raw material. In this method, solutions of nitrate salts of

the components are prepared in water; the solutions are then mixed in stoichiometric ratios required by the final products and stirred while the solution is heated to evaporate the water. When the water is completely evaporated, the solid mixture self ignites to leave the oxide material. The reaction is self sustaining since the combustion process is exothermic.

To avoid precipitation of single components during evaporation, which would lead to inhomogeneity in the final product, often a complexing agent is added in excess in the solution to keep the metal ions dissolved. For example, such agents can be citric acid, oxalic acid or glycine. The complexant also can facilitate the reaction by acting as a fuel, since they get oxidised by the nitrate ions.

A typical nitrate combustion reaction for the preparation of NiCr_2O_4 is, using citric acid as complexant:



2.2 Structural characterization

X-Ray Diffraction

X-ray diffraction (XRD) is used extensively to determine the crystal structure of materials. The technique exploits the elastic scattering of X-ray photons by the electron clouds of the atoms. Crystalline materials are characterized by a periodic repetition of a single asymmetric unit in all three dimensions of space. The distances between crystal planes are in the order of the Å. When X-rays are diffracted by a periodic set of crystal planes, the scattered beams that have difference in traveled path which is an integer multiple of the wave length of the X-ray give constructive interference. The incidence angle between the surface of the material and the X-ray θ can be related to the the

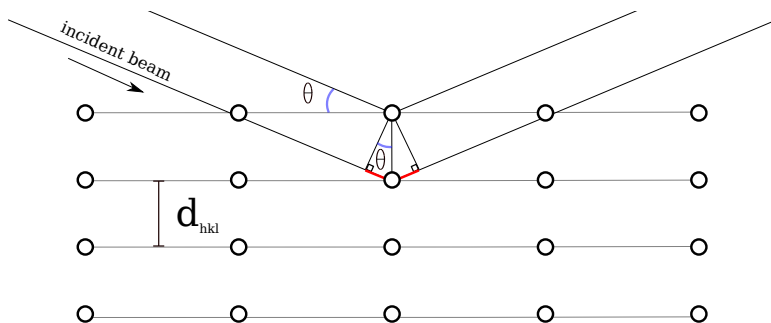


Figure 2.1: Origin of the Bragg law: when the difference in traveled path of different X-rays (red in the figure) is an integer multiple of the radiation wavelength, the X-rays will be diffracted coherently and give constructive interference.

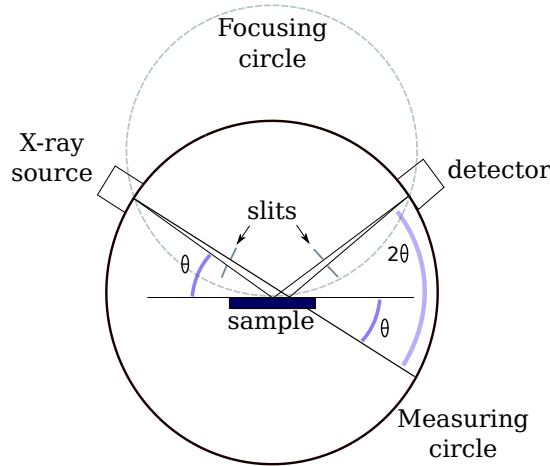


Figure 2.2: Scheme of a diffractometer with Bragg-Brentano configuration

distance between the two atomic planes using Bragg's law [100]:

$$n\lambda = 2d_{hkl}\sin\theta \quad (2.2)$$

where λ is the wavelength of the X-rays, d_{hkl} is the distance between two atomic planes, θ is the incidence angle and n is an integer. If the condition of Bragg is not satisfied, the beam will be diffracted in all the direction resulting in a small intensity.

The interplanar distance d_{hkl} is determined by the cell constants of material as a function of the Miller indices h, k and l , which identify the directions in the crystalline lattice. The number of independent cell constants is determined by the crystalline system of the material. For example, in the case of a system having cubic symmetry:

$$d_{hkl} = \frac{a}{\sqrt{h^2 + k^2 + l^2}} \quad (2.3)$$

where a is the lattice parameter, namely the length of the edge of the cubic crystal cell. For every value of d_{hkl} , there will be a value of θ for which the condition of Bragg is fulfilled. The symmetry of a crystal will determine how many equivalent planes (family of planes with the same interplanar spacing d_{hkl}) are present in the structure.

For measuring X-ray powder diffraction, a common configuration of the diffractometer is the so called Bragg-Brentano configuration (see figure 2.2). The X-ray source, the detector and the sample lay on the circumference of the focusing circle. The source and the detector move simultaneously along the measuring circles while the focusing circle expands and contracts as a function of the angle θ . The sample does not need to be rotated during the measurement: XRD on powdered samples assumes that, statistically, in a powder composed of small crystals there will always be some of them oriented in the correct way to originate diffraction for the specific angle. When the value of θ fulfills the condition of Bragg, the detector records the intensity of a diffracted beam as a function of 2θ (the angle between the scattered beam and the undeviated X-ray coming from the source) and an XRD pattern is formed. The 2θ position of peaks in a pattern are a

fingerprint of the material since they depend on unique properties of the material, such as cell constants and symmetry. Knowing the crystal structure of the material under analysis, it is possible to calculate the cell constants from the measured positions of the peaks in a diffractogram.

A diffractometer in Bragg-Brentano configuration needs to be perfectly aligned so that source, sample and detector lay all the time on the focusing circumference. Sample displacement from the focus point may lead to errors in the peaks position determination.

In this work, powder XRD was performed on different diffractometer with Bragg-Brentano configuration. The source was always Cu K_{α} radiation ($\lambda=1.54056 \text{ \AA}$). The instruments used were a Bruker D8, a Rigaku Smartlab and a PANalytical Empyrean.

Rietveld Refinement

An XRD pattern contains more information than the simple symmetry class and cell constants. In fact, the scattering factor of an atom is proportional to the number of electrons present in atom. Therefore, this means that heavier elements with higher atomic number will scatter more than lighter elements. A diffracted beam will be a composition the x-ray diffracted by the different elements present in the cell of the material. The resulting wave is called the *structure factor* which is defined for each family of planes identified by the Miller indexes hkl as [101]

$$F_{hkl} = \sum_1^N f_n e^{2\pi i(hu_n + kv_n + lw_n)} \quad (2.4)$$

with $1 < n < N$, where N is the total number of atoms in the crystallographic cell, f is the atomic scattering factor of the element of the n atom and u, v and w are the fractional coordinates of the atom n in the cell. The intensity I_{hkl} of a peak in a diffractogram is proportional to $|F_{hkl}|^2$. Moreover, an XRD pattern contains other morphological information of the material under study, such as grain size and strain.

In the late 1960's, Hugo Rietveld [102, 103] introduced a method to extract information from an XRD pattern which is based on fitting the observed intensities of a patterns with a model which comprised structural and chemical parameters of the material, sample effects (e.g strain, particle size, texture) and instrumental parameters (e.g. 2θ displacement, instrument resolution factor). The method, widely known as Rietveld method or Rietveld refinement, minimizes by the least squares method the difference between experimental and calculated intensities. The method requires to know the structure of the material in order to perform the refinement, but it is very powerful: information such as atom positions and site occupancies can be obtained. The quality of the fit is predominantly evaluated by visual inspection of the difference plot between the calculated and experimental intensities, especially at the first stages of the refinement. When the difference with the calculated model and the observed intensities reduces, some indicators, called agreement factors, can be used to evaluate the goodness of further refinement of the parameters. Some of them are [104]:

Profile factor

$$R_p = 100 \frac{\sum_{i=1,n} |y_i - y_{c,i}|}{\sum_{i=1,n} y_i}$$

Weighed Profile factor

$$R_{wp} = 100 \left[\frac{\sum_{i=1,n} w_i |y_i - y_{c,i}|^2}{\sum_{i=1,n} w_i y_i^2} \right]^{\frac{1}{2}}$$

Bragg factor

$$R_B = 100 \frac{\sum_{hkl} |I_{obs,hkl} - I_{calc,hkl}|}{\sum_{hkl} I_{calc,hkl}}$$

Crystallographic R_F – factor

$$R_F = 100 \frac{\sum_{hkl} |F_{obs,hkl} - F_{calc,hkl}|}{\sum_{hkl} F_{calc,hkl}}$$

(2.5)

where n is the total number of pattern points considered in the refinement and $w_i = 1/\sigma_i$ is the standard deviation of the profile intensity y_i . The refinement is normally conducted using a computer program.

In this work, Rietveld refinement was performed on the extract structural parameters from the prepared compounds and in some cases to quantify the fraction of multiple phases present in a pattern. The software FullProf was used [104, 105].

2.3 Electrochemical characterization

An typical three-electrode-cell for conducting electrochemical measurements is composed of a *working* electrode (WE), a *reference* electrode (RE) and a *counter* electrode (CE). All of them are in contact with the *electrolyte*, a ion-conducting medium that allows the electrodes to polarize when a potential is applied.

The WE is the electrode at which the electrochemical reaction of interest takes place. When a current runs through the cell, it flows between the WE and the CE. No current flows between the WE and the RE. RE are built by using electrochemical systems whose redox potential is well defined and reversible. The potential applied on the WE is controlled using the RE as a reference, so that the potential measured on the WE does not include contributions from the reactions taking place at the same time at the CE. Since different types of RE exist, with different relative potentials, the potential scale of an electrochemical experiment is generally reported relative to the Standard Hydro-

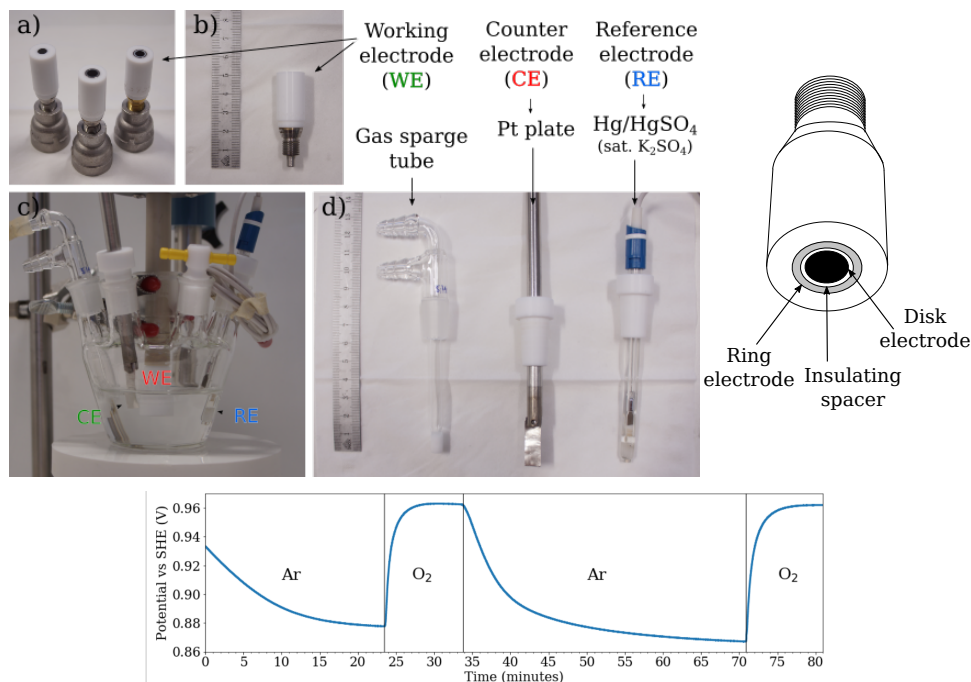


Figure 2.3: Different electrodes and components of the electrochemical cell used in this study: (a and b) the rotating-ring disk and rotating disk electrodes used in this work; (c) the assembled cell with the components immersed in the electrolyte; (d) counter and reference electrode used in this work, together with the gas sparge tube used to bubble gas into the electrolyte; on the right, a schematic representation of a rotating ring-disk electrode is shown; (bottom) evolution of the open circuit potential vs time measured in a Pt wire while bubbling in the electrode different gases (indicated in the image).

gen Electrode (SHE). The relative values of potential of the various RE are well known and tabulated. For example, the Hg/HgSO₄ reference electrode used in this work (sat. K₂SO₄, Radiometer Analytical) electrode used as RE in this work has a difference in potential compared to the SHE of -0.658 V. When no current runs through the cell, the potential difference existing between the WE and the RE is called the *open circuit potential* (OCP). When the OCP is stable over time, the system is in equilibrium and the Nernst equation is valid [106]. For a half-reaction $Ox + ne^- \rightarrow Red$, the Nernst equation can be written as

$$E = E^0 + \frac{RT}{nF} \ln \frac{a_{Ox}}{a_{Red}} \quad (2.6)$$

where E is the potential associated with the reaction, E^0 is the standard potential of the reaction, and a are the activities of the reduced and oxidised species, n is the number of electrons involved in the reaction, T is the temperature, R is the gas constant and F is the Faraday constant. The activity of the species are related to the concentration of the species in the electrolyte. This principle has been used to observe the variation of the dissolved amount of oxygen when deaerating the solutions before the experiments

were conducted. In figure 2.3 it is shown a measurement of the OCP measured as a function of time on the Pt wire while different gases were alternatively bubbled through the electrolyte (0.5 M H₂SO₄); when the OCP reached a plateau, the electrolyte was considered to be saturated with the gas that was bubbled through the solution.

Since the electrolyte does not conduct electricity, when a current flows through the cell, an electrochemical reaction must take place which creates/removes charged species at the WE and CE. A typical electrochemical experiment can either control the current that runs through the cell or the potential that is applied to the WE.

A specific type of electrode is the rotating (ring-) disk electrode ((R)RDE) [19]. A schematic representation of the electrode can be observed in figure 2.3. The electrode is constituted by an cylindrical rod, usually made of PTFE, where a disk of a conducting material is embedded. In the RRDE configuration, another electrode is present in the form of a ring with larger diameter than the disk, which is positioned around it. The two electrodes are separated by an insulating spacer.

The key feature of and RDE is that the electrode can be mounted on a shaft and rotated at controlled speed while it is immersed in the electrolyte. The rotation drags a continuous stream of solution to the surface of the disk, which is used as WE. The rate at which the reactant reaches the surface of the disk will be determined by the rotation speed of the electrode. If the observed reaction is dependent on the concentration of a dissolved species, the mass transport limited current, referred in this case as diffusion-convection limiting current, will be a function of the rotation speed of the RDE.

The techniques is essentially a method to control the flux of reactant to the electrode surface ($\delta \propto 1/\omega^{\frac{1}{2}}$, where δ is the thickness of the diffusion layer and ω is the rotation speed) and finds numerous applications in the study of homogeneous reactions kinetics and diffusion dynamics of dissolved species. The homogeneity of the laminar flow reaching the disk is of capital importance for extracting valuable data from such experiments. The establishment of a laminar flow requires the surface of the electrode being perfectly flat and the rotation avoiding any eccentricity; consequently, these electrodes and the rotation apparatus are manufactured with a high level of precision. None of such methodologies were used in this work and a thorough description is beyond the purpose of this introduction. For a complete covering of the topic, the book from Bard and Faulkner [19] is a classic.

When the electrode is in a RRDE configuration, an extra WE is inserted in the cell. Due to the geometrical relation between disk and ring, the stream of solution that reaches the disk electrode is deflected and moves radially from the disk outwards, reaching the surface of the ring. If a chemical species leaves the surface of the disk (after reacting or due to dissolution), part of it will come in contact with the surface of the ring electrode. The fraction of chemical species that reach the surface of the electrode compared to the total that leaves the disk can be calculated, as it is dependent on the geometrical proportions between the disk and the ring. Such quantity is called the *collection efficiency* of an RRDE, and it is typically between 0.2 and 0.4.

By the use of bipotentiostat, the potential applied at the ring and at the disk can be set and scanned independently. Knowing the possible products of a reaction taking place

at the disk electrode, it is possible to set the potential at the ring so that the products undergo a second reaction. Knowing the collection efficiency of the RRDE, the current recorded on the ring can be compared to the one recorded on the disk.

In this work, electrodes from Pine Research Instrumentation were used. The electrodes used were two RDE with glassy carbon disk (A : 0.196 cm^2) and two RRDE with glassy carbon disk and Pt ring (A_{DISK} : 0.196 and 0.243 cm^2 ; A_{RING} : 0.110 and 0.169 cm^2 ; collection efficiency: 0.26 and 0.38).

For all the electrochemical measurements performed in this work, the instrument used was a bipotentiostat CH Instruments, model 760E.

Cyclic voltammetry

Cyclic voltammetry (CV) is a linear sweep method where the potential is varied linearly ('scanned') with a rate v from an initial potential E_i to a potential E_r ; once the potential E_r is reached, the scanning direction is reversed and the potential is varied, at the same rate v , from E_r to a final potential E_f . In cyclic voltammetry $E_i = E_f$. The current as function of the applied potential is recorded. The data are generally displayed as current as a function of potential applied. An example is reported in 2.4a). When the potential is varied toward more positive potentials is generally defined as the positive going sweep (PGS); conversely, when the potential is scanned negatively is defined negative going sweep.

An electrochemical reaction occurring at the WE induces an increase in the mea-

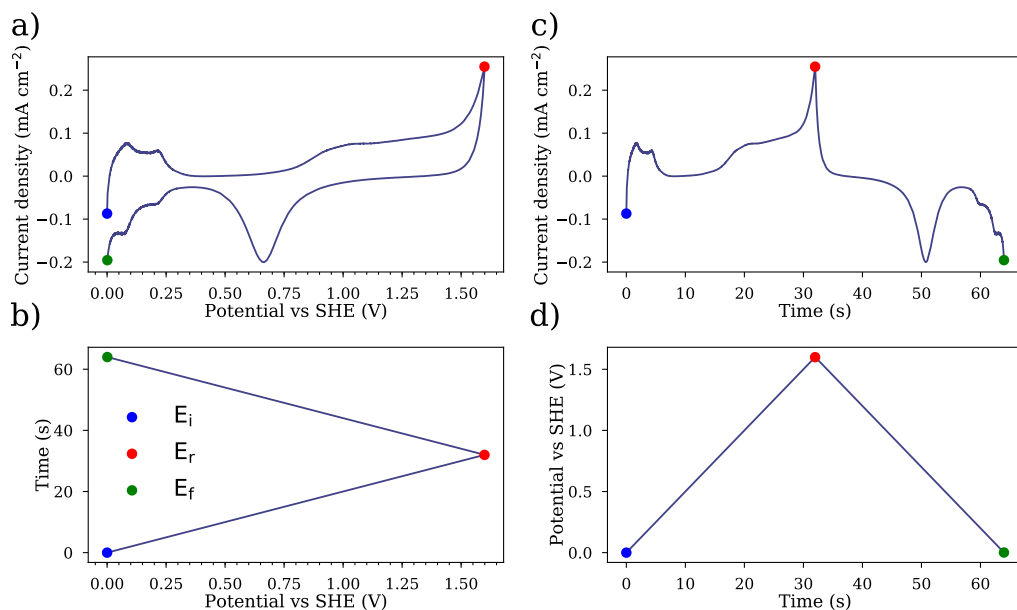


Figure 2.4: Different representation of a CV experiment; E_i , E_r and E_f indicate the initial, reversing and final potential; .

sured current is observed and a peak is formed. The variation of the position of the peak as a function of the scan rate gives information on the reversibility of the reaction. If the electrochemical reaction under study is reversible, two peaks appear, one in PGS and one in the NGS, separated by 59 mV.

The integration of the area below a peak when the current is plotted as a function of the time of the experiment yields directly the charge transferred during the electrochemical process that originates the peak. For a peak that is comprised between the potentials V_1 and V_2 :

$$Q = \int_{t_1}^{t_2} I dt \quad (2.7)$$

where t_1 and t_2 are the time of the experiment when the potential V_1 and V_2 and Q is the charge transferred during the process that originates the peak.

Polarization curves

Polarization curves are common in corrosion science to evaluate the rate of corrosion in a fast way compared to the time-consuming weight loss measurements. The potential is varied slowly (usually $0.5\text{-}1 \text{ mV sec}^{-1}$ or less) from cathodic to anodic and current is recorded.

The point where the current switches from cathodic to anodic is referred as the corrosion potential E_{corr} . The anodic branch of the curve is related to the processes of corrosion of the material under study, typically a metal. If a material undergoes corrosion, $\log i$ increases steeply while the potential increases. Some metals develop an oxide layer as soon as the current switches to anodic; the presence of such layer protects the material from dissolution. Such phenomenon, known as *passivation*, can be observed in a polarization plot as $\log i$ remaining constant for a large range of potential, until the polarization is so strong that the oxide layer breaks down and the metal undergoes dissolution.

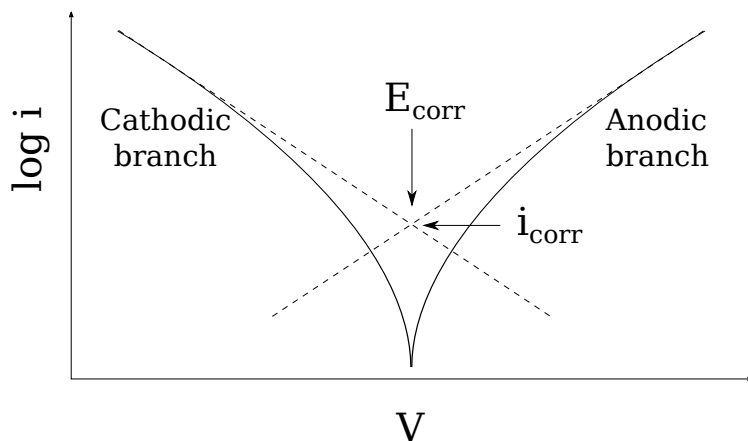


Figure 2.5: Scheme of a polarization curve.

Electrochemical Impedance Spectroscopy

Electrochemical Impedance Spectroscopy (EIS) uses a sinusoidal current or voltage signal to create a perturbation in the investigated system [107]. Since electrochemical reactions are involved, the signal amplitude must be kept small enough for the system to remain in a pseudo-linear regime of voltage-current dependence.

In the case of a voltage perturbation, a typical amplitude value can be 10 mV. The frequency of the signal is varied. A sinusoidal voltage perturbation and the following current response can be expressed as:

$$E_t = E_0 \sin(\omega t) \quad (2.8)$$

$$I_t = I_0 \sin(\omega t + \phi) \quad (2.9)$$

where E_t and I_t are the potential and current at time t , E_0 and I_0 are the amplitude of the signal, ω is the angular frequency ($\omega = 2\pi f$ where f is the frequency of the sinusoidal perturbation) and ϕ is the phase shift that is observed. The impedance is obtained using Ohm's law. In force of the presence of the phase shift, the impedance can be expressed as a complex function as:

$$Z = \frac{E_t}{I_t} = \frac{E_0 \sin(\omega t)}{I_0 \sin(\omega t + \phi)} = Z_0 \frac{\sin(\omega t)}{\sin(\omega t + \phi)} = Z_0 \exp j\phi = Z_0(\cos \phi + j \sin \phi) \quad (2.10)$$

where j is the imaginary unit. Therefore, the impedance Z can be divided in a real and an imaginary part, Z_{real} and Z_{imag} . The response of an electrochemical system to the sinusoidal perturbation is often a combination of various resistive and capacitive contributions. In order to gain insight on the processes taking place, the impedance response can be modeled using an *equivalent circuit*. Such model is used to fit the impedance response obtained experimentally.

Below, the impedance of some typical electrical elements used to build an equivalent circuit model are presented.

Resistor

$$Z_R = R \quad (2.11)$$

Capacitor

$$Z_C = \frac{1}{j\omega C} \quad (2.12)$$

Constant Phase Element

$$Z_{CPE} = \frac{1}{Q(j\omega)^n} \quad (2.13)$$

where R is the direct current resistance of the resistor and C is the capacitance of the capacitor. Most often, electrochemical interfaces present both resistive and capacitive character and are modelled by the Randles circuit, which is constituted by a

resistor in parallel with a capacitor. A constant phase element (CPE) has no electrical equivalent and it is used to model processes where a certain dispersion of time constants is observed and the response of a Randles circuit is not the ideal one. For small deviations of n from the value of 1, the CPE can be regarded as an imperfect capacitor, which is not completely blocking the passage of current.

This element is often used in EIS, e.g. to model surfaces that present a capacitive response but are characterized by a certain degree of roughness. Often, a CPE is just a summation of different capacitors with very similar values of C . Since the units of Q in a CPE are dependent on n , its value cannot be directly compared with other capacitances. From the values of Q and R , the *effective* capacitance of a CPE [108] can be calculated as

$$C_{eff} = Q^{\frac{1}{n}} R^{\frac{1-n}{n}} \quad (2.14)$$

Values of C or C_{eff} can be used for determining the thickness of layers on the surface of the electrode [108, 109] according to

$$C = \frac{\epsilon_0 \epsilon_r A}{d} \quad (2.15)$$

where the ϵ_0 is the dielectric constant of vacuum, ϵ_r is the dielectric constant of the material constituting the layer, A is the area and d is the thickness of the layer.

Typical graphical representation of EIS spectra are Nyquist ($-Z_{imag}$ vs Z_{real}) and Bode plots ($|Z|$ vs frequency).

2.4 Conductivity measurements

The conductivity of materials can be measured with the so-called four-probes method. The measurement need well defined geometrical samples, for example sintered pressed bars.

Two wires of Pt are tied at the extremities of the bar. The outer portion of the extremities is painted with Pt paste. The Pt paste can either be sintered on the sample in a furnace prior to the measurement or sintered inside the furnace where the conductivity is measured while the sample is heating up. The temperature need at least to reach $\sim 700-800^\circ\text{C}$ for the Pt paste to adhere well on the sample and the organics present in the paste to be burnt away. The measurement consist in running a small current through the extremities of the bar (I_{in} and I_{out} in figure 2.6) while the the potential is measured between V_{in} and V_{out} . This is done to avoid including in the measurement the contribution from the contact resistance that may be present at the interface between the material and the current probes. This is particularly important if the resistance to be measured are small ($\mu\Omega$).

From the potential drop across V_{in} and V_{out} , knowin the current which is sent through the sample, the resistance is obtained by the first Ohm's law

$$R = \frac{V}{I} \quad (2.16)$$

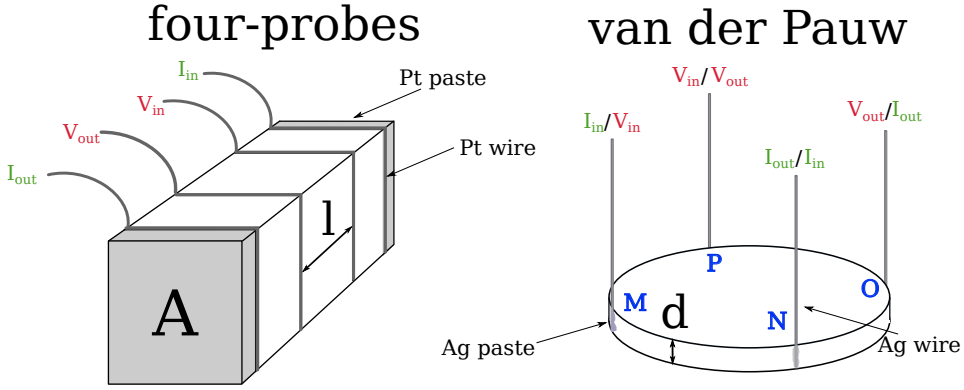


Figure 2.6: The two configurations for measuring conductivity in this work.

where V is the potential difference between V_{in} and V_{out} and I is the current run through the sample. The resistivity of the materials is then obtained by

$$\rho = \frac{AR}{l} \quad (2.17)$$

where A is the area of the cross section of the sample and l is the spacing between the probes of V_{in} and V_{out} .

Another method for measuring the conductivity of lamellae of arbitrary shapes was by L. J. van der Pauw in the late 1950's [110, 111].

The method is based on measuring the conductivity on lamellae of a known thickness d , where the contacts are attached on the side of the lamella as shown in figure 2.6. Then the resistance $R_{MN,OP}$ is measured, which is defined as

$$R_{MN,OP} = \frac{V_P - V_O}{i_{MN}} \quad (2.18)$$

where V_P and V_O are where the voltage probes are connected and the current is sent from point M to point N. Analogously:

$$R_{NO,PM} = \frac{V_M - V_P}{i_{NO}} \quad (2.19)$$

The van der Pauw method states that

$$\exp\left(\frac{\pi d}{\rho} R_{MN,OP}\right) + \exp\left(\frac{\pi d}{\rho} R_{NO,PM}\right) = 1 \quad (2.20)$$

where d is the thickness of the lamella and ρ is the resistivity. For samples which possess an axis of symmetry, the relation can be further simplified and a single measurement is necessary, since $R_{MN,OP} = R_{NO,PM}$:

$$\rho = \frac{\pi d}{\ln 2} R_{MN,OP} \quad (2.21)$$

It should be anyway checked that the relation $R_{MN,OP} = R_{NO,PM}$ is true.

The conductivity of chromites spinels and of Bi-SnO₂ were measured by the four-probes method in a furnace built in-house. A flow of air was passed through the furnace at a rate of 100 ml min⁻¹ for the entire duration of the test. A thermocouple was placed in proximity of the sample to continuously measure the temperature. The conductivity on spinel titanates was measured by the van der Pauw method by inserting the sample in contact with a thermocouple in a glass oven (Büchi B-585).

Oxide materials are usually semiconductors [112], meaning that the the conductivity increases with increasing the temperature.

The conduction process in such material is often a thermally activated processes and obey an Arrhenius type law

$$\sigma = A \exp\left(-\frac{E_a}{kT}\right) \quad (2.22)$$

where σ is the electrical conductivity and A is pre-exponential factor (which contains the concentration of the charge carriers), T is the temperature, k the Boltzmann constant and E_a the activation energy of the conduction plotted. If the conductivity depends on the temperature by an Arrhenius type law, plotting the the logarithm of the conductivity as a function of $1/T$ yields a straight line. The slope of that line will be $-\frac{E_a}{k}$, and the activation energy can be obtained.

2.5 Chemical corrosion test

In this work the material under study were tested preliminary by immersing them in a solution of 1 M 1:1 mixture of nitric and sulfuric acid. The apparatus used for the test is shown in figure 2.7 The samples where inserted in pear-shaped flasks where 25 ml of the mentioned solution were already heated by immersion silicon oil bath kept at 85 °C. The materials were tested as portions of sintered pellets or as powders. If powders were used, a magnetic stirrer was inserted in the flask and kept in rotation to avoid sedimentation.

The sample were left immersed in the acidic solution for 24 hours. Then, in the case of the pieces of pellets, paper filter was used to take out the macroscopic sample. The sample was rinsed with wather and then left to dry in an oven overnight before weighing it. In the case of powders, the suspension of solution and particles was filtered by vacuum pumping through a polyethersulfone filters with nominal pore size of 0.1 μm . The powder and the filters were then left to dry overnight in an evacuated dessicator. To determine the mass lost by the powder during the test, the weight of the filter before the test was subtracted to the weight of the sample and filter after drying.

Other characterization techniques

The following techniques has been used on a limited extent or only indirectly. Since some results are presented coming from such techniques, a brief description is included.

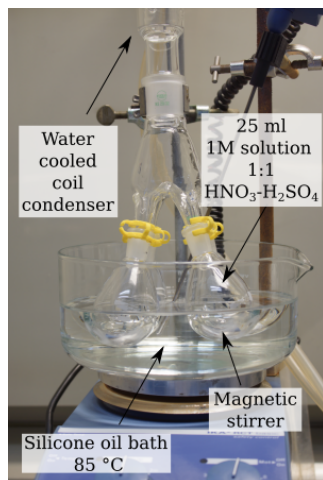


Figure 2.7: Apparatus used for the corrosion testing.

Scanning Electron Microscopy In a scanning electron microscope (SEM) a beam of electrons is focused on the sample by a series of electromagnetic lenses and coils. The beam is scanned on the surface of the sample and the electrons that are re-emitted from the surface are collected from the detectors to form the images. Since the magnification power of a microscope is inversely proportional to the wavelength of the radiation used to perform the observations, an SEM is able to observe much smaller dimensions than a visible light microscope. When the electrons hit the sample, different types of electrons are emitted from the surface. Backscattered electrons escape the sample with energies close to the the one of the electrons of the incident beam. Elements with higher atomic number originate a stronger backscattered signal than the lighter ones; as a result, the areas of the sample with a higher content of heavy elements will result lighter in an image collected with a backscattered electrons detector. The electrons that leave the sample after inelastic interaction with the nuclei and the outer orbitals of the atoms in the material have a lower energy compared with the original beam. These are called secondary electrons and since they escape mainly the top part of the interaction volume of the sample they give mainly topological and morphological informations of the observed material. In this work, mainly a Zeiss Merlin and an Hitachi TM300 were used to collect SEM images.

X-ray Photoelectron Spectroscopy X-ray Photoelectron Spectroscopy (XPS) is a surface analysis technique that samples extremely thin outer layers of the material under study (in the order of the nm). In XPS, x-rays (typically from a mono Al K_α source) are shoot to the surface of the material under study inducing an emission of electrons. The emitted electrons are collected and selected as a function of their energy. The energy of the emitted electron is dependent both on the energy of the incident x-ray and on the binding energy of the electrons. The binding energy depends on the element, the orbital and the chemical environment of the element from where the electron is emit-

ted. An XPS spectrum plots the intensity of the the detected signal of electrons as a function of the binding energy. The resulting signals are then specific for each element, and are dependent on the chemical environment of the material. Most notably, XPS is able to determine the oxidation state of an element. The main disadvantage of the XPS technique is that it needs to operated in high vacuum, so many

The XPS data presented in this work were were performed on a K-alpha (Thermo Electron Limited), using a monochromatic Al-K α X-ray source with a 400 μm spot size. All samples were mounted on the sample holder, which resulted in a chamber pressure of 5×10^{-7} mbar. Atomic concentrations were determined from the average of three broad range spectra and were determined from integrating peak intensities of the characteristic peaks. The broad range spectra were acquired in the range 0-1,300 eV, and collected with 200 eV detector pass energy, 50 ms dwell time, 1.0 energy step size, and collected over three scans. Peaks were fit using a full width at half maximum (FWHM) of 1.4 eV and an 85% Lorentzian/Gaussian function. The binding energies were referenced to the Au 4f peak at 84.0 eV.

Inductively Coupled Plasma - Optical Emission Spectroscopy In Inductively Coupled Plasma - Optical Emission Spectroscopy (ICP-OES) the sample, ususally a solution, is brought to the plasma torch for the atomization. A plasma torch is typically constituted by concentric quartz tubes on the interior of which the gas, usually, that will generate the plasma is fed, together with cooling water. On the tip of the tube a radiofrequency coil is positioned. After an initial spark for generating some charged particles, the radiofrequency induces movement of the ionized particle of the fed gas that will collide with other particles inducing further ionization. In that way the plasma is self-sustained, reaching a temperature of 6000-10000°C.

When the sample is sprayed into the plasma, the compounds are immediately atomized. The electrons in the atoms will be excited by the thermal energy; consequently, upon decaying to fundamental state, they will emit an electromagnetic radiation whose energy is dependent on the difference in energy between excited and ground states. The emission spectrum of an element is effectively a fingerprint of such element. The light from the plasma will then be directed to a monochomator that will select the wavelengths to send to the detector, typically a charged couple device (CCD). excited

In this work, a Vista Axial ICP-OES was used to determine the concentration of dissolved ion in the solutions where chemical and electrochemical corrosion tests were conducted.

CHAPTER 3

Materials: Choice, preparation and characterization

Different classes of material were tested for this thesis work. In this chapter, each class of materials is described with a brief introduction on materials properties and the motivation for the choice of such materials. Then, the preparation and structural characterization of the materials is reported. XRD patterns have been collected on either a Bruker Robot D8 diffractometer (Cu K_{α}), a Rigaku SmartLab (Cu K_{α}) or a PANalytical Empyrean (Cu $K_{\alpha 1}$) in Bragg-Brentano configuration. The Rietveld refinement has been conducted with the software FullProf [105] on the collected datasets.

SEM images have been collected using either a Hitachi TM3000 or a Zeiss Merlin.

3.1 Bi-SnO₂

Tin(IV) oxide (SnO₂) possess a rutile-type structure (see figure 3.1), the same structure as TiO₂ and IrO₂ [113]. From an electrical point of view, it is a native *n*-type semiconductor with a band gap of 3.6 eV. It has been proposed as a solid state oxygen sensor, and also its transparency gave the possibility of using it as a Transparent Conducting Oxide (TCO) [71, 114].

Given its stability as an electrode material [116], SnO₂ has drawn attention on the use of this material as catalyst support in electrochemical cells. Pure SnO₂ has low electrical conductivity, but it can successfully be doped with donors to increase its conductivity up to 10^3 S cm^{-1} for thin films and close to 0.1 S cm^{-1} in the case of bulk materials [117]. The application ranges from PEMFC [66] to PEMEC [61-64]. Beside the chemical stability of the compounds, *n*-type doped SnO₂ exhibited clear evidence of instability during potential cycling up to high potentials (e.g. 2.0 V vs SHE [69]), especially during

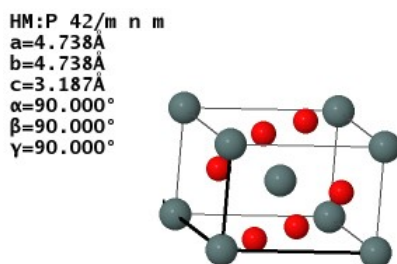
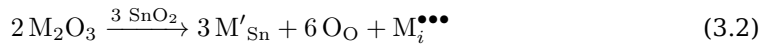
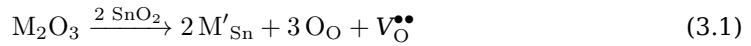


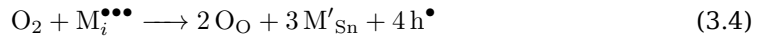
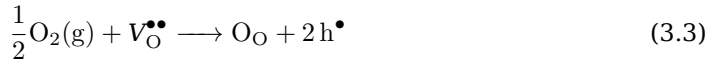
Figure 3.1: Rutile-structure of SnO₂ [115].

the negative going sweep.

To date, no example of corrosion testing of *p*-type doped SnO₂ has been reported. *p*-type can be an attractive choice in a high *p*_{O₂} environment, since the conductivity is higher increasing O₂ partial pressure. *p*-type conductivity is defined as electron holes being the predominant charge carrier in a material. Holes concentration can be increased by doping with an *acceptor* species, which can be an oxide where the cation has a lower valence than the matrix. The possibility of making SnO₂ a *p*-type conductor has attracted the attention, again because of its chemical stability and abundance; yet, theoretical indication discouraged the possibility of this type of doping [118]. Nevertheless, in the literature various attempts have been reported [119–122]. A typical acceptor-inclusion reaction for SnO₂ can be exemplified as follows [123]:



The generation of holes then goes through the incorporation of atmospheric oxygen by reaction with induced defects:



The formation of metallic interstitial defects as in equation 3.2 are unlikely in rutile structure at low temperatures [124]. Bi₂O₃ can in principle act as an acceptor doping for SnO₂ because of its valency. The preparation of Bi-doped SnO₂ has been reported only for thin films, where *n*-type doping with Bi⁵⁺ has shown to lower the conductivity of SnO₂, both theoretically [125] and experimentally [126]: because of the stability of Bi³⁺, the doping is compensated by Bi⁵⁺-Bi³⁺ valence switching, causing pinning of the electrons inside the band gap. On the contrary, when Bi³⁺ is the main doping agent, the conductivity is reported to increase considerably, even at temperatures below 100 °C [127]. In the case of conventional preparation methods, the Bi₂O₃ - SnO₂ system is reported not to form solid solutions, but only a mixture of the pure components and a pyrochlore-structured compound, Bi₂Sn₂O₇ [128, 129]. The reported phase diagram is built with a 10 mol.%_{Bi₂O₃} interval, which means that the smallest composition experimentally investigated is ~ 18 at.%_{Bi} in SnO₂. Smaller at.% of doping cations can already have a strong impact on electrical properties of oxides.

Preparation and characterization

The compositions investigated were 0.5, 1, 1.5, 2, 3, 4, and 5 cat.%_{Bi} in SnO₂. The weighed amounts were firstly mixed in an agathe mortar and milled in a ball mill with ZrO₂ cylinders to ensure proper mixing of the components. The raw mixtures were placed in alumina crucibles and then fired in air for 10 hours at 700 °C to avoid excessive evaporation of Bi₂O₃ (which melting point is at 817 °C). Samples of pure SnO₂ and

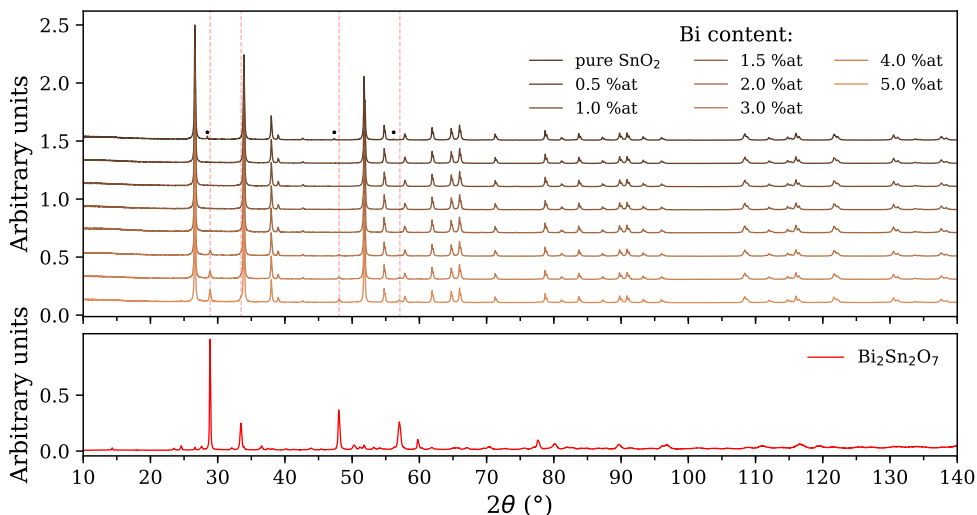


Figure 3.2: (top) XRD patterns collected for the samples with different Bi content; red dashed lines indicate the position of the major peaks of $\text{Bi}_2\text{Sn}_2\text{O}_7$; * markers indicate the position of the peaks from Si, used as internal standard; (bottom) XRD pattern collected for $\text{Bi}_2\text{Sn}_2\text{O}_7$.

of 1:1 Bi_2O_3 - SnO_2 molar mixture ($\text{Bi}_2\text{Sn}_2\text{O}_7$) were prepared and fired with the same procedure. The resulting powdered materials were then pressed with an uniaxial press in a rectangular mold and sintered for 10 hours at 700 °C.

Figure 3.2 shows the XRD pattern collected from the prepared samples. The patterns were collected on powder samples using a Bruker D8 diffractometer in a Bragg-Brentano configuration ($\text{Cu K}\alpha_1$ - $\text{K}\alpha_2$, variable slit, 6 mm). The patterns were corrected afterwards to fixed slit using the software Bruker EVA. For all the compositions, the main phase is the rutile SnO_2 . It can be observed that for compositions bigger than 2 cat.%_{Bi}, a secondary phase is also present. Figure 3.2 also shows the pattern collected from the product resulting from the 1:1 Bi_2O_3 - SnO_2 molar mixture. The phase is identified as the pyrochlore-structured $\text{Bi}_2\text{Sn}_2\text{O}_7$ [130, 131]. The emerging peaks from the secondary phase in the Bi - SnO_2 can be attributed to the $\text{Bi}_2\text{Sn}_2\text{O}_7$ phase. To follow the development of the secondary phase, the intensities of the most intense peaks of the secondary

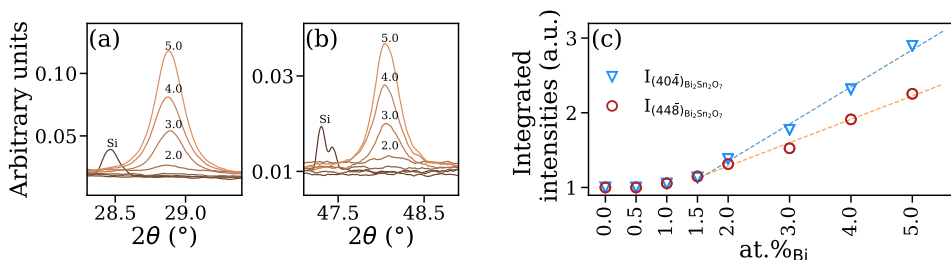


Figure 3.3: Figures (a) and (b) show the the intensities for different levels of cat.%_{Bi} of the peak relative to (404) and (448) reflection from $\text{Bi}_2\text{Sn}_2\text{O}_7$ respectively; figure (c) shows the variation of the integrated intensities of the peaks relative to $(404)_{\text{Bi}_2\text{Sn}_2\text{O}_7}$ and $(448)_{\text{Bi}_2\text{Sn}_2\text{O}_7}$ as a function of cat.%_{Bi}; each value has been normalized by the integrated intensity of the pure SnO_2 .

Table 3.1: Refined parameters of the different samples after Rietveld refinement.

at.% _{Bi}	a/b	c	X _O	R _p	R _{wp}
0.0	4.737967 (56)	3.1868548 (59)	0.30631 (20)	6.87	7.07
0.5	4.7379699 (53)	3.1868942 (55)	0.30608 (19)	6.39	6.64
1.0	4.7380528 (55)	3.1868789 (57)	0.30592 (19)	6.59	6.82
1.5	4.738101 (54)	3.1868298 (56)	0.30607 (19)	6.49	6.64
2.0	4.7381926 (56)	3.1869075 (60)	0.3061 (22)	8.86	7.83
3.0	4.7380643 (54)	3.186815 (57)	0.30623 (21)	7.87	7.47
4.0	4.7380714 (54)	3.1868267 (57)	0.30637 (21)	7.61	7.35
5.0	4.7380519 (55)	3.186806 (59)	0.30636 (22)	7.68	7.85

phase (corresponding to the $(40\bar{4})$ and $(44\bar{8})$ reflections) have been integrated and plotted against cat.%_{Bi} content in the different mixtures (figure 3.3). The integrated intensities show a linear trend with composition starting after 1.5 at.%_{Bi}. Smaller amounts of secondary phase may be difficult to detect by XRD.

Even small incorporation of Bi into the rutile structure should produce a certain distortion in the cell parameters of SnO₂, given the difference in ionic radius between Bi³⁺ and Sn⁴⁺ (1.03 and 0.69 Å respectively in *O_h* coordination [132]). Therefore, Rietveld refinement was conducted on the collected pattern using the FullProf software [**FullProfHomepage**]. In the case of SnO₂, a Si (NIST) internal standard was used for the determination of peak positions, which were then compared with the literature [113]. For samples with cat.%_{Bi}>2, the pyrochlore phase was also included in the refinement and the phase composition of the product mixtures was evaluated.

at.% _N	w.% _{s.p.}	at.% _C
2	0.58	0.2
3	3.29	1.3
4	5.84	2.3
5	8.38	3.4

Table 3.2: Nominal cat.%_{Bi} from the synthesis (a.%_N), mass percentage content of secondary phase obtained by Rietveld refinement (w.%_{s.p.}) and calculated cat.%_{Bi} converted w.%_{s.p.} (a.%_C).

The background was determined by manually selecting pattern background points, whose position were later left free to be refined. The peak shape was modeled using a Thompson-Cox-Hastings pseudo-Voigt with axial asymmetry correction [133]. The refined parameters were the scale factor, the profile parameters, u,v,w (Gaussian) and X,Y (Lorentzian), the unit cell and the atomic position of oxygen. Table 3.1 shows the main outputs of the refinement together with the agreement factors.

As can be observed, no clear variation from the pure SnO₂ phase nor trend can be observed in the analyzed samples for any of the analyzed compositions. The results of the refinement show that the preparation procedure did not produce any measurable incorporation of Bi in the rutile lattice. The calculated w.%_{Bi₂Sn₂O₇} from the refinement are presented in table 4.1. The derived cat.%_{Bi} show a certain deviation from the nominal content aimed during the preparation, indicating a smaller content of Bi in the mixture than the starting amount. Beside the possibility of incorrect determination during the refinement, an amount of Bi in the final mixture smaller than expected could be due to Bi₂O₃ evaporation during the synthesis or to reaction of the oxide with the alumina crucibles [131].

Figure 3.4 shows SEM images collected from the the different samples after sinter-

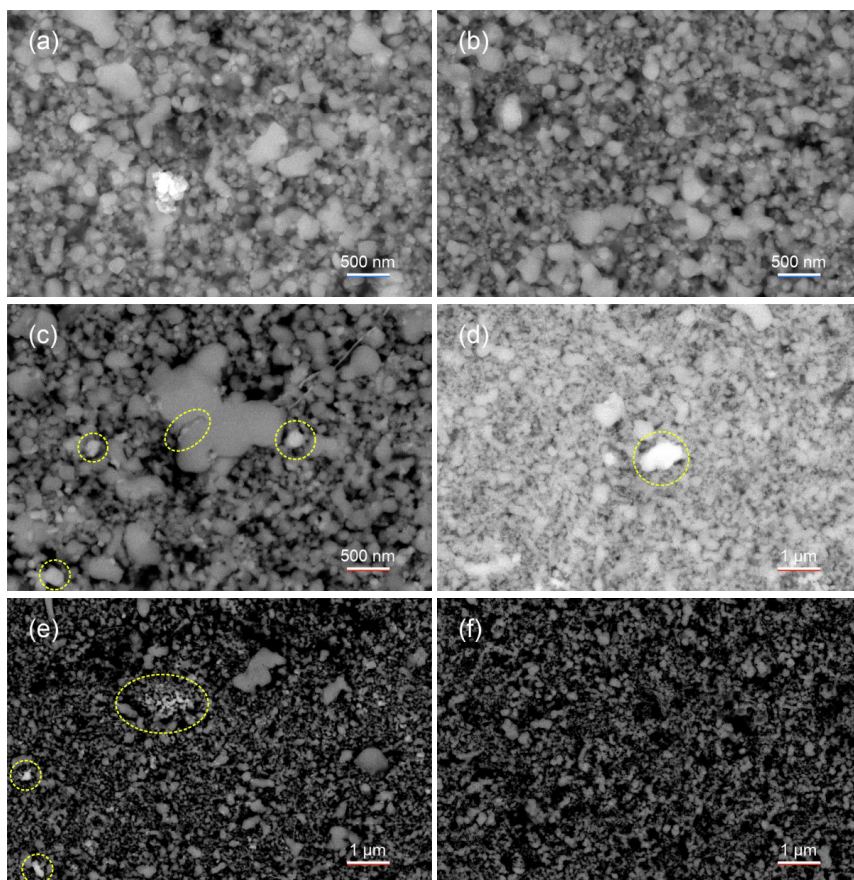


Figure 3.4: SEM images collected on samples with different Bi contents; blue and red marks on the scale bar indicate the detector used for acquiring the image, secondary electrons and backscattered electrons respectively; (a), (c) and (e): 5 cat.%Bi; (d): 2 cat.%Bi; (b) and (f): pure SnO₂ [Zeiss Merlin, acc.volt.: 15 kV].

ing. Portions of the bars were embedded in epoxidic resin. After the surface was polished, SEM images were acquired using both a backscattered electrons detector (BSD) and a secondary electrons detector (SED). The SEM analysis showed that all the samples were poorly sintered and highly porous, possibly because of the low temperature used for the heat treatment of the bars. Muraoka *et al.* [134] showed the effect of Bi₂O₃ in facilitating the sintering of In₂O₃-SnO₂ mixtures. In the case of the prepared samples, the presence of Bi₂O₃ did not affect the final degree of sintering nor the final particles size (as can be noticed comparing image 3.4a and 3.4b). The BSD images revealed the presence of the secondary phase (see yellow dashed circles in figures 3.4(c), (d) and (e)) for samples with cat.%Bi > 2; no secondary phase was detected in the case of samples with lower amount of cat.%Bi.

3.2 Spinel

Spinel structured materials have the general formula AB_2X_4 , where A and B are cations and X is an anion (typically chalcogenides as O or S). Spinel mostly crystallize in the cubic structure $Fd\bar{3}m$ (n° 227 in the International Tables) [135]. The typical cubic cell of a spinel is depicted in figure 3.5. The lattice is constituted by a *ccp* arrangement of X where half of the octahedral interstices (O_h) is occupied by B cations and one eighth of the tetrahedral sites (T_d) is occupied by A cations. O_h interstice is bigger than T_d interstice. Each unit cells contains 4 formula units of the spinel, i.e. 8 A cations, 16 B cations and 32 X atoms, for a total of 56 atoms per unit cell. If the origin of the unit cell is assumed on the O_h site, the A cation coordinates are (0.375 0.375 0.375) and the X coordinates are ($u u u$), where $u=0.25$ for an ideal spinel. Very often the disposition of X deviates from a perfect *ccp* lattice and u can vary to accomodate different sizes of A and B cations [136]: as u increases, T_d site cavity becomes bigger while O_h site cavity becomes smaller, shortening the length of the shared edges of the octahedron (while the unshared edges essentially do not vary).

Electrical conductivity in spinels occurs mainly by thermally activated hopping between O_h sites, since they constitute a three-dimensional network through the crystal lattice (differently from the T_d sites). Also, O_h - O_h distance constitute the shortest metal-metal distance in the spinel structure ($\approx 0.35a$) [135]. A peculiar characteristic of spinels is the ability for A and B to interchange sites, given the similar sizes of the cations. This means that for the same compound it is possible to accomodate cations in different configurations without changing the overall charge balance of the crystal. The general formula of a spinel can then be expressed as $(A_{1-x}B_x)_{T_d}[A_xB_{2-x}]_{O_h}O_4$, where x is called the *inversion parameter*. A *normal* spinel possess $x=0$, while when $x=1$ the structure is defined as *inverse* spinel. Those constitute the limiting cases: x can assume values between 0 and 1. Notably, inverse and normal configurations are both possible ground state of spinel structures. The occupancy of O_h and T_d sites is predominantly determined by cation size, electronic configuration and electrostatic interaction [137, 138]. The principles highlighted by Verwey and Heilman [139] on spinels state that high cation valence have the tendency to have high coordination number to neutralize

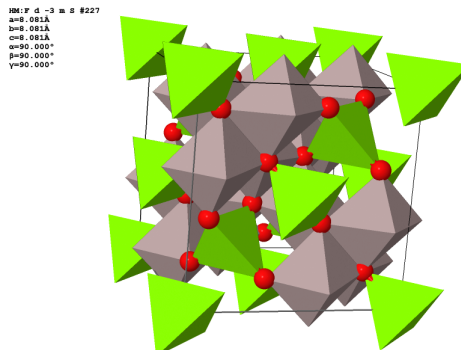


Figure 3.5: Structure of the parent compound for spinel class, $MgAl_2O_4$; T_d sites (A) are the green tetrahedrons, O_h sites (B) are the grey octahedron; O atoms are marked in red [115].

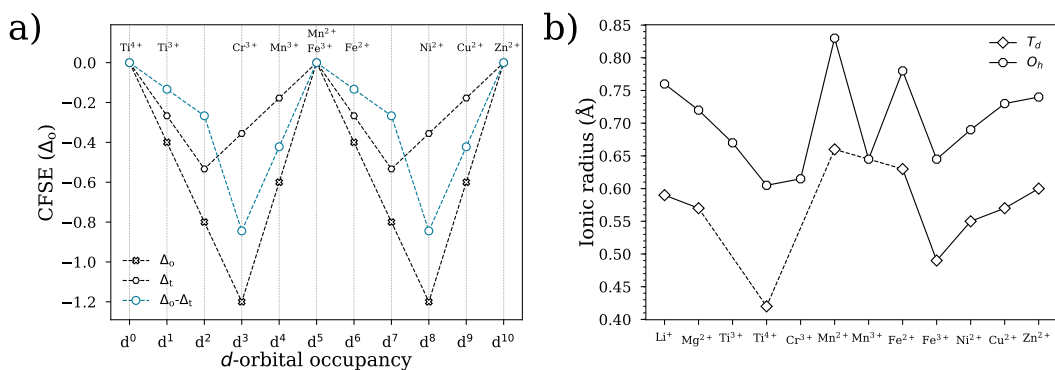


Figure 3.6: (a) CFSE for tetrahedral (Δ_t) and octahedral (Δ_o) coordination for different filling of d orbitals; the Octahedral Site Preference Energy ($\Delta_o - \Delta_t$) is also reported; (b) Ionic radii for the species involved in this study in octahedral (O_h) and tetrahedral (T_d) coordination, dashed line indicate the absence of the coordination for the specific ion.

the charge more efficiently, while it is known that ions with higher valence have smaller ionic radii and prefer smaller coordination shells [132, 135].

Electronic effects play a role when the cation in the spinel structure are transition metals: O_h and T_d coordination remove the degeneracy of d orbitals, which are then split in e_g and t_{2g} orbitals; the population of such orbitals by d electrons generates a Crystal Field Stabilization Effect (CFSE) [138]. The stabilization will be different for O_h and T_d sites: Δ_o and Δ_t (the energy difference between the splitted orbitals for a 6-fold coordination and a 4-fold coordination respectively) are not the same, in fact $\Delta_t \approx \frac{4}{9}\Delta_o$. The filling of the splitted orbitals will determine how much stabilization will be offered by the coordination. Figure 3.6 shows the stabilization energy as function of the population of d orbitals. Such stabilization is often expressed in units of Δ_o ; in the case of O_h coordination, the extreme cases are $-1.2 \Delta_o$ for d^3 and d^8 , and zero for d^5 .

Since the orbitals which are stabilized by coordination are 3 (t_{2g}) and 2 (e_g) in the case of O_h and T_d respectively, filling progressively with electrons the d orbitals will have different impact for 6- and 4-fold coordination. Therefore, the CFSE as a function of the number of d electrons will have different trends for the two sites. The energy difference of the stabilization offered by the two types of coordination can be quantified by the Octahedral Site Preference Energy, which is defined as $\Delta_o - \Delta_t$.

The degree of inversion is strongly dependent on temperature [140-143]. The phenomenon is characteristic of the spinel structure and cation distribution strongly influences the properties of the material [144-149].

Cation vacancies are reported to be the dominant defect in spinels even at low p_{O_2} [150-152]. Interstitial defects, especially interstitial oxygen, are considered unlikely in a close packed structure as the one of spinel [153]. Recent modeling [147, 154, 155] highlighted the role of *anti-site* defects in spinels (exemplified as $A_{T_d}^x + B_{O_h}^x \longrightarrow A_{O_h}^x + B_{T_d}^x$); in spinels structures the ability to switch site between O_h and T_d sites can originate charge compensation within the material to external doping.

3.2.1 $M\text{Cr}_2\text{O}_4$

Spinel structured chromites are the most common form of Cr ores on Earth [156]. Chromite (FeCr_2O_4) is in fact the principal commercial source of chromium metal. Chromites spinels are known to be extremely stable compounds even at high temperatures: they have been investigated as refractory materials [157] and as interconnect coatings in solid oxide fuel cells [158–162]. Iron-chromium-nickel spinels are widely reported to constitute the corrosion product of stainless steels [163–166]. They showed excellent corrosion resistance even in very harsh conditions [167], consequently they have been considered interesting candidates as corrosion resistant ceramics for the intended application.

Cr^{3+} is a d^3 ion and as such possesses a strong preference for octahedral sites. Combined with the high charge of the ion, this effect makes Cr occupy predominantly O_h positions in spinels. Electrical conductivity in spinel chromites goes through the O_h network of Cr by a hole hopping mechanism [157]:



The reported conductivities are generally below $10^{-4} \text{ S cm}^{-1}$ at room temperatures for chromites with full Cr occupancy of O_h sites, due to the difficulty of further oxidise Cr^{3+} , which carries a high stabilization energy together with the maximum exchange contribution.

Preparation and characterization

In the first attempt, the compositions investigated were MgCr_2O_4 , NiFeCrO_4 , NiCr_2O_4 and ZnCr_2O_4 . The raw materials (MgO , ZnO , NiO , Fe_2O_3 , Cr_2O_3) were weighed and mixed in an agate mortar. The mixtures were then transferred to alumina crucibles and covered with an alumina lid. The samples were fired at $1000 \text{ }^\circ\text{C}$ for 10 hours twice with a ramp rate of $60 \text{ }^\circ\text{C min}^{-1}$.

The resulting powders were analyzed by XRD (Bruker D8). An internal standard was used to attribute peak position (Si powder, NIST 640E). Figure 3.7 displays the

Table 3.3: Refined parameters of the different samples after indexing. The cell parameters obtained from the pattern collected experimentally are denoted as a exp., the values taken from the literature are referred as a lit..

Material	a exp. (Å)	a lit. (Å)	ref.
MgCr_2O_4	8.3350(1)	8.3341(2)	[168]
NiFeCrO_4	8.3063(1)	8.3075	[169]
NiCr_2O_4 tet.	5.8431(1)	5.8369(4)	[170]
NiCr_2O_4 tet. *	8.4281(3)	8.4301(6)	[170]
NiCr_2O_4 cub.	8.3202(2)	8.3155(7)	[170]
ZnCr_2O_4	8.3276(1)	8.3267(3)	[171]

* cell parameter c

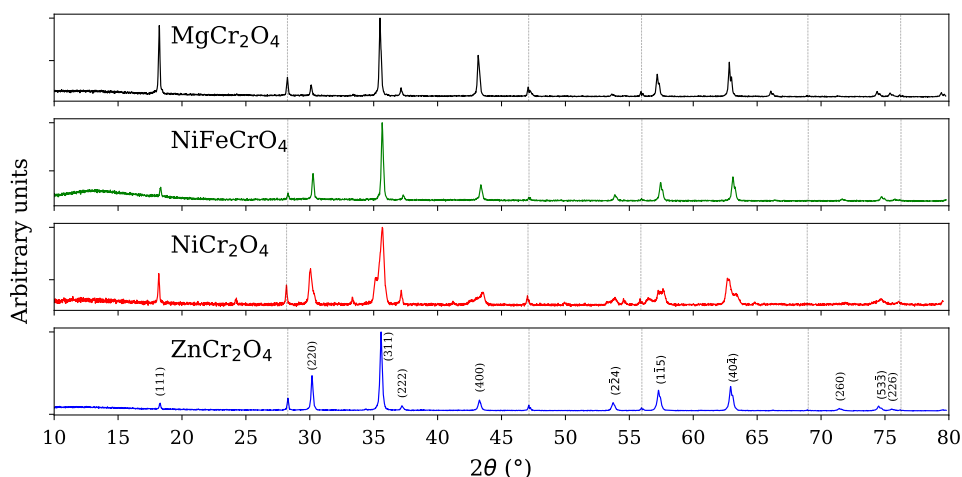


Figure 3.7: XRD pattern collected on the prepared chromites. Grey dashed lines indicate the position of the Si peaks used as a line position reference. The indexing of the peaks is displayed for ZnCr_2O_4

XRD pattern collected from the powder samples. The materials show the phase that are reported in the literature for the same composition of spinels. They all show a cubic spinel phase with the exception of NiCr_2O_4 , which is reported to have a tetragonal structure at room temperature [170]. In fact, the XRD pattern show a mixture of cubic and tetragonal phase. The cell constants have been extracted by performing Rietveld refinement on the collected patterns. In the case of NiCr_2O_4 both the cubic and the tetragonal phase were used in the refinement. The obtained w.% were 72 and 28% for the tetragonal and cubic phase respectively. The values obtained are reported in table 3.3 and show good agreement with the ones reported in the literature.

Figure 3.8 show SEM images collected on the materials. To prepare the SEM specimen, the powder of each material was dispersed in ethanol and then a drop of the suspension was deposited on carbon tape. The materials exhibit a particle size of 0.5-1 μm . Grains from NiFeCrO_4 appear more densely agglomerated than the other compounds. In the sample of NiCr_2O_4 , two types of microstructures can be seen, one with smaller rounded particles and one with bigger faceted particles, with a higher degree of sintering. The two microstructures can reflect the two phases identified by XRD measurements. Multiple SEM micrographs were collected (not shown) and the most abundant phase was the faceted sintered one; given the w.% determined by XRD refinement, it can be inferred that the faceted phase is the tetragonal NiCr_2O_4 while the rounded one is the cubic NiCr_2O_4 . MgCr_2O_4 and ZnCr_2O_4 have markedly shaped particles. ZnCr_2O_4 presents a bimodal distribution of particle size: beside 0.5-1 μm -sized grains, also 2-3 μm -sized grains were present in the sample. (observable at the right side of figure 3.8d).

As will be shown in section 4.2.1, the conductivity of the chromites was far below 0.1 S cm^{-1} at PEMECs operational temperatures, the target value of this study, while the

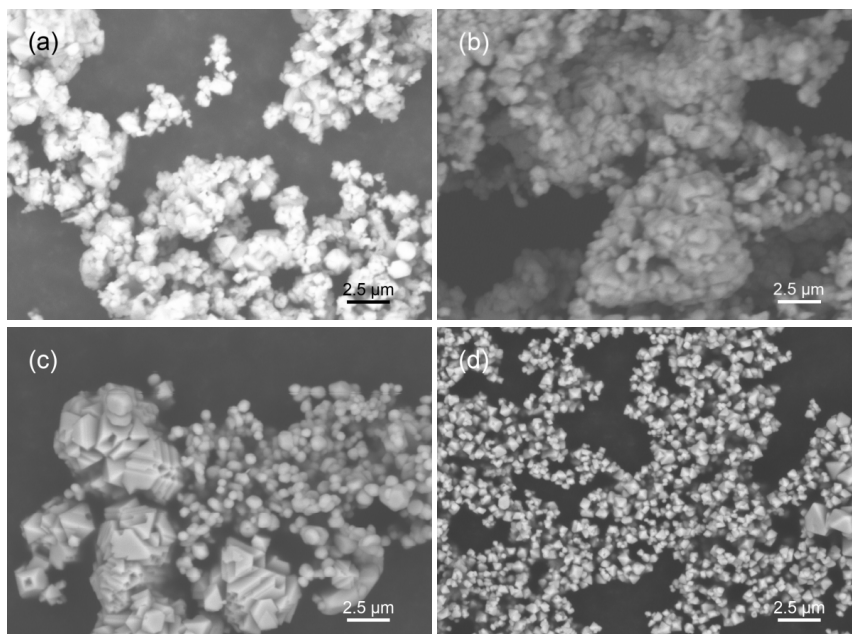


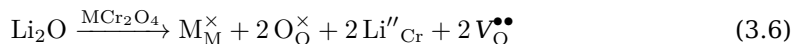
Figure 3.8: SEM images collected on chromites samples: (a) $MgCr_2O_4$, (c) $NiFeCrO_4$, (c) $NiCr_2O_4$ and (d) $ZnCr_2O_4$ [Hitachi TM3000, acc.volt.: 15 kV].

corrosion experiments showed a promising stability of these compounds, with mass loss in the order of 1% or lower. Considering the chromites a good candidate in terms of corrosion stability, it was attempted to increase the conductivity of those by introducing substitutional cations for increasing to the number of charge carriers in the material. As mentioned previously, chromites spinels are p -type conductors and the main charge carrier are electron holes, h^\bullet . Holes can be created incorporating O_2 in the lattice by consumption of oxygen vacancies, V^{**} , as showed in equation 3.3. Since the electrical path in spinels runs through the O_h sites which are dominated by Cr in chromites, it was chosen to substitute Cr ions in the structure. In fact, substituting Cr in spinel chromites is the only way to insert dopants in the O_h site, since the high preference of Cr^{3+} for 6-fold coordination would make the ion occupy all the O_h available. Stefan *et al.* [138] showed previously the positive effect on conductivity of substituting Cr in chromites. The choice of the dopant have to take in account the possible valence of the dopant itself: in the case of an acceptor, a dopant able to increase its valency upon oxidation can led to charge compensation and ineffective doping.

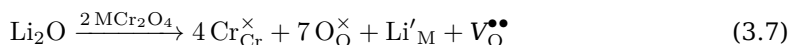
Among the tested spinels, $NiCr_2O_4$ and $NiFeCrO_4$ the best performing in terms of conductivity. It was decided to focus the attention on $NiCr_2O_4$, since even small amount of leached Fe from $NiFeCrO_4$ could lead to degradation of the Nafion membrane due to Fenton reactions [92, 172]. Recently, Fe-, Co- and Cu- substituted $NiCr_2O_4$ have been reported [78, 173, 174]. Cu can act as an effective acceptor dopant since it is difficult to oxidise further to Cu^{3+} [175] and its ionic radius is similar to the ones of Ni and Cr (see figure 3.6). Excellent conductivity at room temperature for Cr-based spinels were reported by Nagaraja *et al.*, who studied Li-doped $MnCr_2O_4$. Here, Mn was substituted

by Li up to 15% I decided to attempt to replicate such results and test such material toward corrosion as a candidate for the application investigated in this study.

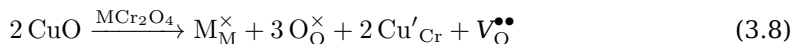
Li and Cu were then chosen as acceptor dopants for two spinel structured materials, MnCr_2O_4 and NiCr_2O_4 . By substituting Cr in MCr_2O_4 , where M is either Mn^{2+} or Ni^{2+} , the incorporation of Li into the structure can take place as,:



One oxygen vacancy is then created per substituted Cr. Substitution on M is unlikely since Cr is under-stoichiometric, but it would be possible in the case of segregation of a Cr-rich phase:



The incorporation of Cu can take place as:



One oxygen vacancy is then created with the substitution of two Cr ions. The incorporation of Cu into the M site would have no effect in terms of defect formation since M and Cu carry the same charge:



The materials were synthesized by nitrate combustion synthesis [161]. The addressed composition were $\text{MD}_x\text{Cr}_{2-x}\text{O}_4$, where M is Mn or Ni, D is Li or Cu and x is 0, 0.25 and 0.5. Solution of $\text{Ni}(\text{NO}_3)_2 \cdot 6\text{H}_2\text{O}$, MnCO_3 , $\text{Cr}(\text{NO}_3)_3 \cdot 9\text{H}_2\text{O}$, $\text{Cu}(\text{NO}_3)_2 \cdot 2.5\text{H}_2\text{O}$ and LiNO_3 were prepared using Milli-DI water (Merck Millipore). The metal content of the prepared solutions was determined by evaporation of weighed amounts of solution in

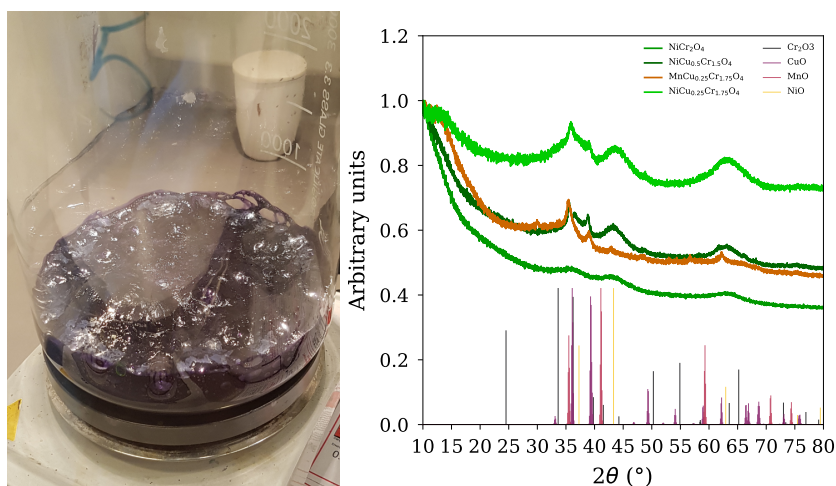


Figure 3.9: (left) Viscous residue during evaporation of nitrate solutions; (right) XRD pattern of the mixtures after calcination at 300 °C; the figure also shows the reference patterns of the oxides of the singular components of the mixtures [176-178].

three alumina crucibles in a furnace. Stoichiometric amounts of the solutions were mixed and a citric acid was added to the solution with a molar ratio between citric acid and total metal content of 1.5. The solution was stirred at 80 °C until a viscous residue was formed (see figure 3.9). The residues were then calcined at 300 °C for 5 hours (1st heat treatment). Figure 3.9 shows the XRD patterns collected on some of the mixtures after the calcination at 300 °C. The patterns do not show a clear crystalline phase, suggesting that the resulting mixture is mainly amorphous or composed of extremely small crystallites.

The figure also shows the patterns of the oxides of the components of the mixture taken from the literature. The very broad peaks emerging from the background can be related to a mixture of the single metal oxides of the components. The sharpest peaks around $2\theta=35^\circ$ and $2\theta=40^\circ$ can be associated with a spinel structure (reflections (311) and (400), see the patterns in figure 3.7). The pattern from $\text{MnCu}_{0.25}\text{Cr}_{1.75}\text{O}_4$ shows also a small sharp peak close to $2\theta=30^\circ$. No peak of the single metal oxides is present at those values of 2θ , while spinel structures present the reflection related to (220) plane: this can be an indication that a spinel structured phase is already present after calcination at 300 °C.

The materials were then calcined at 1000 °C for 10 hours (2nd heat treatment). Figure 3.10 shows the XRD patterns collected on the Li-containing resulting powders (Rigaku SmartLab).

In both NiCr_2O_4 and MnCr_2O_4 the main phase is a spinel phase. $\text{MnLi}_{0.25}\text{Cr}_{1.75}\text{O}_4$ and $\text{MnLi}_{0.5}\text{Cr}_{1.5}\text{O}_4$ show a shift to high angles of the peaks (see figure 3.11) indicating that the incorporation of Li lead to a decrease in the lattice parameter of the material. No secondary phases can be detected. Differently from MnCr_2O_4 -related compounds, NiCr_2O_4 -series exhibit multiple phases in the XRD pattern. The tetragonal and cubic phases reported for NiCr_2O_4 are present in the undoped material (see figures 3.11 and 3.12). Interestingly, the ratio between tetragonal and cubic phase appear to decrease when Li is present in the system. It can be observed that a secondary phase is developing increasing the Li content: the arrows in figure 3.12 indicate the peaks of the emerging secondary phase. In case of limited miscibility or loss of Li (Li_2O is volatile at high temperatures), NiO would be the most probable secondary phase, since it is over-stoichiometric. Figure 3.12 also displays the pattern reported in literature for NiO [177]. The position of the NiO peak and the secondary phase have a difference in 2θ of almost a degree, even if they display similar distribution of reflection peaks. Goode-nough *et al.* [179] studied the crystallographic properties of Li-doped NiO, which shows a decrease in cell parameter due to the incorporation of Li into Ni sites in the rock salt structure. The shrinkage of the crystallographic cell causes a shift of the peak positions toward higher values of 2θ . In figure 3.12 the reflections related to $\text{Li}_{0.3}\text{Ni}_{0.7}\text{O}$ are reported: the material still posses a rock salt structure but with a small crystalline cell. Its peaks are then shifted toward higher 2θ values compared with NiO. The peaks of the secondary phase appear to lay in between the ones from NiO and $\text{Li}_{0.3}\text{Ni}_{0.7}\text{O}$. Therefore, it can be inferred that the secondary phase is composed of $\text{Li}_x\text{Ni}_{1-x}\text{O}$, with $x < 3$. The observation that Li is contained mainly in the secondary phase is also suggested by the

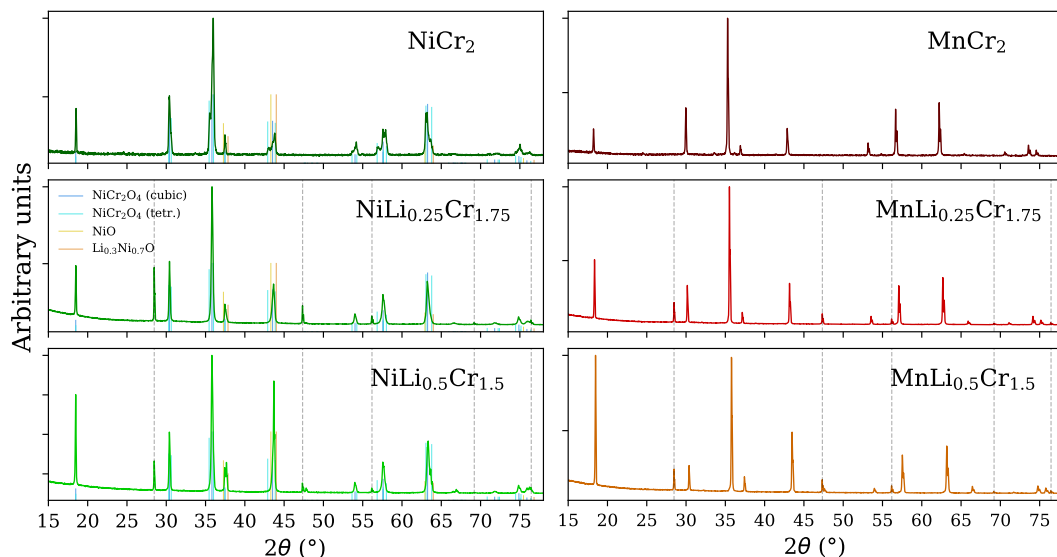


Figure 3.10: XRD pattern collected on the of the mixtures after the 2nd heat treatment; dashed grey lines indicate internal standard Si; patterns of possible secondary phases are reported from the literature in the case of NiCr_2O_4 , $\text{NiLi}_{0.25}\text{Cr}_{1.75}\text{O}_4$ and $\text{NiLi}_{0.5}\text{Cr}_{1.5}\text{O}_4$, together with the pattern from tetragonal and cubic pure NiCr_2O_4 [170, 177, 179]

small variation of peak position of the (311) reflection for NiCr_2O_4 -related compounds observed in figure 3.11.

The Cu-doped samples presented a similar behaviour as the Li-doped ones. Figure 3.13 shows the series $\text{NiCu}_x\text{Cr}_{2-x}\text{O}_4$ with $x=0,0.25,0.5$. As can be observed, the synthesis did not produce a phase pure material and reflections from the oxides of the single components in the mixture can be recognized in the pattern. Figure 3.14 displays the series $\text{MnCu}_x\text{Cr}_{2-x}\text{O}_4$ with $x=0,0.25,0.5$. The Cu-containing material shows a single spinel-structured phase. The peak positions appear shifted toward higher values of 2θ , consistently with the increase of Cu content (see figure 3.15). If the substitution of Cr^{3+}

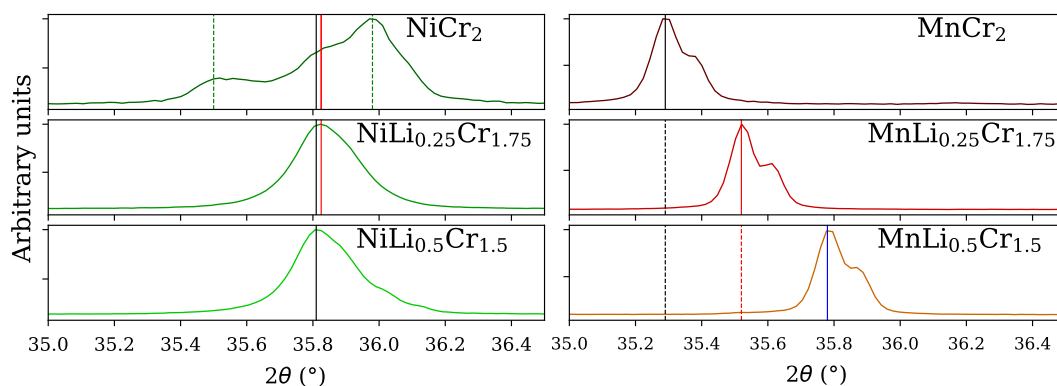


Figure 3.11: XRD pattern collected on the of the mixtures after the 2nd heat treatment; magnification of the pattern around the reflection related to (311) plane; in the case of NiCr_2O_4 , dashed and solid lines indicate reflections related to the tetragonal and cubic phase of NiCr_2O_4 .

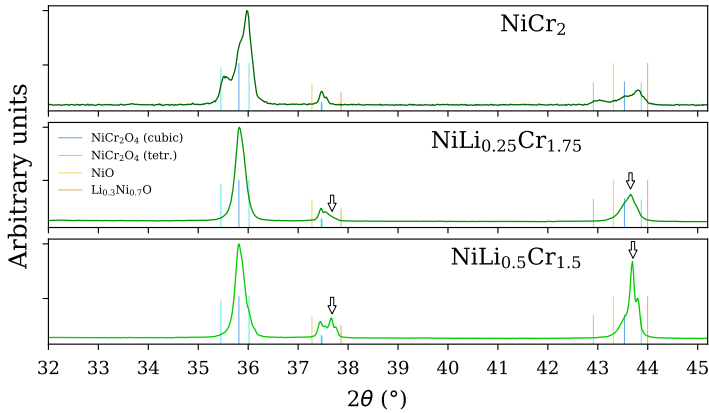


Figure 3.12: Magnification of the XRD pattern collected on the of the mixtures after the 2nd heat treatment for the NiCr₂O₄-related Li-doped materials.

by Cu²⁺ in O_h site is assumed, an expansion of the cell volume can be expected, given the difference in atomic radius between the species (0.755 and 0.87 Å for Cr³⁺ and Cu²⁺ respectively [132]). If instead Cu²⁺ occupies the T_d site, then part of the O_h sites would be occupied by Mn²⁺. In terms of CFSE, Mn²⁺ does not have any stabilization energy due to the six-fold coordination, while Cu²⁺ has a stabilization energy of $-0.6\Delta_o$ and Cu²⁺ is expected to occupy O_h position over Mn²⁺. Yet, Mn³⁺ possess a stabilization energy of $-0.6\Delta_o$, which equals the one for Cu²⁺. According to principles of Verwey and Heilmann [139], a higher-charged ion is expected to occupy O_h site preferentially over a lower-charged ion, due to better charge compensation. Therefore, Mn³⁺ (0.72 Å in O_h in low spin configuration) is prone to occupy the O_h site over Cu²⁺, causing a reduction of the cell parameter. Nonetheless, Mn³⁺ in T_d site carries the same ionic radius as in O_h site and could also cause the shrinking of the cell dimensions in the spinel structure. Figure 3.15 shows the evolution of the cell parameter a in MnM_{*x*}Cr_{2-*x*}O₄ as a function of Li and Cu content. Rietveld was refinement conducted on MnCu_{0.25}Cr_{1.75}O₄ in two different configurations, (Mn)^{*T_d*}[Cu_{0.25}Cr_{1.75}]^{*O_h*}O₄ and (Mn_{0.75}Cu_{0.25})^{*T_d*}[Mn_{0.25}Cr_{1.75}]^{*O_h*}O₄. Site occupancies are difficult to refine from XRD data in multi-elemental compounds [181], especially when the alternative elements are close in electron density as Cu, Mn and Cr. The refinement has been conducted by keeping fixed the occupancies in the aforementioned configurations and letting the other parameters to be refined freely (scale factor, the profile parameters, u, v, w (Gaussian) and X, Y (Lorentzian), overall thermal parameter, unit cell parameters, asymmetry parameters and the atomic position of oxygen). Table 3.4 reports the values of some refined parameters of the two configurations. The R values for (Mn)^{*T_d*}[Cu_{0.25}Cr_{1.75}]^{*O_h*}O₄ are slightly lower than the ones for

Table 3.4: Refined parameters for different elemental distributions in MnCu_{0.25}Cr_{1.75}O₄.

	a (Å)	u	R_{wp}	R_F	R_{Bragg}
(Mn) ^{<i>T_d</i>} [Cu _{0.25} Cr _{1.75}] ^{<i>O_h</i>}	8.41757(1)	0.26144(5)	7.16	6.13	5.93
(Mn _{0.75} Cu _{0.25}) ^{<i>T_d</i>} [Mn _{0.25} Cr _{1.75}] ^{<i>O_h</i>}	8.41756(1)	0.26017(6)	7.77	6.47	6.21

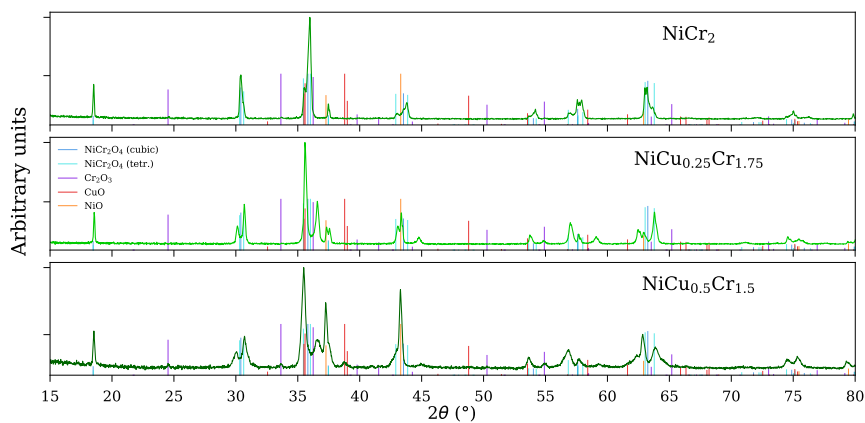


Figure 3.13: XRD pattern collected after the 2nd heat treatment on $\text{NiCu}_x\text{Cr}_{2-x}\text{O}_4$ with $x=0,0.25,0.5$.

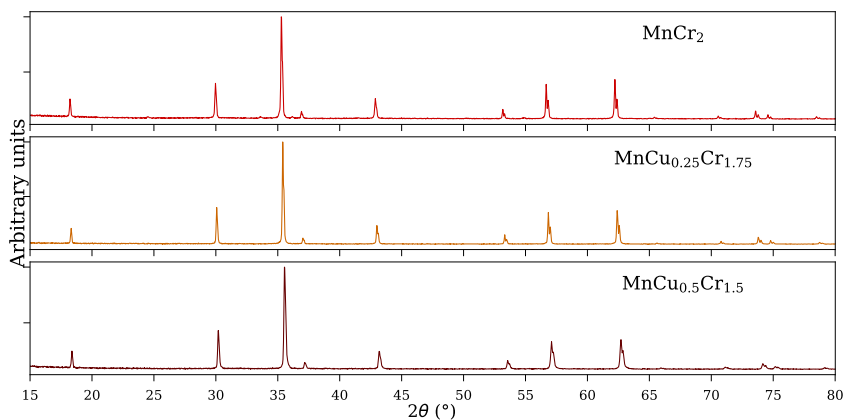


Figure 3.14: XRD pattern collected after the 2nd heat treatment on $\text{MnCu}_x\text{Cr}_{2-x}\text{O}_4$ with $x=0,0.25,0.5$.

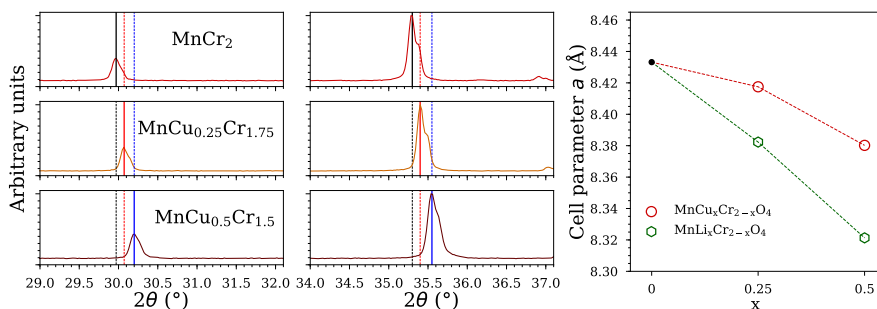


Figure 3.15: (left) Magnification of the (220) and (311) reflections of the XRD pattern collected on $\text{MnCu}_x\text{Cr}_{2-x}\text{O}_4$ with $x=0,0.25,0.5$; (right) evolution of the cell parameter a as a function of x in $\text{MnD}_x\text{Cr}_{2-x}\text{O}_4$ with $x=0,0.25,0.5$ and $D=\text{Li,Cu}$.

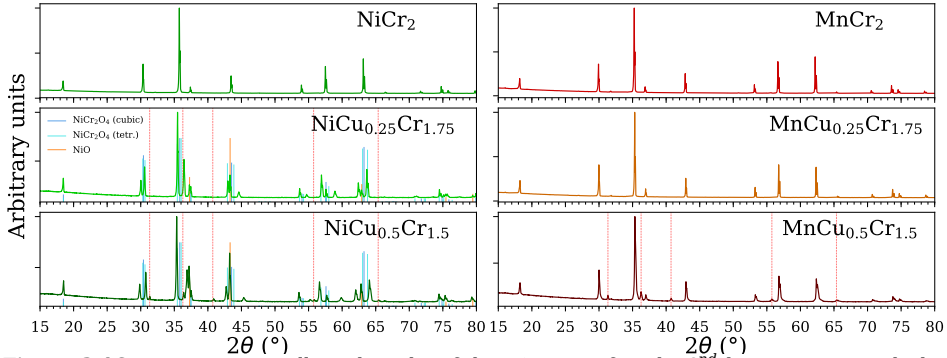


Figure 3.16: XRD pattern collected on the of the mixtures after the 3rd heat treatment; dashed red lines indicate secondary phase identified as CuCrO_2 [180]; the patterns of NiO [177] is reported from the literature in the case of $\text{NiCu}_{0.25}\text{Cr}_{1.75}\text{O}_4$ and $\text{NiCu}_{0.5}\text{Cr}_{1.5}\text{O}_4$, together with the pattern for tetragonal and cubic NiCr_2O_4 .

$(\text{Mn}_{0.75}\text{Cu}_{0.25})^{T_d}[\text{Mn}_{0.25}\text{Cr}_{1.75}]^{O_h}\text{O}_4$: this can be an indication that in the material the real cation distribution among T_d and O_h sites is closer to $(\text{Mn})^{T_d}[\text{Cu}_{0.25}\text{Cr}_{1.75}]^{O_h}\text{O}_4$. For this to be true, part of the Mn^{2+} present in the T_d site must be oxidised to Mn^{3+} , for example as $(\text{Mn}^{\text{II}}_{0.75}\text{Mn}^{\text{III}}_{0.25})^{T_d}[\text{Cu}_{0.25}\text{Cr}_{1.75}]^{O_h}\text{O}_4$, since a shrinking of the cell parameter was observed.

During the preparation of the bars, the materials have been pressed and then sintered at 1300 °C for 24 hours (3rd heat treatment), in order to favour densification, provide more energy for solid state reactions and eliminate secondary phases. Figure 3.16 shows the XRD collected on the crushed bars after the 3rd heat treatment. In the case of MnCr_2O_4 -related materials, the primary phase is a cubic spinel phase as after the 2nd heat treatment. Nevertheless, it can be observed that in the case of $\text{MnCu}_{0.5}\text{Cr}_{1.5}\text{O}_4$ a secondary phase appeared after the heat treatment. The phase has been identified as CuCrO_2 [180], a compound with delafossite-type structure where Cu is present as Cu^+ . This indicates that the temperature reached by the heat treatment was too high, able to reduce Cu^{2+} to Cu^+ in air. In fact, it has been reported that Cu^{2+} is reduced at ambient p_{O_2} above 1100 °C [182]. The formation of CuCrO_2 implies that Cu is subtracted from

Table 3.5: Refined parameters for $\text{NiCu}_{0.25}\text{Cr}_{1.75}\text{O}_4$ and $\text{NiCu}_{0.5}\text{Cr}_{1.5}\text{O}_4$ after the 3rd heat treatment: cell parameters a and c of the tetragonal phase and site occupancies; the values for CuCrO_2 and NiCr_2O_4 are taken from [170]; the calculated w.% and R parameters of the refinement are also reported.

	(T_d)	$[O_h]$	a	c
NiCr_2O_4	(Ni)	$[\text{Cr}_2]$	5.8369(4)	8.4301(6)
$\text{NiCu}_{0.25}\text{Cr}_{1.75}\text{O}_4$	$(\text{Ni}_{0.81}\text{Cu}_{0.28})$	$[\text{Cu}_{0.71}\text{Cr}_{1.35}]$	5.94955(1)	8.12357(2)
$\text{NiCu}_{0.5}\text{Cr}_{1.5}\text{O}_4$	$(\text{Ni}_{0.31}\text{Cu}_{0.69})$	$[\text{Cu}_{0.67}\text{Cr}_{1.33}]$	5.97766(3)	7.98886(5)
CuCr_2O_4	(Cu)	$[\text{Cr}_2]$	6.016(4)	7.981(4)
	w.% NiO	w.% CuCrO_2	R_F	R_{Bragg}
$\text{NiCu}_{0.25}\text{Cr}_{1.75}\text{O}_4$	34.1	-	6.71	7.62
$\text{NiCu}_{0.5}\text{Cr}_{1.5}\text{O}_4$	32.3	8.4	5.73	5.03

the spinel phase: Rietveld refinement conducted on the spinel phase revealed that the cell parameter a for the composition $\text{MnCu}_{0.5}\text{Cr}_{1.5}\text{O}_4$ is 8.41028(3) Å, bigger than the value of a of the same composition after the 2nd heat treatment (4.38023(2) Å). This is an indication that due to the 3rd heat treatment part of the Cu and Cr left the spinel structure to form the new phase CuCrO_2 , leaving a spinel phase with a composition closer to MnCr_2O_4 . No evidence of the secondary phase is present for $\text{MnCu}_{0.25}\text{Cr}_{1.75}\text{O}_4$. The refined cell parameter a did not show a major deviation from the one obtained after the 2nd heat treatment (8.41733(2) and 8.41752(1) respectively), indicating that no major Cu loss had taken place. These results suggest that the solubility of Cu into MnCr_2O_4 decreases when copper in the oxidation state +1.

$\text{NiCu}_{0.25}\text{Cr}_{1.75}\text{O}_4$ and $\text{NiCu}_{0.5}\text{Cr}_{1.5}\text{O}_4$ also contain the compound CuCrO_2 . In the patterns, also NiO is observable, meaning that even the high temperature treatment did not favour the formation of a single phase. Interestingly, NiCr_2O_4 appears as a single phase cubic spinel, while in $\text{NiCu}_{0.25}\text{Cr}_{1.75}\text{O}_4$ and $\text{NiCu}_{0.5}\text{Cr}_{1.5}\text{O}_4$ the main phase has a tetragonal symmetry. The lattice parameters a and c of the tetragonal phase have been refined and they show a variation of the parameters as a function of Cu content. Specifically, the expansion of a and the reduction of c make the crystal cell closer to the values reported for CuCr_2O_4 . This is an indication that Cu partially enters the lattice of NiCr_2O_4 , after the 3rd heat treatment. Occupancies have been refined for the different sites by Rietveld refinement: even if the absolute values should be read with caution (as mentioned before, similar scattering factors as the ones from transition metals are different to refine; for example, the occupancy of Cr is probably underestimated), it can be observed that the occupancy of Cu in the T_d site increases consistently with the formal Cu content and with the w.% of NiO calculated for the different patterns.

3.2.2 MTi_2O_4

In spinels with general formula MTi_2O_4 , Ti exhibits oxidation state +3. If the counterion M carries charge +2, all the Ti is present as Ti^{3+} , while, if M carries charge +1, the Ti is present both in Ti^{3+} and Ti^{4+} , with a nominal oxidation state of +3.5. The presence of Ti^{3+} is necessary for good electronic conduction, as Ti^{4+} has electronic configuration $[\text{Ar}]3d^0$ and the d -band is empty of electrons (in fact, compounds as TiO_2 and stoichiometric perovskite-structured titanates are typically insulators). Interest in these compounds rose after Johnston *et al.* reported LiTi_2O_4 as the first oxide to exhibit superconductivity above 10 K [183]. LiTi_2O_4 is the end member of the spinel-structured solid solution, $\text{Li}_{1+x}\text{Ti}_{2-x}\text{O}_4$, firstly reported by Deschanvres [184], where $0 \leq x \leq \frac{1}{3}$. The other end member of the series, $\text{Li}_{\frac{4}{3}}\text{Ti}_{\frac{5}{3}}\text{O}_4$, correspond to the composition $\text{Li}_4\text{Ti}_5\text{O}_{12}$, an established anode material for Li-ion batteries [185, 186]. Interestingly, the electrical resistivity changes dramatically as soon as $x \leq 0.1$, changing from 10^{-1} to 10^2 Ω cm at room temperature; the reason is that Li^+ sits the lattice in O_h position as $x > 0$, breaking the $[\text{Ti}]_{O_h}$ 3D network.

Due to the significance of the properties of LiTi_2O_4 , other alkali-Ti systems have been investigated, for example MgTi_2O_4 , CaTi_2O_4 and NaTi_2O_4 . Only the former is stable in

a cubic spinel structure at room temperature, and exhibits an electrical conductivity $> 10 \text{ S cm}^{-1}$ at room temperature. CaTi_2O_4 and NaTi_2O_4 possess a pseudo-brookite [187] and CaFeO_4 [188] structure respectively, where 3D network of edge-sharing TiO_6 octahedra is not maintained. The two materials exhibit conductivities below 0.1 S cm^{-1} at room temperature [189]. MgTi_2O_4 is the end member of the solid solution $\text{Mg}_{1+x}\text{Ti}_{2-x}\text{O}_4$, which exhibit a spinel structure for $0 \leq x \leq 1$ [190]. Remarkably, the solid solution exhibit conductivity $> 10 \text{ S cm}^{-1}$ at room temperature up to $x=0.25$ [191].

MnTi_2O_4 is also reported to possess a cubic spinel structure at room temperature [192, 193] and it has been prepared to study the interaction of a magnetic ion such as Mn^{2+} to the magnetic properties of MTi_2O_4 . This material also exhibits conductivity $> 1 \text{ S cm}^{-1}$ at room temperature and the conduction is dominated by p -type polaron mechanism [193].

The reported conductivity of MTi_2O_4 spinels motivated their election for further testing. No explicit stability assessment of such compounds have been found in the literature. Inukai *et al.* reported degradation of the electrical properties due to long term storage of LiTi_2O_4 in humidified environment [194]. Nevertheless, LiTi_2O_4 is also reported to exhibit reversible cation exchange properties in acid solutions [195].

Preparation and characterization

The synthesis of reduced titanates requires to expose the reagents to a reducing environment, usually achieved by conducting the synthesis in vacuum or in H_2/Ar or H_2/N_2 mixtures. One of the most common sources of Ti^{3+} in solid state synthesis is Ti_2O_3 . The material is not stable at room temperature and ambient p_{O_2} and undergoes spontaneous oxidation during storage toward the thermodynamically stable phase rutile. Especially in the case of LiTi_2O_4 , controlling the oxidation state of Ti in the final product is of paramount importance for determining the properties of the reduced Ti-based spinels. Therefore, the phase purity of Ti_2O_3 was investigated before starting the synthesis.

Figure 3.17 shows the XRD pattern collected on the commercial Ti_2O_3 used for the synthesis. It can be observed the presence of multiple secondary peaks at the side of the ones belonging to the corundum phase. Considering the possible oxidation products of Ti_2O_3 , the peaks observed as secondary phases have been assigned as showed by the marks in figure 3.17: alongside rutile TiO_2 , two of the room temperature polymorph of Ti_3O_5 , $\beta\text{-Ti}_3\text{O}_5$ [178] and $\gamma\text{-Ti}_3\text{O}_5$ [196] can be identified. The weight fraction of the different phases was estimated by semi-quantitative analysis conducted on the XRD pattern (software HighScore Plus, PANalytical), which delivered a weight fraction of 84:15:1 for the mixture $\text{Ti}_2\text{O}_3:\text{Ti}_3\text{O}_5:\text{TiO}_2$. To further confirm the obtained quantification, a sample of the raw material was analyzed by thermogravimetry in air (TG 209 cell, Netzsch), which is showed in the inset plot of figure 3.17. Ti_2O_3 is reported to oxidise in air when above $500 \text{ }^\circ\text{C}$ [197]. The oxidation reaction of Ti_2O_3 is



The reaction with oxygen causes an increase in the mass of the starting material of 11.13%. Since in Ti_3O_5 Ti is already partially oxidised to an oxidation state bigger than

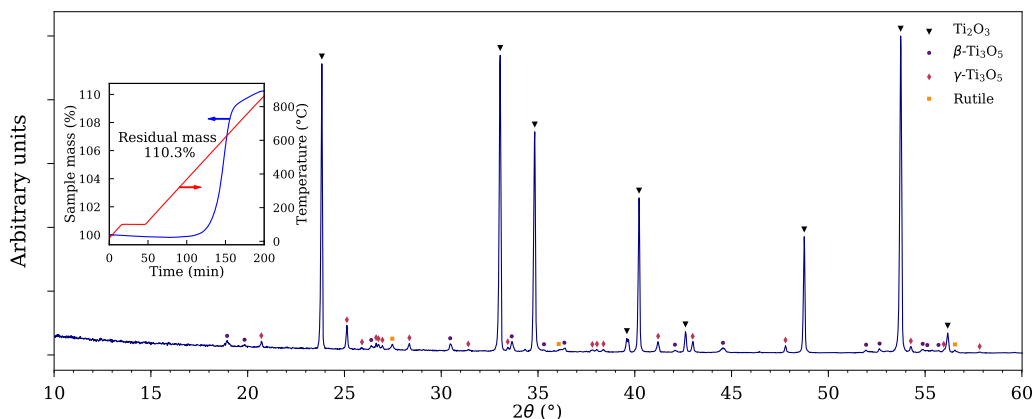
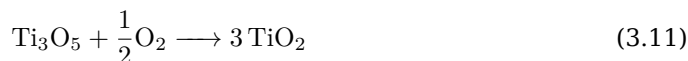


Figure 3.17: XRD pattern collected after on the raw material Ti_2O_3 ; the inset plot shows the TGA measured on the a sample of the same material.

+3, the reaction



causes a smaller mass increase of the starting material of 7.16%. Considering the mass ratio 84:15:1 Ti_2O_3 : Ti_3O_5 : TiO_2 (with 10:5 γ - Ti_3O_5 : β - Ti_3O_5), the expected mass increase of the mixture upon complete oxidation is 10.42%. As can be seen in the thermogravimetric data, the experimental value is very close to the expected value. Therefore, the raw Ti_2O_3 was further treated as composed by the mass fraction determined by XRD semi-quantification. When the material was used as Ti^{3+} source for the spinel synthesis, the oxidised fraction found together with the corundum structure was compensated by adding Ti metal to the mixture. The amount of Ti was added to match the content of the secondary oxidised phases according to the reactions



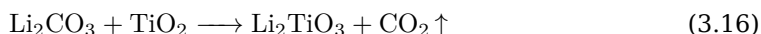
Metallic Ti is also an excellent getter, which can help further eliminate O_2 from the reducing atmosphere where MTi_2O_4 are synthesized. The assumption is made that the reactions in equations 3.12 and 3.13 go to completion in the conditions at which the synthesis of the materials takes place. The mix of raw Ti_2O_3 and Ti metal, $\text{Ti}_2\text{O}_3^{\text{mix}}$, was then regarded as corresponding to phase pure Ti_2O_3 according to equations 3.14 and 3.15

$$\text{mol Ti}_{\text{Ti}_2\text{O}_3^{\text{pure}}} = \text{mol Ti}_{\text{Ti}_2\text{O}_3^{\text{mix}}} = \text{mol Ti}_{\text{Ti}_2\text{O}_3^{\text{raw}}} + \text{mol Ti}_{\text{Ti metal}} \quad (3.14)$$

$$1\text{ g Ti}_2\text{O}_3^{\text{pure}} = 0.987\text{ g Ti}_2\text{O}_3^{\text{raw}} + 0.013\text{ g Ti} \quad (3.15)$$

When further in text it will be referred to Ti_2O_3 for a preparation, the material used is $\text{Ti}_2\text{O}_3^{\text{mix}}$.

The synthesis of LiTi_2O_4 was conducted through a two steps process. Li_2O is known to evaporate substantially at the temperatures required for the synthesis of the spinel, thus Li_2TiO_3 has been used as a Li source, as it is less prone to volatilization than Li_2O [184, 198]. Li_2TiO_3 was prepared by mixing LiCO_3 and TiO_2 according to reaction 3.16. A 2% Li_2CO_3 excess was added to the mixture to account for unwanted Li loss during the synthesis.



The starting materials were grinded in an agathe mortar and then fired at 800°C for 8 h. The product was phase pure Li_2TiO_3 .

The second step of the synthesis is reported in equation 3.17



A mixture of Ti_2O_3 , TiO_2 and the prepared Li_2TiO_3 was ball milled in acetone in a planetary mill for 45 minutes and pressed into cylindrical pellets with an uniaxial press (\varnothing 8 mm, 2.5 t).

The pellets were wrapped in Cu foil (which was previously sanded) and surrounded by powder of the same composition to further minimize Li loss during the heat treatment. Figure 3.18 shows the wrapped samples loaded on an alumina boat. The mixture was fired at 860°C for 16 h in 5% H_2/Ar . The temperature for the synthesis of LiTi_2O_4 must be controlled carefully, since above 900°C the system undergoes a phase transition from spinel to ramsdellite structure [198]. Since leaking or unwanted presence of O_2 can be expected during the synthesis, especially when the gas composing the reactive atmosphere is continuously flowed as in a tube furnace, an excess of Ti^{3+} ions over Ti^{4+} can avoid the formation of unwanted oxidised phases. Different molar ratios of the reagents of equation 3.17 have been tested and they are listed in table 3.6. The overall molar content of Ti was kept constant.

Figure 3.19 shows the XRD patterns collected on the obtained products. All the different mixtures showed a spinel phase as primary phase. Sample A and B showed

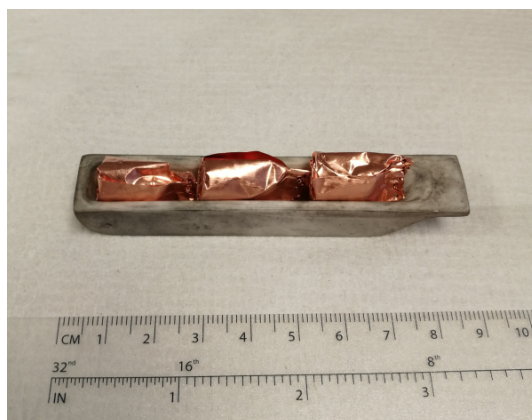


Figure 3.18: Pellets of the reactive mixture for the synthesis of LiTi_2O_4 wrapped in Cu foil prior to the heat treatment.

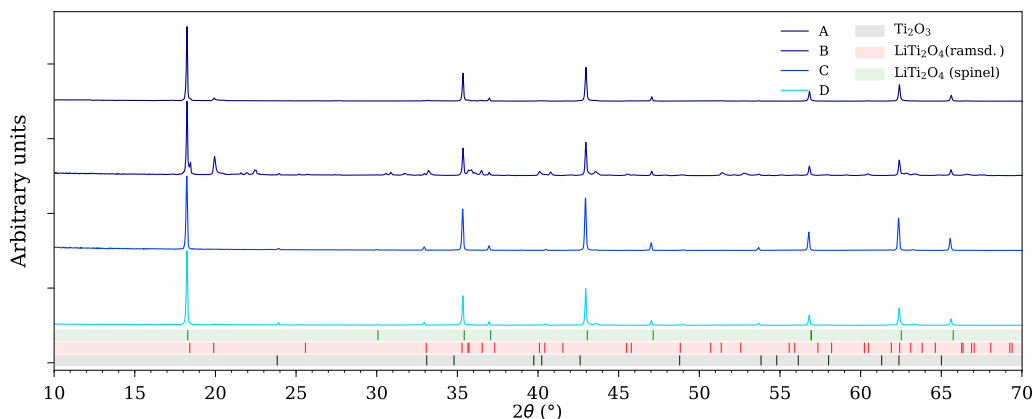


Figure 3.19: XRD patterns collected on the product of the synthesis of LiTi_2O_4 using different $\text{Li}_2\text{TiO}_3:\text{Ti}^{3+}:\text{Ti}^{4+}$ ratios: 1:2:1 (A), 1:2.2:0.8 (B), 1:2.3:0.7 (C) and 1:2.4:0.6 (D).

the presence of a secondary ramsdellite-structured phase. The peak positions appear shifted to higher angles compared with the reported values for ramsdellite structured LiTi_2O_4 , which is consistent with the reduction of the crystalline cell volume of such phase due to partial oxidation. In addition, sample B presents more secondary phases which are probably product of further oxidation. In fact, the Cu foil used for the synthesis of such sample appeared pinched after the synthesis, fact that could have led to Li loss and a less reducing reactive environment. Samples C and D presented Ti_2O_3 as a secondary phase, indicating that the excess Ti^{3+} prevents the formation of partially oxidised phases. Since composition C was the one with the smaller fraction of secondary phase it was selected for further testing. When LiTi_2O_4 will be mentioned in the following text, the corresponding sample is sample C.

In the case of the synthesis of MgTi_2O_4 and MnTi_2O_4 , the raw materials required for the synthesis are less prone to volatilization, thus the compounds can be prepared in vacuum to limit the oxidation during the high temperature solid state synthesis.

MnTi_2O_4 has been prepared by solid state synthesis of reactive mixtures in evacuated quartz tubes [192, 193]. The Mn^{2+} source was MnTiO_3 , which was prepared by calcination of a mixture of MnCO_3 and TiO_2 at 1200 °C for 20 hours according to reaction



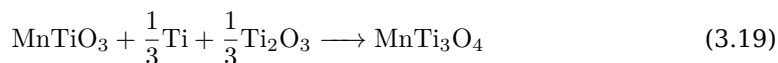
Table 3.6: Molar compositions of the reactive mixtures used for the synthesis of LiTi_2O_4 and the secondary phases observed in the XRD patterns of the resulting products.

Sample	Li_2TiO_3	Ti^{3+}	Ti^{4+}	Secondary phases
A	1	: 2	: 1	Ramsdellite
B	1	: 2.2	: 0.8	Ramsdellite and others
C	1	: 2.3	: 0.7	Ti_2O_3
D	1	: 2.4	: 0.6	Ti_2O_3



Figure 3.20: Pellets wrapped in Mo foil and sealed under vacuum in a quartz tube.

To obtain MnTi_2O_4 , two reaction routes can be used:



Both the synthesis routes were attempted: samples MNTA (prepared according to eq. 3.19) and MNTB (prepared according to eq. 3.20) were mixed in an agate mortar, ball milled and pressed into pellets as described previously for LiTi_2O_4 . The pellets were then wrapped in Mo foil (the preparation temperature was too close to the melting point of Cu) and sealed in evacuated quartz tubes (pressure at sealing 10^{-4} mbar). The samples were then fired at 1000°C for 16 hours. Figure 3.20 shows an example of the quartz tubes prior the thermal treatment.

Figure 3.21 shows the XRD pattern of the products obtained after the heat treatment. The main phase is constituted by MnTi_2O_4 , as can be observed by comparison with the reported pattern [199]. A secondary phase is present, which can be indexed as a corundum-structured phase as Ti_2O_3 . Interestingly, the resulting patterns are very similar both in the case of MNTA and MNTB. In MNTB, the corundum-structured phase is present even if it was not used as a reagent phase. The Rietveld refinement conducted on the data sets revealed that the cell parameters obtained for the two phases are slightly different from the ones reported in literature for MnTi_2O_4 and Ti_2O_3 . The results are reported in table 3.7. The starting structure used for refining the spinel phase was the one reported by Lecerf [199]. More recent experimental results [193, 200] show that the lattice parameter a reported by Lecerf was underestimated. The value of a obtained after the refinement is in good accordance with the ones reported more recently, even if they appear slightly larger. The corundum structure was refined starting from Ti_2O_3 structure and revealed a slight increase both in the cell volume V and in the c/a ratio. The change in c/a confirms that the variations in the cell parameters are not an artifact due to experimental sample displacement or instrument

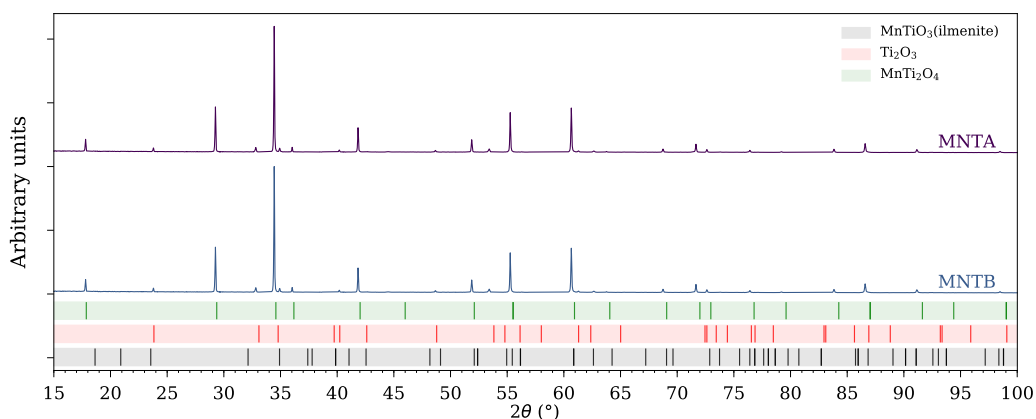


Figure 3.21: XRD pattern collected on the samples of MnTi_2O_4 prepared following equation 3.19 (MNTA) and following equation 3.20 (MNTB).

misalignment. The existence of a solid solution $\text{MnTi}_2\text{O}_4\text{-Mn}_2\text{TiO}_4$ is reported [204], where the compound Mn_2TiO_4 possesses a spinel structure with a larger cell parameter a than MnTi_2O_4 [203]. Therefore, it can be inferred that the resulting spinel phase in both MNTA and MNTB is slightly over-stoichiometric in Mn, since the ionic radius of Mn^{2+} is bigger than the one of Ti^{3+} in O_h environment [132]. On the other hand, the corundum phase shows an enlargement of V and c/a , closer to the values reported for MnTiO_3 . Corundum and ilmenite (the structures of Ti_2O_3 and MnTiO_3 respectively) are closely related crystallographically: in fact, ilmenite constitutes an ordering modification of corundum. Ti-rich members of the $\text{Mn}_x\text{Ti}_{2-x}\text{O}_3$ solid solution are expected to be isostructural with corundum, as it is reported for the $\text{Ti}_x\text{Fe}_{2-x}\text{O}_3$ solid solution [205]. It is suggested that the identified phases are intermediate stages of the synthesis which did not come to completion. Since the spinel structured solid solution $\text{MnTi}_2\text{O}_4\text{-Mn}_2\text{TiO}_4$ can also be written as $(\text{Mn})_{T_d}[\text{Mn}_x\text{Ti}_{2-x}]_{O_h}\text{O}_4$, a refinement of the occupancies of the O_h site was conducted assuming partial substitution of Ti^{3+} by Mn^{2+} . Even if the refinement showed an enhancement of R -factors, the obtained occupancies were considered not reliable since the refinement delivered the compositions $(\text{Mn})_{T_d}[\text{Mn}_{0.265}\text{Ti}_{1.735}]_{O_h}\text{O}_4$

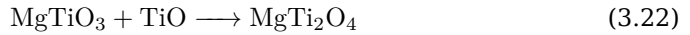
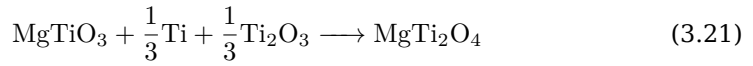
	Spinel		Corundum		R_{Bragg}	R_{F}
	a (Å)	c/a	V (Å ³)			
MNTA	8.628894(1)	2.69847	314.90(1)	4.42	3.51	
MNTB	8.62966(2)	2.69253	315.28(8)	3.51	2.99	
Ti_2O_3 [201]		2.6388	313.61			
MnTiO_3 [202]		2.7791	326.73			
Lecerf <i>et al.</i> [199]	8.600					
Lambert <i>et al.</i> [200]	8.627					
Huang <i>et al.</i> [193]	8.628					
Mn_2TiO_4 [203]	8.68063(7)					

Table 3.7: Refined parameters of MnTi_2O_4 phases, the primary spinel-structured phase and the secondary corundum-structured phase.

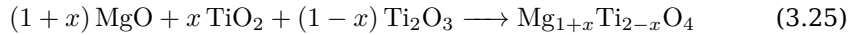
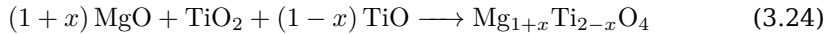
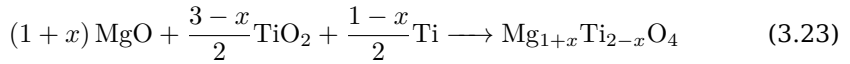
and $(\text{Mn})_{T_d}[\text{Mn}_{0.275}\text{Ti}_{1.725}]_{O_h}\text{O}_4$ for MNTA and MNTB respectively, too large for the observed increase in lattice parameter a . As a rule of thumb, more realistic compositions can be obtained by considering the solid solution to comply to Vegard's law. Considering the a values reported for MnTi_2O_4 [200] and Mn_2TiO_4 [203], the compositions corresponding to the refined value of the cell parameter are $(\text{Mn})_{T_d}[\text{Mn}_{0.036}\text{Ti}_{1.964}]_{O_h}\text{O}_4$ and $(\text{Mn})_{T_d}[\text{Mn}_{0.05}\text{Ti}_{1.95}]_{O_h}\text{O}_4$ for MNTA and MNTB respectively.

For MgTi_2O_4 , the synthesis is reported to be conducted in evacuated sealed quartz tubes as well [190, 206, 207]. Under this conditions, Mg evaporation is mentioned [207]: the process can cause an overall Mg loss and a consequent deviation from the aimed stoichiometry. Two approaches can be used:

- (i) using a precursor less prone to evaporation than MgO as MgTiO_3 , and then running the reaction according to equation 3.21 or 3.22

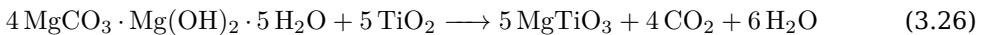


- (ii) using an excess of the Mg source material reactant, where Mg is the only metallic element, for example MgO . The latter approach is necessary for preparing materials with composition $\text{Mg}_{1+x}\text{Ti}_{2-x}\text{O}_4$ with $x > 0$. Using MgO as a precursor, the reaction can proceed according to



The aimed compositions were MgTi_2O_4 (sample MGTA), $\text{Mg}_{1.2}\text{Ti}_{1.8}\text{O}_4$ (sample MGTB) and $\text{Mg}_{1.4}\text{Ti}_{1.6}\text{O}_4$ (sample MGTC). Sample MGTA was prepared according to equation 3.21, while samples MGTB and MGTC were prepared according to equation 3.23.

The precursor MgTiO_3 was prepared following equation 3.26



The reagents (with an excess of 1 mol% in the case of Mg) were calcined for 15 hours at 1200 °C, then reground and calcined again for 15 hours at 1400 °C. XRD analysis of the resulting material were conducted, showing a mixture of ilmenite and spinel structures, the structures of MgTiO_3 and Mg_2TiO_4 respectively. The mixture was used as a

	a (Å)	R_{Bragg}	R_{F}
MGTA	8.50059(3)	8.96	5.13
MGTB	8.47479(3)	8.72	6.34
MGTC	8.47264(2)	7.41	5.50

Table 3.8: Cell parameters of $\text{Mg}_{1+x}\text{Ti}_{2-x}\text{O}_4$ phases obtained by Rietveld refinement.

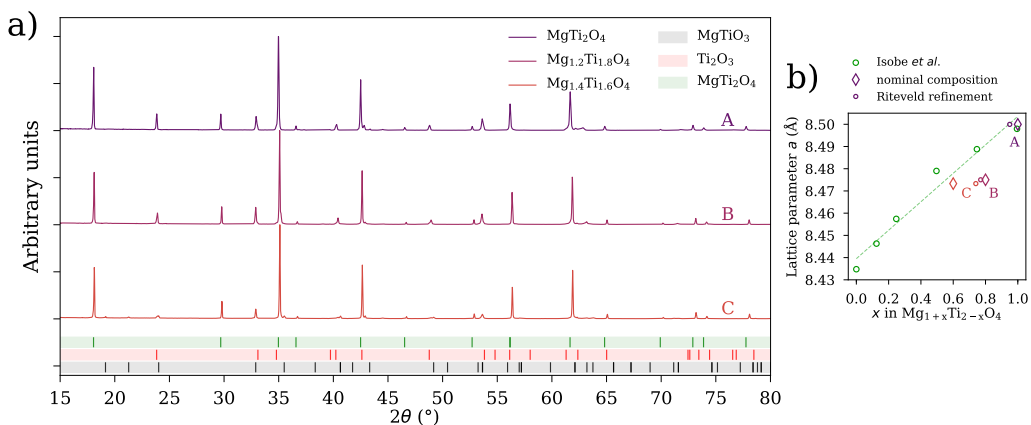


Figure 3.22: (a) XRD pattern collected on $Mg_{1+x}Ti_{2-x}O_4$ samples; (b) cell parameter as a function of x for different $Mg_{1+x}Ti_{2-x}O_4$ compositions; diamond markers indicate x as the nominal composition, rounded markers indicate x as the composition obtained by Rietveld refinement of the occupancies of the O_h sites in the spinels. The values of a reported in [208] are also included.

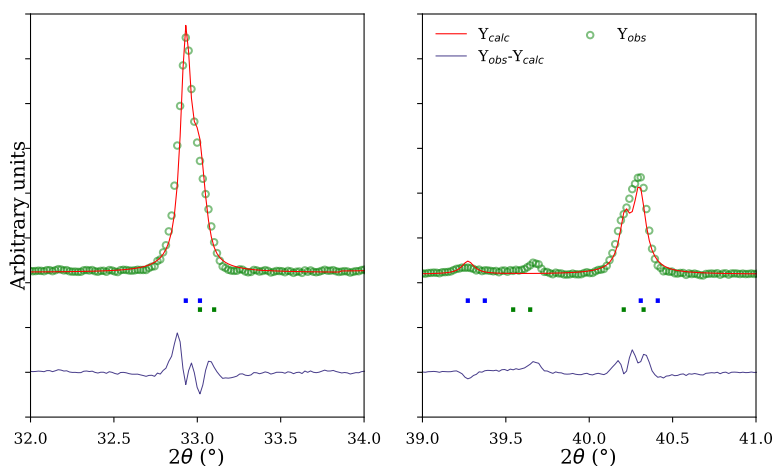


Figure 3.23: Example of the refined XRD data set where it is visible the presence of two secondary phases which can be attributed to a corundum structure (blue and green markers); the XRD pattern are collected with a $CuK_{\alpha 1}$ filtered radiation, the markers show both $K_{\alpha 1}$ and $K_{\alpha 2}$ reflections. In the figure, Y_{obs} and Y_{calc} indicate the observed and calculated intensities respectively.

precursor for the following step of the synthesis assuming the overall composition was the one of $MgTiO_3$. The precursor MgO was prepared by firing $Mg(OH)_2$ for 2 hours at $1000^\circ C$. The obtained material was rapidly transferred to a glass vial previously left in a dessicator overnight, then wrapped in Parafilm[®] and stored in a dessicator until use.

The reactive mixtures of samples MGTa, MGTb and MGTC were pressed into pellets and sealed into evacuated quartz tubes as described for $MnTi_2O_4$. The tubes were then fired at $1000^\circ C$ for 16 hours.

The XRD pattern of the obtained materials can be observed in figure 3.22 a. For all

the samples it can be seen that the primary phase is a spinel phase corresponding to MgTi_2O_4 . In all the samples, a secondary phase is present. In the case of MGTA and MGTB, the secondary phase shows reflections attributable to a corundum structure, while in the case of MGTC the extra peaks that are present in the pattern are consistent with the presence of MgTiO_3 . Other unidentified peaks were present in the pattern as extra phases. Rietveld refinement was conducted using the space group $Fd-3m$ for the spinel phase and either the space group $R-3c$ and $R-3$ (to which corundum and ilmenite belong respectively) for simulating the impurity phases. In figure 3.22 *b* the cell parameters obtained with the refinement are plotted against the nominal composition of the compounds. The cell parameters determined by Inobe *et al.* [208] are also reported for comparison. While in the case of the MGTA the cell parameter a is consistent with the expected composition, a bigger deviation from the linear trend is observed in the case of MGTB and MGTC. In the case of MGTB the deviation is larger. The occupancies of O_h have been refined by introducing also Mg^{2+} in the position of Ti^{3+} . The model used for the refinement was not able to deliver satisfactory R -factors which are still big (see table 3.8). Nevertheless, the compositions obtained by refining the occupancies are more consistent with the observed cell parameters, where similar values of a (as in the case of MGTB and MGTC), showed to refine to similar values of O_h occupancy and composition (see figure 3.22 *b*). The secondary phases could be matched by introducing two phases with a corundum structure (MGTA and MGTB) or with an ilmenite structure and a corundum structure (MGTC), as exemplified for MGTA in figure 3.23. As in the case of MnTi_2O_4 , the secondary phases are probably due to incomplete reaction of the starting materials.

CHAPTER 4

Materials: Properties

In this chapter the conductivity and the corrosion resistance toward chemical testing for the different compounds is reported.

The conductivity of the materials was measured on sintered ceramic bars. The target conductivity of this study was set to 0.1 S cm^{-1} at PEMEC operating temperature range, the average conductivity reported for Nafion[®] in such conditions [21]. Conductivity was measured with a Keithley 197 at different temperatures with the following procedure, unless otherwise stated. The heating rate was $30 \text{ }^\circ\text{C}^{-1}$ between sequential temperature steps. The sample was allowed to equilibrate at the selected temperature for one hour. Due to limitations in the resistance measuring instrumentation, high resistances ($> 200 \text{ k}\Omega$) could not be measured, resulting in conductivity values being available only at high temperatures for very insulating materials. The activation energies for the conductivity process, E_a , were obtained by linear interpolation of the Arrhenius plots obtained from the conductivity measurements. When the Arrhenius plot did not show a linear behaviour throughout the temperature range used for the analysis, the E_a was evaluated by interpolating the lowest temperature range available which showed linearity, in order to obtain activation energies which could be referred as closely as possible to the temperature range of application of PEMECs.

The chemical corrosion test was conducted by immersing weighed amounts of the materials in a mixture 1:1 of 1M H₂SO₄ and 1M HNO₃ kept at 85°C for 24 hours. The solutions were prepared by diluting concentrated H₂SO₄ and HNO₃ in DI water. In the case of Bi-SnO₂ samples, the materials were tested by immersing disks cut from cylindrical pellets with an average thickness of 2 mm. The pieces were weighed before and after the corrosion testing after drying at 120 °C overnight. In the case of spinel chromites, the samples were tested as powder. The powder was kept in suspension by continuous stirring. The suspension was then vacuum filtered on previously weighed polyethersulfone filters (pore size: 0.1 μm, Sartorius Stedim Biotech), before being dried in an evacuated desiccator overnight. Filter and powder were weighed together and the weight loss due to dissolution was determined as percent difference between the initial and final weight of the powder sample

4.1 Bi-SnO₂

Bars of the different compositions were prepared for the conductivity measurements according to the procedure explained in section 2.4. The bars were sintered at 700 °C for 10 hours in order not to cause excessive Bi₂O₃ evaporation. This procedure resulted in poor sintering of the ceramic bars, the density of which was measured using the

Archimedes method in water, revealing a density between 80-90% of the theoretical density. The closed porosity was not measured, but given the similar values obtained for the open porosity among the different samples, it was assumed to be similar in all the samples.

Bars from 1 and 1.5 cat.%_{Bi} were too fragile to be handled and could not be measured. Figure 4.1 show the Arrhenius plots obtained from the conductivity measurements.

Table 4.1: Activation energies for different samples calculated by linear interpolation of the Arrhenius plots.

at.% _{Bi}	E_a (eV)
pure SnO ₂	0.84
0.5	0.95
2	1.46
3	1.53
4	1.55
5	1.55
Bi ₂ Sn ₂ O ₇	1.48

The Arrhenius plots show a sudden drop in conductivity for cat.%_{Bi}>0.5, while the conductivity of 0.5 cat.%_{Bi} is only slightly lower than pure SnO₂. Samples with cat.%_{Bi} from 2 to 5 show only minimal variations in absolute values. The conductivity of the pyrochlore Bi₂Sn₂O₇ is several orders of magnitude lower than the one of SnO₂. SEM analysis (see figure 3.4, p. 35) revealed that the microstructure is similar for all the samples despite the Bi content, therefore the effect of grain boundaries on conductivity should be similar for all the compositions analyzed.

Table 4.1 lists the values of activation energies E_a obtained by linear interpolation of the Arrhenius plots.

Interestingly, the values of activation energies for samples with cat.%_{Bi} from 2 to 5 are much closer to the higher value obtained for BiSn₂O₇ than to the one of SnO₂, while 0.5 cat.%_{Bi} shows a small increase in E_a . The results show that there is an effect of the presence of Bi on the conductivity. The similarity in E_a of the Bi-containing samples with the pyrochlore phase suggests that BiSn₂O₇ comes into play in the conduction mechanism of the samples with high Bi content. A possible explanation of such phenomenon can be that the secondary phase and Bi accumulate at the grain boundaries before forming stand-alone particles. Figure 3.4c (p. 35) shows a possible example of

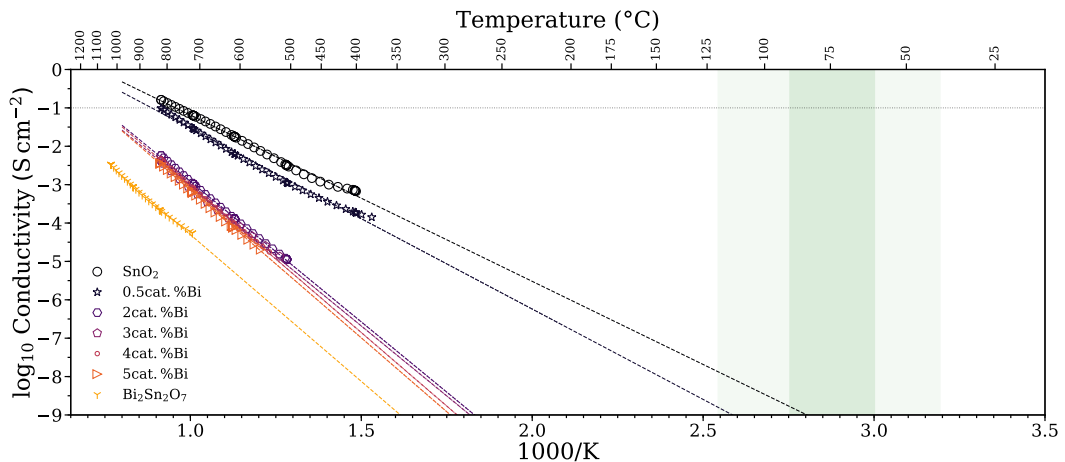


Figure 4.1: Arrhenius plots of the conductivity of samples with different Bi content; the conductivity of Bi₂Sn₂O₇ is also reported. The shaded green areas indicate the usual operating range of a PEMEC while the dotted line indicate the target conductivity of this study.

Table 4.2: Percentage change loss (Δw (%)) of different samples after corrosion testing.

at.% _{Bi}	Δw (%)	St. dev.
pure SnO ₂	-0.4	0.2
0.5	0.6	0.7
1	1.0	0.2
1.5*	2.1	0.4
2	1.6	0.1
3	1.3	0.1
4	3.2	0.5
5	6.6	0.5
Bi ₂ Sn ₂ O ₇	3.6	0.6

* The sample was in pieces at the end of the tests.

that in the biggest dashed oval, where the grain boundary of SnO₂ appear decorated by a denser phase, which is probably the pyrochlore. A composite made of conductive particles of material A embedded in an much-less conductive matrix of material B would be more electrically conductive than material B alone. The apparent complete immiscibility of Bi₂O₃ can be caused by the big difference between Bi³⁺ and Sn⁴⁺ (1.03 and 0.69 Å respectively in 6-fold coordination [132]) and grain boundaries can be the *locus* where Bi ions are accommodated with the minor energy [209].

Table 4.2 shows the results of the corrosion test expressed as weight loss percentages, Δw (%). All the samples tested maintained macroscopical structural stability (with the exception of 1.5 cat.%_{Bi}, where the samples were always broken into pieces after the test, which leads to higher surface area and not comparable results). SnO₂ showed a negligible variation of the weight after corrosion test (the negative value is considered due to uncertainties in the Δw determination). In the case of Bi containing samples, Δw increases as cat.%_{Bi} increases . The test was performed also on Bi₂Sn₂O₇, which showed a higher mass loss compared to SnO₂. The sample with the highest Δw is anyway 5 cat.%_{Bi}. This behaviour could be a further indication of the hypothesis of Bi-enrichment of the grain boundaries. If the secondary phase is located mainly in the grain boundaries, a preferential dissolution of such could cause a failure of the composite leading to the detachment of whole grains of SnO₂ without dissolving them, causing a more pronounced loss of mass.

4.2 Spinels

4.2.1 MCr₂O₄

The conductivity of the pure spinel compounds, MgCr₂O₄, ZnCr₂O₄, NiCr₂O₄ and NiFeCrO₄ was measured on sintered bars. The bars were sintered for 10 hours at 1200 °C. In the case of NiCr₂O₄, the bar sintered at 1200 °C was too fragile to be measured; therefore a bar was prepared and sintered at 1500 °C for 20 hours, on which the conductivity was then measured.

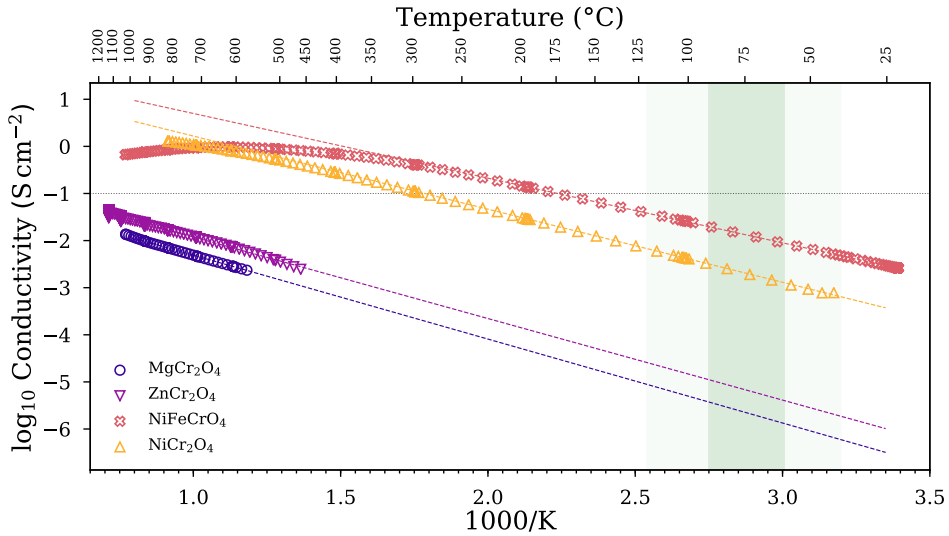


Figure 4.2: Arrhenius plots of the conductivity of pure chromites. The shaded green areas indicate the usual operating range of a PEMEC while the dotted line indicate the target conductivity of this study.

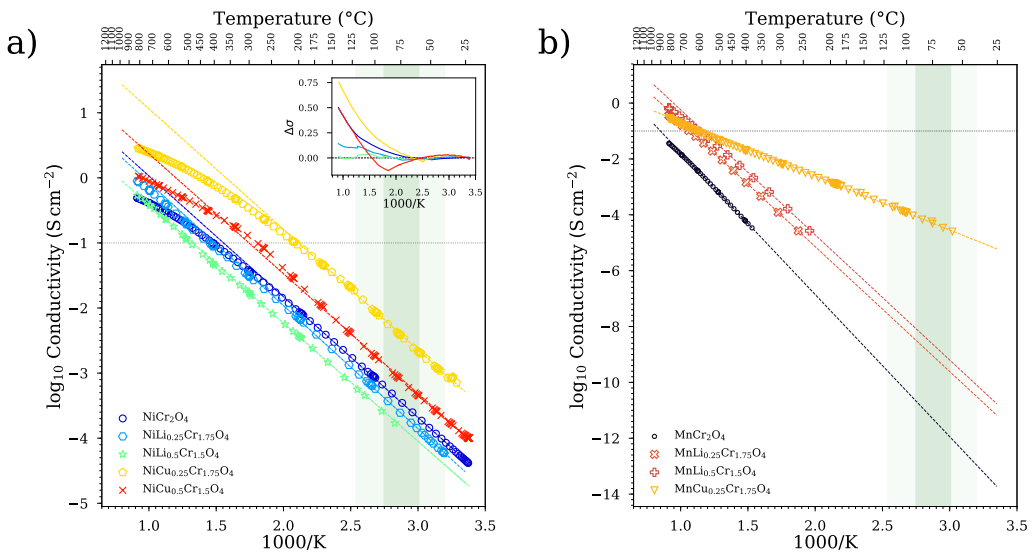


Figure 4.3: Arrhenius plots of the conductivity of (a) NiCr_2O_4 -based and (b) MnCr_2O_4 -based materials. The shaded green areas indicate the usual operating range of a PEMEC while the dotted line indicate the target conductivity of this study. In the case of NiCr_2O_4 , the inset plot shows the difference between the linear interpolation used for extracting the activation energy and the measured values of conductivity ($\Delta\sigma$ in the plot), in the temperature range of the data. The shaded green areas indicate the usual operating range of a PEMEC while the dotted line indicate the target conductivity of this study.

Table 4.3: Activation energies (E_a) extracted from linear interpolation of the Arrhenius plots for the different materials; T_{interp} indicates the temperature starting from which the interpolation is conducted; conductivities extrapolated at 60 and 80 °C (σ_{60}/σ_{80}) are also reported.

Material	E_a (eV)	T_{interp} (°C)	$\log_{10} \sigma_{60}/\sigma_{80}$ (S cm ⁻¹)
MgCr ₂ O ₄	0.35	900	-5.88 / -5.57
ZnCr ₂ O ₄	0.34	900	-5.39 / -5.09
NiFeCrO ₄	0.27	200	-2.05 / -1.82
NiCr ₂ O ₄ S.S.*	0.31	200	-2.89 / -2.62
NiCr ₂ O ₄ N.S.*	0.37	200	-3.69 / -3.37
NiLi _{0.25} Cr _{1.75} O ₄	0.38	300	-3.86 / -3.53
NiLi _{0.5} Cr _{1.5} O ₄	0.36	300	-4.05 / -3.74
NiCu _{0.25} Cr _{1.75} O ₄	0.37	200	-2.64 / -2.33
NiCu _{0.5} Cr _{1.5} O ₄	0.37	200	-3.32 / -3.01
MnCr ₂ O ₄	1.01	500	-11.95 / -11.09
MnLi _{0.25} Cr _{1.75} O ₄	0.89	400	-9.62 / -8.86
MnLi _{0.5} Cr _{1.5} O ₄	0.89	400	-9.21 / -8.45
MnCu _{0.25} Cr _{1.75} O ₄	0.38	200	-4.55 / -4.22

* S.S. = solide state synthesis; N.S. = nitrate combustion synthesis.

The density of the obtained bars was measured with the Archimedes method and was found close to 90% for all the materials. As for the Bi-SnO₂, the closed porosity was not measured but assumed similar among the samples. Figure 4.2 shows the measurements conducted on the materials, while table 4.3 shows the activation energies E_a obtained by linear interpolation of the Arrhenius plots. The conductivity values have been compared with the literature: in the case of NiCr₂O₄, the conductivity values agree with the ones reported in literature [210]. Bigger deviation have been noticed in the case of MgCr₂O₄ [157] and NiFeCrO₄ [169]. In the case of ZnCr₂O₄, no conclusive value could be found to compare the measured conductivity: Gabr *et al.* [211] reported the activation energy for conduction of ZnO · Cr₂O₃ system sintered at different temperatures up to the formation of the ZnCr₂O₄ spinel phase without explicitly reporting the conductivity data; Bangale *et al.* [212] show conductivity data on ZnCr₂O₄, but the results are badly reported and the experimental conditions of the measurement unclear. The conductivity of the different spinels increased as MgCr₂O₄ < ZnCr₂O₄ < NiCr₂O₄ < NiFeCrO₄. NiCr₂O₄ and NiFeCrO₄ show a sensible variation of temperature dependance of the conductivity at high temperatures; NiFeCrO₄ shows a maximum in conductivity at 635 °C, after which the conductivity decreases increasing the temperature, showing a metallic behaviour.

The general trend described before follows the decrease in the lattice constant a observed from the refinement of the cell parameters of the materials (see table 3.3, p. 38). An increase in the lattice parameter determines an enlargement in Cr-Cr distances and therefore a decrease in d orbitals overlapping [138].

Figure 4.3 shows the conductivity measured on the doped materials prepared by nitrate combustion synthesis. In the case of the NiCr₂O₄-based materials, the insertion of Li into the lattice was not successful and no variation of the lattice parameter was detected. The overall conductivity of NiCr₂O₄, NiLi_{0.25}Cr_{1.75}O₄ and NiLi_{0.5}Cr_{1.5}O₄ is very similar, so do the activation energies obtained from linear interpolation of the

Arrhenius plots (0.37, 0.38 and 0.36 eV respectively). In the case of Cu-doped samples, $\text{NiCu}_{0.25}\text{Cr}_{1.75}\text{O}_4$ showed an overall higher conductivity than $\text{NiCu}_{0.5}\text{Cr}_{1.5}\text{O}_4$: this can be explained with the fact that the composition of the main conducting phase is going from NiCr_2O_4 to CuCr_2O_4 as the Cu content increase. CuCr_2O_4 is reported as a worse electrical conductor compared with NiCr_2O_4 [158, 210, 213]. The measurements show that as long as Ni is the major component in the T_d site (as shown in table 3.5, p. 46), the conductivity is increased by the presence of Cu, as it induces a higher concentration of charge carrier. As soon as Cu becomes the dominant species in the T_d site, the structure becomes closer to the one of CuCr_2O_4 and therefore the conductivity is accordingly reduced. Nevertheless, the values of activation energy obtained are close to the one of pure NiCr_2O_4 , as in the case of Li-doped samples.

It was noted that some materials show a higher deviation than others from the low-temperature linear interpolation conducted. While NiCr_2O_4 , $\text{NiCu}_{0.25}\text{Cr}_{1.75}\text{O}_4$ and $\text{NiCu}_{0.5}\text{Cr}_{1.5}\text{O}_4$ show a variation in the slope after 350 °C, the Li-containing samples appear to delay the onset of slope variation at higher temperatures as Li content increases. This phenomenon is highlighted in the inset of figure 4.3a. The figure shows the difference between the linear fitting based on the low-temperature part of the data and the measured experimental data throughout the whole temperature range. As expected, the difference at low temperatures, where the fitting is performed, is very close to zero for all the materials. NiCr_2O_4 shows a deviation from the linear trend starting approximately after 500 °C. In the case of Li-containing materials, the deviation from the linear trend at high temperature decreases sensibly for $\text{NiLi}_{0.25}\text{Cr}_{1.75}\text{O}_4$ compared with NiCr_2O_4 and stays close to zero throughout the whole temperature range in the case of $\text{NiLi}_{0.5}\text{Cr}_{1.5}\text{O}_4$. For the Cu-containing materials, the deviation appear to have the same slope for all the contents of Cu and NiCr_2O_4 . The presence of different activation energies (different slopes in the Arrhenius plot) for different temperature regions can be related to a change from grain boundary to bulk limited conduction [161]. The local minima observed in the inset for $\text{NiCu}_{0.25}\text{Cr}_{1.75}\text{O}_4$ and $\text{NiCu}_{0.5}\text{Cr}_{1.5}\text{O}_4$ at $x = 2.5$ and 1.85 respectively (corresponding to 127 and 267 °C) may be related to a phase transition from tetragonal to cubic structure, which are reported to happen at 47 and 581 °C for pure NiCr_2O_4 and CuCr_2O_4 respectively [170]. Hysteresis in Arrhenius plots is reported for CuCr_2O_4 [213] in air at temperatures close to the phase transition temperature.

The phenomenon of the deviation from linear trend in the Arrhenius plots was noted but the origin of such behaviour is still unclear. Further investigation should be conducted to determine the cause of the deviation itself and the apparent influence that doping has on such variation.

MnCr_2O_4 -based materials showed different effects of the doping on the overall conductivity. The measurement on pure MnCr_2O_4 shows a good agreement with the literature both in terms of conductivity and activation energy extracted [159]. The Li-doped samples show an absolute higher conductivity compared to undoped MnCr_2O_4 . $\text{MnLi}_{0.5}\text{Cr}_{1.5}\text{O}_4$ shows the highest conductivity. The E_a is decreases slightly down to 0.89 eV for the doped compounds. $\text{MnCu}_{0.25}\text{Cr}_{1.75}\text{O}_4$ shows a greater reduction of the activation energy. The effect of Cu and Li doping on chromites conductivity has been

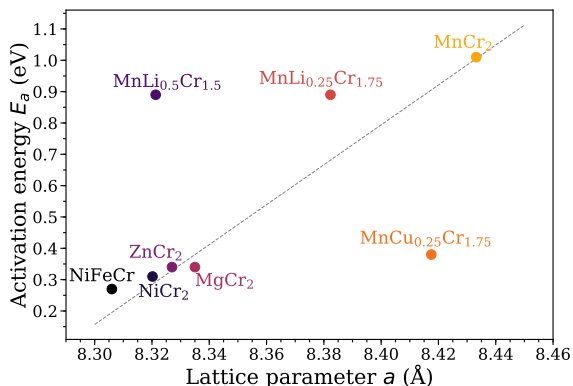
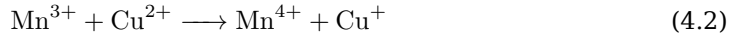
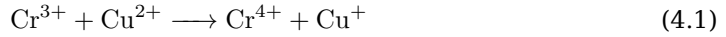


Figure 4.4: Activation energies E_a for the different compounds as a function of cell parameter a ; the dashed line is intended to guide the eye.

reported before [138] and the increase in conductivity is explained as an increase in the charge carriers concentration due to the doping. Nonetheless, the effect of Cu incorporation produces a bigger impact on the overall conductivity properties of MnCr_2O_4 : the extrapolated conductivities show that $\text{MnCu}_{0.25}\text{Cr}_{1.75}\text{O}_4$ has a higher conductivity of several orders of magnitude compared with the other compounds, particularly at temperatures below 300 °C. In oxide materials, Mn normally possess an high spin configuration [214]. Figure 3.6 (page 37) shows that while Mn^{2+} possess no CFSE, both Mn^{3+} and Cu^{2+} possess a stabilization energy of $-0.6\Delta_o$. As the reduction in the cell parameter is consistent with partial oxidation of Mn (see section 3.2.1), Mn^{3+} is present into the lattice and the conduction path is expected to be altered by the presence of either Cu^{2+} or Mn^{3+} . Lu *et al.* [159] studied the solid solution MnCr_2O_4 - Mn_2CrO_4 and showed that the insertion of Mn in the O_h site enhances the conductivity of the material. The variation in E_a measured for $\text{MnCu}_{0.25}\text{Cr}_{1.75}\text{O}_4$ though is much bigger than the one reported from Lu *et al.* for similar substitution of Cr by Mn.

As mentioned before, it has been reported that it exist a linear relation between Cr-Cr distance (proportional to the lattice parameter a) and the activation energy for conduction in spinel chromites [138]. Figure 4.4 shows the activation energy derived for the different samples as a function of the lattice parameter, where the dashed line is the linear interpolation of the values in the case of not doped spinels. For those materials, it can be observed that the E_a increases with the lattice parameter, as the Cr-Cr distance increases. If it is assumed that a linear relation would be valid only if Cr is the dominant species to determine conductivity, materials with elements other than Cr present in the O_h site would fall out of the linear trend, in the case such element are able to participate to the conduction process. Given the high preference for Cr^{3+} for the O_h site (as detailed in section 3.2.1), only spinel chromites with sub-stoichiometric Cr content can enable such situation. NiFeCrO_4 was not included in drawing the interpolation, because half of the Cr has been substituted in this material and the O_h network will not be composed by Cr only. Fe is expected to occupy the T_d site since no CFSE is present, while Ni^{2+} possess a certain stabilization energy (see figure 3.6, p. 37) and will occupy O_h sites. This phenomenon is reported for NiFe_2O_4 , which exhibit an inverse spinel structure

and also for Cr-doped NiFe_2O_4 [215]. Even if with partially substituted O_h Cr sites, NiFeCrO_4 appears to lay in proximity of the linear trend, as if the presence of Ni in the O_h site does not alter the conduction mechanism, which remains dominated by Cr. The doped- MnCr_2O_4 are in fact sub-stoichiometric in Cr; in figure 4.4 they fall outside of the linear trend individuated by the undoped spinels. In the case of Li-doped samples, where Mn is expected to occupy the O_h site the activation energies are comparable with the ones found in literature for $\text{Mn}_{1+x}\text{Cr}_{2-x}\text{O}_4$. In the case of $\text{MnCu}_{0.25}\text{Cr}_{1.75}\text{O}_4$, the lower activation energy can be explained by the presence of Cu^{2+} in O_h site, which could favour the conduction by facilitating the hopping mechanism offering an alternative path to holes propagation, as exemplified in equations 4.2 and 4.1.



A similar effect of Cu doping is reported for $\text{Cu}_x\text{Mn}_{3-x}\text{O}_4$ [216, 217].

Table 4.4 shows the corrosion tests performed on the different chromites spinels. Only the materials which showed a single spinel phase were corrosion tested. All the materials showed a low corrosion loss, with the exception of MnCr_2O_4 which manifested the highest weight loss. Interestingly, doping had a clear impact on the dissolution behaviour of MnCr_2O_4 . This can be related to an increasing fraction of Mn^{3+} in the material: while MnO is reported to dissolved readily in acids [218], Mn_2O_3 is reported to disproportionate in sulfuric acid leaching Mn^{2+} and forming the insoluble MnO_2 [218, 219].

Figures 4.5 and 4.6 show XRD patterns collected on $\text{MnCu}_{0.25}\text{Cr}_{1.75}\text{O}_4$ and NiCr_2O_4 before and after the chemical corrosion test. It can be observed that the spinel structure is preserved after the corrosion test. In the case of NiCr_2O_4 , a bigger fraction of tetragonal phase is present compared to the starting material after the sintering. Since

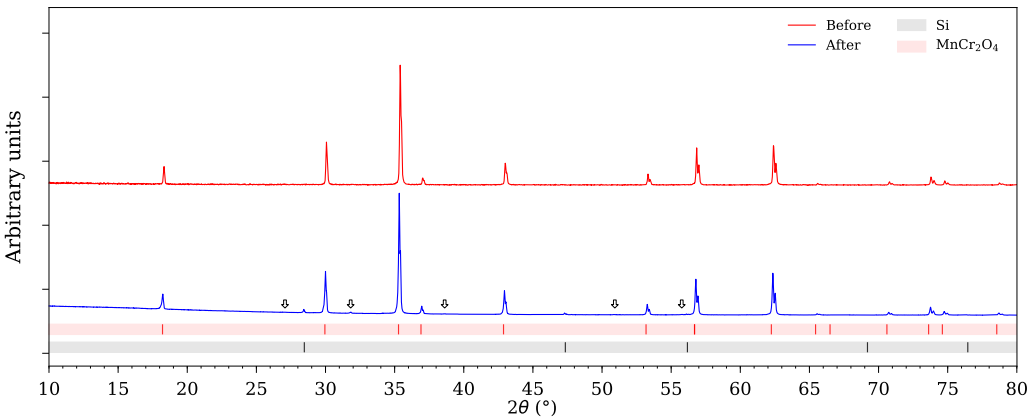
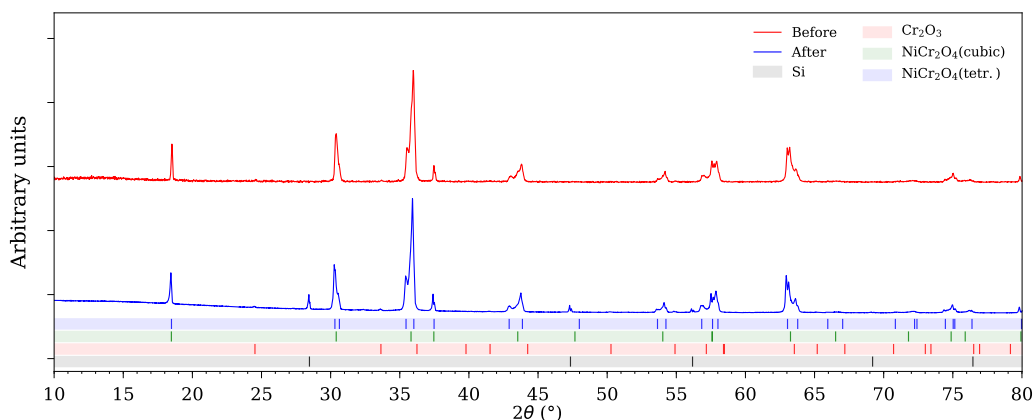


Figure 4.5: XRD pattern collected on $\text{MnCu}_{0.25}\text{Cr}_{1.75}\text{O}_4$ before and after the chemical corrosion test; the MnCr_2O_4 spinel pattern is showed to indicate the positions of the reflections in a spinel phase.

Table 4.4: Percentage change loss (Δw (%)) of different samples after corrosion testing.

Material	Δw (%)
ZnCr ₂ O ₄	< 1
MgCr ₂ O ₄	< 1
NiFeCrO ₄	< 1
NiCr ₂ O ₄	1.5
MnCr ₂ O ₄	4.2
MnCu _{0.25} Cr _{1.75} O ₄	1.3
MnLi _{0.25} Cr _{1.75} O ₄	3.5
MnLi _{0.5} Cr _{1.5} O ₄	2.1

**Figure 4.6:** XRD pattern collected on NiCr₂O₄ before and after the chemical corrosion test.

the transition temperature from cubic to tetragonal is 47 °C, the corrosion test at 85 °C could have worked as an additional thermal treatment which favoured the formation of the low temperature stable tetragonal phase. Only minor secondary peaks can be observed in the patterns collected after the corrosion test. Specifically, small peaks ascribable to Cr₂O₃ can be observed in the case of NiCr₂O₄ after the corrosion test. No secondary phases were identified in the case of MnCu_{0.25}Cr_{1.75}O₄, with the exception of the small peaks indicated by the arrows in figure 4.5: they belong to the most intense reflections of the spinel phase with Cu K_{β} wavelength, which filtering by the instrument was only partial.

4.2.2 MTi₂O₄

The conductivity of the titanates spinels was measured using the Van Der Pauw method [110, 111]. Disks of approximately 2 mm thick were cut out of the pellets prepared during the synthesis of the materials with a diamond wheel in acetone, since contact with water or moisture can cause this materials to develop insulating layers on the surface [220]. Four silver wires were attached using Ag paste to the edge of the

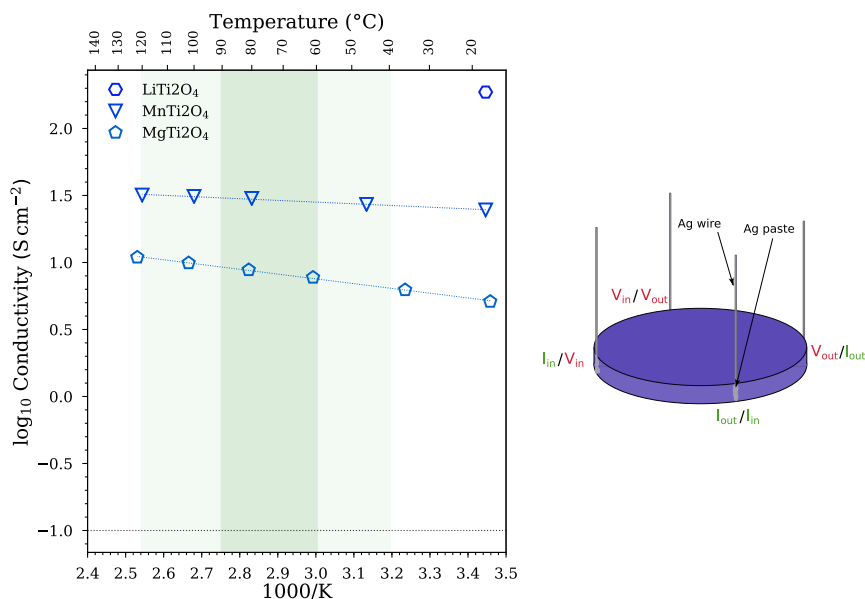


Figure 4.7: Arrhenius plots of the conductivity of spinel titanates. The shaded green areas indicate the usual operating range of a PEMEC while the dotted line indicate the target conductivity of this study; on the right, the sketch shows the wiring configuration of the samples used for measuring the conductivity.

disk perpendicularly to the surface and equally spaced among each other, as depicted in figure 4.7. The samples were then cured at 400 °C for 2 hours in 5% H₂/Ar. The samples were connected to multimeter (Keithley 2401 SourceMeter) and mounted on an alumina tube in close contact with a thermocouple. The sample holder was then inserted in a glass oven (Büchi B-585), where the temperature was adjusted manually and read on the thermocouple in contact with the sample. The access to the glass oven was covered with glass wool to favour temperature equilibration inside the oven. The data were collected when no sensible variation of the measured resistance was observed after thermal equilibration (15-20 min).

Figure 4.7 show the conductivity measurements performed on the selected samples, LiTi₂O₄ (sample C), MgTi₂O₄ (sample MGTA) and MnTi₂O₄ (sample MNTA). The measurement of LiTi₂O₄ was only conducted at room temperature in air. The materials showed high conductivity even at room temperatures. The conductivities room temperature were 5.12, 24.5 and 188.2 S cm⁻¹ for MgTi₂O₄, MnTi₂O₄ and LiTi₂O₄ respectively. MgTi₂O₄ and MnTi₂O₄ showed an increase in conductivity with increasing temperature, an indication of a thermally activated semiconductor behaviour. The obtained activation energies E_a are 0.07 and 0.03 eV respectively for the two materials. The E_a value for MgTi₂O₄ is in good agreement with the values reported in literature [191]. The materials show a conductivity sensibly higher than the target set in this study, and therefore they are expected to introduce a small contribution to the cell total resistance if used in a real cell.

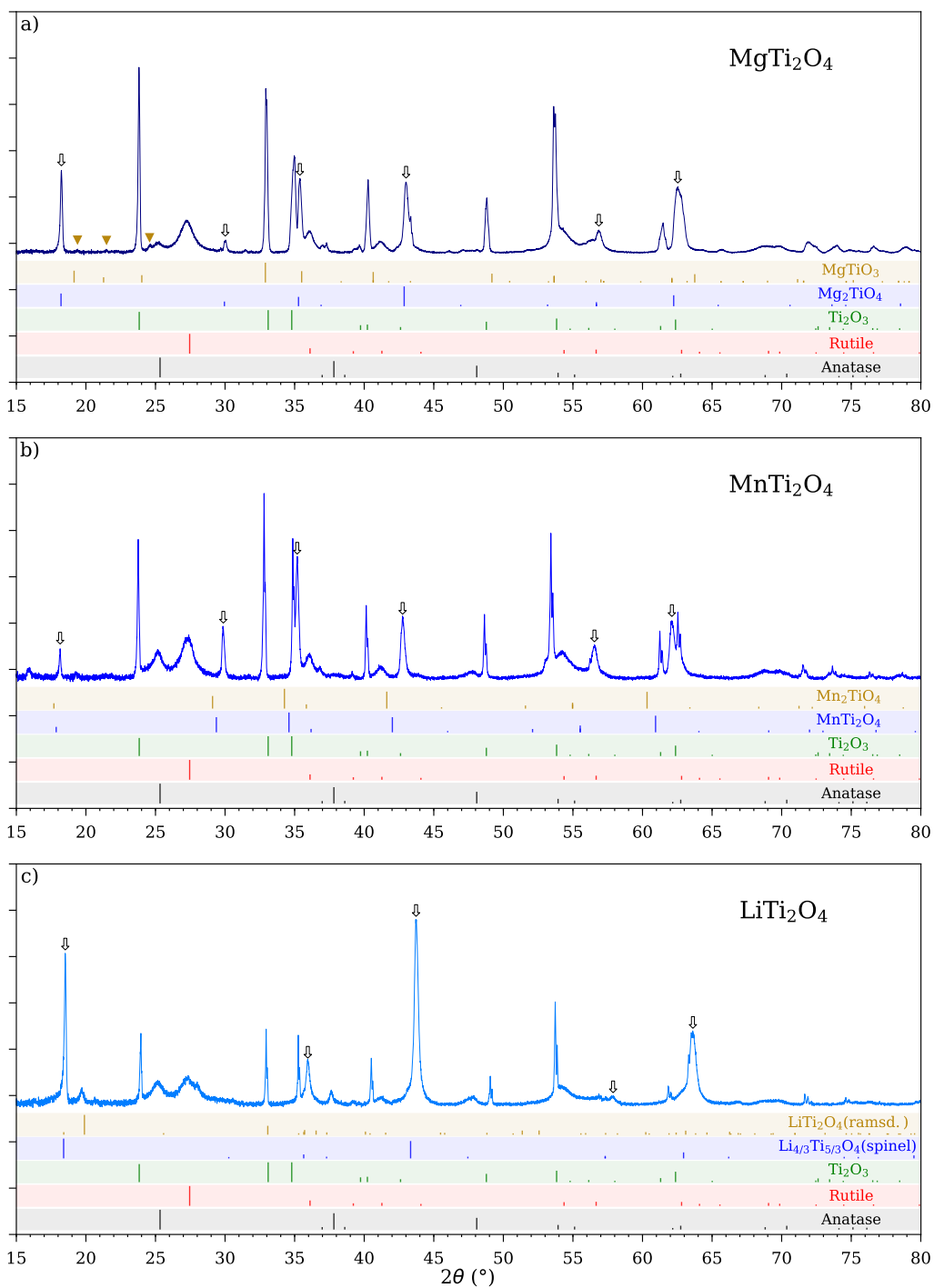


Figure 4.8: XRD pattern collected on $MgTi_2O_4$ (a), $MnTi_2O_4$ (b) and $LiTi_2O_4$ (c) samples after chemical corrosion test.

The results of the chemical corrosion test performed on such materials is reported in table 4.5. As a comparison, Ti_2O_3 was also tested with the same corrosion experiment. The spinels presented visible bubble evolution when they in the hot acid mixture used for the test. All the materials showed to undergo sensible weight loss after the corrosion test. $MnTi_2O_4$ showed the biggest weight loss of all the materials. $LiTi_2O_4$ showed a change in colour from deep blue to pale grey-blue. Interestingly, the sample that showed the least weight loss was Ti_2O_3 . Figure 4.8 reports the XRD measurements collected on the samples after the corrosion test. The patterns revealed that the residuals were composed of a mixture of different phases. The proposed identification of the major reflections is reported in figure 4.8 below the experimental patterns.

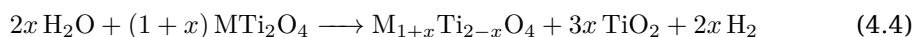
The comparison with the XRD data of the as prepared materials reported in section 3.2.2 show clearly that the materials underwent a substantial transformation with loss of the main spinel phase. All the patterns showed the presence of broad peaks of rutile and anatase TiO_2 . Ti_2O_3 is present in all the cases, with the most sharp peaks. This phase is probably the secondary phase detected after the preparation of the materials. As suggested by the mass loss data from the chemical corrosion experiments, the material may be more corrosion resistant to the condition experienced by the mixture than the main spinel phase. The residuals of $MgTi_2O_4$ showed in figure 4.8 *a* indicate the presence of Mg-containing phases. A small fraction of $MgTiO_3$ can be identified in the region between 20° and 25° as indicated by the triangular markers. The reflections of a spinel structured phase can still be observed in the pattern as indicated by the arrows in the figure. The position of the reflections appear shifted toward higher angles compared to the ones of $MgTi_2O_4$ and they can be identified with the oxidized end-member of the solid solution $Mg_{1+x}Ti_{2-x}O_4$, Mg_2TiO_4 [221]. The same observations can be made also for the residuals of $LiTi_2O_4$, as can be observed in figure 4.8 *b*. In the case of the Li titanate, the spinel $Li_{4/3}Ti_{5/3}O_4$ can be observed among the reflections. The peak at 19° can be attributed to a residual of ramsdellite structured $LiTi_2O_4$ as a secondary phase from the preparation of the material. 4.8 *c* shows the residuals of the chemical corrosion testing of $MnTi_2O_4$. No apparent ilmenite structured $MnTiO_3$ is detected. Beside the TiO_2 and Ti_2O_3 peaks, the reflections of a spinel phase can be recognized in the pattern as the arrows shows; nevertheless, the positions cannot be matched with neither with the ones from the original $MnTi_2O_4$ nor with the other end member of the solid solution, Mn_2TiO_4 [203], and a clear identification of the spinel phase cannot be reported.

The results indicate that the materials are unstable in the conditions of the test, which causes a loss of the spinel phase with formation of different products where Ti is

Table 4.5: Percentage change loss (Δw (%)) of different of spinel titanates after corrosion testing; the mass compositions of the spinels with general formula MTi_2O_4 are also reported.

Material	Δw (%)	M w%	Ti w%	O w%
$LiTi_2O_4$	4	4.16	57.44	38.40
$MgTi_2O_4$	11	13.21	52.02	34.77
$MnTi_2O_4$	24	25.59	44.60	29.81
Ti_2O_3	3			

in oxidation state +4. One of the products of the oxidation is the oxidized end-member of the solid solutions. The formation of TiO_2 means that the material undergoes oxidation, which could be caused by the HNO_3 in the testing solution. The test has been repeated in a solution 1 M H_2SO_4 and the materials underwent the same degradation. Moreover, as can be seen in table 4.5, the weight loss of the different materials is comparable with the mass fraction of the ion M in the spinel structure with general formula MTi_2O_4 , suggesting that the mass loss is mainly due to dissolution of the M ion into solution. The materials undergo the same oxidation mechanism no matter what the ion M is. Given the fact that bubble evolution was also observed during the test after the samples were submerged in the hot mixture, it is proposed that the degradation of the materials progress according to the reactions



where M can be Mn, Mg or Li and n can accordingly be +2 or +1. When M carries a charge +2, x can assume the values $0 < x \leq 1$, while when M has charge +1 then $0 < x \leq \frac{1}{3}$. The evolving gas could be N_2 when the material is tested in the presence of HNO_3 . Figure 4.9 displays SEM images collected on powder samples of the spinel titanates before and after the chemical corrosion test. For all the spinel titanates, the regular and faceted grains before the chemical test is turned in knobbed and irregular agglomerates of smaller particles after the test. Rough particles can be distinguished, which are smaller than the starting materials and they are probably constituted of TiO_2 (the smaller dimensions could then explain the broad XRD peaks for anatase and rutile in the patterns in figure 4.8).

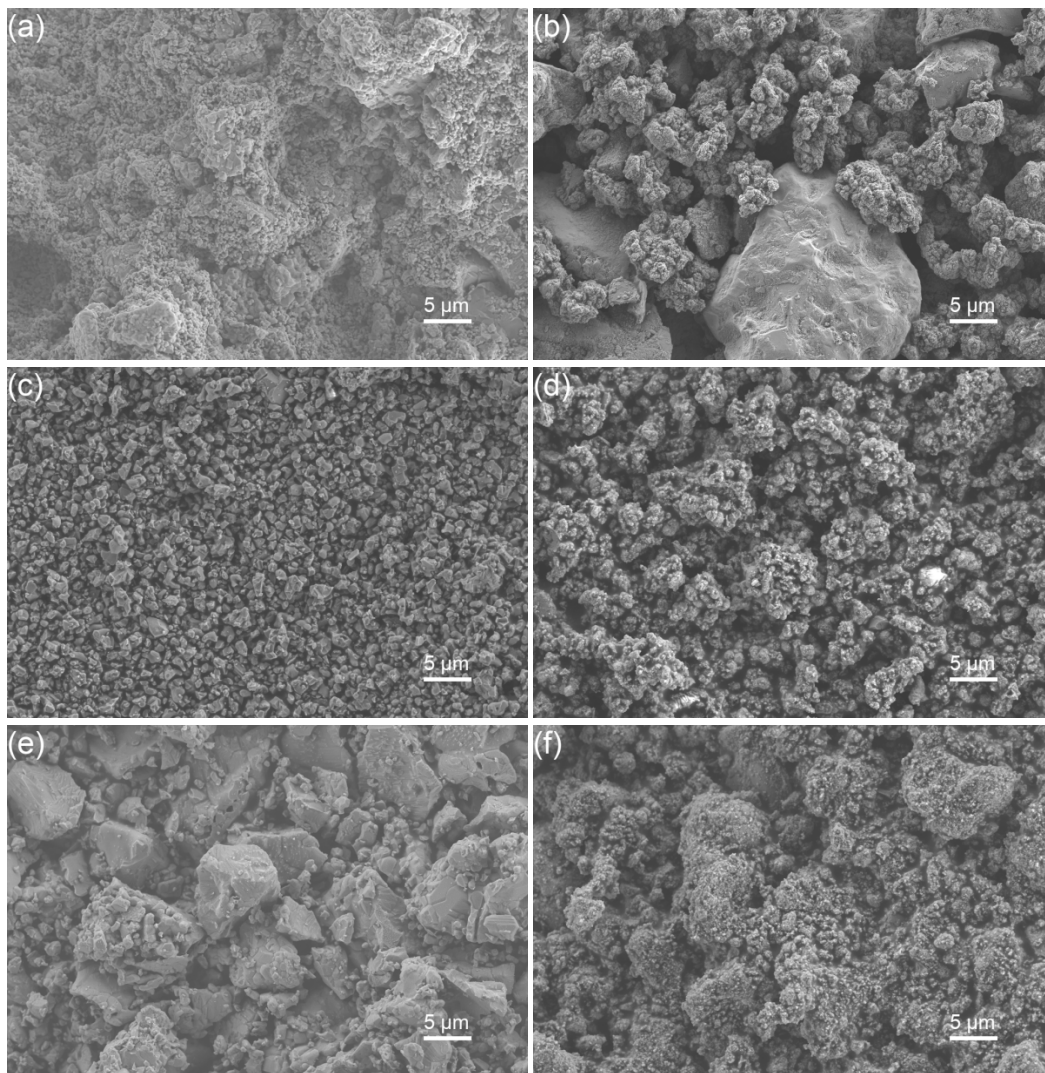


Figure 4.9: SEM images collected on samples of spinel titanates before (a, c and e) and after (b, d and f) after chemical corrosion test: LiTi_2O_4 (a and b), MgTi_2O_4 (c and d) and MnTi_2O_4 (e and f) [Zeiss Merlin, acc.volt.: 5 kV].

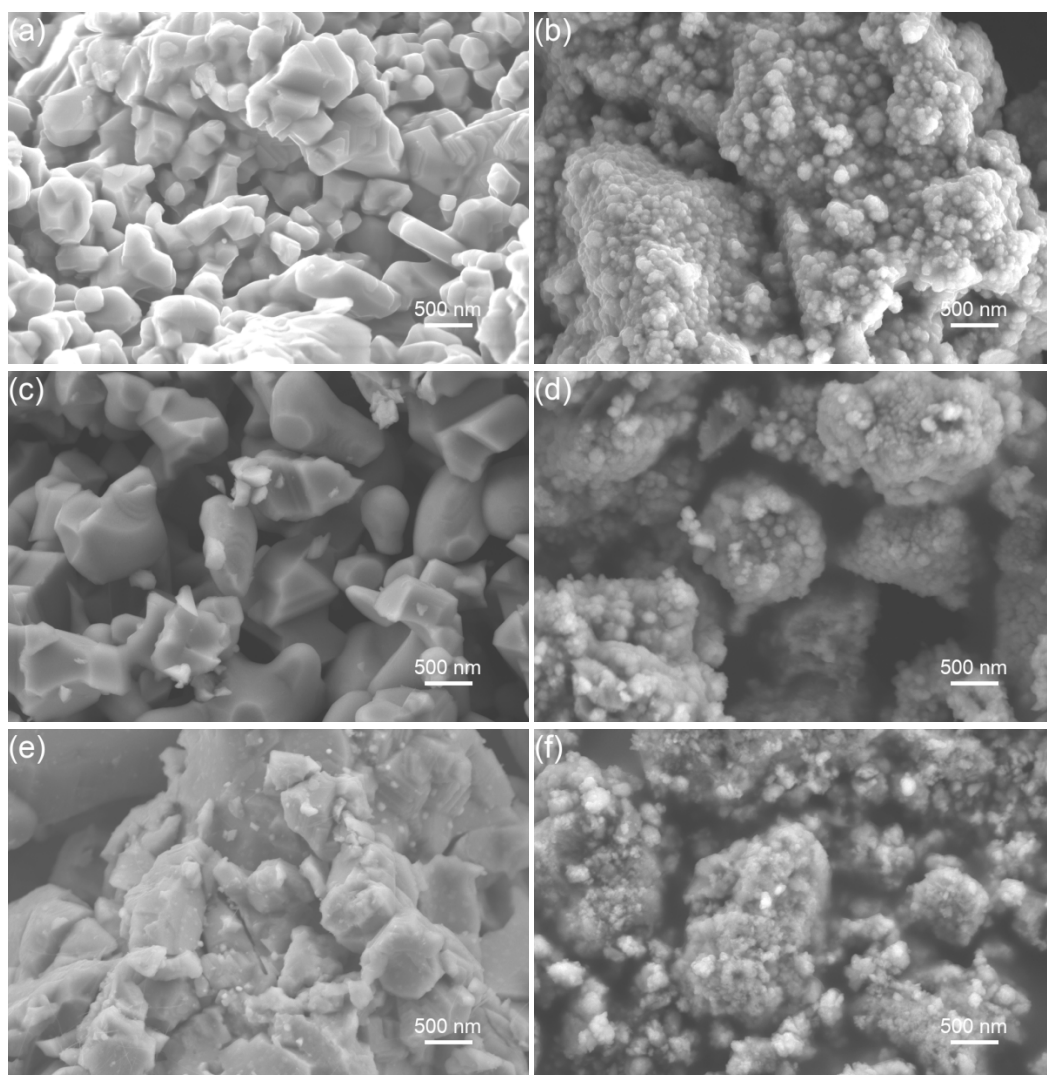


Figure 4.9: (continued) SEM images collected on samples of spinel titanates before (a, c and e) and after (b, d and f) after chemical corrosion test: LiTi_2O_4 (a and b), MgTi_2O_4 (c and d) and MnTi_2O_4 (e and f) [Zeiss Merlin, acc.volt.: 5 kV].

CHAPTER 5

Electrochemical Characterization

The chemical corrosion experiment results described in chapter 4 were useful in giving general information about the stability of the materials. Nevertheless, even at 85 °C, a solution of 0.5 M HNO₃ (as the testing solution used) has a formal potential of 0.96 V vs SHE [222]. A material in the anode of a PEMEC must be able to withstand potentials starting from 1.23 V (the standard OER potential of water splitting) up to potentials as high as 2.0 V vs SHE (a typical operational threshold for cell potential in PEMECs [172]). Determine the behaviour of a material when it is polarized in the environment of a PEMEC anode is unavoidable for assessing the possibility of using such material in the application.

This chapter describes the electrochemical studies that were conducted through the course of this project. Firstly, a classical corrosion science approach was directed toward the characterization of the Ti felt used as current collector in a typical PEMEC. Then, cyclic voltammetry has been used to characterize composite materials made of the best performing ceramics materials identified in the previous chapters (namely NiCr₂O₄, MnCu_{0.25}Cr_{1.75}O₄ and LiTi₂O₄). Finally, an MEA where a mixture of MnCu_{0.25}Cr_{1.75}O₄ and IrO₂ was used as anode layer was prepared. The cell was characterized by chronoamperometry and EIS in the conditions of real operation of a PEMEC.

5.1 Tafel plots and EIS on Ti felt

With the interest in understanding the electrochemical characteristics and the electrical properties of the Ti felt used in PEMEC real operation, a sample of Ti felt delivered by EWII Fuel Cells A/S was characterized by Tafel polarization curves and impedance spectroscopy. More precisely, it was considered of interest to quantify more accurately what would have been the resistance introduced by uncoated Ti during the operation of the cell by the developing oxide layer. The polarization curves were compared with a pure Ti wire which was used as model electrode. One of the purposes of EIS analysis was the determination of thickness of the TiO₂ layer grown as a consequence of the anodic polarization, which was evaluated according to equation 2.15.

Figure 5.1 reports some SEM images collected on the Ti felt. It is characterized by metallic fibers with approximately a squared section. The fibers present a cross section close to 20 μm if the side of the squared section is considered. The value is in agreement with the reported values in the specifications sheet of the material (see appendix B). The cross section appeared slightly thinner than the 350 μm reported in the data sheet for the thickness, but the action of the blade during the cutting of the pieces could have caused a local compression on the cut edges of the felt.

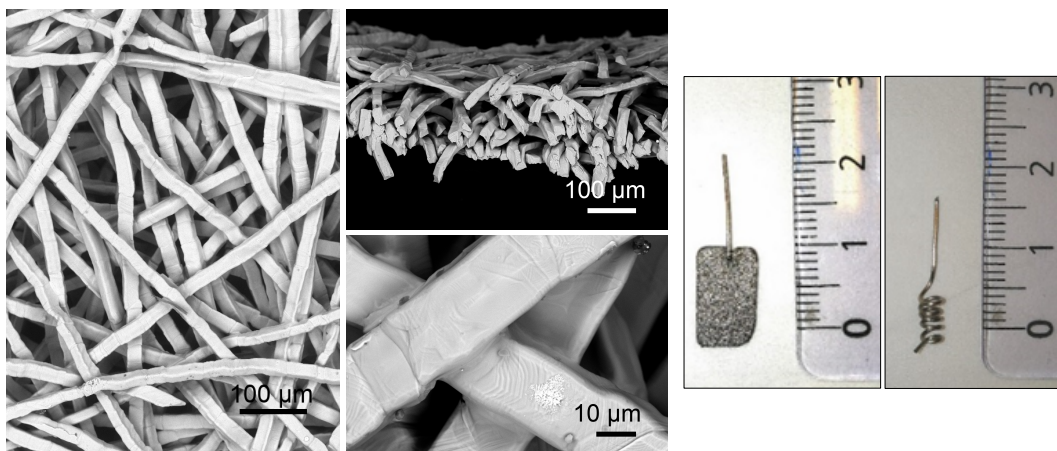


Figure 5.1: (left) SEM images collected by SEM on the Ti felt under study [Hitachi TM3000, acc. volt.: 14 kV, BSD]; (right) Ti felt and Ti wire samples used for the electrochemical characterization.

The electrode used for the characterization of the Ti felt was prepared by cutting out a portion of the original Ti felt. Due to capillarity action of the solution through the pores, it was necessary to prepare an electrode by joining the sample of felt to a piece of Ti wire with a pencil welder. More details on the reason for that are reported in appendix B. The calculations for estimating the real surface area of the Ti felt later used for normalizing the electrochemical data can also be found there.

The sample was immersed in 100 ml of 0.5 M H_2SO_4 saturated with O_2 . The experiments were conducted using a Hg/HgSO_4 reference electrode and a Pt plate as a counter electrode. The polarization curve was obtained by sweeping positively the potential applied on the felt from -0.5 to 2.5 V vs SHE at a scan rate of 1 mV sec^{-1} . The same conditions were applied to the Ti wire. Figure 5.1 shows pictures of felt and wire electrodes used for the electrochemical characterization.

Figure 5.2a shows the obtained polarization curve. The wire and the felt showed a very similar behaviour throughout the whole range. The obtained corrosion potential were -0.035 and -0.058 V vs SHE for the felt and the wire respectively. A certain variability on the value of the corrosion potential can be influenced by the native oxide present before the measurement of the polarization curve [223]: since no pre-treatment of the Ti was conducted in order to remove native oxide layer and the lowest potential was not enough to reduce TiO_2 to Ti [224], it can be possible that the two samples had different thicknesses of oxide present on the surface when the experiment was conducted. Anyway, the difference is small. After that, the two samples go through a current plateau consistent with the passivating region of a valve metal [83].

The two polarization curves differ slightly for potentials $>1.5 \text{ V vs SHE}$. The wire shows a step-like increase in the current which later appear to evolve again into a plateau. A similar behaviour has already been reported in literature for Ti in acidic media [223, 225]. The Ti felt shows a continuous increase in current up to 2.5 V vs SHE.

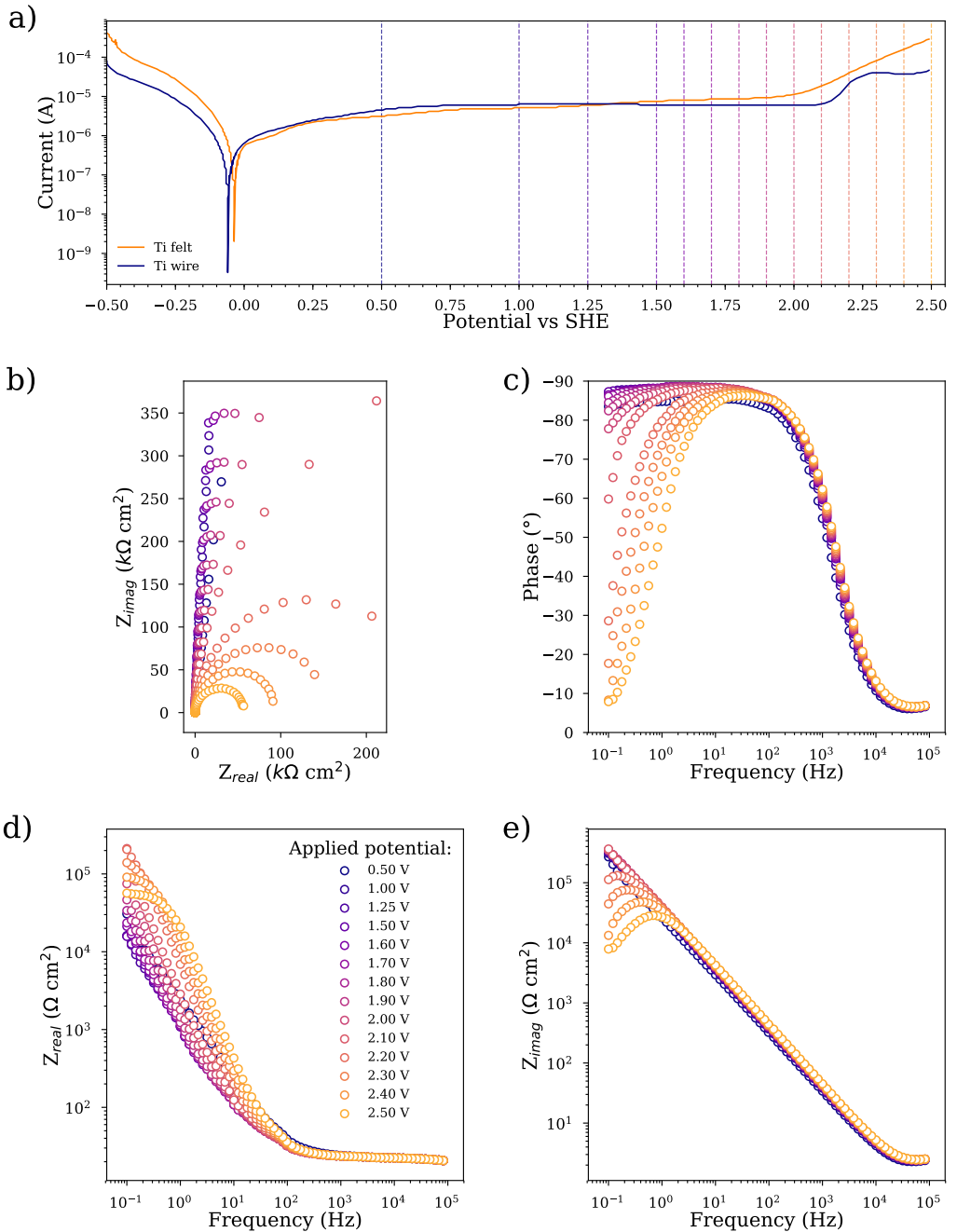


Figure 5.2: a: Polarization curves conducted on SEM images collected on the Ti felt used as current collector provided by EWII Fuel Cells A/S; b,c,d,e: Nyquist and Bode plots showing the EIS spectra measured on the Ti felt sample at different applied potentials.

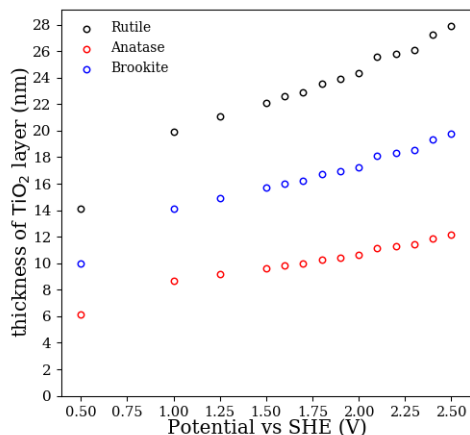


Figure 5.3: Thickness of TiO_2 layer as a function of potential.

The absence of such step-like behaviour of the could be due to the greater morphological inhomogeneity of the Ti felt.

After the polarization curve, impedance spectra were recorded at different applied potentials. The potential was applied for 10 s before the spectrum was recorded. The frequency range was 10^5 -0.1 Hz with a amplitude of 0.005 V. The obtained results are plotted in figure 5.2*b*, *c*, *d* and *e*.

The sample shows a typical blocking electrode behaviour for potentials applied smaller than 1.80 V vs SHE. For more positive potentials, the total resistance measured in the spectrum decreases more and more as the potential increases. Nonetheless, the resistance is very high even at the lowest point. Such big resistances have been reported for EIS studies of anodized Ti [226]. Instead, the origin of this decrease in the resistance could not be fully understood: an increase in potential would imply an increase in TiO_2 thickness and a consequent increase in the resistance would be expected; OER can happen on anodic TiO_2 , but the applied potential seem too low, since typical onset potentials are reported to be ~ 3.0 V vs SHE [223, 227].

The EIS spectra were fitted with a simple Randles circuit R_1 - R_2Q_2 . Values of C_{eff} were calculated according to equation 2.14 (section 2.3, p. 25) and the thickness of the oxide layer was calculated according to equation 2.15 (section 2.3, p. 25) assuming the oxide formed was one of the crystalline polymorphs of TiO_2 . The values of ϵ_r were taken from [228] and were 100, 48 and 78 for rutile, anatase and brookite respectively. The results are reported in figure 5.3. Compared with the literature [227, 228], the values appear larger than the potential applied would imply. One explanation could be that the assumption of a pure crystalline phase is too strict, in fact the result of Ti anodization is often a mixture of amorphous and crystalline phases where Ti can be found in different oxidation states [227]. This would determine a different value of dielectric constant ϵ_r and possibly alter the output of the calculation.

5.2 RRDE studies

The electrochemical characterization of ceramic materials is often impeded by the low conductivity that the materials possess, which hinders the direct characterization of bodies of compacted powders or single crystals. Historically, the analytical electrochemical investigation of insoluble and/or electronic insulating materials has been conducted by the use of *composite electrodes*, where the analyte is mixed with a material which is both electrochemically inert and electrically conductive with the help of a proper binder (often paraffin or silicone oil). The most common constituents of the conductive matrix in such composites are carbon based materials, such as graphite, carbon black (CB) or acetylene black. Such electrodes are known as *carbon paste electrodes* (CPE) and exploit the combination of good electronic conductivity and general electrochemical inertness of carbon materials [229–233]. The analyte is finely subdivided and embedded in the conductive matrix. When a current is drawn through the electrode, the electroactive species are the particles of the material or the products of their dissolution, provided the electrochemical activity of the analyte lies within the stability window of the conductive matrix. Locally, the issue related to low conductivity is overcome due to the small size of the particles and the good electrical contact, but overall the recorded current is the sum of the electrochemical activity of all the material in the active volume of the electrode. A further advancement of the CPE was achieved by Bauer [234], when he introduced the carbon paste electrodes *with electrolytic binder* (CPEEBs). In a CPEEB, ceramic and carbon are mixed together using the electrolyte of the electrochemical experiment as a binder. This fact also allows to study the interaction of the ceramic with the particular electrolyte chosen.

For the purpose of this study, the CPE approach has a major drawback, which is that the experiment is conducted on a static electrode. The electrochemical characterization in this work was intended to be carried out at potentials where OER is expected to take place, therefore a static electrode could suffer O₂ entrapment on the surface and cause an increase in resistance coming from the reduced electroactive area. For this reason it was decided to characterize the materials using a rotating disk electrode (RDE) [235, 236]. The rotation of the RDE drags a continuous flow of electrolyte to the surface of the electrode and helps detaching freshly formed bubbles on the surface. In fact, RDE is widely used in OER catalyst research (for example [42, 44, 117, 237]). Moreover, when the electrode used is in a rotating ring-disk configuration (RRDE), the electrolyte flow carries the reacted species leaving the disk electrode to the ring electrode. If the species are electroactive in the stability window of the electrolyte, they can react once collected on the ring, provided a proper potential is applied to such electrode. Wang *et al.* [238] successfully used this approach to study the dissolution of Mn from LiMn₂O₄. Danilovic *et al.* [23] correlated activity and stability of RuO₂ and IrO₂ by re-depositing dissolved metal species on the ring held at a proper potential while on the disk OER was taking place. The RRDE used in this 'collection mode' can give interesting information on the nature and the quantity of the species which leave the disk, together with a direct link between a certain potential applied to the disk and the detected dissolution. The

major limitation of such approach consists in the limited volume of material that can be deposited on the electrode without sensibly modifying the morphology of the electrode itself and therefore altering its hydrodynamics properties.

Ink-drop deposition is a science on its own, where ink composition, solid particles size and drying conditions determines the quality of the final film. In this study, guidelines to ink-drop casting, ink composition and in general pre-treatment of the RDE were taken from [239]. Morphological homogeneity and reproducibility are common parameters to judge the goodness of the casted film. Nafion was used as a binder in the preparation of the ink. It is used commonly as a binder in ink-drop casted electrodes [235, 236]. Given the low conductivity of the materials under study, it was decided to blend the ceramic with a carbonaceous material. I decided to use graphite over other forms of black carbons because it possesses the highest electrical conductivity among them [240]. As a matter of fact, the preparation of the electrode by ink-drop casting of a mixture of ceramic and graphite using Nafion as a binder can be regarded as an hybrid between CPEs and CPEEBs, given the ionic conductivity of the PFSA chains. The contact with the fluoropolymer is also a condition that the material will likely encounter in the real cell application.

If the composite electrode is exposed to sufficiently high potentials, one has to take into account the possibility of oxidation of the conductive matrix and the support electrode itself, beside the activity of the material under study. Glassy carbon (GC), the constituent of the (R)RDE disks used in this study, experiences oxidation in acid when the potential is greater than 1.2 V vs SHE with a symmetrical redox peak centered at 0.55 V vs SHE of a CV due to electrochemically active surface functional groups [241]. Graphite oxidation to give graphite oxide and/or intercalation compounds is widely known. The intercalation of inorganic anions, such as SO_4^{2-} and ClO_4^- is usually conducted in very concentrated solutions and it can start at relatively low potentials [242-244]. Yet, Beck *et al.* [245] showed that the intercalation peak potential strongly depends on the concentration of the electrolyte used and in the case of H_2SO_4 solutions it approaches 2 V vs SHE when the concentration is less than 2 M.

General procedure for RDE electrode preparation

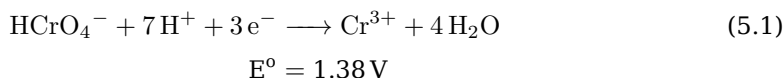
Before each experiment and prior to ink deposition, the RDE was polished with alumina powder of different granulometry mixed with water on a polishing cloth (in the order 1 μm , 0.3 μm and 0.05 μm , Buheler) by forming thirty eight-figure per quarter of a turn. The electrode was rinsed thoroughly with DI water and ethanol to remove the polishing particles, then gently wiped with lens paper.

MCr_2O_4

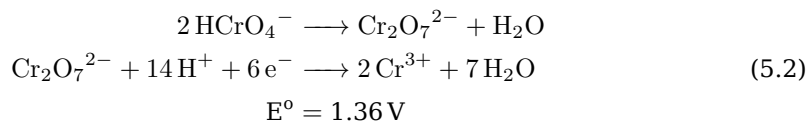
Among the spinel chromites, $\text{MnCu}_{0.25}\text{Cr}_{1.75}\text{O}_4$ and NiCr_2O_4 were selected for further electrochemical characterization since they showed good stability to chemical corrosion and the highest conductivity among the tested Cr-based spinels (see section 4.2.1, p. 59). To get some insight into the electrochemical behaviour of a complex compound,

it is possible to look through the behaviour of similar compounds where only one of the element of the complex compound is present at a time. In the case of spinel $M\text{Cr}_2\text{O}_4$, this means that we can expect that the electrochemical behaviour of the spinel will resemble the behaviour of Cr_2O_3 and MO combined. Sedano *et al.* demonstrated that the characteristic features of Cu and Fe single oxides are also present in copper ferrites [246]. Moreover, Grygar *et al.* showed that, for the system $\text{Fe}_2\text{O}_3 - \text{Mn}_2\text{O}_3$, the variation of electrochemical response followed the change in composition of the solid solution [247].

Despite being very stable to chemical corrosion (see section 3.2.1, p. 38), chromium oxides undergo oxidative dissolution *via* a multiple-steps process, which can be observed on the top of figure 5.4 [249]. Cr(III) on the surface of the Cr oxides is firstly oxidised to Cr(IV) which can either be further oxidised to Cr(V) or disproportionate to give Cr(III) and CrO_4^{2-} in aqueous environment. Cr(V) then dissolves after oxidation to CrO_4^{2-} . CrO_4^{2-} is mostly protonated at the pH of 0.5 M H_2SO_4 , the solution used for conducting electrochemical characterization (see figure 5.4). According to [248], the reduction of HCrO_4^- proceed as

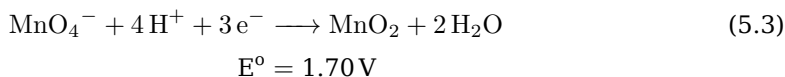


Chromic acid is in equilibrium with dichromate ion in solution, so the reduction can also proceed according to



The two reactions are iso-electronic for the same moles of starting chromium reagent, and they are very close in equilibrium potentials.

Mn(II) ions are oxidized to MnO_2 at potentials $>1.4\text{V}$ vs SHE [250]. Manganese(III,IV) oxides are reported to undergo reductive dissolution when scanned negatively from high to low potentials [251]. The oxidation to higher valencies of MnO_2 in aqueous solution to form soluble species (such as permanganates ions) has been reported [218, 252], but it is conducted in alkaline solution. Permanganate ion can be reduced in acid environment [248], according to



NiO is reported to generate two symmetrical peaks when cycled in 0.5 M H_2SO_4 [253]. A first peak is present at 1 V vs SHE, corresponding to the oxidation Ni(II)/Ni(III) . A second peak centered at 1.4 V vs SHE has been attributed to the oxidation Ni(III)/Ni(IV) . Bonomo *et al.* [254] studied the dissolution of tape casted NiO electrodes in $\text{KH}_2\text{PO}_4/\text{K}_2\text{HPO}_4$

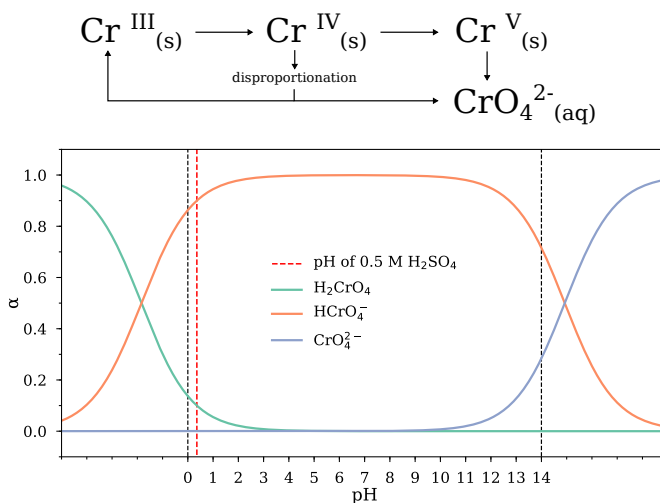
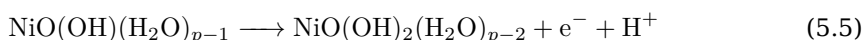
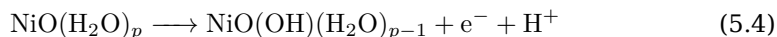


Figure 5.4: (top) Reaction scheme of Cr oxidation in aqueous environment as reported in [247], where s and aq indicate solid state and aqueous species respectively; (bottom): speciation of chromic acid as a function of pH; the values of the dissociation constants used for the calculations were taken from [248].

buffer, showing the same reversible peaks as in [253], even if at different potentials because of the different pH. They attribute the two peaks to the following reactions of hydrated NiO



They also report that the layer undergoes important dissolution upon cycling.

Cu most common oxidation states are +2 and +1. Cu_2O and CuO can be reduced at potentials below 0.5V vs SHE[246], but Cu^{3+} is not a common oxidation state of Cu and its electrochemical formation is not reported to my knowledge. In the solid state, examples of the existence of Cu^{3+} are scarce, a prominent example being the superconducting cuprates, where it is thought that $\text{Cu}^{3+}/\text{Cu}^{2+}$ ratio plays a key role in the superconducting properties of the materials [255]. Cu^{3+} is stable in solution only as a complex [256], otherwise it is unstable in aqueous solution [248].

To cast the materials on the disk of an RDE, reasonably stable inks need to be prepared. A big fraction of the grain size of the crystallites in the chromites was close to 1 μm (see fig 5.5a). To facilitate the formation of stable suspensions, the average size was reduced by ball milling with ZrO_2 cylinders (h : 9 mm, Ø : 5 mm) for five days. Figure 5.5b shows that the average particle size of the ceramics was greatly reduced. In order to evaluate the best ceramic/graphite ratio to be used, a series of trial were conducted. A more detailed description of such preparatory experiments is given in appendix C. The inks used to cast the material on the RDE were prepared as follows. A 5 mg ml^{-1} sus-

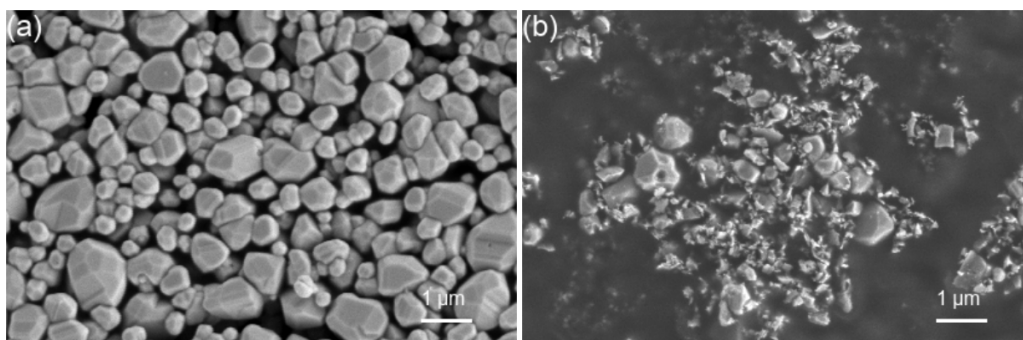


Figure 5.5: SEM images collected on NiCr_2O_4 : (a) as synthesized; (b) after five days of ball milling with ZrO_2 cylinders. $\text{MnCu}_{0.25}\text{Cr}_{1.75}\text{O}_4$ presented a similar behaviour [Zeiss Merlin, SED, acc.volt.: 4 kV].

pension of graphite in 2-propanol (GI) and a 5 mg ml^{-1} suspension of ceramic material in ethanol (CI) were prepared. The suspensions were sonicated for 5 minutes, then 0.5 ml of GI was mixed with 0.5 ml of CI and sonicated again for 5 minutes, to form the ceramic/graphite ink (CGI). A blank ink was prepared by mixing 0.5 ml of GI ink and 0.5 ml of ethanol. The final loading of ceramic material in CGI was 2.5 mg ml^{-1} . Aliquots of CGI were drop casted on the disk of an RRDE (disk: GC; ring: Pt) for a final loading of $25 \mu\text{g}$ of ceramic material deposited, corresponding to $127 \mu\text{g cm}^{-2}$. The deposited droplet was then dried in air or by blowing lightly with N_2 in case the suspension was agglomerating too rapidly. After the ink was dried, $5 \mu\text{l}$ of Nafion solution in ethanol (prepared by adding 9 ml of ethanol to 1 ml of a commercial 5% Nafion solution, Sigma-Aldrich) were deposited on the disk.

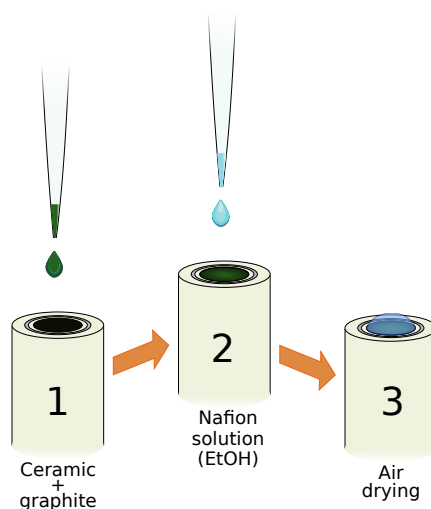


Figure 5.6: Ink-drop casting procedure used in this study for the preparation of ceramic composite electrodes on a RDE.

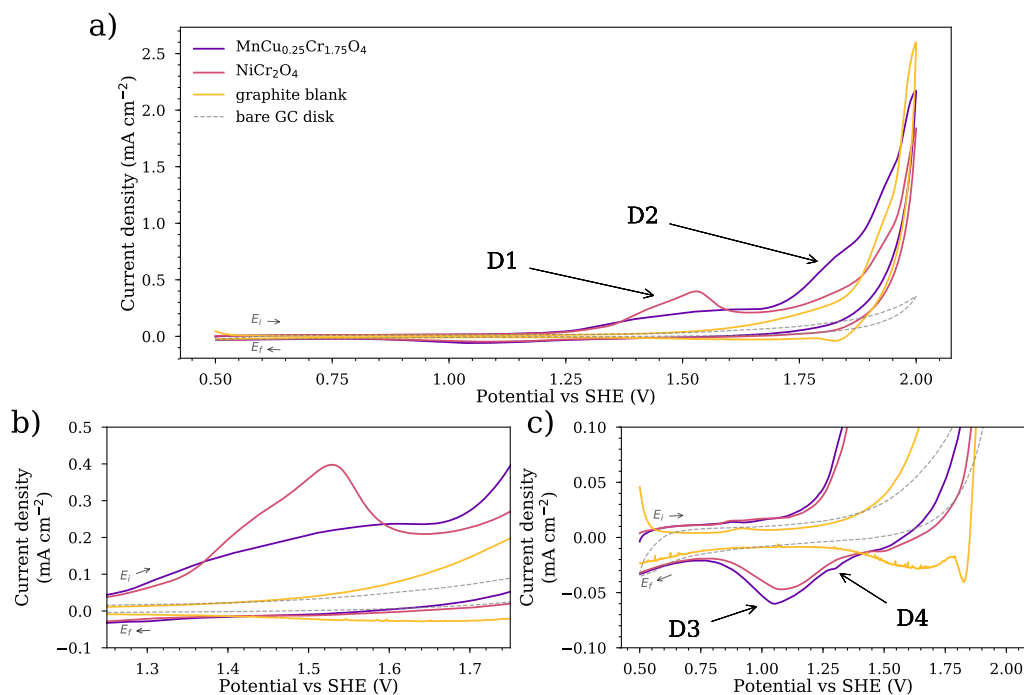


Figure 5.7: CV of $\text{MnCu}_{0.25}\text{Cr}_{1.75}\text{O}_4$ and NiCr_2O_4 composite electrode deposited on RRDE. The same experiment recorded on the bare GC disk where the materials were deposited is shown as dashed grey line. Figures (b) and (c) are close-up views of figure (a). E_i and E_f indicate the direction of the scan from the initial to the final potential respectively [0.5-2.0 V vs SHE, 5 mV sec^{-1} , RE: Hg/HgSO_4 , Ar-saturated 0.5 M H_2SO_4 , 1600 rpm]

The RRDE was immersed in 100 ml of 0.5 M H_2SO_4 saturated with Ar and rotated at 1600 rpm. The experiments were conducted using a Hg/HgSO_4 electrode as a reference electrode and a Pt plate ($A: \approx 3 \text{ cm}^2$) as a counter electrode. The disk was scanned positively from 0.5 to 2.0 V vs SHE at a scan rate of 5 mV s^{-1} for 5 cycles. The ring electrode was held at 0.5 V vs SHE throughout the experiment.

The first cycles of the CV experiments are reported in figure 5.7. A comparison with the blank experiment highlights the presence of distinctive anodic and cathodic features for both the ceramic materials. Specifically, in the anodic branch of the CVs, a peak is distinguishable around 1.6 V (D1). In the case of NiCr_2O_4 , the peak is well resolved, while it appears broader in the case of $\text{MnCu}_{0.25}\text{Cr}_{1.75}\text{O}_4$. A second feature is present in anodic branch of the CV from $\text{MnCu}_{0.25}\text{Cr}_{1.75}\text{O}_4$ around 1.85 V (D2), which is not present in the case of NiCr_2O_4 . The cathodic branch of the CVs again shows distinctive features. A clear cathodic peak centered at 1.0 V (D3) is present in both $\text{MnCu}_{0.25}\text{Cr}_{1.75}\text{O}_4$ and NiCr_2O_4 , while a flat capacitive contribution is present around that potential in the case of the blank experiment. A smaller but evident peak can be seen in the CV of $\text{MnCu}_{0.25}\text{Cr}_{1.75}\text{O}_4$ around 1.3 V (D4). In the case of the blank experiment, it can be noticed a sharp peak right after the scanning direction inversion, followed by a broader signal which disappears before 1.2 V. It is known that oxidation of graphite can lead to the

quantitative analysis of ceramic oxidation.

While the disk was scanned, the Pt ring held at 0.5 V was able to collect species coming from the dissolution processes taking place at the disk. In figure 5.8a, the disk and ring current recorded from the first CV cycle are displayed as a function of time. The ring current has been corrected for the collection efficiency stated by the supplier of the RRDE and multiplied by a factor of 10 for a better graphical clarity. In the case of the blank experiment, no distinguishable signals from the baseline can be observed, with the exception of a small increase in cathodic current at the time the disk reaches 2.0 V, which can be attributed as OER taking place over graphite/GC. In the case of the ceramic materials, the ring current increases sharply when the characteristic anodic signals on the disk are appearing. For both the materials, a cathodic current develops on the ring after the ring passes 1.2 V (peak R1), with the signal apparently mirroring the developing of the anodic peak on the disk. Both the materials show a similar current signal on the ring despite the different compositions, suggesting that the cathodic signal (and therefore the anodic signal on the disk) are related to Cr redox activity. As mentioned before, Cr dissolves as CrO_4^{2-} upon anodic polarization and it is protonated to HCrO_4^- in a solution of 0.5 M sulfuric acid. Even if no oxidation was involved in the dissolution, the reduction of Cr^{3+} in acid solution cannot take place at potentials $> 0\text{V}$ vs SHE, whatever the reduction product [248]. Therefore, the cathodic peak R1 is probably due to reduction of Cr species according to equations 5.2 or 5.3. The reduction must involve Cr species with higher valency, the most stable aqueous species being Cr(VI). Interestingly, R1 peaks before D1 for both the materials.

In figure 5.8b, the evolution of the current upon cycling can be observed. After the first cycle, the signal from the disk where the ceramic materials are deposited resembles the current behaviour of the blank experiment, suggesting that no further evident faradaic process takes place at the disk. The ring current, after the first cycle, shows an increase in cathodic current when the disk approaches 2.0 V, similar to the one observed for the blank experiment, but with higher absolute current density (especially in the case of $\text{MnCu}_{0.25}\text{Cr}_{1.75}\text{O}_4$).

The second cathodic peak on ring current (R2) in the case of $\text{MnCu}_{0.25}\text{Cr}_{1.75}\text{O}_4$ is more difficult to identify. It can be attributed to the material, after comparison with the blank experiment. Nevertheless, multiple reactions beside the oxidative dissolution of the ceramic can take place: above all, OER, together with the parasitic reaction connected to it, such as H_2O_2 production. Manganese oxides (MnO_x) are known to possess a certain activity toward oxygen evolution [257, 258] and it can be expected from the Mn-containing compound to exhibit activity toward oxygen evolution. To rule out the nature of the species originating peak R2, the same experiment was conducted holding the ring at 1.2 V vs SHE, where O_2 cannot be reduced on Pt and H_2O_2 , often present as a side product of OER, is oxidized to O_2 . Figure 5.9 displays the obtained voltammograms. The initial current decay common to all the samples observed for the ring current is the current transient coming from the growth of Pt oxides on the surface of the ring. No cathodic signal is observed in the case of NiCr_2O_4 , graphite blank and GC. In fact, the potential is too high for the reduction/oxidation of $\text{O}_2/\text{H}_2\text{O}_2$. The potential is

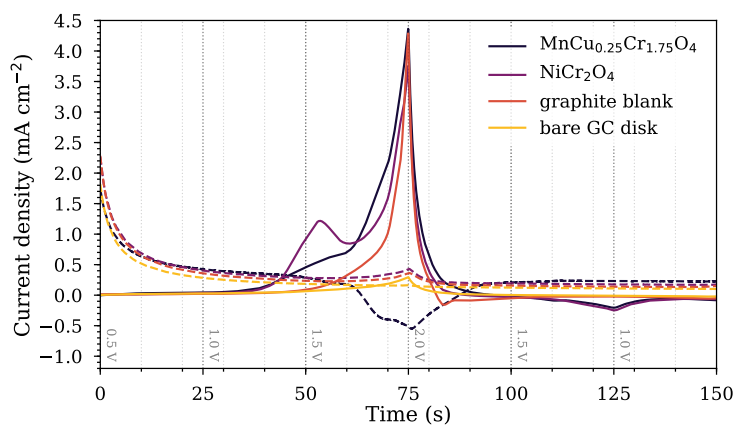


Figure 5.9: CV of $\text{MnCu}_{0.25}\text{Cr}_{1.75}\text{O}_4$ and NiCr_2O_4 composite electrode deposited on RRDE plotted as a function of time showing both the disk current (solid line) and the ring current (dashed line). The ring current has been multiplied by a factor of 10 for a better graphical clarity. The vertical lines indicate the potential applied at the disk at each time. [DISK: 0.5–2.0 V vs SHE, 20 mV sec^{-1} ; RING: 1.2 V vs SHE; RE: Hg/HgSO₄, Ar-saturated 0.5 M H₂SO₄, 1600 rpm]

also probably too high for the reduction of HCrO_4^- (which standard potential of reduction to Cr^{3+} is 1.38 or 1.36 V vs SHE depending if the species which is reduced is HCrO_4^- or $\text{Cr}_2\text{O}_4^{2-}$, see eq. 5.2 and 5.3) as no peak is observed in the position of R1. In the case of $\text{MnCu}_{0.25}\text{Cr}_{1.75}\text{O}_4$, a cathodic current appears on the ring after the disk passes 1.7 V, indicating that a reduction is taking place at the ring. The standard potential of reduction of MnO_4^- is 1.77 V vs SHE (see eq. 5.4) which means that an overpotential of more than 500 mV is present at the Pt ring toward the reduction of permanganate. It can then be deduced that the cathodic peak on the ring is at least partly due to the reduction of permanganate to MnO_x . R2 shows a clear difference in its total area (charge) when it is held at 0.5 or 1.2 V vs SHE, as can be seen comparing figures 5.8 and 5.9. This fact may indicate that, on the disk at potentials between 1.7 and 2.0 V, several concurrent reactions are taking place, such as OER, H_2O_2 production, Mn oxidation. The product of some of those reactions can be reduced on the ring when it is held at 0.5 V vs SHE but not when it is at 1.2 V vs SHE. The difference in area could also be explained by only one reaction (e.g. MnO_4^- reduction), driven to different degrees of completion by the ring being held at 0.5 or 1.2 V vs SHE. It is reported that higher OER activity of MnO_x is related to the presence of Mn^{3+} , which is present on $\text{MnCu}_{0.25}\text{Cr}_{1.75}\text{O}_4$ due to oxidation of the native Mn^{2+} constituent ions and the product of the partial inversion due to exchange with Cu^{2+} in octahedral position, as explained in chapters 3 and 4. It can be assumed that the main cause for the peak in cathodic current observed on the ring held at 0.5 V when the disk is at 2.0 V is due to O_2 reduction. A decrease of absolute cathodic current on the ring upon cycling can be interpreted as the progressive oxidation of Mn ions present on the surface of the material to stable but OER-inactive Mn^{4+} ions, which then lead to a decrease in the oxygen evolution current.

The cathodic peak D3 has been observed previously for the reduction of HCrO_4^- ion [247]. The presence of the peak D4 only in the case of $\text{MnCu}_{0.25}\text{Cr}_{1.75}\text{O}_4$ suggests that

the peak may be related to the presence of Mn (Cu redox activity is found at much lower potentials, as explained before). In fact, a similar sharp peak is reported by Godunov *et al.* [250] for the reduction of $\text{MnO}_{2(s)}$ to $\text{Mn}_{(aq)}^{2+}$. The presence of cathodic peaks D3 and D4 during the negative going sweep (NGS) may indicate a certain degree of reversibility of the reaction taking place on the disk during the positive going sweep (PGS), and be related to the reduction of Cr(VI) and Mn(IV) species on the surface of the ceramic material. Indeed, the presence of cathodic peaks in the first cycle (and the following cycles) is not correlated to the presence of an anodic peak in the subsequent PGS. As can be observed in figure 5.8b, the cathodic peaks fade later than the anodic peaks. To further investigate such phenomenon, the experiments were repeated by increasing the upper potential of the CV (E_u) progressively at each cycle up to 2.0V vs SHE. Figure 5.10 shows the results of such experiments for NiCr_2O_4 . The same experiments have been conducted for $\text{MnCu}_{0.25}\text{Cr}_{1.75}\text{O}_4$, not displayed here, and the following discussion can be considered valid also for it. In order to get a current signal which was sensibly

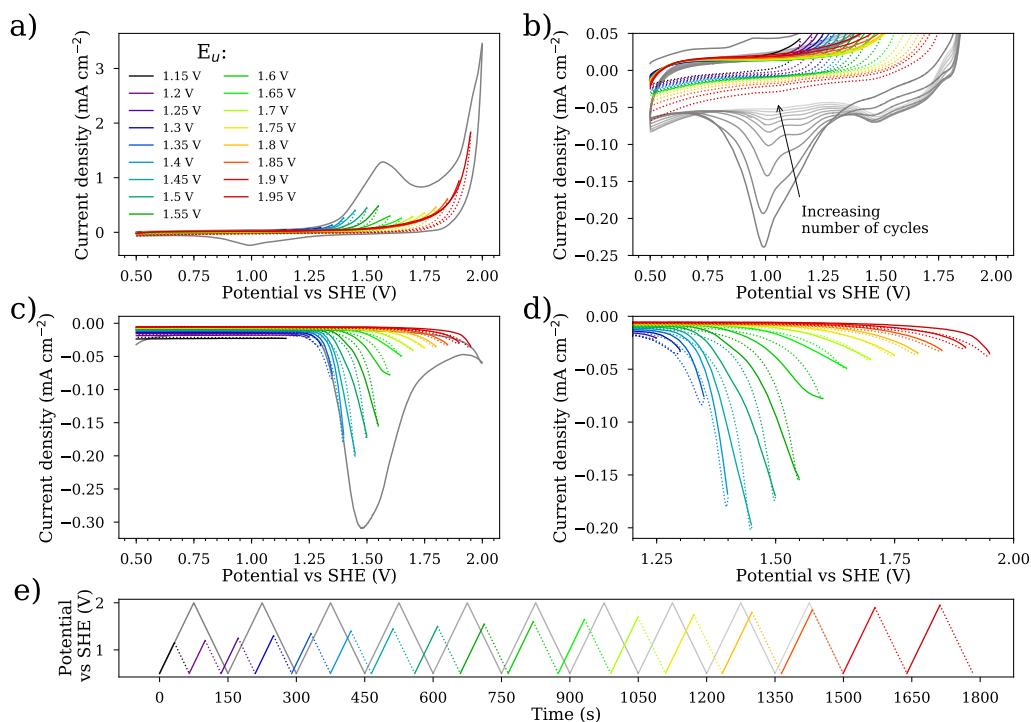


Figure 5.10: CV of NiCr_2O_4 composite electrode deposited on RRDE plotted as a continuous scan up to 2.0V vs SHE (grey line) and with subsequent scans with increasing E_u (coloured lines); in the case of the scans with variable E_u , solid line indicate the PGS while dotted lines indicate the NGS, for clarity. a and b: disk current; c and d: ring current. The first cycle of the CVs is showed in the case of the continuous plot for figures a and c, the first five cycles in the case of figure b. e: potential profile as a function of time for the first five cycles of the continuous scan experiment and for the variable E_u experiment [DISK: 0.5-2.0V vs SHE (grey line) and 0.5- E_u V vs SHE with $1.15 \leq E_u \leq 1.95$ (coloured line), 20 mV sec^{-1} ; RING: 0.5 V vs SHE; RE: Hg/HgSO_4 , Ar-saturated $0.5 \text{ M H}_2\text{SO}_4$, 1600 rpm].

differing from the background current, the double of the ceramic loading was used (total loading: $255 \mu\text{g cm}^{-2}$). The maximum potential reached at each cycle, E_u was increased at each cycle of 0.05 V starting from 1.15 to 1.95 V (identified in the following as variable E_u experiment). A CV experiment where the potential was continuously scanned with the same scan rate from 0.5 to 2 V is also showed in the figure (identified in the following as continuous experiment). Both in the case of disk and ring current, it can be observed that the composition of the single cycles with variable E_u presents higher total currents in the positions where the current peaks and waves are present in the continuous CV. The results also further highlight the potential dependence of the processes taking place on the disk.

Beside lower absolute values of the current in the case of the variable E_u experiment, a clear difference with the continuous scan experiment is the absence of the cathodic peaks D3 and D4. In the case of the continuous CV, the fact that the presence of D3 and D4 is not correlated to any restoration of anodic activity during the subsequent PGS suggests that the reactions causing the peaks are not simply the reverse process of the ones originating the anodic peaks in the previous PGS. Moreover, the cathodic peaks fade away upon cycling (see fig.5.10b) without any comparable change in the anodic side of the CV. Given these observation, it can be inferred that the nature of the cathodic peaks is due to the reduction on the disk of soluble products of the oxidation of the ceramic which could not escape the composite casted layer during the time frame of one single cycle.

During the experiments, the electrolyte is continuously dragged toward the electrode by the rotation of the RDE. A soluble species produced on the disk which remains loosely adsorbed on the electrode would be eventually transported away from by the flux due to the constant rotation. If the potential on the disk is negative enough while the reactive adsorbed species is present in high enough concentration, it can be expected the adsorbed species to be reduced on the disk prior to be dragged away by the flux of electrolyte, and to cause an observable cathodic signal. The emergence of a cathodic signal would therefore be time dependent on the experiment time scale, i.e. the cathodic peak will be present as far as the flux of electrolyte does not remove all the adsorbed species from the disk electrode. Figure 5.10e shows the potential applied on the disk as a function of time for the continuous scan experiment (10 cycles) and for the variable E_u experiment. In the continuous scan experiment, the oxidation reactions which originate the soluble species take place at the first PSG (see fig. 5.8). Part of the soluble products leave the electrode and are collected at the ring, part of them stay adsorbed on the disk and are reduced when the potential on the disk becomes less than 1.1 V vs SHE (if the soluble product is HCrO_4^- , the potential is below the standard potential of the reaction reported in equation 5.2), originating the cathodic peaks. After 10 cycles, where no anodic signal on the disk gives indication of further production of oxidation products, the adsorbed species are either completely reduced or have been removed from the disk by the continuous stream of electrolyte. 10 cycles (1500 s) are then necessary to remove the products of the anodic processes in the first PSG (75 s). In the experiment with increasing E_u , each cycle produces a fraction of the total amount

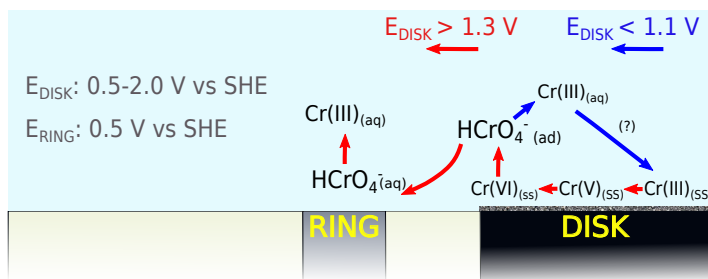


Figure 5.11: Scheme of the interpretation of the processes observed by CV on the ceramic materials, relative to the oxidation of solid state Cr. Red arrows indicate the processes taking place when the potential of the disk is greater than 1.3 V vs SHE, blue arrows indicate the processes taking place when the potential is lower than 1.1 V vs SHE.

of soluble species produced in the first continuous cycle, since $E_u < 2\text{V}$ always. If we consider the oxidation reaction to be completed when the potential is higher than 1.75 V vs SHE (after the anodic peak present in the continuous scan), in the increasing E_u experiment the reaction is completed only after the 13th cycle, corresponding to 1324 s. In such larger time scale, the soluble species adsorbed on the disk are probably too low in concentration or carried away fast enough by the electrolyte flux not to allow the recording of an observable reduction current; therefore the cathodic peaks D3 and D4 are not observed in such experiment.

Given the above discussed results, figure 5.11 summarize the proposed interpretation of the phenomena observed during the CV experiments for the electrochemical anodic dissolution of Cr oxides.

The integration of the CV areas can give information on the amount of reactive material relative to the total amount deposited on the electrode that undergoes electrochemical reactions. The evaluation of the baseline for integration is not trivial when multiple peaks are overlapping. As a first approach (approach A), the signal coming from the blank graphite experiment can be subtracted, which includes the contribution of graphite itself and of GC electrode. Moreover, in the region under analysis OER is expected to become an important contribution, after the potential passes 1.23 V. Integration of the ceramic related peaks even after the subtraction of the blank signal will include also the charge coming from OER faradaic processes, if the ceramic composite electrode and the blank composite electrode have different activity toward OER. This integration approach is expected to be an overestimation of the charge assigned to the ceramic redox processes. Another integration approach (approach B) can be the direct extrapolation of the peak area by using a straight line at the base of the peak as a baseline. This approach removes possible inclusion of OER currents: oxygen evolution involves water as a reactant and therefore, in an aqueous environment a Tafel behaviour can be expected, limited only by electrolyte resistance, and no peak arising from diffusion control of the reaction can be expected; any resolved peak can be ascribed to characteristic faradaic processes involving the ceramic materials. Nevertheless, this approach can lead to underestimation of the charge involved, since the baseline has not

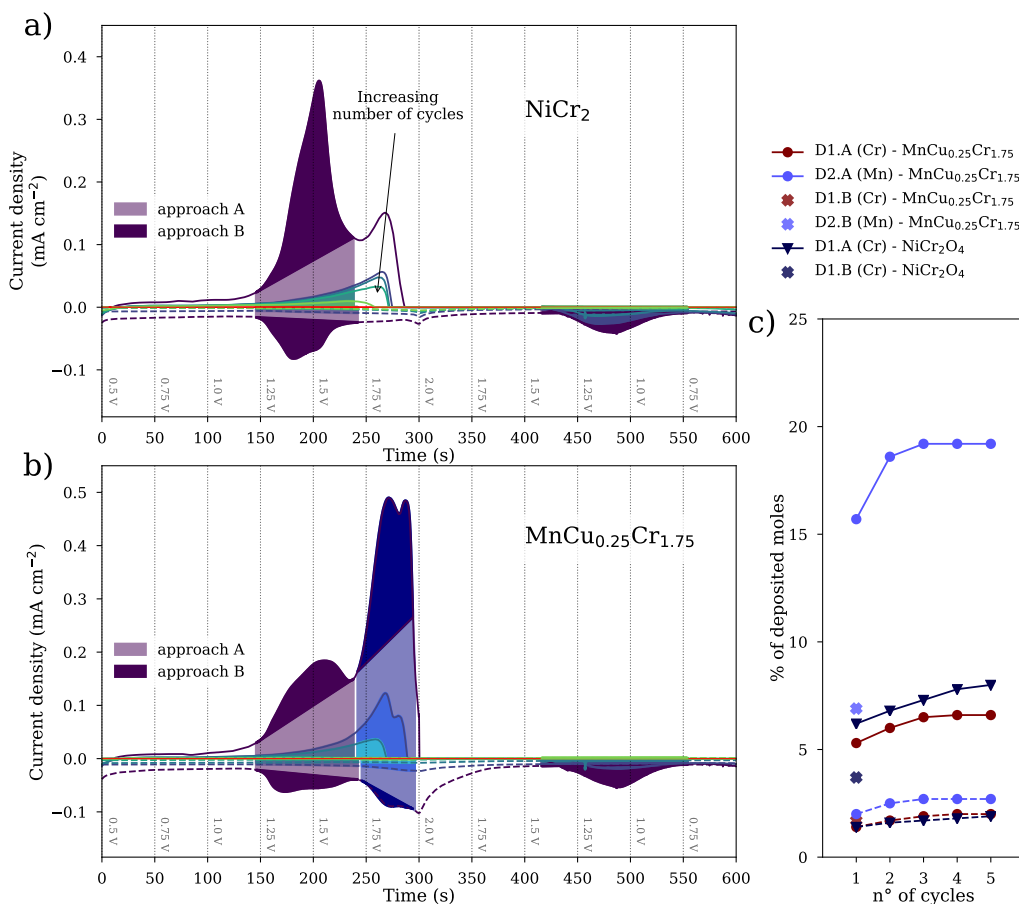


Figure 5.12: CV of $\text{MnCu}_{0.25}\text{Cr}_{1.75}\text{O}_4$ and NiCr_2O_4 composite electrode deposited on RRDE plotted as a function of time showing both the disk current (solid line) and the ring current (dashed line). The ring current has been multiplied by a factor of 10 for a better graphical clarity. The vertical lines indicate the potential applied at the disk at each time. [DISK: 0.5–2.0 V vs SHE, 5 mV sec^{-1} ; RING: 0.5 V vs SHE; RE: Hg/HgSO₄, Ar-saturated 0.5 M H₂SO₄, 1600 rpm]

strictly speaking any physical meaning and it is ultimately drawn arbitrarily. For the purpose of the integration and given the analysis described above, the integration of peaks R1 and D1 have been attributed to Cr and conducted considering a three electron process according to equation 5.2 or 5.3, while peaks R2 and D2 have been attributed to Mn and integrated considering a three electron process according to equation 5.4.

Only the very first cycle showed a clear peak. The integration with the different approaches, even if not quantitative, can give information on the portion of material that undergoes faradaic reactions. The approaches can be regarded as boundary limits for under-/over-estimation, meaning that the real value must lay in between the values obtained with the two approaches. Figure 5.12 illustrates the two approaches for NiCr_2O_4 and $\text{MnCu}_{0.25}\text{Cr}_{1.75}\text{O}_4$, together with the resulting integrated charges as a function of the number of cycles (fig. 5.12c). The integrated charges evolution upon cycling show

that only a fraction of the total amount of moles undergo oxidation during the CV experiment. The area evolution appears to reach a plateau after a few cycles. Areas corresponding to ring currents are corrected considering the collection efficiency of the RRDE, but the absolute values of the integrated areas are well below the values obtained by integration of the disk current, suggesting that not all the oxidation products leave the disk after oxidation. Even assuming that the cathodic peaks D3 and D4 are caused by trapped soluble oxidation products, adding the integration results of those peaks to the ring current to quantify the dissolved materials (not reported) does not influence significantly the amounts of integrated charges. Therefore, the oxidation of the material takes place predominantly in the first anodic sweep of the voltammetry without complete oxidation of the material under study.

To observe the effect of potential cycling on the composite casted electrode, SEM images were collected on the casted material before and after the CV experiment. To prepare the samples for the SEM analysis, one side of an adhesive carbon tape disk was put in contact with the deposited material on the disk of the RRDE and made adhere adequately by applying pressure. An SEM holder was placed in contact with the other side of the adhesive disk. When the SEM holder was lifted from the surface of the RRDE, the carbon tape disk remained attached to it, taking away from the surface of the RRDE disk a good portion of the casted composite.

The images are shown in figure 5.13. In the low magnification images (fig.5.13 *a,b,c* and *d*) the general morphology of the casted composite can be observed. There is a clear difference in average particle size between and graphite and ceramic particles. Moreover, it can be observed that the ceramic is still present in the composite and that it did not undergo complete dissolution upon cycling. No striking difference in morphology of the casted electrode can be observed before and after the CV experiment. Higher magnification images (fig.5.13 *e,f,g* and *h*) further show than no major change in the general aspect of the particles has occurred after the cycling. In the case of $\text{MnCu}_{0.25}\text{Cr}_{1.75}\text{O}_4$ it can be observed that some particles experienced a roughening of the surface together the emergence of a layered aspect on the surface (fig. 5.13*f*: dashed lines enclose areas where roughening can be observed, arrows indicate points where a layered morphology is more evident). This change in morphology can be due to etching of the surface .

The results indicate that the material experience dissolution during potential cycling. Evidence of a certain degree of dissolution of the materials was also indicated by the mass loss of the samples measured after chemical corrosion (see section 4.2.1, p. 59). To further investigate the products of such dissolution, XPS surface analysis was conducted on the samples before and after the chemical corrosion test and the CV experiment. The samples analyzed before and after the CV experiments were prepared analogously as the ones used to collect SEM pictures. The testing solutions of the experiments (1:1 mixture of H_2SO_4 and HNO_3 acid in the case of chemical corrosion testing and 0.5 M H_2SO_4 in the case of CV experiments) were also analyzed by ICP-OES to determine the ratio of the species in solution as a consequence of dissolution. Figure 5.14 shows the results of the XPS and ICP-OES analysis, which are reported as molar ratios χ of the

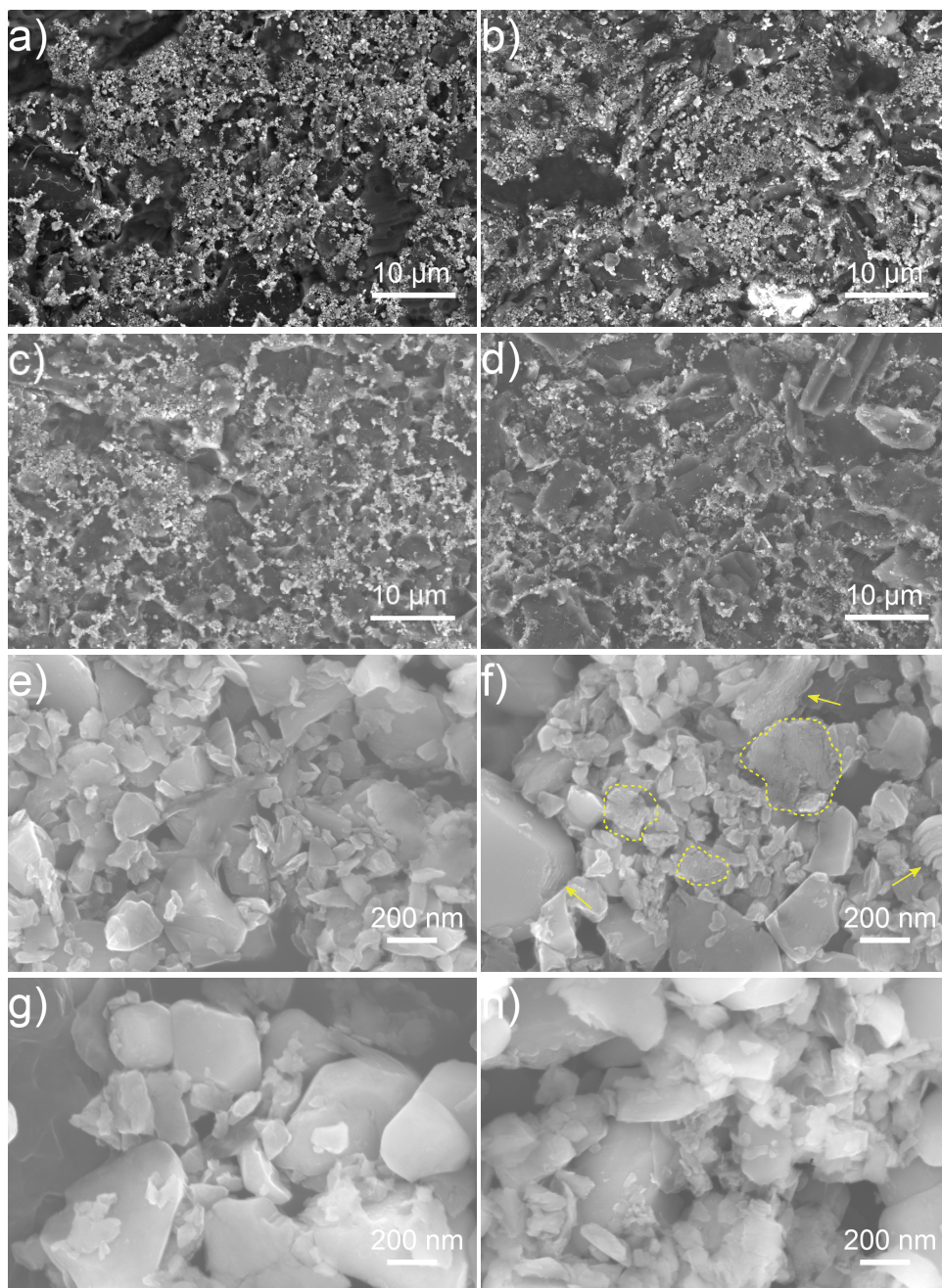


Figure 5.13: SEM images collected on samples of the RRDE-casted composites of $\text{MnCu}_{0.25}\text{Cr}_{1.75}\text{O}_4$ (a,b,e,f) and NiCr_2O_4 (c,d,g,h) before (a,c,e,g) and after (b,d,f,h) after CV experiments [Zeiss Merlin, acc.volt.: 10 kV, a,b,c,d: SED; e,f,g,h: In-lens detector].

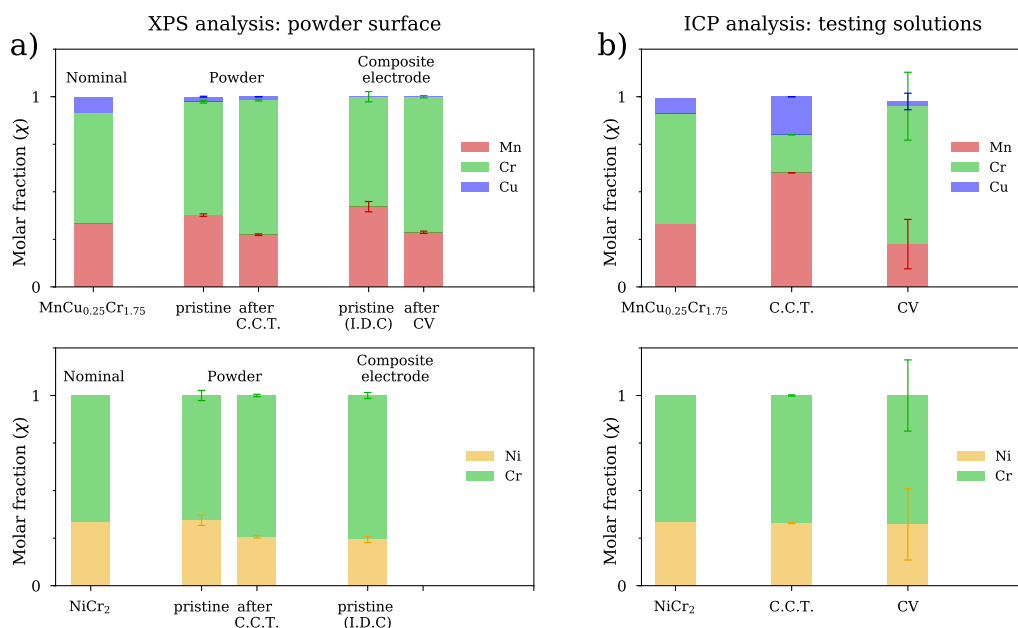


Figure 5.14: (a) Molar fractions derived from surface analysis by XPS of $\text{MnCu}_{0.25}\text{Cr}_{1.75}\text{O}_4$ and NiCr_2O_4 as pristine powder, as as-casted composites (I.D.C.: ink-drop casting), after the chemical corrosion test (C.C.T.) and after potential cycling (CV); (b) Molar fractions of the elements found in the the testing solutions after C.C.T and CV determined by ICP-OES; the nominal compositions of the materials are also reported.

components of the ceramic materials¹. The XPS results on the pristine samples show a good agreement of the measured molar compositions with the nominal one, with the exception of the measured content of Cu in $\text{MnCu}_{0.25}\text{Cr}_{1.75}\text{O}_4$, which is slightly lower than the nominal value. In the case of NiCr_2O_4 , the XPS analysis powder sample after the chemical corrosion test show an enrichment in Cr on the surface of the material. The measurement performed on the sample after the CV experiment was affected by an unknown interference and could not be reliably quantified. The ICP-MS conducted on the testing solution indicate that the dissolution of the components is congruent both in the chemical corrosion test and in the electrochemical test, with the relative amounts of Ni and Cr being close to the nominal composition of the material before the tests.

The sample $\text{MnCu}_{0.25}\text{Cr}_{1.75}\text{O}_4$ behaved differently. After the chemical corrosion test, the XPS results show that the χ_{Cr} is higher compared to the nominal value and the values measured for the pristine samples. Notably, the enrichment of Cr on the surface

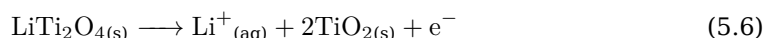
¹As a general comment, the XPS results were conducted on powdered samples in the case of the samples before and after the chemical corrosion test and as transferred ink-drop casted materials and they in general suffered low resolution and low intensity due to uneven surface morphology and small amount of material mounted on carbon tape, especially in the case of the transferred ink-drop casted samples. The ICP measurement can be considered very accurate in the case of the testing solution after chemical corrosion test because the overall concentration of the species of interest was several order of magnitude higher than the background impurities. In the case of the analysis of the electrolyte were the CV experiments were conducted, the small amount of ceramic material in a relatively large amount of solution produced a broader variability of the absolute measured quantity, which is accounted by the larger scale bar in the graphs in figure 5.14b.

of the tested sample is mirrored by a higher value of χ_{Mn} and χ_{Cu} in the metal content measured by ICP-OES in the testing solutions, indicating that Cu and Mn dissolve preferentially compared to Cr. In the case of the material after the CV experiment, the ICP-OES analysis of the electrolyte indicates a different molar fraction of the dissolved species compared to the chemical corrosion test, more similar to the nominal one. This can be taken as an indication that the corrosion stability of the material changes when the ceramic experiences high enough polarization to trigger Cr oxidation and consequent solubilization.

MTi₂O₄

The electrochemical characterization was conducted also on LiTi₂O₄. In the case of this material, the ring electrode was not used during the experiment, since none of the components of the ceramic forms soluble species which can be redox active in the water stability window. The ink preparation and deposition was similar to the procedure used in the case of the Cr-based spinels described above. Briefly, the 1:1 mixture in weight of ceramic and graphite were dispersed in ethanol by sonication to give a suspension of 10 mg ml⁻¹. 20 μ l of a 5% Nafion solution per ml of solvent were added as binder. Three aliquots of 5 μ l of ink were dropped on the RDE disk for a final total loading of 150 μ g of ceramic material ($\sim 700 \mu\text{g cm}^{-2}$). In this case, the CV was run only up to 1.95 V vs SHE, in order to avoid the appearance of the peaks due to graphite intercalation reactions observed in the case of the chromites (see fig. 5.7).

Figure 5.15 shows the obtained results. A clear anodic peak centered at 1.7 V vs SHE can be observed in the PGS, progressively reducing in intensity upon cycling: the signal becomes more and more similar to the one observed for the graphite blank experiment (not reported for clarity, see fig. 5.7). No distinctive reduction peaks are observed in the NGS, indicating that the oxidation taking place is irreversible. In the ceramic material, only Ti³⁺ can exhibit redox activity. Therefore, a comparison could be made with standard oxidation potential of solid oxides with the same nominal oxidation state of Ti in LiTi₂O₄, specifically Ti₂O₃, as a first approximation. In the literature [248], reduction standard potentials of solid Ti₂O₃ are found from around -0.5 to -0.8 V vs SHE, depending on the product of oxidation being TiO₂ or Ti₃O₅, and the reactive species and products being in hydrated or anhydrous form. The difference between the measured potential of the peak and standard oxidation potentials is 1.5 V. Even considering a certain degree of hysteresis due to potential sweeping, this result may indicate that a significant overpotential is necessary to carry out the oxidation of Ti³⁺ in LiTi₂O₄. Given the results obtained from the chemical corrosion test (see chapter 4), the products of the oxidation of the materials are likely to be TiO₂ in one of its forms. The oxidation would then follow the half-reaction:



Integration of the anodic peak has been conducted using the approaches described for the analysis of the Cr-spinels CVs (see fig. 5.12). The obtained charges have been

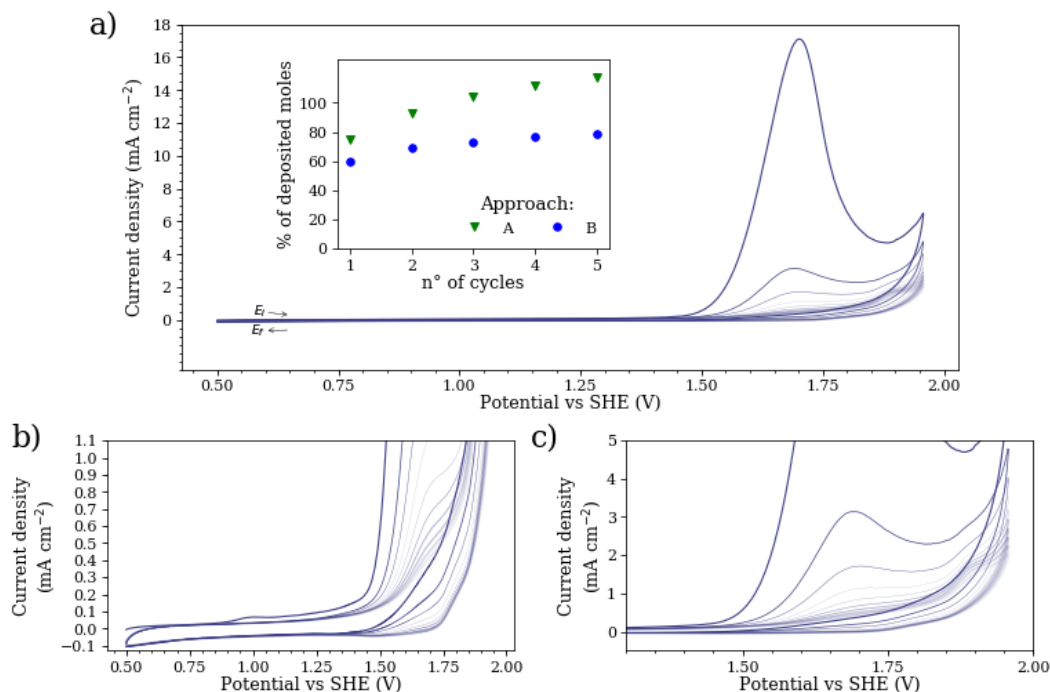


Figure 5.15: a: CV (10 cycles) of LiTi_2O_4 composite electrode on GC disk. b and c: enlargement of the figure a. [DISK:0.5-1.95 V vs SHE, 20 mV sec^{-1} ; RE: Hg/HgSO₄, Ar-saturated 0.5 M H₂SO₄, 1600 rpm].

compared with the total moles of material deposited on the electrode assuming the oxidation mechanism is the one reported in equation 5.6. The results are shown in the inset plot in figure 5.15a. Bearing in mind the possible over- and underestimation related to approach A and B respectively, it can be observed that the total amount of moles extracted from the integration rapidly approaches the total amount of moles of Ti^{3+} present in the material (1 mol Ti^{3+} = 1 mol LiTi_2O_4). Therefore the material proved to undergo oxidation in the potential window applied, the amount of charge related to the anodic peaks observed being consistent with a complete oxidation of the ceramic under study.

5.3 Cell testing

Differently from the Ti-based spinels, the electrochemical characterization of the Cr-based spinels suggested that no complete oxidation of the materials after potential cycling had occurred. Therefore, beside an initial degradation accompanied by partial dissolution of the components of the ceramic, the material could be stable in the conditions of application of a PEMEC and of interest in this study. In order to evaluate the stability of the ceramic material in a real cell application and evaluating the impact of the ceramic material on cell performances, a membrane-electrode assembly (MEA)

was prepared using a mixture of IrO_2 and $\text{MnCu}_{0.25}\text{Cr}_{1.75}\text{O}_4$ on the anode side. The cell was then tested by chronoamperometry followed by EIS measurements at different potentials.

MEA preparation and cell assembling

The cell used for the characterization of the ceramic material was provided by EWII Fuel Cells A/S. In the benchmark cells from EWII Fuel Cells A/S, the anode is loaded with 0.3 mg cm^{-2} IrO_2 catalyst using Nafion as a binder and 2.7 mg cm^{-2} of metallic Ir, again with Nafion binder. A Ti felt is used as current collector. The cathode contains 0.5 mg cm^{-2} Pt supported on carbon, carbon felt is used as current collector. The cell area is approximately 2.9 cm^2

The MEA used for the testing was similar to the benchmark cell by EWII Fuel Cells A/S. The total loading of IrO_2 was kept at 0.3 mg cm^{-2} but the catalyst was loaded as a 1:1 weight ratio of IrO_2 and $\text{MnCu}_{0.25}\text{Cr}_{1.75}\text{O}_4$. No Ir metal was used as a current collector. The polymeric membrane was composed of Nafion[®] 117. The anode and cathode flow plate were made of titanium and carbon respectively. The cell testing set-up and assembling was conducted according to [259] and further details on cell structure and MEA composition can be found there and in [260].

Testing

The electrochemical tests were conducted using the anode as working electrode and the cathode as both reference and counter electrode. Prior to the measurements, the cathode was flushed with humidified H_2 for two hours before the experiments. It is known in the literature that the reactions taking place at the anode side of a PEMEC are comparatively more sluggish than the reactions taking place at the cathode [261], and the contribution to the total polarization resistance of a PEMEC come from the anode rather than the Pt/ H_2 system at the cathode. Moreover, the cathode flushed with H_2 can be considered to possess a potential close to 0V vs SHE at OCV, since the cathode consists in fact of H_2 gas in equilibrium with Pt in an acidic environment such as the one provided by the membrane and it can be used as both a counter and a reference electrode. This approach has been used before [259]. In the text, when the potential is expressed against the cathode flushed with H_2 it will be expressed as *vs H_2 c.e.*

The temperature of the water supplied to the cell was 70°C . The following measurement steps have been followed:

- i. 2 hours flushing humidified H_2 (cathode)/ N_2 -saturated water (anode)
- ii. Recording of cyclic voltammetry, 50 mV s^{-1} , 5 cycles 0.0-1.7V vs H_2 c.e.
- iii. 1 hour flushing O_2 -saturated water at the anode

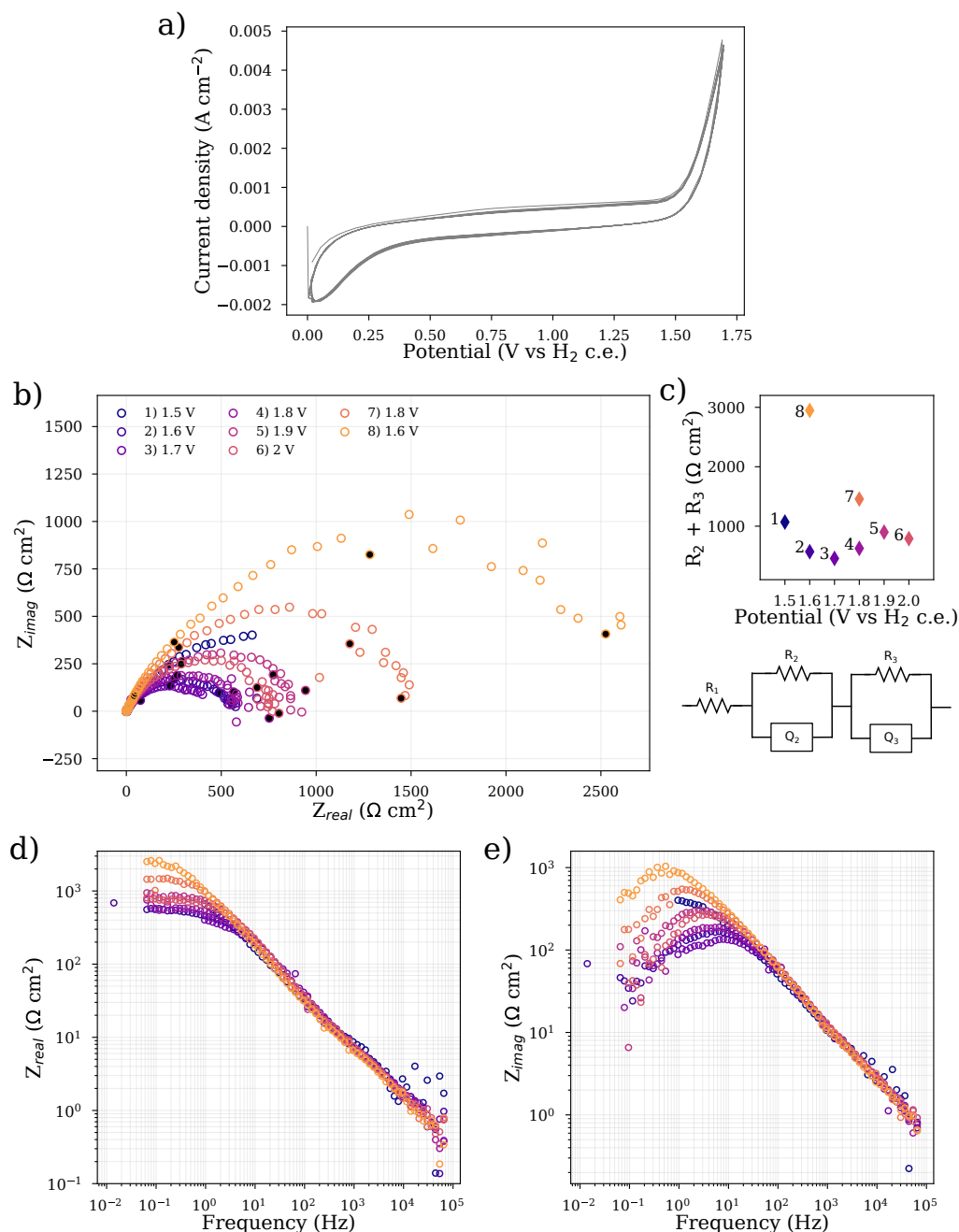


Figure 5.16: *fig. a:* CV (5 cycles) recorded on the MCC-MEA before measuring the EIS spectra; the potential is measured using the counter electrode (cathode) flushed with H₂ as reference electrode (indicated as H₂ c.e. in the plot label); the recorded impedance spectra are reported as Nyquist (b) and Bode plots (d and e). EIS measured at 100 kHz, 10 kHz, 1 kHz, 100 Hz, 10 Hz, 1 Hz and 0.1 Hz is marked with darker signs in each spectrum ; *fig. c:* sum of the resistances obtained by fitting the EIS spectra with a R1-R2Q2-R3Q3 equivalent circuit (also depicted) as a function of the potential applied to the cell. The numbers in the legend indicate the chronological order in which the spectra were recorded.

- iv. Chronoamperometry (10 minutes) followed by EIS measurement (100 kHz-0.1 Hz, 12 points per decade, amplitude: 10 mV): the last step has been repeated for 1.5, 1.6, 1.7, 1.8, 1.9, 2.0, 1.8 and 1.6 V vs H₂ c.e.

The obtained results have been reported in figure 5.16. The current and impedance have been normalized by the geometrical area of the MEA. Figure 5.16a shows the CV recorded on the anode as working electrode. No visible redox peaks can be observed in the CV. The anodic current increases at potentials bigger than 1.50 V, which can be attributed to OER. Approaching to 0 V, the cathodic current can be related to hydrogen adsorption and evolution processes on IrO₂. The latter phenomenon is known in the literature to be related to a significant hysteresis upon cycling [262]. The absence of redox peaks related to IrO_x species and the increased onset potential for OER compared to the benchmark cell [259] can be related to the low conductivity of the material and possibly to a poor contact between the Ti felt current collector and the MEA, since all the components of the cell are unchanged beside the catalyst layer on the anode side. Moreover, the absolute current densities are low compared with the standard cells, a further indication of poor conductivity of the ceramic/catalyst layer.

The EIS spectra were recorded after a potentiostatic current was drawn for 10 minutes, to allow equilibration of the system prior to the EIS measurement. In figure 5.16b,d and e the Nyquist and Bode plots recorded are shown. The numbering in the legend of figure 5.16b refers to the chronological order by which the spectra were acquired. The EIS spectra were fitted using Elchemea Analytical [263]. Using the equivalent circuit

Table 5.1: Results of the fitting of the EIS spectra displayed in figure 5.16; the equivalent circuit used was R_1 - R_2Q_2 - R_3Q_3 . C_{eff} has been calculated according to equation 2.14 (p. 25)

V	R_1 (Ωcm^2)	R_2 (Ωcm^2)	Q_2 ($\text{Fs}^{n-1}\text{cm}^{-2}$)	n_2	C_2 (Fcm^{-2})
1.5	0.1	188.5	0.00034	0.7	0.00967
1.6	0.13	392.08	0.00027	0.69	0.00633
1.7	0.1	158.72	0.00031	0.72	0.01072
1.8	0.1	138.85	0.00035	0.7	0.01012
1.9	0.1	664.1	0.00013	0.8	0.00852
2.0	0.1	173.1	0.00026	1.00	0.09951
1.8	0.1	324.8	0.00030	1.00	0.20834
1.6	0.1	304.79	0.00135	0.71	0.07745

V	R_3 (Ωcm^2)	Q_3 ($\text{Fs}^{n-1}\text{cm}^{-2}$)	n_3	C_3 (Fcm^{-2})
1.5	880.73	0.00019	0.81	0.03039
1.6	178.78	0.00035	0.71	0.00815
1.7	298.41	0.00030	0.68	0.00653
1.8	488.07	0.00021	0.73	0.01363
1.9	236.15	0.00067	0.59	0.00041
2.0	616.83	0.00016	0.69	0.00588
1.8	1131.87	0.00015	0.71	0.00864
1.6	2643.06	0.00017	0.71	0.07337

R_1 - R_2Q_2 - R_3Q_3 gave the best results. Starting with the spectrum at 1.5 V, the total resistance of the cell is much higher than the resistances reported in the literature for EIS studies on PEMECs [259, 264–266]. The total resistance (R_2+R_3) has been plotted in figure 5.16c as a function of the applied potential. The total resistance initially decreases by increasing the potential up to 1.7 V vs H_2 c.e., consistent with an increase in the electrode reaction rate of OER facilitated by the increase in potential. When the potential is further raised, the total resistance increases, with only a slight decrease when the potential reaches 2.0 V. As the potential is then brought back to 1.8 and subsequently to 1.6 V, the total resistance is greatly increased compared with the values recorded previously while increasing the potential.

Comparing the results with the RRDE studies (see for example figures 5.7 and 5.8), it can be noted that the potentials applied to the cell are higher than the ones where oxidation of the ceramic material starts to appear. Therefore, partial dissolution/oxidation of the ceramic material can be expected. The presence of the ceramic also severely affects the performances of the IrO_2 catalyst, increasing the onset potential for the OER and increasing the overall cell resistance. The fact that the cell resistance increases irreversibly after the potential applied to the cell becomes greater than 1.7 V may suggest that the degradation of the ceramic material is accompanied by the formation of more insulating phases. The formation of such insulating phases could also explain the only partial oxidation of the ceramic material and its inertness after few potential cycles, as it appeared in the RRDE studies. Another explanation for the increase in total cell resistance could be that a partial dissolution of the material could have led to an even poorer electrical contact compared with the initial performances of the MEA.

CHAPTER 6

General discussion, conclusion and outlooks

This work is an exploratory investigation of a series of oxide materials with different structure and elemental composition. The first stage of the process was the preparation and structural characterization of the materials, followed by chemical corrosion test of those materials. This study also performed some electrochemical characterization the Ti felt, which is used in PEMEC cells. Electrochemical characterization of NiCr_2O_4 , $\text{MnCu}_{0.25}\text{Cr}_{1.75}\text{O}_4$ and LiTi_2O_4 was conducted. A preliminary cell test of a ceramic-containing PEM electrolysis cell was also performed.

Here, the main conclusions and outlooks are presented, together with some considerations. The results of the different studies are grouped after the various classes of materials, that were objects of this work.

The system $\text{Bi}_2\text{O}_3 - \text{SnO}_2$ does not form a solid solution even at very low content of Bi. The preparation method definitely affects the output material and probably 'softer' methods with a better mixing of the starting reactants (e.g. hydrothermal synthesis) could help in obtaining a partial dissolution of Bi_2O_3 in SnO_2 . That said, it is possible that the big ionic size of Bi^{3+} together with the formation of the pyrochlore phase $\text{Bi}_2\text{Sn}_2\text{O}_7$ could be the reason why the attempt to dope SnO_2 with Bi was unsuccessful. Nevertheless, the presence of the secondary phase affects the conductivity properties of the composite material. An hypothesis is made that the segregation of the secondary phase takes place at the grain boundaries of the SnO_2 and then the conduction through the grain boundaries becomes the rate determining step of the conduction process. This hypothesis is corroborated by the similar activation energies obtained for the samples with higher contents of Bi and the sample of $\text{Bi}_2\text{Sn}_2\text{O}_7$.

p-type SnO_2 would be a novelty in the application and new synthetic strategies and new dopants should be attempted SnO_2 is a very attractive material for the application in PEMECs, given its very good stability toward dissolution and market availability. The material is an insulator and needs to be doped in order to achieve acceptable conductivity. While the successful preparation of conductive derivatives of SnO_2 is widely reported, it is still not completely clear how the doped material behaves when exposed to a corrosive environment or when the material is polarized. The literature reports indications that dopant and Sn do not dissolve congruently, with a preferential leaching of the dopant. These phenomena should be studied and understood before SnO_2 -based materials can find a wide application

LiTi_2O_4 , MgTi_2O_4 and MnTi_2O_4 spinels, prepared by solid state synthesis in reducing

atmosphere, have high ($10\text{-}100\text{ S cm}^{-1}$) at the temperatures of interest for PEMEC technology. The synthesis of LiTi_2O_4 seemed to benefit from an excess of Ti^{3+} , delivering less secondary oxidised phases. Despite the excellent electrical properties, the materials are unstable and undergo dissolution/oxidation in acid aqueous environment. The weight loss of different spinel titanates indicates that the dissolution modes of these materials are independent from the counter-ion present in the structure together with Ti. A chemical dissolution route is proposed: the spinels are oxidised by the protons/nitrate ions in the solution, which leaves as H_2/N_2 , while the material leaches the counter ion and forms the main product of such degradation, TiO_2 , common to all the tested spinels in the form of both rutile and anatase. The degradation leaves also residual spinel phases after oxidation; such phases are consistent with oxidized end members of solid solutions where the starting spinel is the reduced end-member.

Despite the instability observed in the case of the Ti-spinels toward dissolution/oxidation, the origin of such instability is not necessarily related to the sole presence of Ti^{3+} . In fact, after the corrosion test it could be observed that while the main spinel structure essentially disappeared, Ti_2O_3 residues from the synthesis procedure could be observed as one of the residual phase. This fact suggests that the instability of such compounds could be strongly related to the structure of the ceramic itself. Given the electrical performances of the Ti^{3+} -containing compounds (Ti_2O_3 is already a much better electrical conductor than TiO_2), further investigation on these materials (e.g. doped- Ti_2O_3) could be of relevance. Yet, the fact that TiO_2 is the product of the dissolution of these compounds is a further proof of its ultimate stability. This material does not form any soluble species in solution and does not dissolve even under high-currents of OER. Attempts of increasing its conductivity to an acceptable level should be object of great attention.

Several Cr-based spinel structure were prepared and studied. The materials appear very stable in the conditions of interest, but their conductivity is too low. Even one of the most conducting spinels studied in this work, $\text{MnCu}_{0.25}\text{Cr}_{1.75}\text{O}_4$, when applied in a real PEMEC cell led to unacceptable cell resistances.

The preparation of Cu- and Li- doped compounds was attempted in the case of NiCr_2O_4 and MnCr_2O_4 , to further increase the conductivity. While NiCr_2O_4 did not produce pure phase materials, $\text{MnCu}_{0.25}\text{Cr}_{1.75}\text{O}_4$, $\text{MnCu}_{0.5}\text{Cr}_{1.5}\text{O}_4$, $\text{MnLi}_{0.25}\text{Cr}_{1.75}\text{O}_4$ and $\text{MnLi}_{0.5}\text{Cr}_{1.5}\text{O}_4$ where successfully prepared as single phase spinels. MnCr_2O_4 showed the most interesting properties among the studied spinels, specifically for its ability to incorporate dopants. The incorporation of dopants in the MnCr_2O_4 lattice is accompanied by an oxidation of Mn^{2+} to Mn^{3+} . Substitution of Cr with Cu enhanced both the conductivity and the stability to corrosion. Higher contents of Cu substitution could follow the same trend: for example, a compound as MnCuCrO_4 could be envisaged. Based on the results reported, whether the material would assume normal or inverse spinel structure would have profound impact on the electrical and stability properties of the material, and should be further investigated.

The electrochemical characterization of spinels indicated that the materials undergo only partial oxidation upon potential cycling. This can be interpreted as a proof of sta-

bility, but could also implicate the 'passivation' of the materials to redox inactive materials. It should be said that the fact that the integrated charge corresponded to a lower amount of material compared with the one deposited on the electrode does not constitute a definitive proof of the its stability.

Even if the elemental composition, investigated after the electrochemical test, was found not to be very different from the starting composition, the nature and structure of the resulting undissolved products were not determined and they could be constituted of one or more phases, different from the original one. The formation of more electrical insulating phases could be the reason why the material did not show anodic activity after the first cycle of the cyclic voltammetry experiment. Also, the phenomenon could be caused by loss of electrical contact caused by oxidation of the conductive matrix, i.e. graphite, at high potentials, but such effect was not noticed in the case of the electrochemical test of LiTi_2O_4 . The characterization of materials at high potentials in water presents many side-problems. Nevertheless, determining the origin of the loss of redox activity is extremely important if the stability is to be assessed.

As a general remark, the results clearly reminded that the *chemistry* of the species involved in the equilibria of ceramic materials with water must be taken in account while evaluating the stability such of materials under polarization in aqueous environment , e.g. the equilibrium $\text{Cr}^{3+}-\text{HCrO}_4^-$ significantly affects the dissolution of chromites when a potential is applied.

Moreover, the applied potential can have profound implications on the electrical properties of a ceramic material. Above all, the phenomenon of resistance-switching which is at the base of memristors is caused by a chemical modification observed under extreme polarization. Even in milder conditions such effects can play a role: Binninger *et al.* [267] studied the effect of the applied potential on SnO_2 -supported Pt, and observed that the potential was determining the electrical properties of the ceramic material, with important implications on the stability of the supported catalyst.

My conclusion is that in spite of the fact that no acceptable metal oxide based on abundant inexpensive metals was identified, it seems that the results still give hope for finding such a stable and acceptably conductive metal oxide through more work of the kind described in the present thesis

Bibliography

- [1] Directive 2009/28/EC, tech. rep., **2009**.
- [2] News release 17/2018 - Renewable energy in the EU, tech. rep., Eurostat Press Office.
- [3] Renewables 2018: Global Status Report, tech. rep., REN21, **2018**.
- [4] IRENA - International Renewable Energy Agency, www.irena.org.
- [5] Next Generation Wind and Solar Power Next Generation Wind and Solar Power: From cost to value, tech. rep., International Energy Agency, **2016**.
- [6] Balancing responsibility of wind power plants, tech. rep. September, European Wind Energy Association, **2015**.
- [7] T. M. Gür, *Energy & Environmental Science* **2018**, DOI 10.1039/C8EE01419A.
- [8] Electricity storage and renewables: Costs and markets to 2030, tech. rep. October, International Renewable Energy Agency (IRENA), **2017**, p. 132.
- [9] M. Aneke, M. Wang, *Applied Energy* **2016**, 179, 350-377.
- [10] H. Wendt, H. Vogt, G. Kreysa, H. Goldacker, K. Jütner, U. Galla, H. Schmeider in *Ullmann's Encyclopedia of Industrial Chemistry*, 1, **2012**, pp. 76-146.
- [11] W. Frank, W. Haupin, H. Vogt, M. Bruno, J. Thonstad, R. Dawless, H. Kvande, O. Taiwo in *Ullman's Encyclopedia of Industrial Chemistry, Vol. 2*, **2012**, pp. 483-519.
- [12] The Potential of Power-To-Gas, tech. rep. 0, ENEA Consulting, **2016**, p. 51.
- [13] R. Francke, B. Schille, M. Roemelt, Homogeneously Catalyzed Electroreduction of Carbon Dioxide - Methods, Mechanisms, and Catalysts, **May 2018**.
- [14] A. R. Singh, B. A. Rohr, J. A. Schwalbe, M. Cargnello, K. Chan, T. F. Jaramillo, I. Chorkendorff, J. K. Nørskov, Electrochemical Ammonia Synthesis - The Selectivity Challenge, **January 2017**.
- [15] *CRC Handbook of Chemistry and Physics*, 99th Editi, Taylor & Francis Group.
- [16] R. L. LeRoy, *Journal of The Electrochemical Society* **1980**, 127, 1954.
- [17] A. Buttler, H. Spliethoff, Current status of water electrolysis for energy storage, grid balancing and sector coupling via power-to-gas and power-to-liquids: A review, **February 2018**.
- [18] J. E. O'Brien, *Proceedings of American Society of Mechanical Engineers* **2008**, 8, 639-651.
- [19] A. J. Bard, L. R. Faulkner, *Electrochemical Methods: Fundamentals and Applications*, John Wiley & Sons Inc, **2001**.
- [20] M. Carmo, D. L. Fritz, J. Mergel, D. Stolten, *International Journal of Hydrogen Energy* **2013**, 38, 4901-4934.
- [21] L. Liu, W. Chen, Y. Li, *Journal of Membrane Science* **2016**, 504, 1-9.
- [22] S. Trasatti, *Electrochimica Acta* **November 1984**, 29, 1503-1512.
- [23] N. Danilovic, R. Subbaraman, K. C. Chang, S. H. Chang, Y. J. Kang, J. Snyder, A. P. Paulikas, D. Strmcnik, Y. T. Kim, D. Myers, V. R. Stamenkovic, N. M. Markovic, *Journal of Physical Chemistry Letters* **2014**, 5, 2474-2478.
- [24] L. M. Roen, C. H. Paik, T. D. Jarvi, *Electrochemical and Solid-State Letters* **2004**, 7, A19.
- [25] I. Dincer, C. Acar, *International Journal of Hydrogen Energy* **September 2014**, 40, 11094-11111.

- [26] O. Schmidt, A. Gambhir, I. Staffell, A. Hawkes, J. Nelson, S. Few, *International Journal of Hydrogen Energy* **2017**, *42*, 30470–30492.
- [27] Proton On Site, <https://www.protononsite.com/products-proton-site/m-series>.
- [28] Hydrogenics, <https://www.hydrogenics.com/hydrogen-products-solutions/industrial-hydrogen-generators-by-electrolysis/outdoor-installation/>.
- [29] J. Russell, L. Nuttall, A. Fickett, *American Chemical Society Division of Fuel Chemistry Preprints* **1973**, *18*, 24–40.
- [30] N. Konno, S. Mizuno, H. Nakaji, Y. Ishikawa, *SAE International Journal of Alternative Powertrains* **April 2015**, *4*, 2015-01-1175.
- [31] G. G. Scherer, T. Momose, K. Tomiie, *Journal of The Electrochemical Society* **December 1988**, *135*, 3071.
- [32] G. G. Scherer, Private communication.
- [33] A. Hermann, T. Chaudhuri, P. Spagnol in *International Journal of Hydrogen Energy*, Vol. 30, Pergamon, **September 2005**, pp. 1297–1302.
- [34] H. Tawfik, Y. Hung, D. Mahajan, Metal bipolar plates for PEM fuel cell-A review, **January 2007**.
- [35] S. Lædre, O. E. Kongstein, A. Oedegaard, F. Seland, H. Karoliussen, *International Journal of Hydrogen Energy* **2012**, *37*, 18537–18546.
- [36] J. Healy, C. Hayden, T. Xie, K. Olson, R. Waldo, M. Brundage, H. Gasteiger, J. Abbott, *Fuel Cells* **April 2005**, *5*, 302–308.
- [37] M. Langemann, D. L. Fritz, M. Müller, D. Stolten in *International Journal of Hydrogen Energy*, Vol. 40, Pergamon, **September 2015**, pp. 11385–11391.
- [38] S. G. Bratsch, *Journal of Physical and Chemical Reference Data* **1989**, *18*, 1–21.
- [39] P. C. K. Vesborg, T. F. Jaramillo, *RSC Advances* **2012**, *2*, 7933.
- [40] U. Babic, M. Suermann, F. N. Büchi, L. Gubler, T. J. Schmidt, *Journal of The Electrochemical Society* **2017**, *164*, F387–F399.
- [41] C. P. De Pauli, S. Trasatti, *Journal of Electroanalytical Chemistry* **December 2002**, *538-539*, 145–151.
- [42] E. Oakton, D. Lebedev, M. Povia, D. F. Abbott, E. Fabbri, A. Fedorov, M. Nachttegaal, C. Copéret, T. J. Schmidt, *ACS Catalysis* **2017**, *7*, 2346–2352.
- [43] L. C. Seitz, C. F. Dickens, K. Nishio, Y. Hikita, J. Montoya, A. Doyle, C. Kirk, A. Vojvodic, H. Y. Hwang, J. K. Norskov, T. F. Jaramillo, *Science* **September 2016**, *353*, 1011–1014.
- [44] D. Lebedev, M. Povia, K. Waltar, P. M. Abdala, I. E. Castelli, E. Fabbri, M. V. Blanco, A. Fedorov, C. Copéret, N. Marzari, T. J. Schmidt, *Chemistry of Materials* **2017**, *29*, 5182–5191.
- [45] T. Reier, D. Teschner, T. Lunkenbein, a. Bergmann, S. Selve, R. Kraehnert, R. Schlögl, P. Strasser, *Journal of The Electrochemical Society* **2014**, *161*, F876–F882.
- [46] P. Jovanovič, N. Hodnik, F. Ruiz-Zepeda, I. Arčon, B. Jozinović, M. Zorko, M. Bele, M. Šala, V. S. Šelih, S. Hočevar, M. Gaberšček, *Journal of the American Chemical Society* **2017**, *139*, 12837–12846.
- [47] E. Antolini, E. R. Gonzalez, *Solid State Ionics* **May 2009**, *180*, 746–763.
- [48] J. Polonský, I. M. Petrushina, E. Christensen, K. Bouzek, C. B. Prag, J. E. T. Andersen, N. J. Bjerrum, *International Journal of Hydrogen Energy* **February 2012**, *37*, 2173–2181.
- [49] J. Polonský, P. Mazúr, M. Paidar, E. Christensen, K. Bouzek, *International Journal of Hydrogen Energy* **2014**, *39*, 3072–3078.
- [50] Y. Liu, T. G. Kelly, J. G. Chen, W. E. Mustain, *ACS Catalysis* **2013**, *3*, 1184–1194.
- [51] A. Jorge, I. Dedigama, T. Miller, P. Shearing, D. Brett, P. McMillan, *Nanomaterials* **June 2018**, *8*, 432.
- [52] M.-S. Balogun, W. Qiu, W. Wang, P. Fang, X. Lu, Y. Tong, *J. Mater. Chem. A* **2015**, *3*, 1364–1387.

- [53] M. Messner, D. J. Walczyk, B. G. Palazzo, Z. A. Norris, G. Taylor, J. Carroll, T. X. Pham, J. D. Hettinger, L. Yu, *Journal of The Electrochemical Society* **January 2018**, *165*, H3107–H3114.
- [54] B. Avasarala, P. Haldar, *Electrochimica Acta* **2010**, *55*, 9024–9034.
- [55] S. Zhao, A. Stocks, B. Rasimick, K. More, H. Xu, *Journal of The Electrochemical Society* **January 2018**, *165*, F82–F89.
- [56] W. Hu, S. Chen, Q. Xia, *International Journal of Hydrogen Energy* **April 2014**, *39*, 6967–6976.
- [57] C. Hao, H. Lv, C. Mi, Y. Song, J. Ma, *ACS Sustainable Chemistry and Engineering* **2016**, *4*, 746–756.
- [58] E. Slavcheva, G. Borisov, E. Lefterova, E. Petkucheva, I. Boshnakova, *International Journal of Hydrogen Energy* **2015**, *40*, 11356–11361.
- [59] A. T. Marshall, R. G. Haverkamp, *Electrochimica Acta* **February 2010**, *55*, 1978–1984.
- [60] X. Wu, K. Scott, *International Journal of Hydrogen Energy* **May 2011**, *36*, 5806–5810.
- [61] J. Xu, G. Liu, J. Li, X. Wang, *Electrochimica Acta* **2012**, *59*, 105–112.
- [62] V. Ávila-Vázquez, J. Cesar Cruz, M. Galván-Valencia, J. García-Ledesma, L. G. Arriaga, C. Guzmán, S. M. Durón-Torres, *Journal of Electrochemical Science* **2013**, *8*, 10586–10600.
- [63] M. P. Gurrola, J. Gutiérrez, S. Rivas, M. Guerra-Balcázar, J. Ledesma-García, L. G. Arriaga, *International Journal of Hydrogen Energy* **2014**, *39*, 16763–16770.
- [64] V. K. Puthiyapura, M. Mamlouk, S. Pasupathi, B. G. Pollet, K. Scott, *Journal of Power Sources* **2014**, *269*, 451–460.
- [65] H. S. Oh, H. N. Nong, P. Strasser, *Advanced Functional Materials* **2015**, *25*, 1074–1081.
- [66] Y. Senoo, K. Taniguchi, K. Kakinuma, M. Uchida, H. Uchida, S. Deki, M. Watanabe, *Electrochemistry Communications* **2015**, *51*, 37–40.
- [67] Y. Chino, K. Kakinuma, D. A. Tryk, M. Watanabe, M. Uchida, *Journal of The Electrochemical Society* **2016**, *163*, F97–F105.
- [68] B. Han, M. Risch, S. Belden, S. Lee, D. Bayer, E. Mutoro, Y. Shao-Horn, *Journal of The Electrochemical Society* **July 2018**, *165*, F813–F820.
- [69] S. Geiger, O. Kasian, A. M. Mingers, S. S. Nicley, K. Haenen, K. J. Mayrhofer, S. Cherevko, *ChemSusChem* **2017**, *10*, 4140–4143.
- [70] G. Cognard, G. Ozouf, C. Beauger, G. Berthomé, D. Riassetto, L. Dubau, R. Chattot, M. Chatenet, F. Maillard, *Applied Catalysis B: Environmental* **February 2017**, *201*, 381–390.
- [71] S. Das, V. Jayaraman, *Progress in Materials Science* **2014**, *66*, 112–255.
- [72] L. Yu, Y. Liu, F. Yang, J. Evans, J. A. Rodriguez, P. Liu, *Journal of Physical Chemistry C* **July 2015**, *119*, 16614–16622.
- [73] S. Cherevko, T. Reier, A. R. Zeradjanin, Z. Pawolek, P. Strasser, K. J. Mayrhofer, *Electrochemistry Communications* **2014**, *48*, 81–85.
- [74] S. Cherevko, S. Geiger, O. Kasian, A. Mingers, K. J. Mayrhofer, *Journal of Electroanalytical Chemistry* **2016**, *774*, 102–110.
- [75] S. Siracusano, N. Hodnik, P. Jovanovic, F. Ruiz-Zepeda, M. Šála, V. Baglio, A. S. Aricò, *Nano Energy* **2017**, *40*, 618–632.
- [76] H. S. Oh, H. N. Nong, T. Reier, A. Bergmann, M. Gliech, J. Ferreira De Araujo, E. Willinger, R. Schlögl, D. Teschner, P. Strasser, *Journal of the American Chemical Society* **2016**, *138*, 12552–12563.
- [77] W. Sun, Z. Zhou, W. Q. Zaman, L.-m. Cao, J. Yang, *ACS Applied Materials & Interfaces* **2017**, *9*, 41855–41862.
- [78] J. Zhao, X. Li, G. Cui, X. Sun, *Chemical Communications* **May 2018**, *54*, 5462–5465.
- [79] A. S. Aricò, V. Baglio, N. Briguglio, G. Maggio, S. Siracusano in *Fuel Cells : Data, Facts and Figures*, Wiley-VCH Verlag GmbH & Co. KGaA., Weinheim, Germany, **February 2016**, pp. 343–356.

- [80] Tricor Metals , Inc. , www.tricormetals.com.
- [81] S. Mahabunphachai, Ö. N. Cora, M. Koç, *Journal of Power Sources* **August 2010**, *195*, 5269–5277.
- [82] P. Conradie, D. Dimitrov, G. Oosthuizen in *Procedia CIRP*, Vol. 46, Elsevier, **January 2016**, pp. 412–415.
- [83] M. M. Lohrengel, *Materials Science and Engineering R* **1993**, *11*, 243–294.
- [84] M. Seo, Y. Kurata in *Electrochimica Acta*, Vol. 48, Pergamon, **September 2003**, pp. 3221–3228.
- [85] D. Shih, I. Robertson, H. Birnbaum, *Acta Metallurgica* **January 1988**, *36*, 111–124.
- [86] H. Y. Jung, S. Y. Huang, B. N. Popov, *Journal of Power Sources* **April 2010**, *195*, 1950–1956.
- [87] H. Wang, J. A. Turner, Reviewing metallic PEMFC bipolar plates, **April 2010**.
- [88] M. T. Lin, C. H. Wan, W. Wu in *Thin Solid Films*, Vol. 544, **October 2013**, pp. 162–169.
- [89] T. J. Toops, M. P. Brady, F. Y. Zhang, H. M. Meyer, K. Ayers, A. Roemer, L. Dalton, *Journal of Power Sources* **December 2014**, *272*, 954–960.
- [90] S. Lædre, O. E. Kongstein, A. Oedegaard, H. Karoliussen, F. Seland, *International Journal of Hydrogen Energy* **2017**, *42*, 2713–2723.
- [91] P. Lettenmeier, R. Wang, R. Abouatallah, F. Burggraf, A. S. Gago, K. A. Friedrich, *Journal of The Electrochemical Society* **2016**, *163*, F3119–F3124.
- [92] T. Sugawara, N. Kawashima, T. N. Murakami, *Journal of Power Sources* **March 2011**, *196*, 2615–2620.
- [93] A. S. Gago, S. A. Ansar, B. Saruhan, U. Schulz, P. Lettenmeier, N. A. Cañas, P. Gazdzicki, T. Morawietz, R. Hiesgen, J. Arnold, K. A. Friedrich, *Journal of Power Sources* **2016**, *307*, 815–825.
- [94] C. Rakousky, G. P. Keeley, K. Wippermann, M. Carmo, D. Stolten, *Electrochimica Acta* **2018**, *278*, 324–331.
- [95] H. Ito, T. Maeda, A. Nakano, C. M. Hwang, M. Ishida, A. Kato, T. Yoshida, *International Journal of Hydrogen Energy* **May 2012**, *37*, 7418–7428.
- [96] P. Lettenmeier, R. Wang, R. Abouatallah, S. Helmly, T. Morawietz, R. Hiesgen, S. Kolb, F. Burggraf, J. Kallo, A. S. Gago, K. A. Friedrich, *Electrochimica Acta* **2016**, *210*, 502–511.
- [97] P. Lettenmeier, S. Kolb, N. Sata, A. Fallisch, L. Zielke, S. Thiele, A. S. Gago, K. A. Friedrich, *Energy and Environmental Science* **2017**, *10*, 2521–2533.
- [98] Z. Kang, G. Yang, J. Mo, S. Yu, D. A. Cullen, S. T. Retterer, T. J. Toops, M. P. Brady, G. Bender, B. S. Pivovar, J. B. Green, F. Y. Zhang, *International Journal of Hydrogen Energy* **August 2018**, *43*, 14618–14628.
- [99] B. Talic, S. Molin, K. Wiik, P. V. Hendriksen, H. L. Lein, *Journal of Power Sources* **December 2017**, *372*, 145–156.
- [100] P. Atkins, J. de Paula, *Atkins' Physical Chemistry*, 7th Edition. **2002**, 1149 pp.
- [101] B. Cullity, *Elements of X-ray Diffraction*, 2nd, Addison-Wesley Inc., **1978**.
- [102] H. M. Rietveld, *Acta Crystallographica* **January 1967**, *22*, 151–152.
- [103] H. M. Rietveld, *Journal of Applied Crystallography* **June 1969**, *2*, 65–71.
- [104] J. Rodríguez-Carvajal, *FullProof guide*.
- [105] FullProf Suite Homepage, <https://www.ill.eu/sites/fullprof/index.html>.
- [106] J. O. M. Bockris, A. K. N. Reddy, M. Gamboa-Aldeco, *Modern Electrochemistry Vol. 2A: Fundamentals of Electrode Processes*, Plenum Press, **2002**, p. 817.
- [107] M. E. Orazem, B. Tribollet, *Electrochemical Impedance Spectroscopy*, **2017**.
- [108] B. Hirschorn, M. E. Orazem, B. Tribollet, V. Vivier, I. Frateur, M. Musiani, *Electrochimica Acta* **August 2010**, *55*, 6218–6227.
- [109] M. Schneider, S. Schroth, J. Schilm, A. Michaelis, *Electrochimica Acta* **2009**, *54*, 2663–2671.

- [110] L. Van Der Pauw, *Philips Tech Rev* **1958**, *20*, 220-224.
- [111] L. J. van der Pauw, *Philips Research Reports* **1958**, *13*, 1-11.
- [112] P. Kofstad, *Wiley-Interscience* **1972**, DOI 10.1002/maco.19740251027.
- [113] W. H. Baur, A. A. Khan, *Acta Crystallographica* **1971**, 2133-2139.
- [114] M. Batzill, U. Diebold, *Progress in Surface Science* **2005**, *79*, 47-154.
- [115] A. Posner, A. Perloff, A. Diorio, Inorganic Crystal Structure Database (ICSD), **1958**.
- [116] C. Quijada, J. L. Va, F. Vicent, E. Morallo, D. D. I. Textil, E. P. S. D. Alcoy, U. P. D. Valencia, *Journal of applied electrochemistry* **1998**, *28*, 607-612.
- [117] H.-S. Oh, H. N. Nong, T. Reier, M. Gliech, P. Strasser, *Chemical Science* **2015**, *6*, 3321-3328.
- [118] D. O. Scanlon, G. W. Watson, *Journal of Materials Chemistry* **2012**, *22*, 25236.
- [119] C. Y. Tsay, S. C. Liang, *Journal of Alloys and Compounds* **2015**, *622*, 644-650.
- [120] C. Wei, G. Zhang, Y. Bai, D. Yan, C. Yu, N. Wan, W. Zhang, *Solid State Ionics* **2015**, *272*, 133-137.
- [121] M.-M. Bagheri-Mohagheghi, M. Shokooh-Saremi, *Semiconductor Science and Technology* **2004**, *19*, 764-769.
- [122] C. B. Fitzgerald, M. Venkatesan, A. P. Douvalis, S. Huber, J. M. D. Coey, T. Bakas, *Journal of Applied Physics* **2004**, *95*, 7390-7392.
- [123] D. Smyth, *The Defect Chemistry of Metal Oxides*, Oxford University Press, **2000**.
- [124] W. Göpel, K. Schierbaum, H. D. Wiemhöfer, J. Maier, *Solid State Ionics* **1989**, *32-33*, 440-443.
- [125] H. Peng, J. D. Perkins, S. Lany, *Chemistry of Materials* **2014**, *26*, 4876-4881.
- [126] Q. W. Liu, S. S. Pan, Y. Y. Luo, X. H. Li, G. H. Li, *Journal of Physics D: Applied Physics* **2016**, *49*, DOI 10.1088/0022-3727/49/13/135102.
- [127] C. Rastomjee, R. Dale, R. Schaffer, F. Jones, R. Egdell, G. Georgiadis, M. Lee, T. Tate, L. Cao, *Thin Solid Films* **1996**, *279*, 98-105.
- [128] R. D. Shannon, J. D. Berlein, J. L. Gillson, G. A. Jon, A. W. Sleight, *J. Phys. Chem. Solids* **1980**, *41*, 117-122.
- [129] N. A. Asryan, T. N. Kol, A. S. Alikhanyan, G. D. Nipan, **2002**, *38*, 1141-1147.
- [130] J. I. R. Evans, J. A. K. Howard, J. S. O. Evans, *Journal of Materials Chemistry* **2003**, *13*, 2098-2103.
- [131] L. T. Denisova, Y. F. Kargin, L. A. Irtyugo, V. M. Denisov, *Inorganic Materials* **2015**, *51*, 650-654.
- [132] R. D. Shannon, *Acta Crystallographica Section A* **1976**, *32*, 751-767.
- [133] P. Thompson, D. E. Cox, J. B. Hastings, *Journal of Applied Crystallography* **1987**, *20*, 79-83.
- [134] M. Muraoka, M. Suzuki, Y. Sawada, *Journal of Materials Science* **1998**, *3*, 5621-5624.
- [135] K. E. Sickafus, J. M. Wills, N. W. Grimes, *Journal of the American Ceramic Society* **1999**, *82*, 3279-3292.
- [136] R. J. Hill, J. R. Craig, G. V. Gibbs, *Physics and Chemistry of Minerals* **1979**, *4*, 317-339.
- [137] V. Stevanović, M. D'Avezac, A. Zunger, *Journal of the American Chemical Society* **2011**, *133*, 11649-11654.
- [138] E. Stefan, P. a. Connor, A. K. Azad, J. T. S. Irvine, *J. Mater. Chem. A* **2014**, *2*, 18106-18114.
- [139] E. J. Verwey, P. W. Haayman, F. C. Romeijn, *The Journal of Chemical Physics* **1947**, *15*, 181-187.
- [140] B. A. Wechsler, A. Navrotsky, *Journal of Solid State Chemistry* **November 1984**, *55*, 165-180.
- [141] A. Seko, K. Yuge, F. Oba, A. Kuwabara, I. Tanaka, *Physical Review B - Condensed Matter and Materials Physics* **May 2006**, *73*, 184117.
- [142] A. Seko, F. Oba, I. Tanaka, *Physical Review B - Condensed Matter and Materials Physics* **February 2010**, *81*, 054114.

Bibliography

- [143] H. S. C. O'Neill, A. Navrotsky, *American Mineralogist* **1983**, *68*, 181–194.
- [144] D. Das, S. Ghosh, **April 2017**.
- [145] N. Ponpandian, P. Balaya, A. Narayanasamy, *Journal of Physics: Condensed Matter* **2002**, *14*, 3221–3237.
- [146] K. E. Sickafus, L. Minervini, R. W. Grimes, J. A. Valdez, M. Ishimaru, F. Li, K. J. McClellan, T. Hartmann, *Science* **August 2000**, *289*, 748–751.
- [147] D. M. Ramo, P. D. Bristowe, *Journal of Chemical Physics* **2014**, *141*, DOI 10.1063/1.4893556.
- [148] M. Dekkers, G. Rijnders, D. H. A. Blank, *Applied Physics Letters* **2007**, *90*, 10–13.
- [149] R. Zhang, Q. Yuan, R. Ma, X. Liu, C. Gao, M. Liu, C. L. Jia, H. Wang, *RSC Advances* **April 2017**, *7*, 21926–21932.
- [150] H. Moriwake, I. Tanaka, F. Oba, Y. Koyama, H. Adachi, *Physical Review B* **2002**, *65*, 153103.
- [151] F. W. Poulsen, Methods and Limitations in Defect Chemistry Modelling, Doctoral tThesis, **2007**.
- [152] D. M. Flot, J. T. Irvine, *Solid State Ionics* **November 2000**, *135*, 513–518.
- [153] C. J. Ting, H. Y. Lu, *Journal of the American Ceramic Society* **April 1999**, *82*, 841–848.
- [154] T. R. Paudel, A. Zakutayev, S. Lany, M. D’Avezac, A. Zunger, *Advanced Functional Materials* **2011**, *21*, 4493–4501.
- [155] Y. Shi, P. F. Ndione, L. Y. Lim, D. Sokaras, T. C. Weng, A. R. Nagaraja, A. G. Karydas, J. D. Perkins, T. O. Mason, D. S. Ginley, A. Zunger, M. F. Toney, *Chemistry of Materials* **March 2014**, *26*, 1867–1873.
- [156] G. Anger, J. Halstenberg, K. Hochgeschwender, C. Scherhag, U. Korallus, H. Knopf, P. Schmidt, M. Ohlinger in *Ullmann’s Encyclopedia of Industrial Chemistry*, Wiley-VCH Verlag GmbH & Co. KGaA, Weinheim, Germany, **June 2000**.
- [157] L. V. Morozova, V. P. Popov, *Glass Physics and Chemistry* **2010**, *36*, 86–91.
- [158] A. Petric, H. Ling, *Journal of the American Ceramic Society* **2007**, *90*, 1515–1520.
- [159] Z. Lu, J. Zhu, E. Andrew Payzant, M. P. Paranthaman, *Journal of the American Ceramic Society* **2005**, *88*, 1050–1053.
- [160] E. Stefan, G. Tsekouras, J. T. Irvine, *Advanced Energy Materials* **2013**, *3*, 1454–1462.
- [161] E. Stefan, J. T. S. Irvine, *Journal of Materials Science* **2011**, *46*, 7191–7197.
- [162] E. Stefan, P. a. Connor, J. T. S. Irvine, *Journal of Materials Chemistry A* **2013**, *1*, 8262.
- [163] C. F. Cheng, *CORROSION* **November 1964**, *20*, 341t–349t.
- [164] B. Stellwag, *Corrosion Science* **February 1998**, *40*, 337–370.
- [165] V. A. Kurepin, D. A. Kulik, A. Hiltbold, M. Nicolet, Thermodynamic modelling of Fe-Cr-Ni spinel formation at the light-water reactor conditions, **2002**.
- [166] A. La Fontaine, H. W. Yen, P. J. Felfer, S. P. Ringer, J. M. Cairney, *Scripta Materialia* **2015**, *99*, 1–4.
- [167] Q. Zhao, C. jun Liu, B. kuan Li, M. fa Jiang, *International Journal of Minerals Metallurgy and Materials* **2017**, *24*, 1361–1369.
- [168] H. S. C. O’Neill, W. A. Dollase, *Physics and Chemistry of Minerals* **May 1994**, *20*, 541–555.
- [169] F. Bræstrup, K. K. Hansen, *Journal of Solid State Electrochemistry* **January 2010**, *14*, 157–166.
- [170] O. Crottaz, F. Kubel, H. Schmid, *Journal of Materials Chemistry* **1997**, *7*, 143–146.
- [171] H. Sawada, *Mater. Res. Bull.* **1997**, *32*, 873–878.
- [172] L. Grahl-Madsen, Private communication.
- [173] P. Mohanty, C. J. Sheppard, A. R. Prinsloo, W. D. Roos, L. Olivi, G. Aquilanti, *Journal of Magnetism and Magnetic Materials* **April 2018**, *451*, 20–28.
- [174] K. George, S. Sugunan, *Catalysis Communications* **2008**, *9*, 2149–2153.

- [175] M. S. Hegde, P. Ganguly, *Physical Review B* **1988**, *38*, 4557-4561.
- [176] H. Sawada, *Materials Research Bulletin* **March 1994**, *29*, 239-245.
- [177] S. Sasaki, K. Fujino, Y. Takéuchi, *Proceedings of the Japan Academy. Ser. B: Physical and Biological Sciences* **1979**, *55*, 43-48.
- [178] S. Åsbrink, L. J. Norrby, *Acta Crystallographica Section B Structural Crystallography and Crystal Chemistry* **January 1970**, *26*, 8-15.
- [179] J. B. Goodenough, D. G. Wickham, W. J. Croft, *Journal of Physics and Chemistry of Solids* **January 1958**, *5*, 107-116.
- [180] Y. Ono, K. I. Satoh, T. Nozaki, T. Kajitani, *Japanese Journal of Applied Physics Part 1: Regular Papers and Short Notes and Review Papers* **March 2007**, *46*, 1071-1075.
- [181] L. B. Mccusker, R. B. Von Dreele, D. E. Cox, D. Louër, P. Scardi, *Journal of Applied Crystallography* **February 1999**, *32*, 36-50.
- [182] R. D. Schmidt-Whitley, M. Martinez-Clemente, A. Revcolevschi, *Journal of Crystal Growth* **1974**, *23*, 113-120.
- [183] D. C. Johnston, H. Prakash, W. H. Zachariasen, R. Viswanathan, *Materials Research Bulletin* **July 1973**, *8*, 777-784.
- [184] A. Deschanvres, B. Raveau, Z. Sekkal, *Materials Research Bulletin* **1971**, *6*, 699-704.
- [185] G.-N. Zhu, Y.-G. Wang, Y.-Y. Xia, *Energy & Environmental Science* **April 2012**, *5*, 6652.
- [186] S. Chauque, F. Y. Oliva, A. Visintin, D. Barraco, E. P. Leiva, O. R. Cámara, *Journal of Electroanalytical Chemistry* **August 2017**, *799*, 142-155.
- [187] M. P. Rogge, J. H. Caldwell, D. R. Ingram, C. E. Green, M. J. Geselbracht, T. Siegrist, *Journal of Solid State Chemistry* **December 1998**, *141*, 338-342.
- [188] J. Akimoto, H. Takei, *Journal of Solid State Chemistry* **April 1989**, *79*, 212-217.
- [189] M. J. Geselbracht, A. S. Erickson, M. P. Rogge, J. E. Greedan, R. I. Walton, M. W. Stoltzfus, H. W. Eng, P. M. Woodward, *Journal of Solid State Chemistry* **November 2006**, *179*, 3489-3499.
- [190] T. J. Cogle, C. A. S. Mateus, J. H. Binks, T. S. John, **1991**, *1*, 289-291.
- [191] H. Hohl, C. Kloc, E. Bucher, *Journal of Solid State Chemistry* **1996**, *223*, 216-223.
- [192] T. Sonehara, K. Kato, K. Osaka, M. Takata, T. Katsufuji, *Physical Review B* **2006**, *74*, 104424.
- [193] Y. Huang, Z. Yang, Y. Zhang, *Journal of Magnetism and Magnetic Materials* **2012**, *324*, 2075-2081.
- [194] T. Inukai, T. Murakami, T. Inamura, *Japanese Journal of Applied Physics* **1981**, *20*, L681-L682.
- [195] C. W. Chen, P. A. Chen, C. J. Wei, H. L. Huang, C. J. Jou, Y. L. Wei, H. P. Wang, *Marine Pollution Bulletin* **2016**, 2-6.
- [196] S. H. Hong, S. Åsbrink, *Acta Crystallographica Section B Structural Crystallography and Crystal Chemistry* **October 1982**, *38*, 2570-2576.
- [197] Y. Li, Y. Yang, X. Shu, D. Wan, N. Wei, X. Yu, M. B. Breese, T. Venkatesan, J. M. Xue, Y. Liu, S. Li, T. Wu, J. Chen, *Chemistry of Materials* **July 2018**, *30*, 4383-4392.
- [198] M. R. Harrison, P. P. Edwards, J. B. Goodenough, *Journal of Solid State Chemistry* **1984**, *54*, 136-155.
- [199] A. Lecerf, A. Hardy, *Comptes Rendus Hebdomadaires des Seances de l'Academie des Sciences* **1961**, *252*, 131-133.
- [200] P. M. Lambert, M. R. Harrison, P. P. Edwards, *Journal of Solid State Chemistry* **1988**, *75*, 332-346.
- [201] C. E. Rice, W. R. Robinson, *Materials Research Bulletin* **1976**, *11*, 1355-1359.
- [202] K. Kidoh, K. Tanaka, F. Marumo, H. Takei, *Acta Crystallographica Section B* **1984**, *40*, 329-332.
- [203] I. K. Sedler, A. Feenstra, *Eur. J. Mineral.* **1994**, *6*, 873-885.
- [204] Y. B. Kang, H. G. Lee, *IsIJ International* **2005**, *45*, 1552-1560.

Bibliography

- [205] A. Putnis, *An Introduction to Mineral Science*, Cambridge University Press, Cambridge, **1992**.
- [206] M. Isobe, Y. Ueda, *Journal of Alloys and Compounds* **2004**, 383, 85–88.
- [207] H. D. Zhou, J. B. Goodenough, *Physical Review B - Condensed Matter and Materials Physics* **2005**, 72, 2–6.
- [208] M. Isobe, Y. Ueda, *Journal of the Physical Society of Japan* **2002**, 71, 1848–1851.
- [209] P. Wynblatt, G. S. Rohrer, F. Papillon, *Journal of the European Ceramic Society* **2003**, 23, 2841–2848.
- [210] W. Qu, L. Jian, J. M. Hill, D. G. Ivey, *Journal of Power Sources* **2006**, 153, 114–124.
- [211] R. M. Gabr, M. M. Girgis, A. M. El-Awad, B. M. Abou-Zeid, *Materials Chemistry and Physics* **November 1994**, 39, 53–62.
- [212] S. V. Bangale, S. R. Bamane, *Journal of Materials Science: Materials in Electronics* **January 2013**, 24, 277–281.
- [213] K. De, J. Ghose, K. Murthy, *Journal of Solid State Chemistry* **July 1982**, 43, 261–266.
- [214] D. M. Sherman, *Am. Mineral.* **1984**, 69, 788–799.
- [215] S. Winell, Ö. Amcoff, T. Ericsson, *physica status solidi (b)* **2008**, 245, 1635–1640.
- [216] M. Bobruk, K. Durczak, J. Dąbek, T. Brylewski, *Journal of Materials Engineering and Performance* **April 2017**, 26, 1598–1604.
- [217] B. Gillot, M. Kharroubi, R. Metz, R. Legros, A. Rousset, *Physica Status Solidi (a)* **March 1991**, 124, 317–325.
- [218] K. Lohbeck, H. Haferkorn, W. Fuhrmann, N. Fedtke in *Ullmann's Encyclopedia of Industrial Chemistry*, Vol. 22, **2012**, pp. 223–244.
- [219] D. K. Walanda, *Proceeding of The International Seminar on Chemistry* **2008**, 2008, 180–184.
- [220] T. Inukai, T. Murakami, T. Inamura, *Japanese Journal of Applied Physics* **1981**, 264.
- [221] B. A. Wechsler, R. B. Von Dreele, *Acta Crystallographica Section B* **1989**, 45, 542–549.
- [222] S. S. Pannu, *Journal of Chemical Education* **1984**, 61, 174.
- [223] M. Herranen, J. O. Carlsson, *Corrosion Science* **February 2001**, 43, 365–379.
- [224] R. Torresi, O. Cámara, C. De Pauli, M. Giordano, *Electrochimica Acta* **1987**, 32, 1291–1301.
- [225] S. L. De Assis, S. Wolyneć, I. Costa in *Electrochimica Acta*, Vol. 51, Pergamon, **January 2006**, pp. 1815–1819.
- [226] M. V. Diamanti, F. Bolzoni, M. Ormellese, E. A. Pérez-Rosales, M. P. Pedferri, *Corrosion Engineering Science and Technology* **2010**, 45, 428–434.
- [227] D.-S. Kong, J.-X. Wu, *Journal of The Electrochemical Society* **2008**, 155, C32.
- [228] A. G. Mantzila, M. I. Prodromidis, *Electrochimica Acta* **April 2006**, 51, 3537–3542.
- [229] W. Gruner, J. Kunath, L. N. Kalnishevskaja, J. V. Posokin, K. Z. Brainina, *Electroanalysis* **1993**, 5, 243–250.
- [230] F. Scholz, B. Meyer, *Electrochemical solid state analysis: State of the art*, **January 1994**.
- [231] T. Grygar, F. Marken, U. Schröder, F. Scholz, *Collection of Czechoslovak Chemical Communications* **2002**, 67, 163–208.
- [232] A. Doménech-Carbó, J. Labuda, F. Scholz, *Pure and Applied Chemistry* **2012**, 85, 609–631.
- [233] M. Sander, T. B. Hofstetter, C. A. Gorski, *Environmental Science and Technology* **May 2015**, 49, 5862–5878.
- [234] D. Bauer, M. P. Gaillochet, *Electrochimica Acta* **October 1974**, 19, 597–606.
- [235] T. J. Schmidt, H. A. Gasteiger, G. Stäb, P. Urban, D. Kolb, R. Behm, *Journal of the Electrochemical Society* **1998**, 145, 2354–2358.

- [236] J. Suntivich, H. a. Gasteiger, N. Yabuuchi, Y. Shao-Horn, *Journal of The Electrochemical Society* **2010**, *157*, B1263.
- [237] J. T. Mefford, X. Rong, A. M. Abakumov, W. G. Hardin, S. Dai, A. M. Kolpak, K. P. Johnston, K. J. Stevenson, *Nature communications* **2016**, *7*, 11053.
- [238] L.-F. Wang, C.-C. Ou, K. a. Striebel, J.-S. Chen, *Journal of The Electrochemical Society* **2003**, *150*, A905-A911.
- [239] Y. Garsany, O. a. Baturina, K. E. Swider-Lyons, S. S. Kocha, *Analytical Chemistry* **2010**, *82*, 6321-6328.
- [240] B. Marinho, M. Ghislandi, E. Tkalya, C. E. Koning, G. de With, *Powder Technology* **May 2012**, *221*, 351-358.
- [241] Y. Yi, G. Weinberg, M. Prenzel, M. Greiner, S. Heumann, S. Becker, R. Schlögl, *Catalysis Today* **2017**, *295*, 32-40.
- [242] J. O. Besenhard, H. P. Fritz, The Electrochemistry of Black Carbons, **December 1983**.
- [243] J. O. Besenhard, P. Minderer, M. Bindl, *Synthetic Metals* **December 1989**, *34*, 133-138.
- [244] B. Gurzęda, P. Florczak, M. Kempniński, B. Peplińska, P. Krawczyk, S. Jurga, *Carbon* **April 2016**, *100*, 540-545.
- [245] F. Beck, H. Krohn, *Synthetic Metals* **December 1983**, *7*, 193-199.
- [246] A. B. A. Sedano, M. L. T. García, M. D. V. Barbado, P. S. Batanero, *Journal of Electroanalytical Chemistry* **2004**, *566*, 433-441.
- [247] T. Grygar, S. Bakardjieva, P. Bezdicka, P. Vorm, *Ceramics - Silikaty* **2001**, *45*, 55-61.
- [248] A. J. Bard, R. Parsons, J. Jordan, International Union of Pure and Applied Chemistry., *Standard potentials in aqueous solution*, **1985**, xii, 834 p.
- [249] T. Grygar, P. Bezdicka, *Journal of Solid State Electrochemistry* **1998**, *3*, 31-38.
- [250] E. B. Godunov, A. D. Izotov, I. G. Gorichev, **2017**, *53*, 831-837.
- [251] S. Bakardjieva, P. Bezdicka, T. Grygar, P. Vorm, *Journal of Solid State Electrochemistry* **2000**, *4*, 306-313.
- [252] F. J. Primus, M. D. Goldenberg, S. Hills, PROCESS FOR THE PRODUCTION OF ALKALI PERMANGANATE, **1991**.
- [253] D. Yohe, A. Riga, R. Greef, E. Yeager, *Electrochimica Acta* **1968**, *13*, 1351-1358.
- [254] M. Bonomo, G. Naponiello, D. Dini, *Journal of Electroanalytical Chemistry* **May 2018**, *816*, 205-214.
- [255] R. Supadanaisan, T. Panklang, C. Wanichayanan, A. Kaewkao, T. Nilkamjon, P. Udomsamuthirun, S. Tiyasri, W. Wongphakdee, T. Kruaehong, *Materials Today: Proceedings* **January 2018**, *5*, 14896-14900.
- [256] M. Melník, M. Kabešová, *Journal of Coordination Chemistry* **June 2000**, *50*, 323-338.
- [257] M. Huynh, D. K. Bediako, D. G. Nocera, *Journal of the American Chemical Society* **2014**, *136*, 6002-6010.
- [258] M. Huynh, C. Shi, S. J. L. Billinge, D. G. Nocera, *Journal of the American Chemical Society* **2015**, *137*, 14887-14904.
- [259] K. Elsøe, L. Grahl-Madsen, G. G. Scherer, J. Hjelm, M. B. Mogensen, *Journal of The Electrochemical Society* **2017**, *164*, F1419-F1426.
- [260] K. Elsøe, PhD thesis, Technical University of Denmark, **2018**, p. 127.
- [261] J. Rossmesl, Z. W. Qu, H. Zhu, G. J. Kroes, J. K. Nørskov, *Journal of Electroanalytical Chemistry* **September 2007**, *607*, 83-89.
- [262] J. C. F. Boodts, S. Trasatti, *Journal of Applied Electrochemistry* **March 1989**, *19*, 255-262.
- [263] Koch S., Graves C., Hansen K.V., Elchemea Analytical, <https://www.elchemea.dk>.

Bibliography

- [264] M. Mandal, A. Valls, N. Gangnus, M. Secanell, *Journal of The Electrochemical Society* **May 2018**, *165*, 543-552.
- [265] S. H. Frensch, A. C. Olesen, S. S. Araya, S. K. Kær, *Electrochimica Acta* **February 2018**, *263*, 228-236.
- [266] S. Siracusano, S. Trocino, N. Briguglio, V. Baglio, A. S. Aricò, *Materials* **August 2018**, *11*, 1368.
- [267] T. Binninger, R. Mohamed, A. Patru, K. Waltar, E. Gericke, X. Tuaev, E. Fabbri, P. Levecque, A. Hoell, T. J. Schmidt, *Chemistry of Materials* **April 2017**, *29*, 2831-2843.

APPENDIX **A**

Materials and chemicals

Bi₂O₃	99.9%, Alfa Aesar
Cr(NO₃)₃ · 9 H₂O	98.5%, metal basis, Alfa Aesar
Cr₂O₃	>98%, metal basis, Alfa Aesar
Cu(NO₃)₂ · 2.5H₂O	998-102%, metal basis, Alfa Aesar
ethanol	Ethanol absolute ≥99.8%, VWR
Fe₂O₃	99.9%, metal basis, Alfa Aesar
graphite	>99%, particle size < 20 μm, Fluka
H₂SO₄	95%, trace metal basis, Alfa Aesar
HNO₃	>65%, Merck
lens paper	Assistent
LiCO₃	≥ 99%, Sigma-Aldrich
LiNO₃	99%, metal basis, Alfa Aesar
Mg(OH)₂	95-100.5%, Aldrich
4 MgCO₃ · Mg(OH)₂ · 5 H₂O	Magnesium carbonate hydroxide pentahydrate Sigma Ultra, Sigma Aldrich
MgO	>99.9%, trace metal basis, Alfa Aesar
MnCO₃	>99.9%, metal basis, Sigma Aldrich
MnNO₃ · 4 H₂O	99.9+%, Aldrich
Nafion solution	Nafion [®] 117 ≈5% in a mixture of lower aliphatic alcohols and water
Ni(NO₃)₂ · 6 H₂O	98%, metal basis, Alfa Aesar
NiO	99%, metal basis, Alfa Aesar
2-propanol	anhydrous, 99.5%, Sigma Aldrich
Ti wire	Ø:0.5mm, Purity:99.6+%, Temper:As drawn, GoodFellow
Ti	≥99.5%, max. particle size 150 μm, Good-Fellow
Ti₂O₃	99.9%, 100 mesh, Aldrich
TiO₂	anatase, 99.6% (metal basis), 325 mesh, Alfa Aesar
ZnO	>99.0%, metal basis, Alfa Aesar

APPENDIX B

Ti felt surface area

The specifications of the Ti felt provided by EWII Fuel Cells A/S are reported in table B.1. The estimation of the surface area of the Ti felt were conducted as follows. The density of the felt d_F as calculated as

$$d_f (\text{g cm}^{-3}) = \frac{W_p}{t} \cdot 10^{-4}$$

where W_p is the planar weight and t is the thickness. Assuming a fiber length l of 1 cm (an arbitrary choice, but reasonable given the dimensions of the sample used for the electrochemical characterization) and assuming that the area of the exposed cross sections is small compared to the area belonging to the sides of a fiber, it is possible to estimate the area of a single fiber A_f , its volume V_f and its weight w_f as

$$A_f (\text{cm}^2) = 4sl$$

$$V_f (\text{cm}^3) = s^2l$$

$$w_f (\text{g}) = V_f \cdot d_{Ti}$$

where s is the side width of the squared fiber, l is the length of the fiber and d_{Ti} is the density of Ti.

The number of fibers per unit volume n_f can then be calculated as

$$n_f (\text{cm}^{-3}) = \frac{d_F}{w_f}$$

Assuming the contact points between the fibers are not changing dramatically the total surface area of the fibers, the surface area per gram of Ti felt A_F can be calculated as

$$A_F (\text{m}^2 \text{g}^{-1}) = \frac{n_f A_f}{d_F} \cdot 10^{-4}$$

or expressed as *planar area* A_p , surface area per m^2 of felt

$$A_p (\text{m}^2 \text{m}^{-2}) = A_F W_p$$

Table B.1: Specifications of the Ti felt provided by EWII Fuel Cells A/S.

	Symbol		units
Planar weight	W_p	300	g m^{-2}
Fibre diameter	s	20	μm
Felt thickness	t	0.035	cm
Porosity		81	%

Given the specifications of the Ti felt under analysis, the calculations yielded $A_F = 0.04438 \text{ m}^2 \text{ g}^{-1}$ and $A_p = 13.31 \text{ m}^2 \text{ m}^{-2}$. Given the geometrical area of the felt sample used for the electrochemical characterization ($1.2 \times 0.7 \text{ cm}^2$, shown in fig. 5.1, p. 74), the area A used for normalization was calculated as

$$A = 1.2 \times 0.7 \times A_p = 11.18 \text{ cm}^2$$

In the case of the the samples used for the electrochemical characterization of the felt, the welding with Ti wire was necessary because of the porous morphology of the felt. Preliminary tests were conducted by using an electrode holder equipped with a stainless steel screw where the piece of Ti felt was mounted; even if the electrode holder was placed far out of the surface of the electrolyte, during electrochemical testing the sulfuric acid solution was brought in contact with the stainless steel screw by capillarity due to the porous structure of the felt, resulting in Fe leaching in the solution and failure of the experiment. Consequently, it was attempted to use a thin Pt wire as electrical connection between the electrode holder and the felt. When the solution rose to come in touch with the Pt, the cyclic voltammetry revealed that the signal coming from the Pt wire was more intense than the one coming from Ti, which was obscured. Therefore, it was decided to use a piece of Ti wire as connector between the electrode holder and the felt, since even if the solution would have come in contact with the wire due to capillarity the electrochemical signal would be similar to the one of the felt yet negligible taking in consideration the difference in total surface area between the felt and the portion of the wire in contact with the solution. To avoid any uncertainty regarding how much area was electrochemically active during the experiment, the whole Ti felt was submerged into the solution with only a small portion of the wire in contact with the solution, whose contribution was considered negligible.

Ink formulation trials

Before starting the characterization experiments reported in section 5.2, a series of trials changing ink composition and final material loading were conducted.

Firstly, a suspension of pure ceramic in ethanol was used as ink for the drop casting deposition. Given the poor outcome of such approach, graphite/ceramic suspensions were prepared. As detailed in section 5.2, 5 mg/ml suspension of graphite in 2-propanol and a 5 mg/ml suspension of ceramic material in ethanol were mixed together in different amounts to prepare mixtures with different ceramic/graphite ratios. The comparison between the electrode prepared with a graphite/ceramic ink and a ceramic only ink can be observed in figure C.2a and b in the case of $\text{MnCu}_{0.25}\text{Cr}_{1.75}\text{O}_4$. The electrochemical signal of the ceramic material is greatly enhanced in the case of the composite electrode. The two figures also highlight the role of the Nafion film deposited after the first ink drop deposition in the case of the ceramic/graphite mixture. The cathodic peaks during the n.g.s. were detected only when the Nafion film was casted on the deposited electrode.

Figure C.2c and d compare the effect of increasing total amount of ceramic deposited on the electrode using a ceramic based ink and a ceramic/graphite based ink. In the case of pure ceramic material (fig. C.2c), the linear variation of ceramic mass deposited does not correspond to a corresponding variation of current signal, indicating that not all the material deposited on the electrode is electroactive. On the contrary, in the case of 1:1 ceramic/graphite ink (fig. C.2d) an increase in the amount of material deposited generates an increase in the absolute current, and the signal is accordingly amplified.

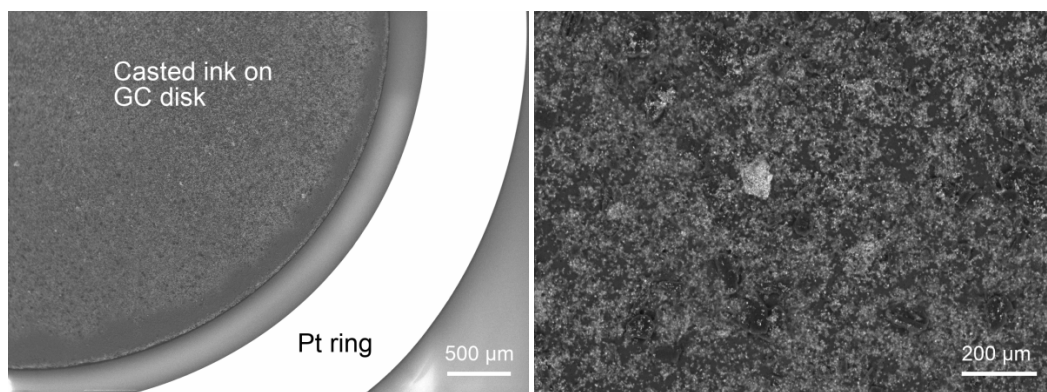


Figure C.1: On the left: image of the as deposited ink on the surface of the RDE. On the right: close-up view of the deposited layer of ceramic/graphite mixture, brighter areas correspond to the ceramic material, while darker areas correspond to graphite; to appreciate the size of graphite grains in the mixture, some of them are highlighted by yellow dashed lines [Hitachi TM3000; acc.volt.: 15 kV].

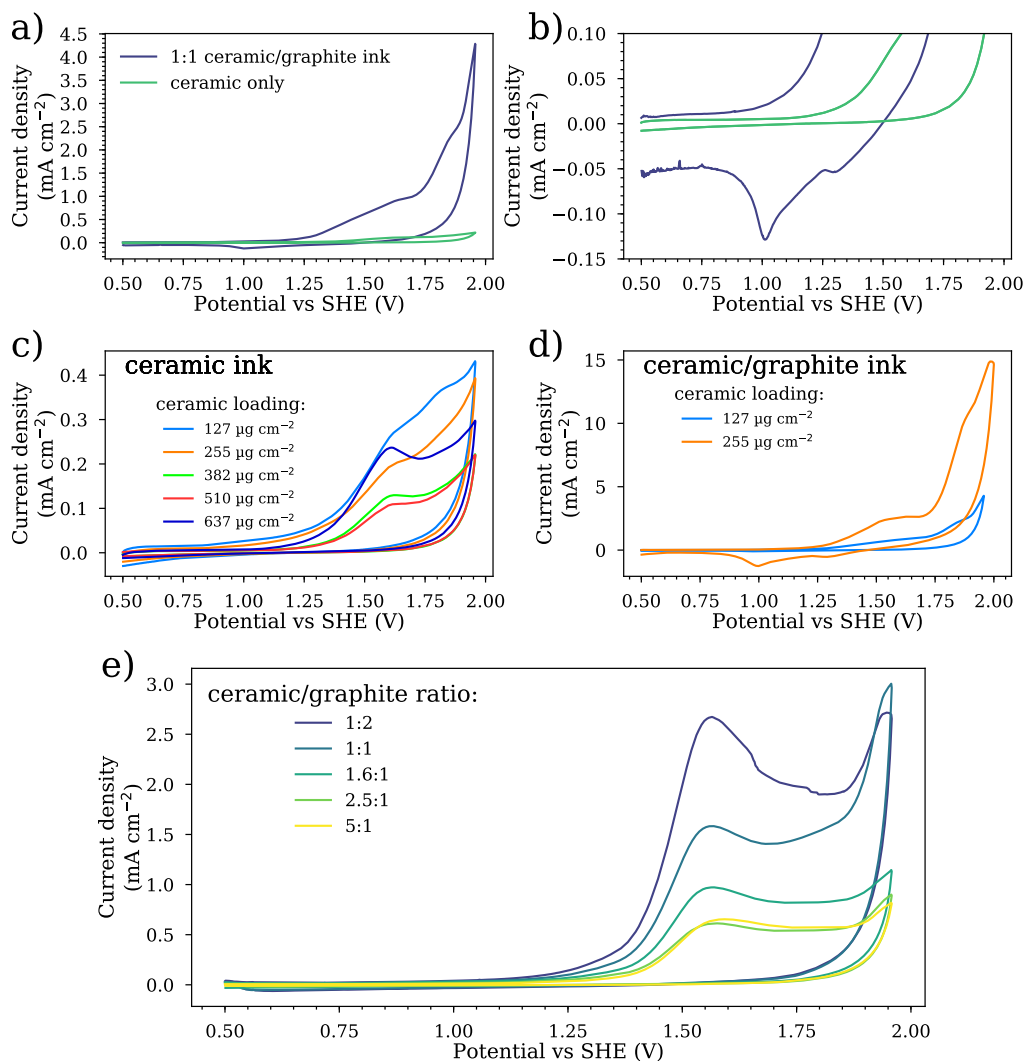


Figure C.2: CV conducted in Ar saturated 0.5 M H₂SO₄, 20 mV sec⁻¹.

Since the overall better electrical contact achieved in the case of the deposition of the ceramic/graphite ink, it is also possible that controlling the ink drying condition is less important to achieve quality and reproducibility, compared to the casting of the ceramic material alone. Figure C.1 shows SEM images collected on the dried ink on the surface of the GC disk of an RDE in the case of MnCu_{0.25}Cr_{1.75}O₄/graphite. The obtained layer shows a good homogeneity, with the exception of an outer band where less material appear to be present and a very narrow 'coffee stain' deposit on the very edge of the disk.

Different ratios of ceramic/graphite used for casting the composite electrode were also attempted. The amount of total ceramic material deposited was kept fixed to 25 µg

(corresponding to $127 \mu\text{g cm}^{-2}$, normalized for the area of the GC carbon disk of the RDE) and different inks were used with different ceramic/graphite ratio. It can be observed that a continuous increase of the total charge of the CV can be observed after the ration passes 2.5:1. Before that, possibly the graphite is not enough to develop a continuous network of electron path throughout the layer. The final choice of using the ratio 1:1 was twofold: beside the higher current output compared to bigger ceramic/graphite ratio, the total volume of deposited material was smaller than for smaller ratios, resulting in more easy casting operations.

APPENDIX D

Publications and contributions

Synthesis and dissolution behaviour of Bi-SnO₂ as a corrosion resistant material for anodic catalyst support in PEM electrolysis cells

F. Fenini, K.K. Hansen, M.B. Mogensen
Fundamentals & Development of Fuel Cells
Stuttgart, 30.01-02.02 2017, *Oral presentation*

Spinel-structured materials as catalyst support/current collector materials for PEM electrolysis cells

F. Fenini, K.K. Hansen, M.B. Mogensen
International Conference on Electrolysis (ICE)
Copenhagen, 12.06-15.06 2017, *Poster presentation*

MCr₂O₄-based spinels as materials for anodic catalyst support in PEM electrolysis cells: boosting the LT conductivity of corrosion stable p-type conductors

F. Fenini, K.K. Hansen, M.B. Mogensen
Solid State Ionics
Padua, 18.06-23.06 2017, *Oral presentation*

Cr- and Ti-Based Spinel as Materials for Anodic Catalyst Support in PEM Electrolysis Cells: Assessing Corrosion Stability and Support Role in Catalyst Activity of Corrosion Stable Ceramics

F. Fenini, K. K. Hansen, C. Savaniu, J. T. S. Irvine, M. B. Mogensen
ECS Transactions, 85 (11) 65-77 (2018)

Cr- and Ti-Based Spinel as Materials for Anodic Catalyst Support in PEM Electrolysis Cells: Assessing Corrosion Stability and Support Role in Catalyst Activity of Corrosion Stable Ceramics

F. Fenini^a, K. K. Hansen^a, C. Savaniu^b, J. T. S. Irvine^b, M. B. Mogensen^a

^a Department of Energy Conversion and Storage, Technical University of Denmark, 4000, Roskilde, Denmark

^b School of Chemistry, University of St. Andrews, Fife, KY16 9ST, UK

This work aims to determine the stability of Cr- and Ti- based spinels as catalyst supports for oxygen evolution reaction (OER) catalyst in PEM electrolyzers (PEMECs). Different compositions of $M\text{Cr}_2\text{O}_4$ ($M=\text{Ni}$, NiFe , Zn , Mg) and MTi_2O_4 (Li , Mg , Mn) have been synthesized by solid state synthesis. Pure and doped Cr-based spinels exhibit low conductivities at the operating temperatures of PEMECs ($<10^{-4}$ S cm^{-1}), while Ti-based spinels showed very high conductivities at room temperature ($\sim 10\text{-}100$ S cm^{-1}). Cr-spinels proved to be very stable to chemical corrosion testing, while Ti-spinels manifested substantial weight loss. The most promising materials (LiTi_2O_4 , MnCr_2O_4 , $\text{Cu-MnCr}_2\text{O}_4$) showed redox activity at potentials >1.5 V vs SHE. LiTi_2O_4 is completely oxidized upon cycling up to 2.0 V vs SHE. Mixtures of IrO_2 /oxide support deposited on glassy carbon were tested toward OER, which showed a 10% higher absolute current at 2.0 V vs SHE in the case of IrO_2 / $\text{Cu-MnCr}_2\text{O}_4$ compared with pure IrO_2 .

Introduction

One of the biggest challenges in Polymer Electrolyte Electrolysis Cells (PEMECs) research is the lack of an inexpensive stable catalyst support for the Oxygen Evolution reaction (OER) catalyst, which to date is IrO_2 (1–3). Carbon black, the typical PEM fuel cell catalyst support, is not stable in the harsh environment present in the anode compartment of a PEMEC (high potential, low pH due to the contact with the Nafion membrane) and oxidizes to CO_2 (4). A particular attention has been given in recent research to the potential use of oxides as corrosion stable materials, such as SnO_2 and TiO_2 (5–10): the common approach is engineering such corrosion resistant material, which are often insulators at the operating temperature of a PEMEC, and then increase the conductivity by doping. It has been proposed that the presence of the support could enhance catalyst stability toward dissolution due to strong catalyst-support interaction (8,9).

Cr-based oxide spinels (CrOS) are known to be extremely stable compounds. In fact, they have been extensively studied as interconnects materials in solid oxide fuel cells (11,12). CrOS have also been reported as corrosion passivating layer on stainless steels (13), and therefore they are excellent candidates for applications where corrosion resistance is required. The larger part of spinels belong to the $Fd3m$ space group, where the anion sublattice forms a cubic close packed arrangement, where 1/8 of the tetrahedral

sites (T_d) and 1/2 of the octahedral sites (O_h) are occupied by cations (14). Spinel structures are often p-type conductors (15). The conduction is enabled by electron transfer between O_h sites: they constitute a 3D network of electrical paths which makes spinel structured materials isotropic electrical conductors. In CrOS, holes move via a hopping-type mechanism which involves the oxidation of Cr^{3+} to Cr^{4+} . The high stability of Cr^{3+} in O_h environment hinders this electron transfer process and CrOS are typically insulators at low temperatures ($<100^\circ C$) (15).

Other compounds with spinel structure may exhibit very high electrical conductivities at low temperature ($<100^\circ C$). In Ti-based oxide spinels (TiOS), with general formula MTi_2O_4 , Ti possess an oxidation state which is between +3 and +3.5 depending on the counter-ion M. These compounds exhibit extremely high conductivities even at room temperature (16–20). For example, $LiTi_2O_4$ is reported to have very high conductivities even at room temperature (10-100 $S\ cm^{-1}$ (21)). $LiTi_2O_4$ has shown a certain degree of surface exchange ability toward protons (22), which could enable a certain degree of proton conductivity on the surface of the support, normally achieved by mixing Nafion as a binder in the catalyst layer.

In this study, several compositions of Cr- and Ti-based spinels have been synthesized and tested toward corrosion: first, a chemical corrosion test has been conducted where the anode environment of a PEMEC has been simulated by a mixture of nitric and sulfuric acid kept at $85^\circ C$, in which the materials were immersed overnight under continuous agitation; then, the best candidates have been deposited on a rotating disk electrode (RDE) and cycled between 0.5 and 2.0 V vs SHE to estimate the electrochemical stability of the materials. The testing procedure highlighted characteristic features of the materials which are compatible with partial or complete oxidation upon cycling of the substrate materials. Preliminary activity test toward OER of oxide/ IrO_2 mixtures show an increase in the absolute current obtained from the same amount of catalyst.

Experimental section

Synthesis and Characterization

MCr_2O_4 : Pure MCr_2O_4 ($M=Mg, Zn, Ni, NiFe$) were synthesized by solid state route. Stoichiometric amounts of the oxides of the starting material (MgO : $>99.9\%$ trace metal basis, Sigma-Aldrich; NiO : 99% metal basis, Alfa Aesar; ZnO : $>99.0\%$, Sigma-Aldrich; Fe_2O_3 : 99.9%, Alfa-Aesar; Cr_2O_3 : $>98\%$, Sigma-Aldrich) were mixed in an agate mortar and then fired in alumina crucibles at $1000^\circ C$ for 10 hours twice. Cu- and Li-doping of $NiCr_2O_4$ and $MnCr_2O_4$ have been attempted using nitrate combustion synthesis (11). Stoichiometric amounts of metal nitrates solutions in de-ionized water (DW) ($LiNO_3$: 99%, Alfa Aesar; $Ni(NO_3)_2 \cdot 6H_2O$: 98%, Alfa Aesar; $Cu(NO_3)_2 \cdot 2.5H_2O$: 98.0-102.0%, Alfa Aesar; $Cr(NO_3)_3 \cdot 9H_2O$: 98.5%, Alfa Aesar) were mixed and stirred at $80^\circ C$ to evaporate water until a viscous residue was formed. The residue was heated at $300^\circ C$ for 5 hours. The product was then crushed and fired in alumina crucibles at $1000^\circ C$ for 10 hours.

MTi_2O_4 ($M=Li, Mg, Mn$): The synthesis of $LiTi_2O_4$ was conducted through a two steps process. Due to the volatility of Li_2O , first step consisted in the preparation of a precursor to be used as a Li source according to equation 1



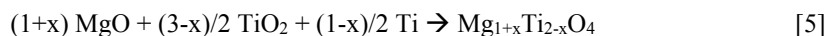
The raw materials (Li_2CO_3 : $\geq 99\%$, Sigma-Aldrich; TiO_2 : anatase, 99.6% metal basis, 325 mesh, Alfa Aesar) were ground in an agate mortar and then fired at 800°C for 8 hours. In the second step, the precursor was mixed with Ti_2O_3 (99.9%, 100 mesh, Aldrich) and TiO_2 according to equation 2



Preliminary XRD analysis of the reagents showed a partial oxidation of Ti_2O_3 to Ti_3O_5 and TiO_2 . The amount of the oxidized phases was determined by semi-quantitative analysis conducted on the XRD pattern (HighScore Plus, PANalytical) and further confirmed by TGA analysis of the raw Ti_2O_3 (TG 209 cell, Netzsch). In order to match the overall oxidation state of Ti_2O_3 , Ti metal powder ($\geq 99.5\%$, max. particle size $150\ \mu\text{m}$, GoodFellow) was added to the reaction mixture according to reaction 3 and 4



The materials were ball milled in acetone in a planetary mill for 45 minutes and pressed into cylindrical pellets with a uniaxial press ($\varnothing\ 8\ \text{mm}$, 2.5 t). The pellets were wrapped in Cu foil (previously sanded) and embedded in powder of the same composition before being fired at 860°C for 16 hours in a flow of $5\%\text{H}_2/\text{Ar}$. MgTi_2O_4 and MnTi_2O_4 were prepared using both a single or a two-step process. Thus, MgTi_2O_4 and MnTi_2O_4 were prepared by a two-step process similar to the one used for LiTi_2O_4 , while $\text{Mg}_{1.4}\text{Ti}_{1.6}\text{O}_4$ and $\text{Mg}_{1.2}\text{Ti}_{1.8}\text{O}_4$ were prepared using a single step process. Briefly, in the two-step process, $4\text{MgCO}_3 \cdot (\text{MgOH})_2 \cdot 5\text{H}_2\text{O}$ (Sigma Ultra, Sigma) and MnCO_3 ($\geq 99.9\%$, Aldrich) were fired together with TiO_2 at 1200°C for 20 hours to obtain MgTiO_3 and MnTiO_3 respectively. The precursors were then mixed with stoichiometric amounts of Ti_2O_3 and Ti to form MgTi_2O_4 and MnTi_2O_4 . For the single step process, $\text{Mg}(\text{OH})_2$ (95-100-5%, Alfa Aesar) was fired at 1000°C for 2 hours to obtain MgO, which was kept at 150°C before being put in a dessicator. Stoichiometric amounts of MgO, TiO_2 and Ti were mixed according to equation 5



with $x=0.2, 0.4$. The mixtures were ball milled in acetone in a planetary mill for 45 minutes and pressed into cylindrical pellets with a uniaxial press ($\varnothing\ 8\ \text{mm}$, 2.5 t). The pellets were wrapped into Mo foil (0.05mm thick, 99.95% metal basis, Alfa Aesar), sealed in evacuated quartz tubes ($\sim 10^{-4}$ mbar) and then fired at 1000°C for 16 hours. Powder XRD experiments were performed on a PANalytical Empyrean (monochromatic $\text{CuK}\alpha 1$) and a Rigaku SmartLab ($\text{CuK}\alpha$) both in Bragg-Brentano configuration. The diffraction patterns have been indexed using WinXPow (STOE, Germany). In the case of the Cr-based spinels, the synthesized powders were pressed into bars using uniaxial pressing (1.5 t, $8 \times 35\ \text{mm}$ mold). The bars were then sintered at 1300°C for 24 hours (1100°C for the doped chromites, with an intermediate step of 1 hour at 700°C). Portions of the bars were mounted into a 4-point measuring set-up using Pt wires ($\varnothing\ 0.1\ \text{mm}$). The temperature of the sample was recorded by placing a thermocouple in direct contact with

it. The extremities of the sample bars were painted with Pt paste (Ferro) in order to guarantee proper electrical contact throughout the conductivity measurement. The paste was sintered in the furnace during ramping up of the temperature ($60\text{ }^{\circ}\text{C h}^{-1}$) and the resistance was measured using a Keithley 2700 Multimeter during the ramping down stage ($30\text{ }^{\circ}\text{C h}^{-1}$) leaving the sample to equilibrate for 1 h at each temperature chosen for measuring the conductivity. The furnace was flushed with a flux of 100 ml min^{-1} of air during the experiments. In the case of Ti-based spinels, disks of $\sim 2\text{ mm}$ thickness were cut from the synthesized pellets for electrical measurements. Electrical connections in Van Der Pauw configuration (23) were made by attaching portions of Ag wire with Ag paste, which was cured at $400\text{ }^{\circ}\text{C}$ for 2 hours in a flux of $5\%\text{H}_2/\text{Ar}$ to avoid oxidation of the samples

Chemical corrosion test: The chemical corrosion test was conducted by immersing weighed amounts of the materials in a mixture 1:1 of $1\text{M H}_2\text{SO}_4$ and 1M HNO_3 kept at $85\text{ }^{\circ}\text{C}$ for 24 hours. The solutions were prepared by diluting concentrated H_2SO_4 (95%, VWR Chemicals) and HNO_3 (>65%, Merck) in DI water. The powder was kept in suspension by continuous stirring. The suspension was then vacuum filtered on previously weighed polyethersulfone filters (pore size: $0.1\text{ }\mu\text{m}$, Sartorius Stedim Biotech), before being dried in an evacuated desiccator overnight. Filter and powder were weighed together and the weight loss due to dissolution was determined as percent difference between the initial and final weight of the powder sample.

Electrodes preparation and electrochemical test: The electrodes were prepared by ink-drop casting. Glassy carbon rotating disk electrode (RDE) (Pine research instrumentation, USA) were polished by subsequently decreasing size of the aluminum oxide powder (Buehler), 1.0, 0.3 and $0.05\text{ }\mu\text{m}$ respectively. The inks were prepared by dispersing two types of mixtures: (i) a 60:40 mixture of the oxide materials and graphite (purity: >99%, particle size $< 20\text{ }\mu\text{m}$, Fluka), to provide good electrical contact throughout the film even in the case of poorly conducting materials; (ii) a 60:40 mixture of the oxide materials and IrO_2 (99.9% metal basis, Aldrich). The mixture was homogenized in an agate mortar and then dispersed in ethanol by sonication to give a suspension of 10 mg ml^{-1} . $20\text{ }\mu\text{l}$ of a 5% Nafion solution (Sigma Aldrich) per ml of solvent were added as binder. Three aliquots of $5\text{ }\mu\text{l}$ of ink where dropped on the RDE disk for a final total loading of $\sim 600\text{ }\mu\text{g cm}^{-2}$.

The electrochemical experiments were conducted in $1\text{M H}_2\text{SO}_4$, deaerated with Ar, using a bipotentiostat (model 760E, CH instruments, USA). A Pt plate was used as counter electrode, while a Hg/HgSO_4 electrode (Radiometer Analytical SAS, France) was

TABLE I. Cell constants a for the compositions under study

Composition	a (Å)	a (Å)(literature)	Reference
LiTi_2O_4	8.4074(1)	8.4033(1)	(24)
MnTi_2O_4	8.6295(6)	8.628	(19)
MgTi_2O_4	8.4997(5)	8.5066(5)	(16)
$\text{Mg}_{1.2}\text{Ti}_{1.8}\text{O}_4$	8.4757(1)	8.49	(25)
$\text{Mg}_{1.4}\text{Ti}_{1.6}\text{O}_4$	8.4727(2)	8.48	(25)
MnCr_2O_4	8.4335(1)	8.43757(1)	(15)
$\text{MnCu}_{0.25}\text{Cr}_{1.75}\text{O}_4$	8.4166(3)		
$\text{MnLi}_{0.25}\text{Cr}_{1.75}\text{O}_4$	8.3833(11)		
$\text{MnLi}_{0.5}\text{Cr}_{1.5}\text{O}_4$	8.3210(10)		

used as a reference electrode. All the potentials are reported vs Standard Hydrogen Electrode (SHE). Two types of cyclic voltammetry (CV) experiments were conducted: (i) a stability test, where the oxide materials were cycled from 0.5 to 2.0 V vs SHE at 20 mV s⁻¹ for 20 cycles; (ii) an activity test, where the mixtures of the oxide materials with IrO₂ were cycled from 1.0 to 2.0 V at 5 mV s⁻¹ for 5 cycles. The same deposition technique was used to compare blank samples with the same loading of graphite and IrO₂ in order to assess the stability and activity test respectively. The disk was rotated at 1600 rpm during the stability test and at 2700 rpm during the activity test.

Results and Discussion

Materials synthesis and characterization

Figure 1 shows the XRD powder pattern collected for some of the samples. All the materials were found to form single phase cubic spinels and main phase in all the materials could be indexed as cubic spinel structures with space group *Fd-3m* (14). In the case of Ti-based spinels, minor secondary phases were also detected, specifically MgTiO₃ (26) and Ti₂O₃ (27).

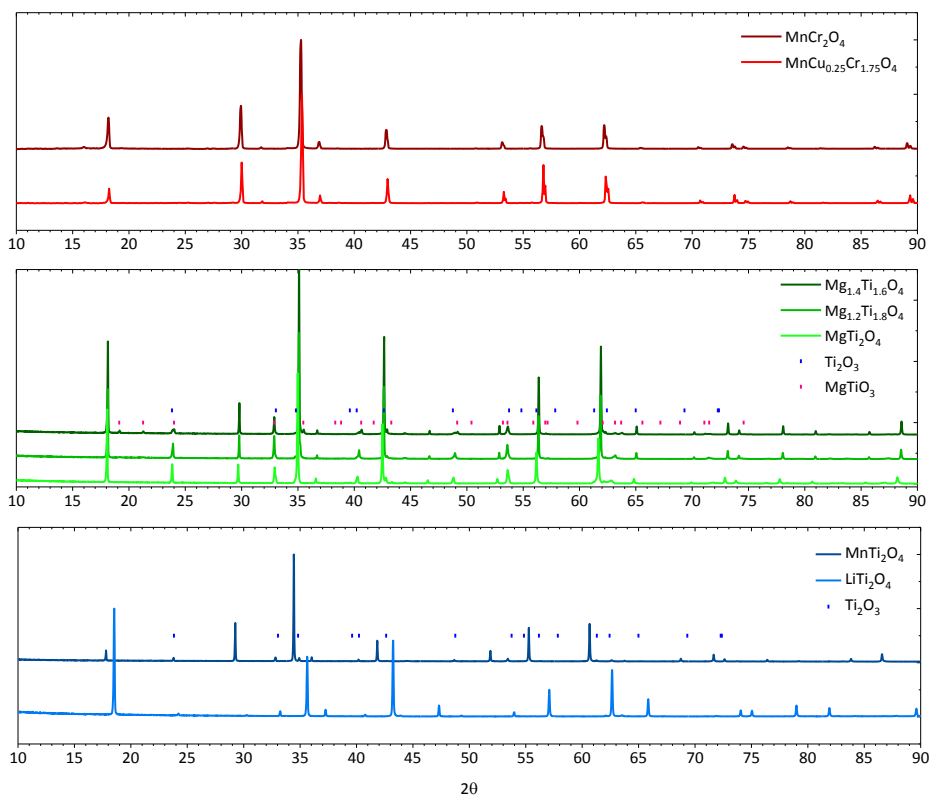


Figure 1: XRD patterns of the materials under study

Beside the incomplete reaction of the starting materials in case of titanates, partial oxidation due to sample handling has been reported (28), which could lead to a surface accumulation of oxidized species as MgTiO_3 or MnTiO_3 . Table I reports the lattice parameter a for the materials analyzed.

The comparison with a values reported in literature shows good agreement. The largest deviation is related to the composition $\text{Mg}_{1.2}\text{Ti}_{1.8}\text{O}_4$. In fact, the system $\text{Mg}_{1+x}\text{Ti}_{2-x}\text{O}_4$ forms a solid solution for every value of x (25,29) and a deviation from the stoichiometry of reagent mixture can be due to the preparation procedure and thermal history.

Cu- and Li- doping of NiCr_2O_4 attempts failed to produce a single phase material and were not investigated further. $\text{MnLi}_x\text{Cr}_{2-x}\text{O}_4$ show a decrease in the cell parameter, as previously reported in the case of Li-doped MnCr_2O_4 (30). In the case of $\text{MnCu}_{0.25}\text{Cr}_{1.75}\text{O}_4$, the substitution of Cr^{3+} by Cu^{2+} should lead to an expansion of the crystal cell, due to the difference in crystal radius (0.755 and 0.87 Å respectively (31)), while the experimental value obtained by indexing shows a contraction of the cell. If it is assumed that all the Cu occupies only T_d sites, and Mn^{2+} occupies the vacant O_h , then the average crystal radius of the T_d site decreases more than the increase of the radius on the O_h site (-2.8% and +0.9% respectively, compared to the ideal MnCr_2O_4), since Cu^{2+} is smaller than Mn^{2+} in the T_d site (0.71 and 0.8 Å respectively). If the crystal field stabilization energy (CFSE) for O_h sites is considered (15), the stabilization energy due to the six-fold anion coordination is 0 and $-0.6\Delta_o$ for Mn^{2+} and Cu^{2+} respectively (where Δ_o is the crystal field splitting parameter, the resulting split of d orbitals due to the ligand field), while it is equal to $-0.6\Delta_o$ for both Mn^{3+} and Cu^{2+} , the synthesis procedure

TABLE II. Activation energies for conductivity of the Cr-based and Ti-based spinels

Composition	E_a (eV) ⁺⁺	Log Cond @ 70 °C (S cm ⁻¹)
LiTi_2O_4	-	~2
MnTi_2O_4	0.03	0.91
MgTi_2O_4	0.07	1.46
ZnCr_2O_4	0.47	-5.44*
MgCr_2O_4	0.48	-5.76*
NiFeCrO_4	0.26	-1.92
NiCr_2O_4	0.34	-2.70
MnCr_2O_4	1.05	-11.2*
$\text{MnCu}_{0.25}\text{Cr}_{1.75}\text{O}_4$	0.48	-4.35*
$\text{MnLi}_{0.25}\text{Cr}_{1.75}\text{O}_4$	0.97	-9.18*
$\text{MnLi}_{0.5}\text{Cr}_{1.5}\text{O}_4$	0.92	-8.40*

⁺⁺evaluated as $\ln(\sigma T)$ vs $1/T$ (40)

*=extrapolated

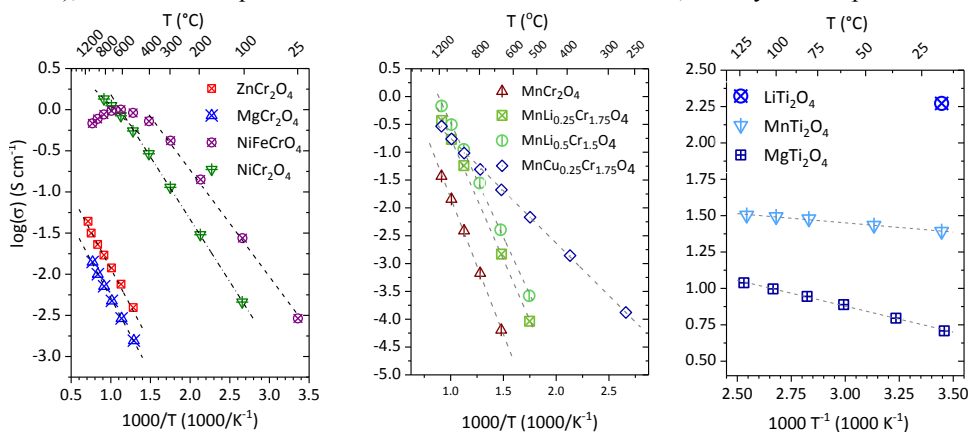


Figure 2: Arrhenius plots for the spinels at different temperatures. In the case of the chromites, conductivity was measured on bars with a 4-probe configuration, in the case of titanates, Van Der Pauw configuration on disks was used.

probably produced an oxidation of Mn^{2+} to Mn^{3+} . In that case, the preference of Mn for the O_h site compared to Cu (higher charge) would be explained as this would cause a reduction of both the T_d and O_h average radii (-2.8% and -0.5% respectively).

The conductivity measurements were performed in different ranges of temperature depending on the overall conductivity of the materials. Figure 2 shows Arrhenius plots obtained from the conductivity data. The activation energies obtained from the fitting of the Arrhenius plots are reported in Table II.

Pure Cr-based spinels show very low conductivities at low temperature (R.T.-100°C). The bending of the Arrhenius plots for $NiCr_2O_4$ and $NiFeCrO_4$ can be related to the resistance going from grain boundary to bulk domination (15), with $NiFeCrO_4$ switching to a metallic-like conduction at $T > 600^\circ C$. The overall decrease in activation energy follows the increase in degree of inversion of chromite spinels, $Mg \approx Zn < Ni < NiFe$ (32–34). The doped $MnCr_2O_4$ show all an increase in conductivity compared with the pure spinel. In the Li-doped samples, the contraction of the crystal cell causes a decrease in the Cr-Cr distances, facilitating the hopping process. In the case of Cu doping, the presence of ions different from Cr in the O_h sites causes a reduction of the activation energy; the effect of Mn in O_h sites on conductivity of Cr-based spinels has been reported (35,36). Overall, the absolute conductivities of the Cr-based spinels under study is low compared with other components of a PEMEC (9). The conductivity of Ti-based spinels is very high even at room temperature, for a ceramic material. The presence of the insulating secondary phases identified in the XRD patterns (Fig. 1) is therefore of negligible influence upon the conductivity of the composite.

Chemical corrosion test

TABLE III. Mass loss (%) after chemical corrosion test

Composition	Mass loss (%)
$LiTi_2O_4$	4
$MnTi_2O_4$	24
$MgTi_2O_4$	11
$Mg_{1.2}Ti_{1.8}O_4$	15
$MgCr_2O_4$	< 1
$ZnCr_2O_4$	< 1
$NiCr_2O_4$	< 1
$NiFeCrO_4$	< 1
$MnCr_2O_4$	4
$MnCu_{0.25}Cr_{1.75}O_4$	2

The chemical corrosion test showed that $ZnCr_2O_4$, $MgCr_2O_4$, $NiCr_2O_4$ and $NiFeCrO_4$ are extremely resistant to dissolution in the hot acidic-oxidant solution used in the test. The weight loss was below 1%, which was estimated to be the detection limit of the measuring method (see Table III). $MnCr_2O_4$ showed a slightly higher mass loss, compared to the other CrOS. Probably, the presence of Mn^{2+} , which can easily undergo oxidation to higher oxidation states, reduces the overall stability of the materials. Interestingly, the Cu-doped compound showed a weight loss close to half the one of the undoped counterpart. TiOS exhibited globally a low corrosion stability to the chemical test conducted, where $MnTi_2O_4$ and

$Mg_{1+x}Ti_{2-x}O_4$ showed both mass losses larger than 10%. Also $LiTi_2O_4$ showed a certain degree of mass loss, even though of a much lower amount compared with the other titanates.

Electrochemical characterization

The chemical corrosion test showed quite different dissolution behavior between CrOS and TiOS. Among the titanates, $LiTi_2O_4$ was selected as best candidate and further tested. Among the chromites, $MnCr_2O_4$ and $MnCu_{0.25}Cr_{1.75}O_4$ were selected for further

testing in order to study the effect of doping on the stability properties of the materials. During the stability test, all the materials showed redox activity in the potential window under study.

Figure 3 displays the 1st, the 2nd and the 5th cycles. The small boxes show an enlarged view of the low-current part of the CV, away from the OER region. For all the materials, the peaks faded away upon cycling. LiTi_2O_4 showed an intense anodic activity and no cathodic peaks in the potential window studied. Specifically, a clear anodic peak at 1.70 V vs SHE is seen decreasing upon cycling. A pre-wave peak is seen around 1 V in the first cycle. The absence of any reduction peak is a clear sign that the oxidation taking place is irreversible. Only Ti^{3+} can exhibit redox activity. To our knowledge, this study reports the first electrochemical characterization of LiTi_2O_4 in sulfuric acid solution. Therefore, a comparison could be made with standard oxidation potential of solid oxides with the same nominal oxidation state of Ti in LiTi_2O_4 , specifically Ti_2O_3 , as a first approximation.

Taking in consideration solid-to-solid redox chemistry in acidic environment, the test is conducted in close-to-standard conditions (in fact, the activity of solids can be considered unity and the activity of protons is close to the standard state in 0.5 M H_2SO_4).

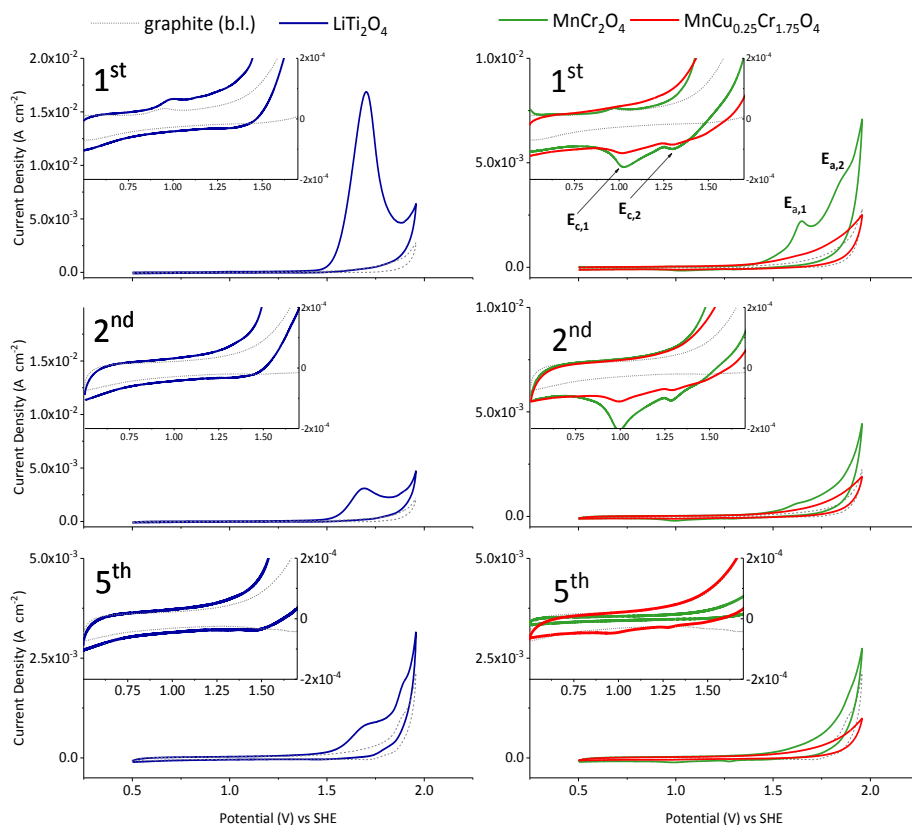


Figure 3: Cyclic voltammetry at different cycles of the materials under study; the dashed line represents the cyclic voltammetry conducted on graphite only, to be used as a baseline (b.l.). 20 mV s^{-1} in 0.5 M H_2SO_4 , 1600 rpm.

In the literature (37), reduction standard potentials of solid Ti_2O_3 are found from around -0.5 to -0.8 V vs SHE depending on the product of oxidation being TiO_2 or Ti_3O_5 and the reactive species and products being in hydrated or anhydrous form. The difference between the measured potential of the peak and standard oxidation potentials is ~ 1.5 V. Even considering a certain degree of hysteresis due to potential sweeping, this result may indicate that a significant overpotential is necessary to carry out the oxidation of Ti^{3+} in LiTi_2O_4 .

MnCr_2O_4 and $\text{MnCu}_{0.25}\text{Cr}_{1.75}\text{O}_4$ showed both anodic and cathodic activity. Anodic peaks can be seen at 1.64 ($E_{1,a}$) and 1.84 V ($E_{2,a}$), while cathodic peaks appear in the negative going sweep at 1.29 ($E_{2,c}$) and 0.99 V ($E_{1,c}$) vs SHE. The peaks are present in both MnCr_2O_4 and $\text{MnCu}_{0.25}\text{Cr}_{1.75}\text{O}_4$; in the latter they appear broader and less intense. In this case, identifying the processes that are taking place is complicated by the fact that both Mn and Cr show redox activity in that region of potential (37). If it is assumed that the cathodic and anodic peaks belong to the same reversible redox processes, the difference $\Delta E = E_a - E_c$ gives $\Delta E_1 = 65$ mV and $\Delta E_2 = 55$ mV, which is close to 59 mV, the difference in redox peaks of reversible mono-electronic processes (38).

In order to estimate the extent of the oxidation experienced by the materials under study upon cycling, the current peaks have been integrated as a function of time. The obtained charge was converted to moles of electrons and then plotted as a function of the number of CV cycles. The results of this procedure are plotted in figure 4a. The dashed horizontal lines correspond to the moles of each material calculated from the mass of material deposited by ink-drop casting on the RDE. When anodic and cathodic peaks were present in the CVs, the total charge used to calculate the moles was estimated as difference of the absolute values of the integration of anodic and cathodic peaks. In all the cases studied, when redox peaks were present, the total current signal was not simply the addition of the area of the peaks and the blank experiments conducted on

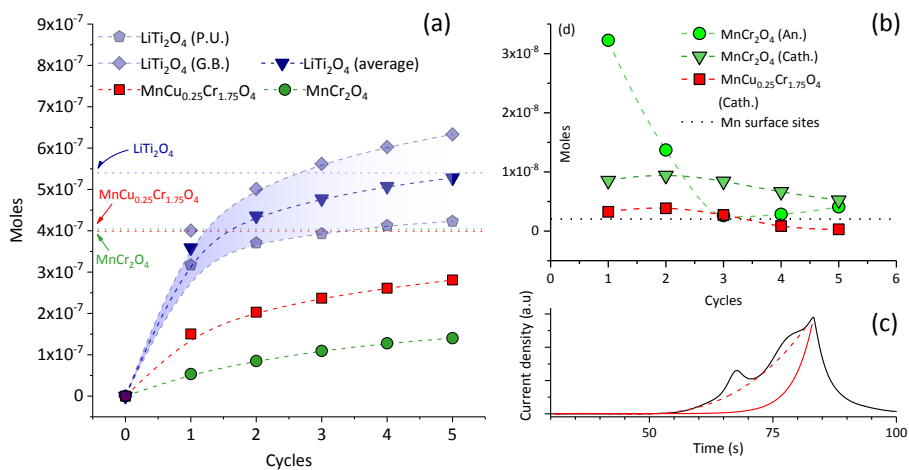
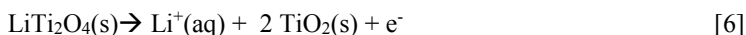


Figure 4: (a) Cumulative charge evolution as a function of cycles number expressed as moles of electrons (P.U. = peak undercutting; G.B. = graphite blank; see text for description); (b) moles of electrons per cycle obtained from integrated areas of cathodic current peaks; (c) example of current vs time plots to show the two baseline models used for integration of redox peaks: dashed line indicate the peak undercutting approach, solid line is the current vs time of the blank experiment conducted with only graphite.

graphite only, especially at potentials > 1.5 V. This effect can be observed in figure 4c, which also tells the two approaches used for measuring the integration area of the redox peaks: the dashed line shows the peak undercutting performed by fitting the curve points which could be considered not strictly part of the peak; the solid line is the current signal at the same cycle of the blank experiment conducted with only graphite. The two methods probably constitute an over-estimation and an under-estimation of the real peak area, respectively. If not otherwise stated, the cumulative charge is plotted as average of the results obtained with the two methods. In figure 4a the results from the two approaches are seen for LiTi_2O_4 (where P.U. stands for peak undercutting approach and G.B. for graphite blank). It can be seen how for all the materials, the cumulative moles obtained from charge approaches a plateau after a few cycles. In the case of LiTi_2O_4 , after a few cycles the number of moles approaches the total amount of material deposited. Since the moles of LiTi_2O_4 are equal to the moles of Ti^{3+} (the only species which can get oxidized), this result shows that LiTi_2O_4 undergoes complete oxidation. A possible oxidation mechanism could be the half-reaction reported in equation 6



The latter equation has to be seen as an interpretation tool for the reader to help visualizing the results, since *stricto sensu* no evidence of TiO_2 formation neither of Li^+

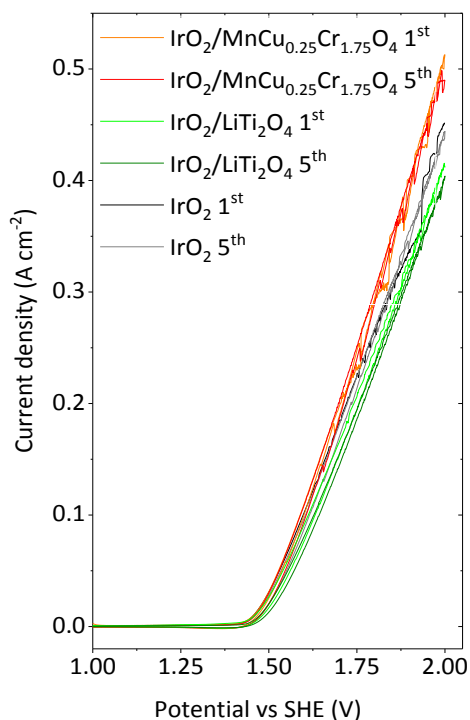


Figure 5: Activity test conducted on different mixtures $\text{IrO}_2/\text{oxide support}$ and pure IrO_2 ; cyclic voltammetry, 5 mV s^{-1} in $0.5 \text{ M H}_2\text{SO}_4$, 2700 rpm.

dissolution have been acquired. Other species than TiO_2 can be the oxidation product of the material. Nevertheless, the products of the oxidation of this compound are insulating materials (28,39).

In the case of MnCr_2O_4 and $\text{MnCu}_{0.25}\text{Cr}_{1.75}\text{O}_4$, the charge appear to approach a plateau before reaching the number of moles deposited on the electrode. It has to be noted that the charge in figure 4a is the sum of the integration of the two peaks seen in the CVs; if we consider the peaks as due to mono-electronic processes happening on the same sites, the corresponding number of moles of atomic species which generate the signal would then be lower than the moles estimated from the total integrated charge since the same species undergoes multiple redox processes. If for example the redox peaks are due to the succession of oxidation $\text{Mn}^{2+} \rightarrow \text{Mn}^{3+} + \text{e}^- \rightarrow \text{Mn}^{4+} + \text{e}^-$, the moles of reacting Mn species would be half the moles of electrons leaving the material overall. Assessing if the two processes are due

to multiple oxidation of the same species and sites or mono-electronic oxidation of the same species in different sites or locations (for example, surface sites vs bulk sites, grain boundaries vs bulk sites) can be very important to describe the behavior of the material to the conditions of the test. Interestingly, as previously indicated by the chemical corrosion test, the Cu-doped chromite appears to be more stable than the undoped MnCr_2O_4 , the integrated cumulative charge being around half for the same amount of deposited material position of the anodic and cathodic peaks.

The difference between anodic and cathodic peaks in terms of total charge can be observed in figure 4b. The rate of decrease in intensity of the cathodic peaks is slower compared to the one of the anodic peaks. The dashed line in figure 4b indicates the estimated surface sites of Mn, calculated considering a one-unit-cell thick layer on the surface of $1\ \mu\text{m}$ spheres of the material under study (the average dimension of the particle, $\sim 1\ \mu\text{m}$, was determined by SEM microscopy images, not shown here). As can be seen, while the extent of the oxidation is much bigger than the estimated surface sites, the reduction peaks can be related to a number of moles close to the estimated moles of surface sites. This suggests that the cathodic reaction is limited to the surface of the particles, while the anodic reaction is probably the combination of surface and bulk oxidation, and possibly ions dissolution.

Figure 5 shows the activity test conducted on pure IrO_2 and on mixtures $\text{IrO}_2/\text{MnCu}_{0.25}\text{Cr}_{1.75}\text{O}_4$ and $\text{IrO}_2/\text{LiTi}_2\text{O}_4$. The noisy signal at high potentials is due to bubbles detachment, which were still forming even at high rotation speeds of the electrode (max. rotation speed = 3000 rpm for the RDE used in this study). The onset potential appears to be similar in all the mixtures tested, around 1.40 V. The absolute current density at 2.0 V showed to decrease according to $\text{IrO}_2/\text{MnCu}_{0.25}\text{Cr}_{1.75}\text{O}_4 > \text{IrO}_2 > \text{IrO}_2/\text{LiTi}_2\text{O}_4$, with absolute values of 0.51, 0.45, 0.41 A cm^{-2} respectively. Therefore, the mixture $\text{IrO}_2/\text{MnCu}_{0.25}\text{Cr}_{1.75}\text{O}_4$ showed an absolute current density value close to 10% larger than the same loading of IrO_2 .

Conclusions

The synthesis of Cr- and Ti-based spinels produced cubic spinel oxides, in some cases with minor presence of secondary phases. The doping of MnCr_2O_4 with Cu and Li produced single phase cubic spinels. Chemical corrosion testing indicated that Ti-based spinels are unstable for the application, despite the very good conductivity at the temperature of application of PEMECs. Further electrochemical characterization on the most resistant candidate among titanates, LiTi_2O_4 , showed that the material undergoes irreversible oxidation at the potentials of interest for the application as anode materials in PEMEC. Cr-based spinels showed excellent corrosion resistance to the chemical corrosion test. MnCr_2O_4 and $\text{MnCu}_{0.25}\text{Cr}_{1.75}\text{O}_4$ were further tested electrochemically, showing anodic and cathodic activity with reversibility character. The overall oxidation of the material is limited, and the doped material exhibited a better corrosion resistance upon cycling. Mixtures of IrO_2 with the spinel oxides under study showed that $\text{IrO}_2/\text{MnCu}_{0.25}\text{Cr}_{1.75}\text{O}_4$ produced a higher absolute current density at 2.0 V compared with the same amount of IrO_2 .

Acknowledgements

This work was funded by Innovation Fund Denmark via e-STORE project, contract no. 4106-00025B.

References

1. M. Carmo, D. L. Fritz, J. Mergel, and D. Stolten, *Int. J. Hydrogen Energy*, **38**, 4901–4934 (2013).
2. H.-S. Oh, H. N. Nong, T. Reier, M. Glied, and P. Strasser, *Chem. Sci.*, **6**, 3321–3328 (2015) <http://xlink.rsc.org/?DOI=C5SC00518C>.
3. T. Reier et al., *J. Electrochem. Soc.*, **161**, F876–F882 (2014) <http://jes.ecsdl.org/content/161/9/F876.abstract>.
4. L. M. Roen, C. H. Paik, and T. D. Jarvi, *Electrochem. Solid-State Lett.*, **7**, A19 (2004) <http://esl.ecsdl.org/cgi/doi/10.1149/1.1630412>.
5. M. P. Gurrola et al., *Int. J. Hydrogen Energy*, **39**, 16763–16770 (2014).
6. J. Xu, G. Liu, J. Li, and X. Wang, *Electrochim. Acta*, **59**, 105–112 (2012) <http://www.sciencedirect.com/science/article/pii/S0013468611015489>.
7. C. Hao, H. Lv, C. Mi, Y. Song, and J. Ma, *ACS Sustain. Chem. Eng.*, **4**, 746–756 (2016).
8. H. S. Oh et al., *J. Am. Chem. Soc.*, **138**, 12552–12563 (2016).
9. C. Spöri, J. T. H. Kwan, A. Bonakdarpour, D. P. Wilkinson, and P. Strasser, *Angew. Chemie - Int. Ed.*, **56**, 5994–6021 (2017) <http://doi.wiley.com/10.1002/anie.201608601>.
10. E. Oakton et al., *ACS Catal.*, **7**, 2346–2352 (2017) <http://pubs.acs.org/doi/10.1021/acscatal.6b03246>.
11. E. Stefan and J. T. S. Irvine, *J. Mater. Sci.*, **46**, 7191–7197 (2011).
12. E. Stefan, G. Tsekouras, and J. T. S. Irvine, *Adv. Energy Mater.*, **3**, 1454–1462 (2013) <http://doi.wiley.com/10.1002/aenm.201300361>.
13. A. La Fontaine, H. W. Yen, P. J. Felfer, S. P. Ringer, and J. M. Cairney, *Scr. Mater.*, **99**, 1–4 (2015) <http://dx.doi.org/10.1016/j.scriptamat.2014.09.028>.
14. K. E. Sickafus, J. M. Wills, and N. W. Grimes, *J. Am. Ceram. Soc.*, **82**, 3279–3292 (1999) <http://onlinelibrary.wiley.com/doi/10.1111/j.1151-2916.1999.tb02241.x/abstract>.
15. E. Stefan, P. a. Connor, A. K. Azad, and J. T. S. Irvine, *J. Mater. Chem. A*, **2**, 18106–18114 (2014) <http://xlink.rsc.org/?DOI=C4TA03633F>.
16. H. Hohl, C. Kloc, and E. Bucher, *J. Solid State Chem.*, **223**, 216–223 (1996).
17. Y.-Y. Zhu et al., *Chinese Phys. Lett.*, **31**, 97201 (2014) <http://stacks.iop.org/0256-307X/31/i=9/a=097201?key=crossref.7e911099ef32c5c35d5c8e837f589b7d>.
18. T. Sonehara, K. Kato, K. Osaka, M. Takata, and T. Katsufuji, *Phys. Rev. B*, **74**, 104424 (2006) <http://link.aps.org/doi/10.1103/PhysRevB.74.104424>.
19. Y. Huang, Z. Yang, and Y. Zhang, *J. Magn. Magn. Mater.*, **324**, 2075–2081 (2012) <http://dx.doi.org/10.1016/j.jmmm.2012.02.013>.
20. T. Inukai, T. Murakami, and T. Inamura, *Japanese J. Appl. Phys. Tak. Inukai al Jpn. J. Appl. Phys.*, **20** (1981).
21. D. C. Johnston, *J. Low Temp. Phys.*, **25**, 145–175 (1976).
22. C. W. Chen et al., *Mar. Pollut. Bull.*, **124**, 1106–1110 (2017) <http://dx.doi.org/10.1016/j.marpolbul.2017.01.078>.
23. L. J. van der Pauw, *Philips Res. Reports*, **13**, 1–11 (1958).

24. R. J. Cava, D. W. Murphy, S. Zahurak, A. Santoro, and R. S. Roth, *J. Solid State Chem.*, **53**, 64–75 (1984).
25. M. Isobe and Y. Ueda, *J. Alloys Compd.*, **383**, 85–88 (2004).
26. R. P. Liferovich and R. H. Mitchell, *Acta Crystallogr. Sect. B Struct. Sci.*, **60**, 496–501 (2004).
27. J. T. Mefford et al., *Nat. Commun.*, **7**, 11053 (2016) <http://www.nature.com/ncomms/2016/160323/ncomms11053/full/ncomms11053.html>.
28. R. K. B. Gover and J. T. S. Irvine, *J. Solid State Chem.*, **141**, 365–372 (1998).
29. K. Isawa, *Phys. Rev. B*, **49**, 1462–1465 (1994).
30. N. R. Arpun et al., *Chem. Mater.*, **26**, 4598–4604 (2014).
31. R. D. Shannon, *Acta Crystallogr. Sect. A*, **32**, 751–767 (1976).
32. R. J. Hill, J. R. Craig, and G. V. Gibbs, *Phys. Chem. Miner.*, **4**, 317–339 (1979).
33. C. Karatas, *J. Nucl. Mater.*, **168**, 144–150 (1989).
34. S. Winell, Ö. Amcoff, and T. Ericsson, *Phys. status solidi*, **245**, 1635–1640 (2008) <http://doi.wiley.com/10.1002/pssb.200743507>.
35. A. Petric and H. Ling, *J. Am. Ceram. Soc.*, **90**, 1515–1520 (2007).
36. W. Qu, L. Jian, J. M. Hill, and D. G. Ivey, *J. Power Sources*, **153**, 114–124 (2006).
37. A. J. Bard, R. Parsons, and J. Jordan, *Standard potentials in aqueous solution*, International Union of Pure and Applied Chemistry, (1985).
38. A. J. Bard and L. R. Faulkner, *Electrochemical Methods: Fundamentals and Applications*, John Wiley & Sons Inc, (2001).
39. T. Inukai, T. Murakami, and T. Inamura, *Jpn. J. Appl. Phys.*, **20**, L681–L682 (1981).